University of Bergen
Department of physics and technology

Investigation of nonlinear effects in piezoelectric discs and radiated sound field

By

Aslak Jentoft Thorbjørnsen

UNIVERSITY OF BERGEN

June, 2023

Abstract

Ferroelectric piezoceramics are inherently nonlinear and their behavior change with drive level. Nonlinear effects are especially prominent around the resonances of the piezoceramics, which is the commonly exploited feature in various applications. For transducers operating in gas, a significant impedance mismatch between the transmitter and medium limits the radiation efficiency, and higher drive levels are desirable to increase the signal-to-noise ratio.

A modified I-V circuit was configured in order to measure the impedance of soft piezoelectric ceramic discs for higher excitation levels around the two first radial modes and the thickness mode. The electrical behavior of the discs for different drive levels was further investigated through measured voltage and current signals. The radiated sound field of the discs for the various drive levels was then studied to determine the piezodiscs effect of different excitation amplitudes.

Changes to the discs' resonance frequencies and bandwidths were observed as the drive levels were increased. Distortion of the current and voltage signals across the piezoceramic discs revealed marginal harmonic distortion in the measured signals for the voltage drive levels utilized. Measurements of the radiated axial sound pressure and the propagated sound beam in air carried out for the two soft piezodiscs displayed seemingly linear sound propagation. Finite difference simulations for the acoustic radiation in air conducted for each disc supported the perception of linear sound propagation, and showed that losses in the medium due to nonlinear effects were minuscule for the transducer drive levels utilized. A nonlinear relation between the radiated sound field and the voltage excitation amplitude was however prominent, which indicates nonlinear behavior and losses in the piezoceramic discs themselves.

Acknowledgements

I would like to express my sincere gratitude to my supervisor Audun Oppedal Pedersen for guiding me through this work. His invaluable insights and devoted guidance through this work have been instrumental in the completion of this thesis.

I am also deeply grateful for the time and willingness to assist and guide me in the acoustic laboratory by doctoral research fellow Eivind Nag Mosland. The help and conversations have been most appreciated.

I would also like to thank Bilal Hasan Qureshi and Kjetil Vedelden Heitmann for their assistance along the way. I would further like to thank everyone in the Acoustic group, the staff in charge of the Ocean Technology study program, and other staff members at the Department of Physics and Technology for an accommodating and stellar academic environment.

Last, but not least, a heartfelt thank you to my friends and family for unwavering support and good conversations. A special thank you to the students at Ocean Technology for the impeccable companionship, wonderful memories, and enriching discussions over the last five years.

`Aslak J. Thorbjørnsen`
Thursday 1st June, 2023

Contents

List of Figures

List of Tables

Chapter 1

Introduction

1.1 Background and motivation

In the development of ultrasonic gas flow meters, a need for accurate measurements of the composition of the gas is necessary, and precise measurements of the speed of sound are needed. The potential of high precision sound velocity cells for natural gases under high pressures has been studied in [1], where the two- and three-way pulse-echo methods were investigated. These methods require precise measurements of the transit time Δt in the gas, which showed limitations due to the transducer drive level. The upper limit for the linear regime of the transducer investigated was set as low as 1 V_{pp} [1]. Drive levels of this amplitude displayed an increased variance in Δt attributed to flickering in the air, as a result of the low signal-to-noise ratio (SNR) due to the acoustic impedance mismatch between the transducer and gas. Higher excitation amplitudes are thus wanted but resulted in an increased measurement uncertainty, attributed to nonlinear effects [1].

Later work at the Institute of Physics and Technology has reported nonlinear effects for higher generator voltages, and further suggested that the effects observed are largely due to the piezoelectric material, and not the medium (air) [2]. The nonlinear behavior was especially prominent around resonances of the transducers tested, but less noteworthy outside this area. The sound pressure was found to increase less and less with higher amplitudes. Thus, a need for a better understanding of the nonlinear effects, and restrictions to transducer drive level so unwanted effects are limited [1, 2].

The use of piezoelectric ceramics under more extreme operating conditions, such as high-power acoustic transducers and electromechanical actuators [3], has led to the need for a better understanding of the material's behaviour [4, 5]. The use of bulk acoustic wave resonators in smartphones and telecommunications has also raised the need for a better understanding of the piezoelectric material, as it is found to expel problematic nonlinear behavior with increasing power levels [6, 7, 8].

Piezoelectric materials are most frequently described through linear relations which holds for relatively low levels of applied electric fields, but nonlinear behaviour become increasingly noticeable with higher field levels [4]. The performance of systems utilizing transducers driven at higher field levels becomes increasingly unstable, and thus significantly limited, as the nonlinear domain for piezoelectric ceramics is reached [9, 3].

Nonlinear behavior can however be desirable and is intentionally incorporated in some piezoelectric generators used in energy harvesting technologies that utilize the direct piezoelectric effect to exploit ambient vibration energy [10, 11]. The intention is to broaden the bandwidth of such harvesters by facilitating nonlinear behavior, thereby allowing for more efficient energy harvesting under random vibrations [10].

A variety of nonlinear phenomena linked to material imperfections in solids have been used for crack detection for several years, as they have proven more sensitive to crack identification compared to linear methods [12, 13, 14]. A crack in a material, which can be modeled as a nonlinear system, exhibits nonlinear symptoms when exposed to harmonic

input [13, 14]. Different excitation amplitudes are utilized, as the nonlinear response of the cracks becomes increasingly prominent [13], thus the need for accurate modeling of the transmitter becomes evident.

An accurate, but general, nonlinear model of piezoelectric elements is desirable to better understand the impacts of higher levels of applied electric field or stress [3, 5, 9, 7, 8]. Shim & Feld presented a nonlinear Mason model for thin piezoelectric film, where nonlinear terms are added as additional voltage sources to the linear Mason model [6, 7]. Determination of the significant nonlinear coefficients for such a model is a prerequisite and a difficult task that requires appropriate measurements relevant to the problem [6].

An increased excitation amplitude is desirable for transducers operating in gases, due to their low efficiency, as a result of the mismatch in acoustic impedance between transducers and gases. Intricate acoustic impedance matching of piezoelectric ceramics with backing and matching layers are a prerequisite to achieve desirable efficiency (for short pulses) [15]. Some applications incorporate impedance-matched acoustic metasurfaces using slits of gases such as argon and xenon to reduce the mismatched acoustic impedance and increase the efficiency of transducers operating in gases [16, 17, 18].

For research purposes focusing on transducer characterization, a higher amplitude is desirable to increase the signal-to-noise ratio with regard to, amongst other, characterization of the beam pattern [19].

1.2 Objective

The main objective of this thesis is to study the behavior of soft piezoelectric ceramic discs and their response to higher excitation amplitudes at resonance in air and separate the main contributor to the reported increased losses. A method of early detection of significant nonlinear effects would be desirable.

1.3 Thesis outline

The work carried out in this thesis is divided into seven chapters. Chapter 2 attends to some of the relevant theory to this thesis, including some characteristics of piezoelectric elements, theoretical expressions of piezoelectric discs as uniform pistons, and an elaboration of the KZK equation used for modeling nonlinear sound propagation. The third chapter is primarily divided into two parts. The first one covers the experimental setup and processing of the electrical measurements carried out, while the second part attends to the setup for acoustical measurements of piezoelectric transducers in air. Finite element and finite difference simulation are touched upon in Chapter 4. Chapter 5 presents the results of the piezodiscs, from electrical measurements and finite element simulation

of electrical properties, the effects of soldering, and acoustical pressure- and directivity measurements, accompanied by finite difference simulation results. Chapter 6 takes on a discussion of the results. Finally, chapter 7 concludes the thesis, and suggestions for further work are presented. An appendix containing supplementary figures, and MATLAB scripts, can be found at the very end of this document, following the bibliography.

Chapter 2

Theory

2.1 Modeling of piezoelectric ceramics

2.1.1 Electrical characteristics

Electrical measurements are commonly used to investigate and/or control the characteristics of a piezoelectric transducer [20, 21]. The electrical admittance is given as

$$\boldsymbol{Y}(f) = G(f) + iB(f) = |Y|e^{j(\omega t - \varphi_Y)}, \tag{2.1}$$

where $G(f)$ and $B(f)$ are the conductance and susceptance, respectively, ω is the angular frequency, and φ a corresponding phase term. The quantities $|Y|$, G and B are expressed in Siemens. The characterization can also be expressed as impedance, which is the reciprocal of the admittance, given as

$$\boldsymbol{Z}(f) = \frac{1}{\boldsymbol{Y}(f)} = R(f) + iX(f) = |Z|e^{j(\omega t - \varphi_Z)}, \tag{2.2}$$

where $R(f)$ and $X(f)$ are the resistance and reactance, respectively, and the quantities are expressed in Ohms. Both admittance and impedance serve their own purpose, often dependent on the equivalent circuit used for the electrical modeling of a transducer, and conversion from either one to the other is readily available. One can, e.g., find expressions of resistance and reactance, expressed through admittance, conductance, and susceptance as

$$\boldsymbol{Z} = R + iX = \frac{1}{\boldsymbol{Y}} = \frac{1}{G + iB} = \frac{G - iB}{G^2 + B^2} = \frac{G}{|Y|^2} - i\frac{B}{|Y|^2}, \tag{2.3}$$

which yields the expressions

$$R = \frac{G}{|Y|^2}, \quad X = \frac{-B}{|Y|^2}, \tag{2.4}$$

for the resistance and reactance, respectively.

Commonly, the transducer complex admittance as a function of frequency is plotted in the complex plane, known as a Kennelly diagram [20] or GB-plot [21]. From such a diagram, a multitude of quantities can be determined and derived, e.g., resonance frequencies and bandwidth, amongst others.

2.1.2 Piezoelectric constitutive equations

The piezoelectric constitutive equations in the linear approximations can be given in tensor notation as

$$T = c^E S - eE, \tag{2.5}$$

$$D = eS + \varepsilon^S E, \tag{2.6}$$

where T, S, E, and D, are the stress, strain, electric field, and dielectric displacement, respectively [6, 22]. All four are tensors of rank two. The variables c, e, and ε are material-specific coefficient matrices, and the superscript signifies that the values are given for a constant, e.g., electric field E.

From a linear Mason model, the voltage potential V on the electrical side of a equivalent circuit of a piezoelectric element, in a 1-dimensional case, can be stated as [6, 23]

$$V = -\int_{z_1}^{z_2} E dz \quad \Longrightarrow \quad V = \frac{1}{\varepsilon^S}\int_{z_1}^{z_2}(eS - D)dz, \tag{2.7}$$

where $z_2 - z_1$ is the thickness of the element, ε^S is the dielectric permittivity coefficient for constant strain, e is the piezoelectric charge coefficient (frequently denoted d in other literature, e.g., [4]), and the electric field is found by solving Eq. (2.6) above for E.

2.2 Resonance modes of piezoelectric discs

In the IEEE Standard on Piezoelectricity, the resonance frequency f_1 and antiresonance frequency f_2 are defined as the frequency of maximum admittance and -impedance, respectively, for a lossless resonator [24]. These critical frequencies have, for a lossy piezoelectric resonator, three associated frequencies each, $f_1 \rightarrow (f_m, f_s, f_r)$ and $f_2 \rightarrow (f_n, f_p, f_a)$. For f_1, they correspond to the frequency of maximum absolute admittance, maximum conductance, and zero susceptance, and for f_2, the frequency of maximum absolute impedance, maximum resistance, and zero reactance [24]. The critical frequencies exist for each of the resonance modes described in the two following sections.

2.2.1 Radial extensional modes

The radial extensional modes (R modes), also called radial dilatational modes [25] or just radial modes [26], to mention some, are the resonance modes with the lowest frequencies in piezoelectric discs [27, 28]. The latter is due to the diameter to thickness ratio (D/T) of such discs usually being large, thus making the R modes resonance frequencies significantly lower than that of other modes, e.g., thickness extensional modes (TE modes) [26]. Meaning that a thicker disc (lower D/T ratio) would make other resonance modes appear at lower frequencies, and thus shorten the frequency gap between the R modes and other modes. A feature of the radial modes is the contraction of the disc in the radial direction and an expansion in the thickness direction, as a result of Poisson's ratio effects [26]. Due to the changing thickness for the R modes, it too can be used to transmit and receive in the thickness direction.

In the case of a circular disc, the pattern of the R modes' expansion in the thickness direction follows multiples of $\lambda/2$ [29], where λ is the wavelength, and the displacement approaches zero towards the rim but can have various shapes following the order of the

mode. For the fundamental radial mode (R1), the displacement in the thickness direction is described by $\lambda/2$, so that there is maximum displacement in the center of the disc. Whereas the second radial mode (R2) corresponding to $3\lambda/2$, has both a minimum and maximum in the thickness direction. The minimum falls to the center of the disc, while the maximum displacement is found at about 3/4's of the distance from the center towards the rim moving from the center. An illustration of this is presented in Figure 2.1 below, for the three first radial modes.

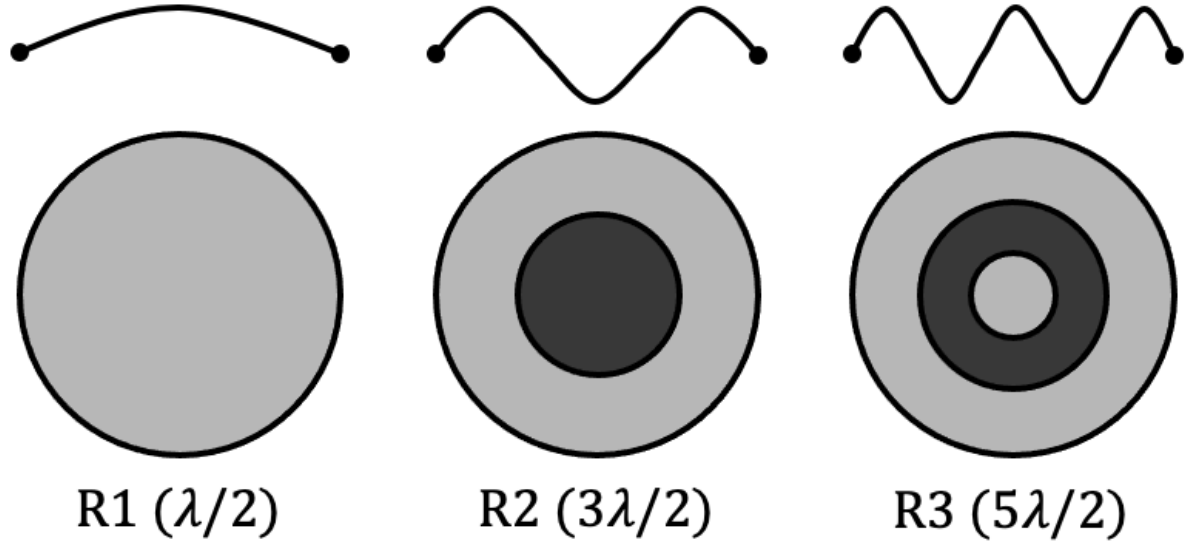

Figure 2.1: Illustration of the (idealized) displacement in the thickness direction of a circular disk for the first three radial modes (R1, R2, and R3).

2.2.2 Thickness extensional modes

The fundamental thickness extensional mode (TE mode) is the most commonly used extensional mode in transducer applications utilizing piezoelectric discs. Higher order modes of the fundamental TE mode are present in piezoelectric discs and said mode is therefore often denoted TE1 to distinguish it from those higher order modes [27]. At the TE1, a disc's vibration most resembles that of a plane piston, frequently used for modeling piezoelectric sources, e.g., in theoretical expressions found in [29, 30].

2.2.3 Resonance frequency

As described above, a piezoelectric element has multiple resonance modes originating from various mechanical properties. The resonance frequency f_s of such a mode can be found from an inspection of the conductance as a function of frequency, or through a GB-plot [21, 31]. Resonances appear as peaks in conductance, and the resonance frequency is defined as the frequency of maximum conductance. Thus, the frequency

interval considered has to be restrained to cover one of these peaks. The resonance frequency then yields

$$f_s = f|_{G(f)=\max\{G(f)\}} \quad \forall \quad f \in [f_l, f_u], \tag{2.8}$$

where f_l and f_u denote the minimum- (lower) and maximum (upper) frequency on the limited frequency interval in question. Increasing the frequency interval to cover a broader range of frequencies could lead to false results for a given mode, as new peaks in conductance appear, e.g., for higher radial- or thickness modes.

2.2.4 Bandwidth

Given a constant applied voltage amplitude, the electrical dissipated effect is proportional to conductance [21]. The -3 dB frequencies are then defined as the frequencies nearest f_s on either side of the peak, where the normalized dissipated effect, or conductance, equals one-half. This can be stated as

$$G(f^-_{-3\text{ dB}}) = G(f^+_{-3\text{ dB}}) = \frac{1}{2}G(f_s), \tag{2.9}$$

where $f^-_{-3\text{ dB}}$ and $f^+_{-3\text{ dB}}$ are the frequencies nearest f_s on the left- (negative superscript) and right (positive superscript) side, respectively. Normally, impedance analyzers utilize the constant voltage method [32] where the condition of the constant applied voltage is held, and Eq. (2.9) thus holds.

However, the prerequisite that the applied voltage remain constant over the measured frequency interval, cannot be guaranteed for all the measurements conducted in this thesis. Thus, an alternative description has to be used. The method described above can be used to locate the two frequencies f_s^- and f_s^+ where the conductance has been cut in half on either side of a resonance peak so that a bandwidth can be expressed as

$$\Delta f = f_s^+ - f_s^-. \tag{2.10}$$

In the following, Δf is referred to as the bandwidth, which is similar-, but not equivalent, to the -3 dB bandwidth.

Using the resonance frequency and corresponding bandwidth of a resonance mode, a mechanical quality factor Q_M can be stated as [21, 33]

$$Q_M = \frac{f_s}{\Delta f}, \tag{2.11}$$

where Δf usually is the 3 dB bandwidth, but here used with the bandwidth described previously. The quality factor serves as a measure of the sharpness of a resonance peak.

2.3 Acoustic source radiation

2.3.1 Radiation from a plane circular piston

A plane circular piston is frequently used as a model of an acoustic sound source and is particularly well suited to model a piezoelectric disc. The following model considered assume a piston to be mounted on a flat rigid baffle of infinite extent, and that the surface has uniform motion on its entirety [29]. The latter is, of course, a simplification of a real-life transducer, but remains useful for modeling purposes.

The derivation is based on the geometry and coordinate system depicted in Figure 2.2 below. A piston with radius a is mounted in the xy-plane, with the face of the piston in $z = 0$, so that the z-axis is perpendicular to the surface of the piston, and passes through its center. In this configuration, the acoustic axis aligns with the z-axis of the coordinate system. The distance from the center of the piston to any point in space is denoted r, and θ is the angle between the z-axis and a line drawn from the center of the piston to this point. The dashed line in the figure illustrates the difference between r and z-coordinates when $\theta \neq 0$. However, $r = z$ on the acoustic axis ($\theta = 0$).

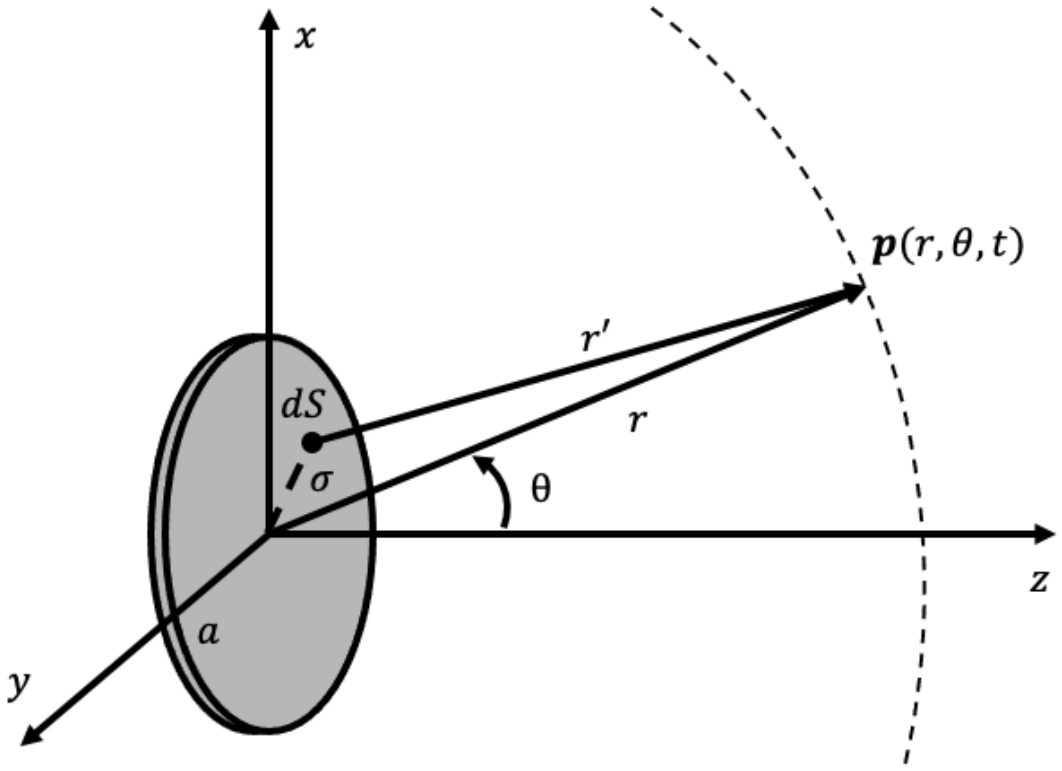

Figure 2.2: Illustration of the geometry and coordinate system used in derivation of the acoustic pressure for a plane circular piston.

The complex pressure is calculated for an arbitrary point in space by dividing the piston's surface S into infinitesimal small elements dS, where each element acts as a baffled simple

source [29], and integrating over the surface of the piston. The contribution of every little element dS to the total complex pressure can be expressed as [29]

$$\boldsymbol{p}(r,\theta,t) = j\rho_0 c_0 \left(\frac{u_0}{\lambda}\right) \int_S \left(\frac{1}{r'}\right) e^{j(\omega t - kr')} dS, \tag{2.12}$$

where ρ_0 is the ambient density of the radiation medium, c_0 the speed of sound of the medium, ω the angular frequency, k the wave number, and λ the wavelength. The piston moves uniformly with the speed $u_0 \exp(j\omega t)$ normal to the baffle, and r' is the distance from a simple source to the point in space shown in Figure 2.2 above.

The problem can be simplified by consideration of the pressure along the acoustic axis. Here, the pressure is given as [29]

$$\boldsymbol{p}(r,\theta=0,t) = j\rho_0 c_0 \left(\frac{u_0}{\lambda}\right) e^{j\omega t} \int_0^a \frac{\exp(-jk\sqrt{r^2+\sigma^2})}{\sqrt{r^2+\sigma^2}} 2\pi\sigma d\sigma, \tag{2.13}$$

where σ is the distance from the center of the piston to an infinitesimal element dS ($\sigma \leq a$), and $\sqrt{r^2+\sigma^2}$ is the distance r' from each of these elements to the point along the acoustic axis. Following the integration of Eq. (2.13) above, the pressure amplitude on the acoustics axis can be further expressed as a function of distance from the source, and yields [29]

$$P(r,\theta=0) = 2\rho_0 c_0 u_0 \left| \sin\left(\frac{1}{2} kr \left[\sqrt{1+(a/r)^2} - 1\right]\right)\right|. \tag{2.14}$$

Inspection of the argument of the sine expression reveals pressure extremes along the axis for values of r that satisfy

$$\frac{1}{2} kr \left[\sqrt{1+(a/r)^2} - 1\right] = m\pi/2, \qquad m = 0, 1, 2, ..., \tag{2.15}$$

originating from strong interference effects close to the source [29, 30] which is characteristic of the near field of a radiating source.

2.3.2 Directivity function of a plane circular piston

A common expression of directivity can be derived from the above model depicted in Figure 2.2, for small-signal radiation of a circular piston. Instead of dividing the piston into infinitesimal elements, the source is divided into line segments of different lengths parallel to the y-axis, so that the far-field point is on the acoustic axis of each line segment. Each line source's contribution to the field point is then, by imposing the restriction $r \gg a$, the far field axial pressure of the associated line source [29]. The angular dependency can be sorted into a separate term so that the far-field pressure amplitude can be given as

$$|\boldsymbol{p}(r,\theta)| = P_{\mathrm{ax}}(r) D(\theta), \tag{2.16}$$

where $P_{\text{ax}}(r)$ is the pressure amplitude on the acoustic axis, corresponding to $P(r, \theta = 0)$ in Eq. (2.14) above, and $D(\theta)$ is the directivity function. The latter is defined as [29, 30]

$$D(\theta) = \left| \frac{2J_1(v)}{v} \right|, \quad \text{where} \quad v = ka \sin \theta, \tag{2.17}$$

and J_1 is the Bessel function of the first kind.

In general, a range-independent expression for finite amplitude radiation does not exist but can be postulated for a quasi-linear case as elaborated in [30]. An accurate expression would, in addition to direction and dimension, be dependent on the excitation amplitude of the acoustic source.

2.3.3 Source sensitivity

The voltage source sensitivity of a piezoelectric transducer can be defined as the ratio of the acoustic sound pressure amplitude at the sound axis, taken at a reference distance d_0, and the corresponding exerted voltage amplitude [34]. The reference distance is typically set to 1 m. Thus, the expression becomes

$$|S_V| = \left| \frac{p(r = d_0, \theta = 0)}{V} \right|, \tag{2.18}$$

where V is the voltage applied to the source, and S_V has the unit of Pa/V at 1 m. The quantities p and V are typically given as effective values. Sensitivity describes the efficiency of electro-acoustic energy conversion, and is, amongst others, a suited indicator of transducer performance [35].

2.3.4 Sound pressure level

The sound pressure level (SPL) is defined as

$$\text{SPL} = 20\log_{10}\left(\frac{p_{\text{eff}}}{p_{\text{ref}}} \right), \tag{2.19}$$

where p_{ref} is the reference pressure amplitude of 20 µPa, for the current work in air.

2.3.5 Absorption

Waves propagating in a medium experience losses due to scattering and energy conversion, which is known as attenuation. The conversion of acoustic energy to other forms of energy is referred to as absorption and will be covered in the following.

A monochromatic, plane wave traveling along the acoustic sound axis in the $+r$ direction, can be expressed as

$$\boldsymbol{p}(r, \theta = 0, t) = P_0 e^{j(\omega t - kr)} e^{-\alpha r}, \tag{2.20}$$

where P_0 is the initial amplitude of the wave, and α the absorption coefficient in Neper per meter (Np/m).

The classical absorption coefficient for a gas under the Stokes assumption, $\eta_B = 0$, is [29]

$$\alpha_{\mathrm{c}} = \frac{\omega^2 \eta}{2\rho_0 c^3} \left(\frac{4}{3} + \frac{(\gamma - 1)}{\mathrm{Pr}} \right), \tag{2.21}$$

where Pr is the Prandtl number which relates the importance of viscosity with respect to thermal conductivity. The classical absorption coefficient shows good agreement with absorption in monatomic gases but falls short when it comes to polyatomic gases [29], as other loss mechanisms such as relaxation become relevant.

The time required to achieve equilibrium in a new thermodynamic state in a medium is referred to as relaxation time [36, 37]. Relaxation is linked with energy dissipation, and due to the frequency-dependent relation with the relaxation time of an acoustic disturbance, dispersion is also introduced. In the air, the vibration of oxygen and nitrogen molecules are the main contributors [30, 29, 38].

When variations in the phase speed as a function of frequency are only a small correction to a reference value, for example, c_0, dispersion is considered to be weak. In the case of sufficiently weak dispersion, variations in the waveform as a function of distance, are considered to be slow [30].

The classical absorption coefficient presented above does not account for relaxation mechanisms in the medium. Thus, a better description is desirable, and a more rigorous expression following the ANSI/ASA S1.26-2014 Methods for Calculation of the Absorption of Sound by the Atmosphere has to be utilized. The absorption coefficient α can be expressed as a sum of four terms [29, 39]

$$\alpha = \alpha_{\mathrm{c}} + \alpha_{\mathrm{rot}} + \alpha_{\mathrm{vib,O}} + \alpha_{\mathrm{vib,N}}, \tag{2.22}$$

where α_{c} is the classical absorption coefficient noted above, α_{rot} is an absorption term due to molecular rotation relaxation, and $\alpha_{\mathrm{vib,O}}$ and $\alpha_{\mathrm{vib,N}}$ denotes absorption as a result of molecular vibration relaxation of oxygen and nitrogen, respectively. The classical- and rotational attenuation term can be stated as [39]

$$\alpha_{\mathrm{c}} + \alpha_{rot} = a_{\mathrm{T}} b_{\mathrm{P}} f^2, \tag{2.23}$$

where a_{T} and b_{P} are pure temperature- and pressure dependent coefficients, respectively. Whereas the two latter terms of Eq. (2.22) are given as [29, 39]

$$\alpha_{\mathrm{vib,O}} = [(a\lambda)_{\mathrm{max,O}}] \left(\frac{f}{c}\right) \left(\frac{2f_{\mathrm{rO}}f}{f_{\mathrm{rO}}^2 + f^2}\right), \tag{2.24}$$

$$\alpha_{\mathrm{vib,N}} = [(a\lambda)_{\mathrm{max,N}}] \left(\frac{f}{c}\right) \left(\frac{2f_{\mathrm{rN}}f}{f_{\mathrm{rN}}^2 + f^2}\right). \tag{2.25}$$

Here $(a\lambda)_{\mathrm{max}}$ is the maximum absorption per wavelength due to vibrational relaxation, and f_{r} is the relaxation frequency, for the respective gases. A detailed elaboration on how to calculate Eqs. (2.23)-(2.25) are given in Appendix A.1 for completeness, but are not covered here. The main purpose of these three equations is to highlight the shared squared frequency dependency, which in turn comes to light in Eq. (2.26) below.

The final expression of the absorption coefficient sketched in Eq. (2.22) above, in decibels per meter (dB/m), are given in [39] as

$$\alpha = 8.686 f^2 \left(\begin{array}{c} \left[1.84 \times 10^{-11} \left(\frac{p_{\mathrm{a}}}{p_{\mathrm{r}}}\right)^{-1} \left(\frac{T}{T_{\mathrm{r}}}\right)^{\frac{1}{2}}\right] + \left(\frac{T}{T_{\mathrm{r}}}\right)^{-\frac{5}{2}} \\ \times \left\{ 0.01275 \left[\exp\left(\frac{-2239.1}{T}\right)\right] \left[\frac{f_{\mathrm{rO}}}{f_{\mathrm{rO}}^2 + f^2}\right] \right. \\ \left. +0.1068 \left[\exp\left(\frac{-3352.0}{T}\right)\right] \left[\frac{f_{\mathrm{rN}}}{f_{\mathrm{rN}}^2 + f^2}\right] \right\} \end{array} \right), \tag{2.26}$$

where the factor 8.686 yields a conversion from Np/m to dB/m. Thus, removing this factor in Eq. (2.26 yields the absorption coefficient in Np/m.

2.4 Nonlinear sound propagation

2.4.1 Coefficient of nonlinearity

The ratio B/A originates from the Taylor series expansion of the pressure as a function of density, for constant specific entropy ($s = s_0$), and has become a common term in the field of nonlinear acoustics [30]. The Taylor series expansion with the two first terms is given as

$$P - P_0 = \left(\frac{\partial P}{\partial \rho}\right)_{s,0} (\rho - \rho_0) + \frac{1}{2!} \left(\frac{\partial^2 P}{\partial \rho^2}\right)_{s,0} (\rho - \rho_0)^2 + \cdots, \tag{2.27}$$

where ρ and P are the density and pressure, respectively, and the subscript zero denotes their unperturbed values. The subscript $s, 0$ denotes that the partial derivatives are to be evaluated at the unperturbed state (ρ_0, s_0). Equation (2.27) can be written as [30]

$$p = A \left(\frac{\rho'}{\rho_0}\right) + \frac{B}{2!} \left(\frac{\rho'}{\rho_0}\right)^2 + \frac{C}{3!} \left(\frac{\rho'}{\rho_0}\right)^3 + \cdots, \tag{2.28}$$

where $p = P - P_0$ is the sound pressure, and $\rho' = \rho - \rho_0$ is the excess density, and [30]

$$A = \rho_0 \left(\frac{\partial P}{\partial \rho}\right)_{s,0} \equiv \rho_0 c_0^2, \tag{2.29}$$

$$B = \rho_0^2 \left(\frac{\partial^2 P}{\partial \rho^2}\right)_{s,0}, \tag{2.30}$$

$$C = \rho_0^3 \left(\frac{\partial^3 P}{\partial \rho^3}\right)_{s,0}, \tag{2.31}$$

where ρ_0 is the ambient value of the density and c_0 is the isentropic small-signal sound speed. The parameters B and A are proportional to the quadratic and linear terms in the Taylor series, respectively. The following expression of the quantity B/A

$$\frac{B}{A} = \frac{\rho_0}{c_0^2} \left(\frac{\partial^2 P}{\partial \rho^2}\right)_{s,0}, \tag{2.32}$$

requisites that the density is adiabatically varied, as noted by the authors in [40].

Using the relation $c^2 = (\partial P/\partial \rho)_s$ [30] for the sound speed c, Eq. (2.28) can be rewritten as

$$\frac{c^2}{c_0^2} = 1 + \frac{B}{A}\left(\frac{\rho'}{\rho_0}\right) + \frac{C}{2A}\left(\frac{\rho'}{\rho_0}\right)^2 + \cdots, \tag{2.33}$$

By taking the square root of Eq. (2.33) and performing a binomial expansion, one obtains [30]

$$\frac{c}{c_0} = 1 + \frac{B}{2A}\left(\frac{\rho'}{\rho_0}\right) + \frac{1}{4}\left[\frac{C}{A} - \frac{1}{2}\left(\frac{B}{A}\right)^2\right]\left(\frac{\rho'}{\rho_0}\right)^2 + \cdots, \tag{2.34}$$

Discarding higher order terms and substituting the linear relation for a progressive, locally plane wave $\rho'/\rho = u/c_0$ [29, 30] into the right-hand side of Eq. (2.34) one obtains

$$c = c_0 + (B/2A)u, \tag{2.35}$$

where u is the particle velocity. The local propagation speed of a point with constant phase becomes [30]

$$dx/dt|_u = c_0 + \beta u, \qquad \beta = 1 + B/2A, \tag{2.36}$$

with β referred to as the coefficient of nonlinearity [41, 30]. Visiting the expression of the shock formation distance due to nonlinearity in the medium, which for a plane wave that is sinusoidal at the source, is given as $\overline{x} = 1/\beta\varepsilon k$, it becomes apparent that β is the significant measure of the acoustic nonlinearity [30, 29]. Here $\varepsilon = u_0/c_0$ is the acoustic Mach number, with u_0 the peak particle velocity at the source.

2.4.2 Basic Equations

The four basic equations needed to describe the general motion of a heat-conducting, viscous fluid are mass conservation, momentum conservation, entropy balance, and thermodynamic state [30]. Assumptions of the fluid are that of homogeneous composition, uniform pressure, and density at an unperturbed state, and neglection of the dependence of the heat conduction and viscosity coefficients on the disturbance due to the sound wave [30]. The latter assumption anticipates the ordering scheme introduced in Section 2.4.3 (dissipation terms are retained to lowest order) in order to reach the Khokhlov-Zabolotskaya-Kuznetsov (KZK) equation.

The equation of mass conservation, or continuity, is

$$\frac{D\rho}{Dt} + \rho \boldsymbol{\nabla} \cdot \boldsymbol{u} = 0, \tag{2.37}$$

where $\boldsymbol{u}$ is the fluid velocity vector, ρ is the mass density, and $D/Dt = \partial/\partial t + \boldsymbol{u} \cdot \boldsymbol{\nabla}$ is the material time derivative [30]. The equation of momentum can be stated as

$$\rho \frac{D\boldsymbol{u}}{Dt} + \boldsymbol{\nabla} P = \mu \nabla^2 \boldsymbol{u} + (\mu_B + \frac{1}{3}\mu) \boldsymbol{\nabla}(\boldsymbol{\nabla} \cdot \boldsymbol{u}), \tag{2.38}$$

where μ is the shear viscosity, and μ_B is the bulk viscosity.

Assuming that all relaxation times are much shorter than the acoustic disturbance, the entropy equation takes the form of [30]

$$\rho T \frac{Ds}{Dt} = \kappa \nabla^2 T + \mu_B (\boldsymbol{\nabla} \cdot \boldsymbol{u})^2 + \frac{1}{2}\mu \left(\frac{\partial u_i}{\partial x_j} + \frac{\partial u_j}{\partial x_i} - \frac{3}{2}\delta_{ij} \frac{\partial u_k}{\partial x_k} \right)^2, \tag{2.39}$$

where κ is the thermal conductivity, and T is the absolute temperature. The last term in Eq. (2.39) uses Cartesian tensor notation where u_i is the component of $\boldsymbol{u}$ in direction x_i, and δ_{ij} is the Kronecker delta, equal to unity for $i = j$ and zero otherwise [30].

Lastly, the equation of state in terms of (P, ρ, s) variables, which for a perfect gas (both $P/\rho T$ and the specific-heat ratio are constants), can be expressed in explicit form as

$$P/P_0 = (\rho/\rho_0)^\gamma \exp[(s - s_0)/c_v], \tag{2.40}$$

where $\gamma = c_p/c_v$ is the ratio of specific heats at constant pressure (c_p) and volume (c_v) [30].

2.4.3 Approximations for thermoviscous fluids

To reach a model describing three-dimensional finite-amplitude sound fields for dissipative fluids, an approximation scheme based on Eqs. (2.37)-(2.40) are sought. Such a

description, to the second order in the acoustic Mach number

$$\varepsilon = \frac{u_0}{c_0}, \tag{2.41}$$

where u_0 denotes the magnitude of a typical acoustic velocity, is desirable. The Mach number takes the value of $\varepsilon = 10^{-2}$ for 154 dB (re 20 µPa) in air and 264 dB (re 1 µPa) in water, which serves as an indication of its suitability as a small ordering parameter [30].

However, if all $\mathrm{O}(\varepsilon^2)$ terms are retained the description will remain too complex and cumbersome to handle. Thus, for situations of practical interest, a second small parameter η is desirable to determine what terms can be neglected in order to further reduce the problem [30]

$$\eta = \frac{\mu\omega}{\rho_0 c_0^2}. \tag{2.42}$$

Here η is a measure of the importance of viscous stresses in a plane progressive sound wave, relative to the fluctuating pressure, and μ is the shear viscosity of the fluid. The ordering scheme sought makes it possible to discard terms of higher order than $O(\eta)$, and $O(\varepsilon^2)$ that are zero order in η, in Eqs. (2.37)-(2.40) [30].

Small disturbances with respect to a uniform state of rest, are described through the variables $p = P - P_0$, $\rho^{'} = \rho - \rho_0$, $T^{'} = T - T_0$, $s^{'} = s - s_0$, and $\boldsymbol{u}$, for a viscous heat-conducting fluid. Dispersion relations can be found for three "modes" of small-signal disturbances in an unbounded fluid, based on linearized versions of Eqs. (2.37) to -(2.40) [30]. These three modes are called the acoustic, vorticity, and entropy (or thermal) modes, and are related as follows

$$\boldsymbol{u} = \boldsymbol{u}_{\mathrm{ac}} + \boldsymbol{u}_{\mathrm{vor}} + \boldsymbol{u}_{\mathrm{ent}}, \tag{2.43}$$

where the coupling of the modes occurs by inflicting boundary conditions. For example, an inbound acoustic disturbance is scattered by the boundary, and reflected fields are produced in all three modes. The magnitudes of the right-hand side of Eq. (2.43) can be shown to be related as [30]

$$|\boldsymbol{u}_{\mathrm{vor}}/\boldsymbol{u}_{\mathrm{ac}}| \simeq e^{-x/l_{\mathrm{vor}}}, \quad |\boldsymbol{u}_{\mathrm{ent}}/\boldsymbol{u}_{\mathrm{ac}}| \simeq [(\gamma-1)/\mathrm{Pr}^{1/2}]\eta^{1/2} e^{-x/l_{\mathrm{ent}}} \tag{2.44}$$

close to a boundary with incident acoustic waves. Here, l_{vor} and l_{ent} are the boundary-layer thicknesses, which for small η are only a tiny fraction of an acoustic wavelength, and x is the distance to the boundary. Pr is the Prandtl number which is O(1) in terms of ε and η [30].

Due to the exponential decay factors in Eq. (2.44), the modes of vorticity and entropy are effectively absent outside the thermoviscous boundary layer. The latter is used to reduce the number of terms in the equation of momentum and the entropy equation in order to reach appropriate model equations.

A generic small parameter $\tilde{\varepsilon}$ that characterizes the smallness of both ε and η is introduced to simplify further derivation. Model equations valid at $\mathrm{O}(\tilde{\varepsilon}^2)$ outside thermoviscous boundary layers are derived using the above approximations and simplifications to

reach a wave equation of second order, which is the foundation of the Westervelt equation introduced in the following section.

2.4.4 KZK Equation

The KZK equation accounts for the combined effects of nonlinearity, absorption, and diffraction in directional sound beams, and is the most widely used model. To reach the KZK equation, one has to start with the Westervelt equation, given as [30]

$$\Box^2 p + \frac{\delta}{c_0^4}\frac{\partial^3 p}{\partial t^3} = -\frac{\beta}{\rho_0 c_0^4}\frac{\partial^2 p^2}{\partial t^2}, \tag{2.45}$$

where the operator $\Box^2 = \nabla^2 - c_0^{-2}(\partial^2/\partial t^2)$ is known as the d'Alembertain operator, and δ is the diffusivity of sound given as

$$\delta = \frac{1}{\rho_0}\left(\frac{4}{3}\mu + \mu_B\right) + \frac{\kappa}{\rho_0}\left(\frac{1}{c_v} - \frac{1}{c_p}\right) = \nu\left(\frac{4}{3} + \frac{\mu_B}{\mu} + \frac{\gamma - 1}{\mathrm{Pr}}\right), \tag{2.46}$$

where $\nu = \mu/\rho_0$ is the kinematic viscosity. The last term, $\nu(\gamma - 1)/\mathrm{Pr}$, accounts for heat conduction, and is typically more significant for gases than for liquids [30].

The validity of the Westervelt equation, from which the KZK equation is derived, depends on the approximation $\tilde{p} \simeq p$, where the variable $\tilde{p}$ is given as [30]

$$\tilde{p} = p + \frac{\rho_0}{4}\left(\nabla^2 + \frac{1}{c_0^2}\frac{\partial^2}{\partial t^2}\right)\phi^2, \tag{2.47}$$

and ϕ is the velocity potential of the medium. The solution of the Westervelt equation for p thus differs from the auxiliary solution $\tilde{p}$ by a function only depends on the local properties of the sound field. In other words, when local nonlinear effects can be neglected in comparison to cumulative nonlinear effects, the Westervelt equation is an appropriate approximation of the full second-order wave equation. This neglection of local effects is reasonable for distances more than a wavelength away from the source, and for directional sound beams [30].

The geometry of the problem is similar to the illustration in Figure 2.2, but here described in Cartesian coordinates (xyz-space). Assumptions regarding the source are that it is defined in the plane $z = 0$, that it has characteristic radius a, and that it radiates at frequencies satisfying $ka \gg 1$, i.e., the beam is reasonably directional (narrow main lobe). The latter condition is fulfilled in the far field [30], where the transition from the near field to the far field is said to occur for $z > \frac{1}{2}ka^2$. The distance $\frac{1}{2}ka^2$ is known as the Rayleigh distance, denoted $r_0 = \frac{1}{2}ka^2$ in [30], but other (equivalent) descriptions of the transition to the far field, such as $z > \frac{\pi a^2}{\lambda}$ in [29], can be found in the literature.

To reach the KZK equation, the following slow scale is introduced

$$p = p(x_1, y_1, z_1, \tau), \quad (x_1, y_1, z_1) = (\tilde{\varepsilon}^{1/2}x, \tilde{\varepsilon}^{1/2}y, \tilde{\varepsilon}z), \quad \tau = t - z/c_0. \tag{2.48}$$

where τ is the retarded time, and $\tilde{\varepsilon}$ is the generic parameter of smallness introduced previously. The slow scale is then applied to the Westervelt equation, where the Laplacian operator transforms into

$$\nabla^2 = \tilde{\varepsilon}\left(\frac{\partial^2}{\partial x_1^2} + \frac{\partial^2}{\partial y_1^2}\right) + \tilde{\varepsilon}^2\frac{\partial^2}{\partial z_1^2} - \tilde{\varepsilon}\frac{2}{c_0}\frac{\partial^2}{\partial z_1 \partial \tau} + \frac{1}{c_0^2}\frac{\partial^2}{\partial \tau^2}, \tag{2.49}$$

and the Westervelt equation yields, after discarding $\mathrm{O}(\tilde{\varepsilon}^3)$ terms,

$$\tilde{\varepsilon}\left(\frac{\partial^2}{\partial x_1^2} + \frac{\partial^2}{y_1^2}\right)p - \tilde{\varepsilon}\frac{2}{c_0}\frac{\partial^2 p}{\partial z_1 \partial \tau} + \frac{\delta}{c_0^4}\frac{\partial^3 p}{\partial \tau^3} = -\frac{\beta}{\rho_0 c_0^4}\frac{\partial^2 p^2}{\partial \tau^2}, \tag{2.50}$$

expressed on the slow scale. Conversion back to Cartesian coordinates yields the final expression

$$\frac{\partial^2 p}{\partial z \partial \tau} - \frac{c_0}{2}\nabla_\perp^2 p - \frac{\delta}{2c_0^3}\frac{\partial^3 p}{\partial \tau^3} = \frac{\beta}{2\rho_0 c_0^3}\frac{\partial^2 p^2}{\partial \tau^2}, \tag{2.51}$$

known as the KZK equation, where $\nabla_\perp^2 = \partial^2/\partial x^2 + \partial^2/\partial y^2$ is a Laplacian that operates in the xy-plane perpendicular to the beam axis.

2.5 Nonlinearity in piezoelectric ceramics

2.5.1 Origin and categorization

Piezoelectric ceramics (piezoceramics) are by construction exposed to a strong electric field to polarize the material (in a preferred polarization direction) in order to induce a piezoelectric response to the ceramics. The relation between the polarization and electric field is nonlinear for high field strengths, and thus it follows that the dielectric properties of piezoceramics are inherently nonlinear [4, 42]. This nonlinear relationship is attributed to the reorientation of spontaneous polarization caused by the electric field, which in turn produces a corresponding change in strain [4]. Thereby, a nonlinear piezoelectric strain-electric field response is also inherent for piezoelectric ceramics. Applied mechanical stress can cause reorientation of ferroelectric domains in piezoceramics, and thus a nonlinear strain-stress relationship too is inherent for piezoceramics [4].

The nonlinear behavior of piezoceramics can be divided into three main categories; dielectric, piezoelectric, and elastic (mechanical) nonlinearity, with corresponding losses [4, 3, 43]. The two latter have received relatively little attention, among other things, due to increased complexity [4]. The authors of [44, 45, 46] looked into the mechanical nonlinear behavior of piezoelectric ceramics. It was in [45] found a nonlinear characterization with dependence on all three categories mentioned above to the mean stress

amplitude in the resonant piezoceramic.

The dielectric properties have on the other hand been studied to a greater extent, as investigations are more easily approachable through electrical measurements. The dielectric and mechanical losses are considered to be independent of each other, while the existence of piezoelectric losses is based on the other two [3]. The mechanical losses are however found to be more prominent than the dielectric losses for devices operation around resonance, as noted in [43].

A threshold field level E_t was identified by [47], where electric field strengths E_0 weaker than this threshold did little to the dielectric properties. Whereas field amplitudes $E_0 > E_t$ caused a significant increase in the dielectric permittivity and loss. Values of the threshold field level are dependent on the type of material, and somewhat arbitrary defined [4], but typical values for soft PZT (lead zirconate titanate piezoelectric ceramics) are 10 V/mm, and 300 V/mm for hard PZT [48].

Further work by the authors [48, 49], specifically on hard PZT elements, showed a clear distinction between three electric field dependent regions; a 'low field' region ($E_0 < E_t$), an intermediate region called the Rayleigh region ($E_t < E_0 < E_c$), and a 'high field' region ($E_c < E_0$). Here E_c denotes the coercive field strength, which marks the transition between the Rayleigh region and the high field region, and for $E_0 > E_c$ introduces irreversible effects causing degradation of the transducer. Values of E_c were found to range between ± 0.9 kV/mm to ± 2.3 kV/mm for hard PZT elements tested by [49].

The real part of the dielectric permittivity ε' was investigated by [48, 49], and found to remain reasonably constant in the low field region, as noted above. However, for field strengths greater than E_t, the values of ε' showed a nearly linear increase with E_0. Eventually, for $E_0 > E_c$, the permittivity displayed an exponential increase. The preceding investigation was carried out for hard PZT, but this behavior of dielectric properties was proposed to apply to all types of ferroelectric ceramics [4]. Due to the incredibly low threshold field levels found for soft PZT, the low field region becomes close to indistinguishable from the Rayleigh region [48]. Thus, the assumption of constant dielectric material values falls short, and the need for better modeling becomes apparent.

2.5.2 Harmonic generation

Generation of higher-order electric current or stress signals from a pure sinusoidal time-dependent electric field $E = E_0 \sin(\omega t)$, are typical characteristics of nonlinearity in the dielectric and piezoelectric properties in piezoelectric ceramics [4]. This effect is more significant for devices driven around resonance, as was noted by the authors in [9]. Significant harmonic generation and distortion of the current were observed to increase with the excitation level of the device.

A study carried out by the authors of [50] found that material nonlinearities led to

the generation of harmonic voltage signals. The piezoelectric transducer was in this case driven by a pure sinusoidal current density $J = J_0 \sin(\omega t)$. A polynomial relation explaining the harmonic voltage signals was presented as [50]

$$E = -hx + \beta'' J + \gamma' J^2 + \xi' J^3, \tag{2.52}$$

where h is a piezoelectric voltage coefficient, and β'', γ', and ξ' are constants related to the linear and nonlinear dielectric coefficients [4].

2.5.3 Nonlinear piezoelectric constitutive equations

When a linear model of a piezoelectric transducer is unsatisfactory, an accurate nonlinear description is needed [9, 3, 6, 7]. One such model is presented in [6] as an expansion of the linear Mason equivalent circuit and the linear piezoelectric constitutive equations described in Section 2.1.2. Here, the nonlinear contributions are added in terms of additional nonlinear voltage sources to both the electrical and acoustic branches of the circuit.

The nonlinear piezoelectric constitutive equations are written in [6] as

$$T = c^E S - eE + \Delta T, \tag{2.53}$$

$$D = eS + \varepsilon^S E + \Delta D, \tag{2.54}$$

where the arbitrary nonlinear terms are represented by ΔT and ΔD, which both are a function of E and S. The nonlinear terms have to obey Lippmann's relation as a requirement for the conservation of energy, and ignoring body force, the relation yields [6]

$$\left.\frac{\partial T}{\partial E}\right|_S = -\left.\frac{\partial D}{\partial S}\right|_E, \tag{2.55}$$

meaning that a change in the electric field has an accompanying change in stress, for constant applied strain. Similarly, for a constant applied electric field, a change in strain yields a corresponding change in the dielectric displacement.

In general, there are $n+2$ independent nonlinear coefficients in the n^{th} power nonlinearity, and including only the 2^{nd} order nonlinearity terms gives [6]

$$\Delta T = -\delta_1 eSE + \delta_2 \varepsilon^S E^2/2 + \delta_3 c^E S^2/2, \tag{2.56}$$

$$\Delta D = \delta_1 eS^2/2 - \delta_2 \varepsilon^S SE + \delta_4 \varepsilon^S \frac{e}{c^E}\frac{E^2}{2}, \tag{2.57}$$

where δ_1 to δ_4 are dimensionless material-specific constants.

The nominal voltage potential in a Mason equivalent circuit follows Eq. (2.7), but with the addition of nonlinear voltage sources V_c to the circuit, modeled in [6] as

$$V_c = \frac{1}{\varepsilon^S}\int_{z_1}^{z_2} \Delta D dz, \tag{2.58}$$

where again the integral is taken over the thickness of the piezoelectric element, and ΔD is given in Eq. (2.57). The nonlinear voltage source V_c was derived based on a thin piezoelectric film, but the equivalent circuit may be extended by adding a cascade of the additional voltage sources to the circuit, to model other devices [6].

An alternative expression of the nonlinear contributions to the stress is presented in [9] as

$$T = cS + eE + \alpha_1 S^2 + \gamma SE, \tag{2.59}$$

where α_1 and γ are referred to in [9] as the nonlinear piezoelectric coefficients. The main differences between Eq. (2.53) and -(2.59) can be seen by comparing the complete ΔT term in Eq. (2.56) to Eq. (2.59). In the first equation, three contributions are included, namely SE, S^2, and E^2. While in the latter, only two terms, S^2 and SE are taken into account, and the purely electric field-dependent term E^2 is excluded.

Another approximate model to nonlinear piezoelectric constitutive equations was presented by [51], where equations of the stress T and electric field E were found in terms of both higher-order (separate) terms of S and D, as well as cross terms of the two.

Chapter 3

Experimental setup and measurement methods

3.1 Piezoelectric transducers

In this thesis, both electric- and acoustic measurements were carried out using two piezoelectric discs of different dimensions. The piezoelectric discs are made of soft PZ27 material produced by Ferroperm [52], and have the measured dimensions listed in Table 3.1 below.

The diameter and thickness of each disc were measured at different points, with ten measurements in total per dimension. The listed quantities are the averaged values. The measurements were conducted with a micrometer of type Mitutoyo 293-100-10, which have a systematic uncertainty of 0.0005 mm. Uncertainties in the table were calculated in accordance with the Type A evaluation of standard uncertainty following JCGM 100:2008 Evaluation of measurement data - Guide to the expression of uncertainty in measurement [53].

Table 3.1: Dimensions of the piezoelectric discs as measured with a digital micrometer. Listed values are the average of ten measurements, and the uncertainty computed according to Type A evaluation of standard uncertainty.

Piezoelectric disc	**Diameter [mm]**	**Thickness [mm]**
PZ27 20x2 mm	20.131 ± 0.005	1.996 ± 0.001
PZ27 13x2 mm	12.880 ± 0.006	2.0009 ± 0.0008

An impedance analyzer of type HP 4192A was initially used to characterize the piezoelectric discs in the frequency range of 1 kHz to 1300 kHz. Special attention, in the form of finer sampling in the frequency domain, was paid to the 1st and 2nd radial modes (R1 and R2), and the thickness mode (TE1) of the discs.

3.2 Impedance measurement circuit

The commercial impedance analyzers available at the acoustic laboratory at the Department of Physics and Technology (IFT) have maximum excitation voltages at about one volt root mean square (RMS). To enable impedance measurements of the piezoelectric elements with higher excitation amplitudes, a suitable circuit had to be utilized. One simple way to achieve this was to measure the voltage drop over a known shunt resistor in series with the device under test (DUT), known as the I-V method for impedance measurements [54, 55, 56]. The I-V method usually requires a voltage differential probe to measure the current flow in the circuit, and due to this being available, a modified circuit involving two voltage measurements is utilized [54, 55].

Measuring the voltage drop $\Delta \boldsymbol{V}$ across an accurately known resistor, the current in

the series circuit can be calculated, and the unknown impedance of the DUT can be determined. The expression of $\boldsymbol{Z_{DUT}}$ yields

$$\boldsymbol{Z_{DUT}} = \frac{\boldsymbol{V_2}}{\boldsymbol{I}} = \frac{\boldsymbol{V_2}}{\boldsymbol{V_1 - V_2}} R, \qquad \boldsymbol{I} = \frac{\Delta \boldsymbol{V}}{R} = \frac{\boldsymbol{V_1 - V_2}}{R}, \tag{3.1}$$

where $\boldsymbol{V_1}$ is the measured voltage across the signal generator output terminal, and $\boldsymbol{V_2}$ is the voltage across the DUT. The current $\boldsymbol{I}$ running through the circuit is mirrored for both the resistor R and the DUT. A sketch of the measurement circuit is presented in Figure 3.1 below.

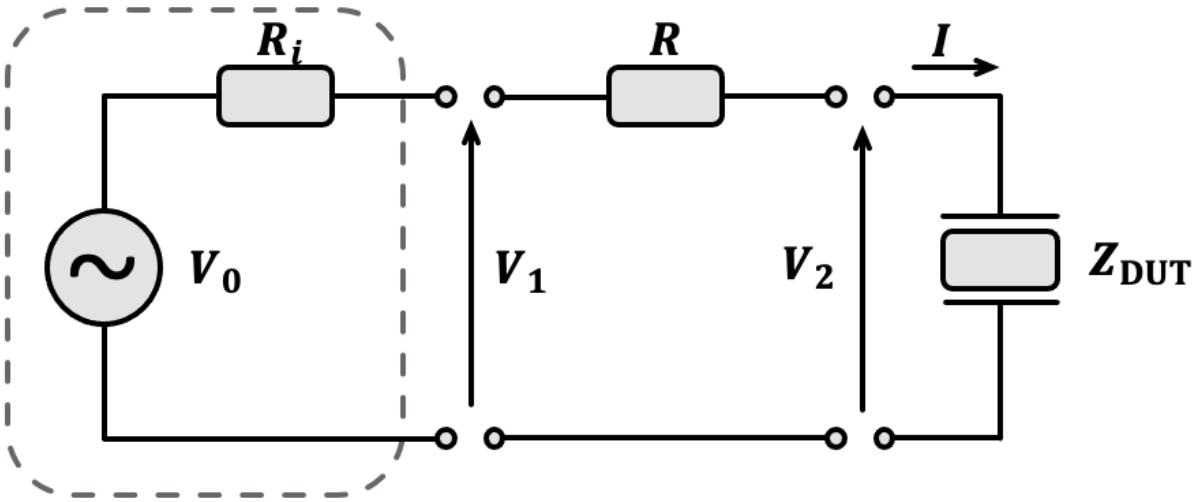

Figure 3.1: Schematic of the I-V measurement circuit used to determine the impedance of the DUT. The grey, dashed line to the left symbolizes the Agilent 33220A signal generator. The voltages $\boldsymbol{V_1}$ and $\boldsymbol{V_2}$ are measured with a Tektronix DPO3012 oscilloscope.

When operating the signal generator, the voltage displayed on the front panel assumes 50 Ω termination, which is the default setting. It can however be given an alternative output termination value as specified by the user. The chosen output termination has to match the actual load of the circuit to correctly display the voltage amplitude and offset on the output terminal. In other words, if the load of the circuit does not match the output termination, the displayed amplitude and offset on the signal generator display will be incorrect [57]. With the 50 Ω termination setting, the maximum peak-to-peak amplitude is 10 V_{pp}. After changing the output termination to *high impedance* (>10 kΩ) the same amplitude is displayed as 20 V_{pp}. In any case, it has to be measured on the output terminal to know the actual voltage applied to the circuit, which is the voltage here denoted as $\boldsymbol{V_1}$.

Listed in Table 3.2 are the instruments and other equipment used in the experimental setup of this impedance measurement circuit.

Table 3.2: Equipment used in the impedance measurements circuit. An illustration of the circuit is presented in Figure 3.1.

Model/Brand	**Equipment**
Agilent 33220A	Signal generator
Tektronix DPO3012	Oscilloscope
Agilent 34410A	Benchtop multimeter
Ferroperm PZ27	Piezoelectric disc
N/A	Coaxial cables
N/A	Banana connectors
N/A	Pinches
N/A	Electrical wire
N/A	A piece of styrofoam
N/A	Breadboard

3.2.1 Determination of resistor $\boldsymbol{R}$

It is desirable to choose a sufficiently low value of the resistor R to ensure the highest possible excitation of the DUT. The ideal resistor R in the circuit has a resistance as close to zero as possible, but large enough to enable measurement of the voltage drop in order to calculate the current $\boldsymbol{I}$. The value of R depends both on the applied voltage from the signal generator as well as the specifications of the oscilloscope.

The oscilloscope has vertical scales from 1 mV per division (mV/div) to 10 V/div, and stores the waveform as 16-bit signed integers in the case of 2-byte data. In this mode, there are 6400 digitizing levels per vertical division [58]. However, the analog to digital converter (ADC) is 8-bit and limits the resolution. Higher resolution (than 8-bit) can still be achieved by repeated averaging, where the resulting effective bits attainable follow $8 + \frac{1}{2}\log_2(N)$, where N is the number of averages. However, this number converges and a roof of about 12 bits with repeated averaging is talked about [19]. It is thus desirable to find a low value of the resistor while still being able to differentiate the two measured voltages in the presence of noise.

As mentioned above, the signal generator has an internal, fixed series output impedance of 50 Ω denoted R_i. The impedance of the DUT are denoted $\boldsymbol{Z}_{\mathbf{DUT}}$. The total voltage in a series circuit is the sum of the individual voltage drops around the circuit. From Figure 3.1 above, there are three directed potentials in the sketched circuit. Firstly, a voltage drop across the internal impedance matching resistor in the signal generator. Secondly, a drop over the known resistor R, and lastly, a voltage drop across the DUT. Following Kirchhoff's second law, which can be stated as

$$\sum_{k=1}^{n} \boldsymbol{V}_k = 0, \tag{3.2}$$

for n directed potential differences in a circuit. The I-V circuit in Figure 3.1 then yields

$$\sum_{k=1}^{3} \boldsymbol{V}_k = 0 \quad \Longrightarrow \quad -\boldsymbol{V_0} + \boldsymbol{V_{R_i}} + \Delta \boldsymbol{V_R} + \boldsymbol{V_2} = 0, \tag{3.3}$$

where $\boldsymbol{V_0}$ is the internal voltage in the signal generator, $\boldsymbol{V_{R_i}}$ is the voltage across the internal impedance matching resistor, and $\Delta \boldsymbol{V_R}$ the voltage drop over the shunt resistor in the circuit. The voltage drops across the internal impedance matching resistor and the shunt resistor in the circuit can be found by the following expressions

$$\Delta \boldsymbol{V_{R_i}} = \boldsymbol{V_0} \left(\frac{R_i}{R_i + R + \boldsymbol{Z_{DUT}}} \right), \qquad \Delta \boldsymbol{V_R} = \boldsymbol{V_0} \left(\frac{R}{R_i + R + \boldsymbol{Z_{DUT}}} \right), \tag{3.4}$$

so that the voltage over the DUT, $\boldsymbol{V_2}$, can be stated as

$$\boldsymbol{V_2} = \boldsymbol{V_0} \left(1 - \frac{R_i + R}{R_i + R + \boldsymbol{Z_{DUT}}} \right) = \boldsymbol{V_0} \left(\frac{\boldsymbol{Z_{DUT}}}{R_i + R + \boldsymbol{Z_{DUT}}} \right), \tag{3.5}$$

where again $\boldsymbol{V_0}$ is the applied voltage at the signal generator.

From Eq. (3.5) it is clear that to maximize the excitation amplitude at the DUT, i.e, to achieve the largest $|V_2|$ possible, the resistor R should be as small as possible since R_i is fixed. In the case where $R \to 0$ the applied voltage $|V_0|$ would be split solely between R_i and the DUT, and $|V_1| \approx |V_2|$ if one were to ignore loss in cables, wires, and components. Noise in the circuit could then be problematic, in the sense that the measurable voltage drop over R could be dominated by electrical noise.

3.2.2 Impedance calculation based on the measured voltages

Impedance is by definition a complex quantity, and the same applies to both voltage and current. The latter two can be expressed as

$$\boldsymbol{V} = |V| e^{j(wt - \varphi_V)}, \quad \boldsymbol{I} = |I| e^{j(wt - \varphi_I)}, \tag{3.6}$$

where all the expressions have a magnitude and frequency dependence with a corresponding phase. Using the expression of the impedance given in Eq. (3.1), and altering the expression of $\boldsymbol{Z_{DUT}}$ on the right hand side by reducing the fraction with $\boldsymbol{V_1}$, one ends up with

$$\boldsymbol{Z}_{DUT} = \frac{\boldsymbol{V_2}}{\boldsymbol{V_1} - \boldsymbol{V_2}} R \quad \Longrightarrow \quad \boldsymbol{Z}_{DUT} = \frac{\left(\frac{\boldsymbol{V_2}}{\boldsymbol{V_1}} \right) R}{1 - \left(\frac{\boldsymbol{V_2}}{\boldsymbol{V_1}} \right)}. \tag{3.7}$$

From Eq. (3.7), given equal frequency for both voltages, the fraction $\boldsymbol{V_2}$ over $\boldsymbol{V_1}$ can be expressed as

$$\left(\frac{\boldsymbol{V_2}}{\boldsymbol{V_1}} \right) = \frac{|V_2| e^{-j\varphi_{V_2}}}{|V_1| e^{-j\varphi_{V_1}}} = \frac{|V_2|}{|V_1|} e^{-j(\varphi_{V_2} - \varphi_{V_1})}, \tag{3.8}$$

where the exponential part is a phase difference between $\boldsymbol{V_2}$ and $\boldsymbol{V_1}$. A phase shift can be expressed as $\Delta\varphi = 2\pi\Delta t/T$, where $\Delta t = t_2 - t_1$, in this instance, and T is the period of the signal, equal for both $\boldsymbol{V_1}$ and $\boldsymbol{V_2}$. The problem of evaluating the impedance based on the two measured voltages has thereby been reduced to a measure of the amplitudes of the two signals, and the corresponding phase difference between them. Following in Section 3.2.3, two different methods to determine the phase shift are discussed.

3.2.3 Determination of phase shift

The DUT have as mentioned an unknown impedance, which for a piezoelectric element is expected to change with both frequency and amplitude of the excitation signal. Following the discussion of the previous section, two different methods to calculate the phase shift between the measured signals $\boldsymbol{V_1}$ and $\boldsymbol{V_2}$ are presented. A third method relying on the cross-correlation of the two signals was initially tried out but was quickly discarded.

Zero crossing method
One robust and common technique to determine the phase shift between two signals is known as the zero-crossing method. It is the measure of the time of an even number of zero crossings N, i.e., when the measured signal crosses the zero axis. A sample period short enough to capture the sample closest to the zero crossing is favorable, but different techniques can be utilized to enhance the resolution. The condition that must be fulfilled for a zero crossing, given a sampled time signal $s[n]$, can be represented as

$$\{s[n] \leq 0 \ \wedge \ s[n+1] < 0\} \quad \text{or} \quad \{s[n] \geq 0 \ \wedge \ s[n+1] > 0\}, \tag{3.9}$$

which for an even number of zero crossings avoids errors due to voltage bias. A positive (or negative) voltage bias would move the zero crossings (two per full signal period) in the direction of the positive (or negative) peak of the waveform. Since the two signals can have individual voltage biases, moving the zero crossings in one or the other direction (increasing or decreasing the time of the first crossing), would give erroneous results between the two.

Increasing the number of signal periods measured, and thus zero crossings, helps reduce the errors caused by noise, since the perturbations in zero crossings become small in comparison to the total period of the measurement [59]. In other words, the computed time of a zero crossing might be affected by random, local noise in the waveform, and deviate from the actual zero crossing of the fundamental frequency component. Thus, one gets deviations in the computed times t_i for each crossing, in which the discrepancy differs between consecutive crosses. When the number of crossings N is increased, the perturbations in the computed times t_i become progressively smaller relative to the total time of all the zero crossings ($\sum_i^N t_i$). Moreover, the discrepancies between the actual crossings will to some extent cancel each other out, due to the deviations being random by nature (assuming the fluctuations to be mainly random noise). Thus, increasing the even number of periods N of the signal evaluated contributes to an increased precision to determine the phase shift. That said, in the case of a significant voltage bias, the zero

crossings would be moved in the direction of one of the peaks. In the vicinity of a peak, the waveform is typically noisier (than around the equilibrium position, i.e., no displacement/oscillation), which could require even more periods to be evaluated but might still be problematic.

With an even number of N zero crossings determined for both signals, the zero crossings at times t_i are summed up and divided by the total number of crossings,

$$\bar{t} = \frac{\sum_i^N t_i}{N}. \tag{3.10}$$

The time shift between two arbitrary signals A and B, given a common time axis, is then the difference between the two averages

$$\Delta t = \bar{t}_A - \bar{t}_B, \tag{3.11}$$

which in turn can be used to calculate the phase difference between the signals, as outlined in Eq. (3.8) and discussed following the equation.

An issue that quickly arises when implementing the zero crossing technique numerically, is the determination of the actual zero crossing of a sampled signal. Only choosing the closest sample yield fairly low accuracy, as noted by the authors of [60]. Determination of the zero crossing point can be done by linear interpolation. For noisy signals, linear interpolation too gives low accuracy, and polynomial approximation is preferable [60, 61]. However, for the application in the current thesis, the error due to the chosen approximation scheme is likely to be far less than the uncertainty and inaccuracies posed by the experimental setup itself. That being said, more discussion on this will follow in the result section.

Frequency domain method
A second method relies on the Fourier transform of the signals in question. The discrete Fourier transform (DFT) is given as

$$X[k] = \sum_{n=0}^{N-1} x[n] e^{-j(2\pi/N)kn}, \tag{3.12}$$

when the transform is discrete in both time and frequency. The DFT transforms N samples from the time domain into values $X[k]$ in the frequency domain. After the transformation, the values $X[k]$ are complex-valued [62].

Given two signals A and B, and the Fourier transformed values $X_A[k]$ and $X_B[k]$, one can simply extract the value of the frequency component of interest from both signals. The phase difference between the signals is then computed by dividing the complex quantities and extracting the angle between them,

$$\Delta\varphi_k = \text{angle}\left\{\frac{X_A[k]}{X_B[k]}\right\}, \tag{3.13}$$

where $\Delta\varphi_k$ is the phase difference between the two signals. Noise at other frequencies in the signals is by this method naturally removed.

3.2.4 Noise reduction by digital filtering

The values received from the oscilloscope of the measured voltages are averaged 64 times but still carry some high-frequency fluctuations in the waveform causing noise in later calculations. It is desirable to reduce this noise by utilizing digital filters, for some of the calculations. For the application of the data in this thesis with regard to impedance calculations, low- and band-pass filters are the most appropriate, as the rapid fluctuations originate from higher frequencies. Commonly used filters to achieve this are the Butterworth- and Chebyshev type I and -II filters [63, 64]. The Butterworth filter is often used due to its extremely flat magnitude response with little ripple in the passband region [63, 65], and is the one chosen in this work.

3.2.5 Waveform characteristics

Measurements of the impedance around the resonance modes of the discs were carried out using both continuous waveform and burst excitation. Continuous waveform is the most straightforward method, and perhaps the most robust/simple approach. It is often used in high-power applications but can result in significant heat generation [3]. Measurement series using continuous waveform were averaged 64 times before reading the data registers of the oscilloscope.

Excitation of the piezodisc using bursts of 120 periods was also utilized. Bursts are used to avoid heating effects, which in some applications are necessary [45], and besides most resemble the excitation of transducers in practice. Due to increased noise/fluctuation in the measured voltage signals using bursts, the oscilloscope was set to average 256 times, before the registers were read.

For both types of output signals, a simple sine waveform with zero starting phase, and zero voltage bias was specified, for every nominal applied voltage, and frequency. The purity of the sine waveform is attended later in Section 5.2.2.

3.2.6 Data acquisition

Electrical measurements in the I-V circuit were controlled through MATLAB with serial communication to the signal generator and oscilloscope. An illustration of the measurement routine is presented in the flowchart in Figure 3.2, and a walk through the measurement routine will be presented in the following. The MATLAB scripts described can be found in Appendix C.1.

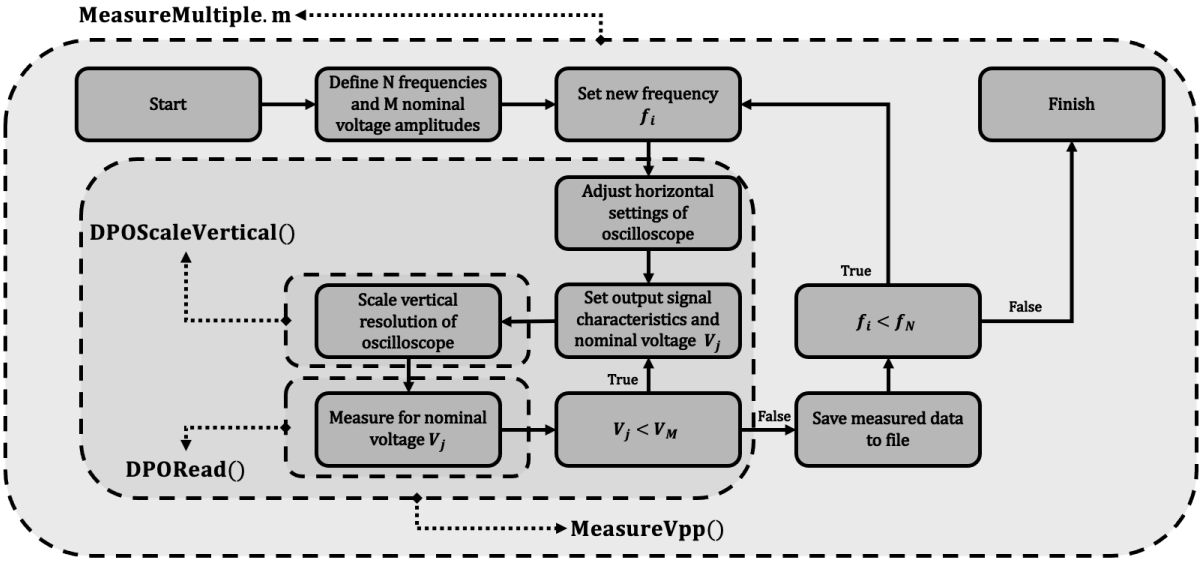

Figure 3.2: Flowchart of the measurement routine for the I-V circuit.

In the MATLAB file MeasureMultiple.m, which encapsulates the whole flowchart in Figure 3.2, the frequency range covering N frequencies f_i and M nominal voltage levels V_j are defined, as well as the resistance of the resistor R in the circuit. Specifications such as the type of output measurement signal (continuous or burst), dimensions of the element measured, and path to save, are also defined here. When the file is run, MATLAB loops over the frequencies specified, and for every frequency f_i, as illustrated in the flowchart in Figure 3.2, calls on the functions MeasureVpp() or MeasureVppV2(), depending on the type of output signal.

Firstly, the horizontal scaling of the oscilloscope (scope) is adjusted. The latter also includes setting a relative delay on the time axis of the oscilloscope (in case of burst excitation), to center the burst and utilize more of the measurement resolution of the oscilloscope. The number of samples and repeated measurements (averages) for each measurement is also set, and the oscilloscope is asked for its sampling frequency due to the new settings. The sampling frequency is then stored alongside measurements in the file.

The signal generator is then asked for its output load setting, which is set to INF (high impedance setting), if the value returned from the generator is less than 10 kΩ, in other words, if the load setting is something else than INF. The signal generator is then fed instructions on the type of waveform (either burst excitation (MeasureVppV2() is called), or continuous waveform (MeasureVpp() is called), waveform characteristics, and nominal voltage amplitude, before the generator output is enabled.

Following the enabled output, both channels of the oscilloscope are horizontally aligned, set to zero vertical offsets, and scaled according to the nominal applied voltage (in the case of burst excitation). For the continuous output signal, a more interactive approach is used with regard to vertical scaling. Here, the DPOScaleVertical() method is called,

which reads the oscilloscope registers (one channel at a time), and checks the value of the returned signed 16-bit data. If less than half the available resolution is utilized, the vertical scale is increased. The vertical scale adjustment is repeated until a significant amount of the available resolution is utilized. In the case of overscaling, an equal scaling loop follows and similarly checks for too large values, and scales back down using the same predefined vertical scale levels.

To ensure old values in the oscilloscope registers are cleared out, the acquisition setting is set to sample mode, and acquisition started before it is set back to average mode. This routine is carried out before every reading of the oscilloscope after new generator settings have been initiated. The final step is to read the oscilloscope channels through DPORead() and turn off the output of the signal generator, before continuing the looping over the nominal voltages V_j.

When the final nominal voltage is reached, the M voltage measurements are returned to MeasureMultiple.m, and saved to a file. This measurement routine continues until all N frequencies specified have been looped over, and the for-loop end.

The DPOScaleVertical() method was created when the vertical scaling options were identified manually by adjusting the scaling on the scope, thus the hard-coded values listed in the MATLAB file. It was later discovered that the vertical scale per division could be set to a user-defined value. This user-defined vertical scale was then truncated to three significant digits by the oscilloscope [58], e.g., specifying a vertical scale of 2.34567 V/div (volts per division) would be interpreted by the oscilloscope as 2.34 V/div. The discovery of this functionality was due to issues with the measurement series utilizing burst excitation, where the loop consistently would scale down to the minimum vertical scale defined. To overcome this issue, it was decided to use the less interactive approach, where the vertical scaling per division was set to 1/6 of the nominal applied voltage V_j.

Interactive vertical scaling through DPOScaleVertical() encountered few problems for measurements using continuous output signal, but at some point, the oscilloscope would seem to freeze during measurements series, and had to be rebooted, and so did MATLAB due to a faulty serial connection. There was however no error message from MATLAB when the freeze occurred, and the loop in MATLAB would seemingly still be running, but the signal generator would have entered sleep mode due to lack of interaction. A suspicion that the vertical scaling loop would enter an unbreakable state, being a while-loop, a limit to the number of iterations was added. As this showed no effect, and the loop seemingly did not cause the problem, attention was put to the signal generator, in order to locate the problem. The signal generator was asked for system errors after setting waveform characteristics, but it was quickly identified that the generator was not the root of the problem. Due to the persistent issue of the freezing of the loop, and a continual, growing suspicion that the oscilloscope did, in fact, cause the problem, it was replaced with an identical oscilloscope. After replacing the oscilloscope, the freezing issue vanished, and the root of the problem was assigned to the oscilloscope.

3.3 Acoustic measurement setup

The electrical measurements conducted serve as a foundation onward for acoustic measurements in a fluid. Available at the acoustic laboratory at IFT is a setup for measurements in air, used by several former master students, such as [66, 67, 2, 68].

In the following, the measurement setup with equipment and instruments used are walked through in Section 3.3.1 and -3.3.2, respectively. Positioning of the linear stage for the z-axis, and an alignment of the transmitter and receiver, are then attended in Section 3.3.4 and -3.3.5. A note about the microphone sensitivity in Section 3.3.6 and the procedure of calculating the pressure in Section 3.3.7. Testing and characterization of the receiving electronics are elaborated in Section 3.3.8, and finally in Section 3.3.9, some of the limitations of the measurement setup are addressed.

3.3.1 Equipment

Listed in Table 3.3 is the equipment used in the experimental setup.

Table 3.3: Measurement instruments and motion controllers used in the acoustic measurement setup depicted in Figures 3.4 and -3.5 below.

Model/Brand	**Equipment**	**Serial number**	**Manual**
Agilent 33220A	Signal generator	MY44023589	
Tektronix DPO3012	Oscilloscope	C010246	
Ferroperm/Meggitt PZ27	Piezoelectric disc	N/A	
Brüel & Kjær 4138	1/8-inch pressure-field microphone	1832479	
Brüel & Kjær UA-160	Adaptor - microphone to preamplifier	N/A	
Brüel & Kjær 2633	Preamplifier	N/A	
Brüel & Kjær 2636	Measurement amplifier	1815638	
Krohn-Hite 3940	Filter	AM2626	
Vaisala HMT313	Humidity- and temperature meter	F4850018	
ASL F250 MKII	Thermometer	1365026993	
Paroscientific 740	Barometer	67325	
KEYENCE LK-G32	Laser sensor	2041141/2041143	
KEYENCE LK-G3001PV	Controller with display	1741187	
PI SMC Hydra TT	Motion Controller	1404-0153	
PI C-843.41	Motion Controller	0095103296	
PI C-852.12	Signal processor/Encoder	1460497	
PI M-531.DG	Linear stage (X axis)		
PI M-535.22	Linear stage (Y axis)	1460497	
PI LS270	Linear stage (Z axis)	414000926	
PI M-037.PD	Rotation stage	109040312	

3.3.2 Measurement setup and signal path

In Figure 3.3 below, a schematic of the signal path is presented. The excitation signal generated by the Agilent 33220A signal generator is connected in parallel with the piezoelectric element used as a projector (piezodisc) and the Tektronix DPO3012 oscilloscope. The piezodisc (Tx) mounted in the setup radiates freely in air, and the Brüel & Kjær 4138 pressure-field microphone (Rx) measures the transmitted signal. A Brüel & Kjær adaptor and -preamplifier are then used to terminate the microphone in the Brüel & Kjær 2636 measurement amplifier. The amplified, measured response of the microphone is further passed through the Krohn-Hite 3940 analog filter before the signal is terminated and read by the oscilloscope.

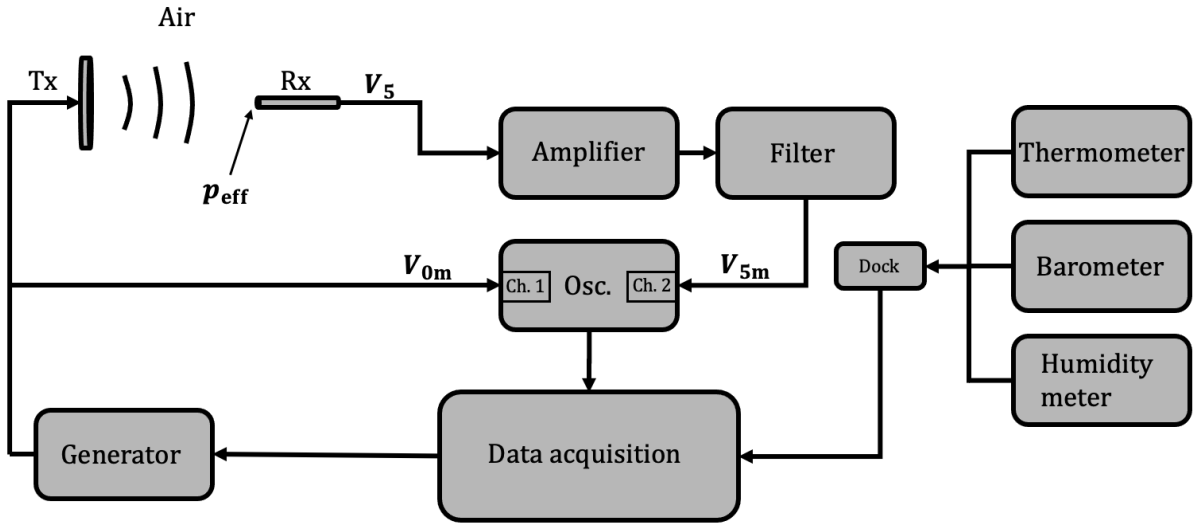

Figure 3.3: Schematic of the signal path in the acoustic measurement setup.

The wanted characteristics of the excitation signal are defined in MATLAB, alongside configurations of the other instruments, besides the Brüel & Kjær measurement amplifier which have to be set manually. Alignment and positioning of the transmitter and receiver are also carried out through serial communication to the motion controllers via MATLAB. Environmental parameters, such as temperature, relative humidity, and barometric pressure, are read from the respective instruments before reading the registers of the oscilloscope. More on these instruments in the following section. An image of the setup of the instruments is shown in Figure 3.4 below. The measurement area with a mounted piezodisc and microphone is depicted in Figure 3.5 to the bottom of this section.

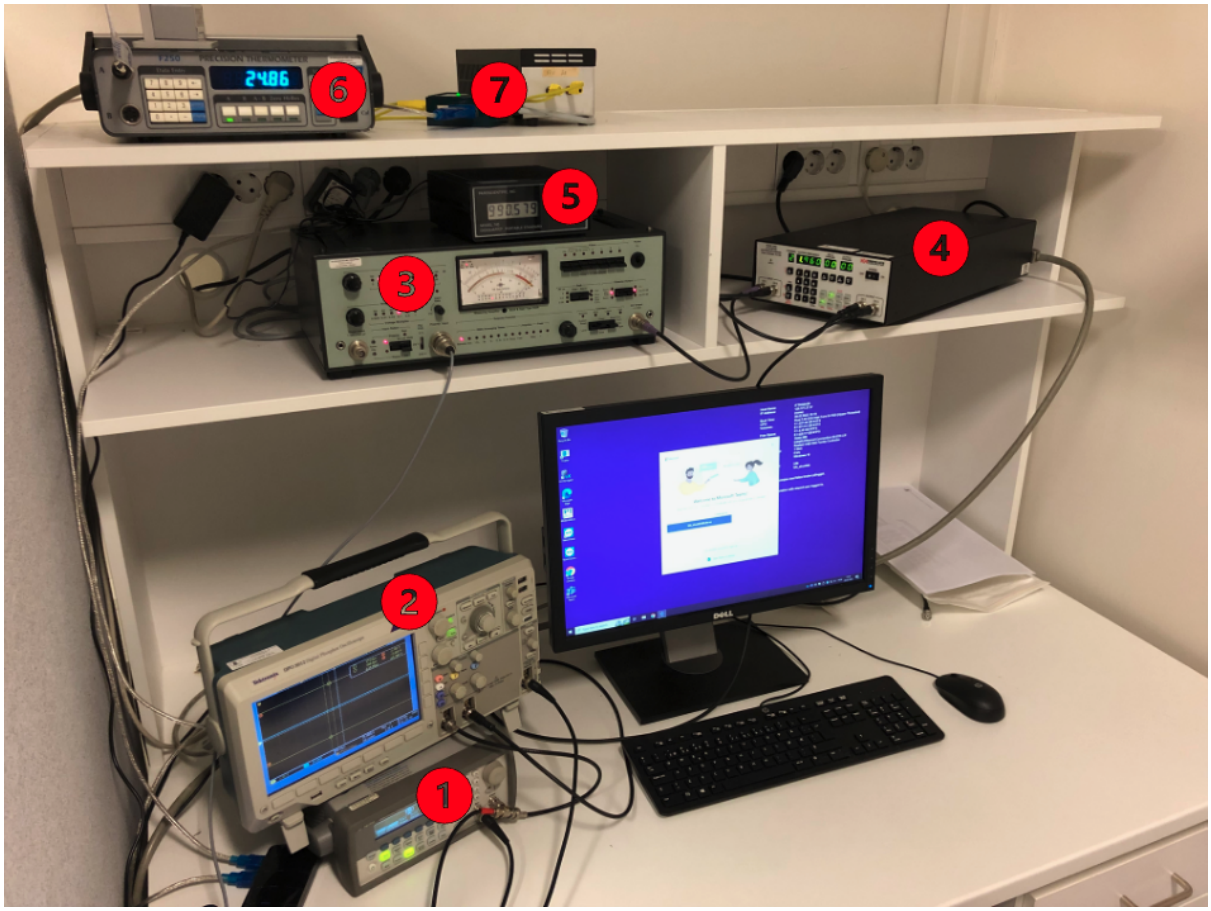

Figure 3.4: Setup of the instruments integrated in the acoustical measurement setup for air measurements controlled through the computer. (1) Agilent 33220A signal generator, (2) Tektronix DPO3012 oscilloscope, (3) Brüel & Kjær 2636 measurement amplifier, (4) Krohn-Hite 3940 filter, (5) Paroscientific 740 barometer, (6) ASL F250 MkII thermometer and (7) Vaisala HMT313 measuring humidity and temperature.

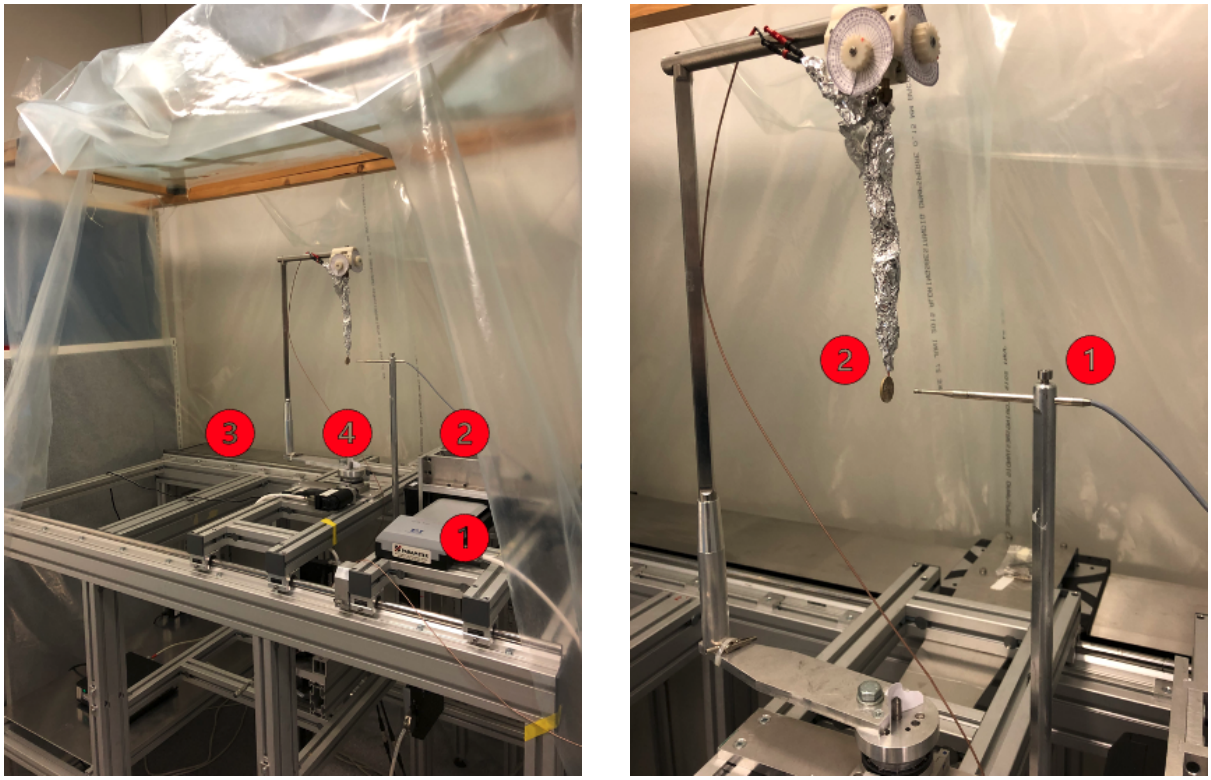

(a) (b)

Figure 3.5: Measurement setup. Figure 3.5a: Overview of the measurement area, and the stages for moving the transmitter and/or receiver. (1) Linear stage (LS) for the x-position of the receiver, (2) LS for the y-position (vertical position) of the receiver, (3) LS for the z-position (axial position) of the transmitter, and (4) rotation stage for the transmitter. All stages controlled through MATLAB. Figure 3.5b: (1) Brüel & Kjær 4138 pressure-field microphone, and (2) Ferroperm PZ27 20x2 mm piezodisc (transmitter).

3.3.3 Environmental parameters

The setup includes three instruments for measurements of environmental parameters. Temperature, relative humidity, and barometric pressure are measured as a part of the measurement routine. These serve as an important supplement to calculate accurate medium properties, such as the density of the medium, the speed of sound, the attenuation of sound, and the specific heat ratio.

The manufacturer of the Vasisala HMT313 humidity and temperature meter lists a factory calibration uncertainty at 20°C of ± 0.6 % on the interval 0 % to 40 %, and ± 1.0 % from 40 % to 100 % [69], for the relative humidity. The accuracy of the measurement is listed as ± 1.0 % for temperatures between 15-25°C for relative humidity from 0 % to 90 %. The typical temperature accuracy at 20°C is listed as ± 0.2°C [69], which is fairly high. However, the ASL F250 MKII precision thermometer has an uncertainty of ± 0.01°C when only the F250 instrument is used, whereas higher accuracy can be achieved

with the use of various probes [70]. Thus, the latter becomes the preferred alternative for temperature measurements.

The Paroscientific 740-16B barometer proclaims a typical accuracy of 0.01 % of the read value both in field- and laboratory applications [71]. It has an operating range of 800-1100 hPa. The uncertainty thus corresponds to about ± 10 Pa at 1 atm.

3.3.4 Definition of the z-axis and measurement of the distance between transmitter and receiver

The linear stage has predefined limitations in its movement along the z-axis. This restricts the movement, and can, amongst others, be used to ensure that the transmitter does not collide with the microphone.

On reboot of the SMC Hydra TT motion controller, its position on the axis is lost, and it will then assume it rests in an absolute position of 0 mm. In addition to the limits, which can be redefined when the controller is turned on, the controller stops the stage on either end of its motion path. A 'move home' command can be initiated, and the controller will move the stage to the end of the axis, regardless of defined limitations. The latter is however problematic, as the microphone with its finite length is mounted in proximity to the 'home' position of the stage, and collision will occur. However, a similar command can be used to send the stage to the far end in the opposite direction, until a switch is encountered, signaling to the controller that the end of the motion path is met.

Initially, the linear stage was sent to the end of its axis, and both the current position and the movement limitation registers were verified. The stage with the mounted piezodisc was then moved closer to the microphone. A second stage located in between and parallel to the sender and receiver, with a laser measuring device mounted on top, was hoisted up to accurately measure the distance between the piezodisc's center and the tip of the microphone, as shown in Figure 3.6 below.

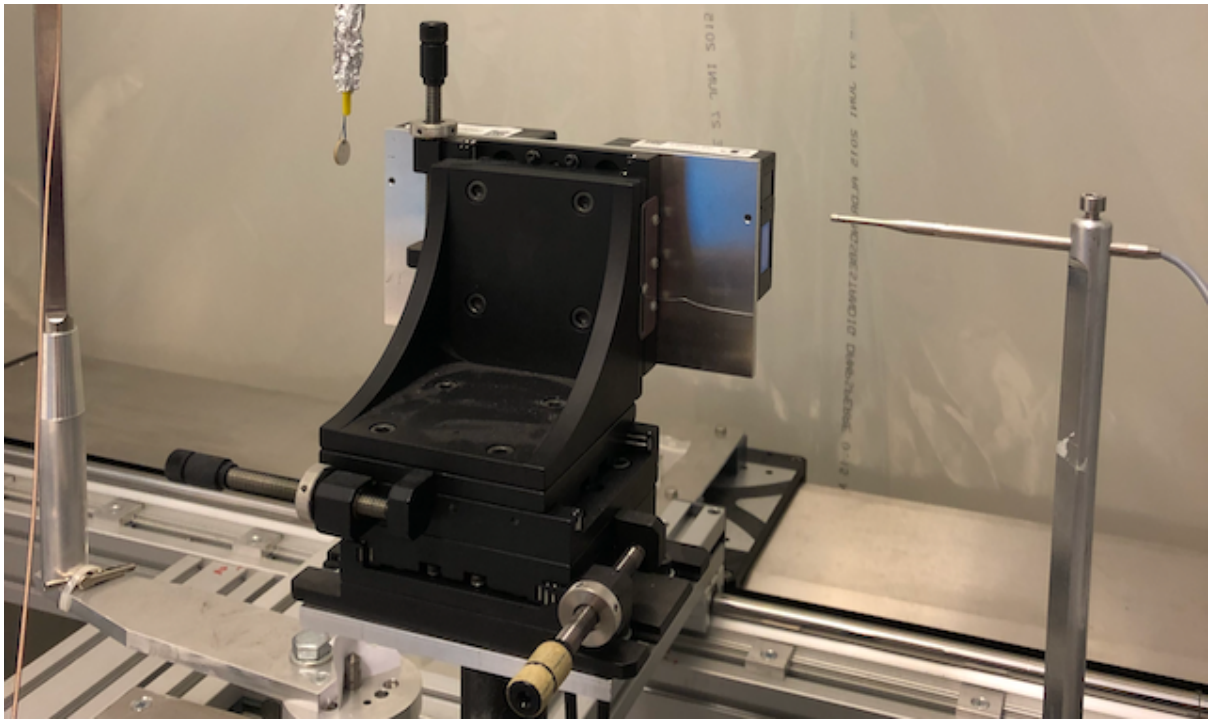

Figure 3.6: Keyence LK-G32 laser displacement sensor used to adjust the piezodiscs, and measure the distance between transmitter and microphone.

The Keyence LK-G32 laser displacement sensor measures the distance to an object resting (30 ± 5) mm away from the laser on both sides. A measurement uncertainty of ± 0.05 % of 5 mm (± 2.5 µm) [72] when the diffuse reflection setting mode is used. A temperature dependency of ± 0.01 % of 5 mm per °C (± 0.5 µm/°C) is also noted for ambient operating temperatures of 0 °C to 50 °C [72]. Ambient operational light is given as a maximum of 10000 lux of incandescent- or fluorescent light [72], similar to large amounts of sunlight through windows [73].

When the laser's extension is known, the distance between the transmitter and receiver can be calculated based on the measurements. Thus, the piezodiscs absolute position in regard to the microphone was made known.

At last, the axis of the linear z-stage was redefined so that an absolute position of $z = 0$ mm of the stage corresponded to a distance of 0 mm from the center of the disc and the tip of the microphone. However, movement along the axis was restricted to a minimum distance of 5 mm between the piezodisc and microphone to prevent a collision, in the case of erroneous positions fed to the motion controller.

3.3.5 Alignment of the sound beam axis to the microphone

Before initializing the measurement series in the setup described above, an alignment of the sound beam axis and the microphone was carried out. The piezodisc was initially

aligned, rotated, and tilted to face the microphone at a close distance, as illustrated in Figure 3.7. Positive directions for x, y, and z are as depicted in the illustration above. The discussed rotation θ in this section is relative to the y-axis.

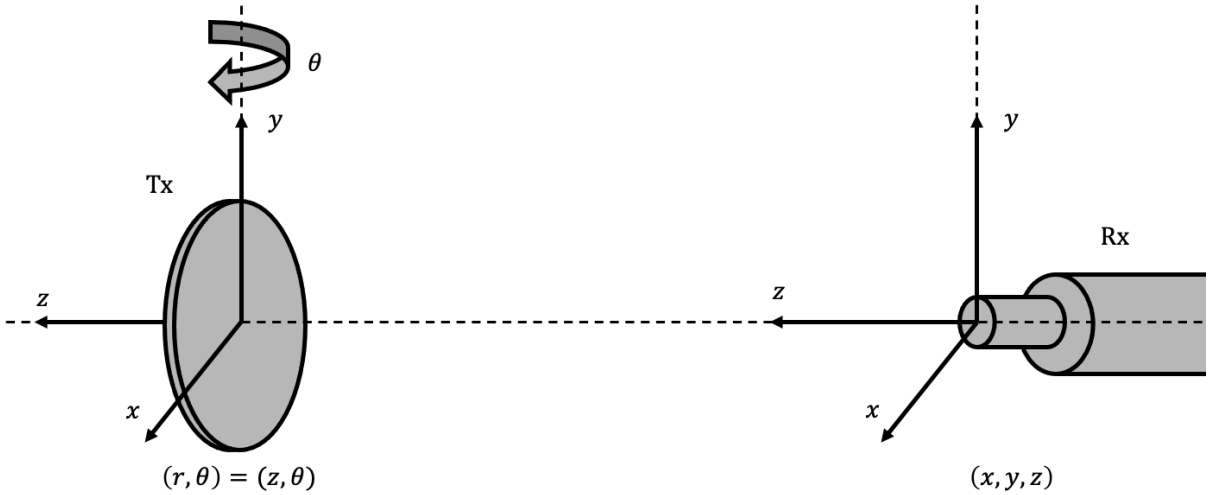

Figure 3.7: Sketch of the transmitter (Tx) and receiver (Rx) in the acoustic measurement setup, and the corresponding coordinate system.

The piezodisc, suspended from a solid arm mounted on a rotation stage, has a small tilt relative to the x-axis. The laser described in the last section was hoisted up to measure the piezodisc's tilt and rotation. The distances from the laser to the upper- and lower edge of the disc were measured, and the disc was gently pushed to reduce the differences measured by the laser. This was repeated until the measured distances eventually were reasonably equal, but due to the mounting of the disc, some tilt remained. Thus, the tilt had to be accounted for by elevating the microphone, as described in the last part of this section.

Following the alignment of the top and bottom of the disc, the right- and left edges of the disc were measured. The rotation stage was used to adjust the face of the piezodisc to be perpendicular to the z-axis translation stage, so that the angle θ between the sound axis of the piezodisc and the z-axis of the microphone aligned. Lastly, the two-sided laser was centered on the disc, and the tip of the microphone was adjusted in both x- and y-direction to best align with the laser.

To ensure the best possible alignment of the acoustic sound axis with regard to the microphone, the piezodisc was moved along the z-axis to $z = 600$ mm. Here, the alignment of the axis was checked again. From this point, only rotation of the piezodisc and modification of the y-position of the microphone were altered. From the initial measured response on the oscilloscope, a significant amplitude drop in the response of the signal was manually marked on the scope with cursors. The measured response of the microphone was studied as the disc was rotated some degrees relative to its original position to the left and right. Once the signal aligned with the locked cursor, the absolute rotation angle of the piezodisc was noted, for both sides of the transmitted main lobe. The mid-point was

then chosen and was verified as the maximum response when the disc was rotated to its new position. Secondly, the described technique was applied to adjust the microphone's elevation (y-position). Lastly, the rotation of the disc was checked again to verify the best possible fit. This procedure was carried out again closer to the microphone, at $z = 100$ mm, then another time at the initial position.

From the above steps, two (θ, y)-pairs were found and a line intersecting both z-positions of the piezodisc was calculated to best capture the center of the main lobe. The rotation of the disc in both positions was found to yield an equal angle, thereby reducing the problem to an adjustment of the y-position of the microphone. The adjustment of the microphone for a given z-position could thereby be given by calculation of the absolute position of y needed to yield the best fit, given as

$$y(z) = (z - 100 \text{ mm}) \left(\frac{9.50 \text{ mm}}{500 \text{ mm}} \right) + 67.80 \text{ mm}. \tag{3.14}$$

Coordinates in the x, y, and z axis are all given in millimeters as input to the motion controllers, and the rotation in degrees. The constant term in Eq. (3.14) above corresponds to the best alignment at $z = 100$ mm, and $y(z = 600)$ yields the best measured fit at $z = 600$ mm. At the latter position, the y-position was 9.50 mm higher than for $z = 100$ mm. It was thereby assumed that y changes linearly along the z-axis for $z \in$[0 mm, 870 mm].

3.3.6 Microphone sensitivity

The Brüel & Kjær 1/8-inch pressure-field microphones type 4138 are designed to have a flat frequency response and yield a 0 dB response for frequencies on the interval 20 Hz to 50 kHz. The response decreases somewhat on the interval 50 kHz to 100 kHz, before increasing as the frequency approaches the resonance of the diaphragm at 160 kHz.

The microphone requires an external polarization voltage [74], and a preamplifier and adaptor are thus needed. In this measurement setup, a Brüel & Kjær 2633 preamplifier, and Brüel & Kjær UA-0160 adaptor are utilized.

Calibration of the microphone is carried out at 250 Hz with a pistonphone, and the correction is applied to the frequency response. A free-field correction chart for the wanted angle of incidence (here 0°), supplied by the manufacturer, is further added to the actuator response to yield the microphone sensitivity.

The calibration of the microphone mounted in the setup was carried out by master student Håvard R. Økland. From the resulting microphone sensitivity, a Fourier curve fit was added in MATLAB to provide a finer resolution of the sensitivity curve. Details about the curve fit of the microphone sensitivity are provided in Appendix B.8.

3.3.7 Pressure calculations

From the expression of the free-field open circuit microphone sensitivity given in [34], one can obtain the effective pressure amplitude p_{eff} as

$$|M_V(f)| = \frac{V_{\text{eff}}(f)}{p_{\text{eff}}(f)} \quad \Longrightarrow \quad p_{\text{eff}}(f) = \frac{V_{\text{eff}}(f)}{|M_V(f)|}, \tag{3.15}$$

when the microphone sensitivity is known. The effective voltage amplitude V_{eff}, calculated through

$$V_{\text{eff}}(f) = \frac{V_{5,\text{pp}}(f)}{2\sqrt{2}} = \frac{1}{2\sqrt{2}} \frac{V_{5\text{m,pp}}(f)}{10^{(\text{GAIN}/20)}}, \tag{3.16}$$

is then used in the right of expression in Eq. (3.15). Here, $V_{5,\text{pp}}$ is the peak-to-peak voltage amplitude at the microphone, $10^{(\text{GAIN}/20)}$ an amplitude correction due to the measurement amplification settings at the Brüel & Kjær 2636 Measuring Amplifier, and $V_{5\text{m,pp}}$ the voltage amplitude measured by the oscilloscope after amplification and filtering of the voltage response of the microphone. Thus, the wanted effective pressure can be calculated for a given frequency as

$$p_{\text{eff}}(f) = \left(\frac{1}{2\sqrt{2}}\right) \frac{V_{5\text{m,pp}}(f)}{10^{(\text{GAIN}/20)}} \left(\frac{1}{|M_V(f)|}\right). \tag{3.17}$$

Modifications to the signal amplitude due to cables, and the Krohn-Hite 3940 analog filter, are thus assumed to be negligible. The analog filter also has gain options for both channels. These were however set to zero during all measurements. Verification of correct termination and (expected) zero gain of the filter was carried out before measurements were carried out.

3.3.8 Receiving electronics

Preparatory measurements in the acoustic setup were carried out with a soft PZ27 piezodisc with dimensions 20x2 mm, already mounted in the setup. The measurements displayed strange harmonic behavior, especially when the distances between the transmitter and receiver were small, and higher voltages were applied at the signal generator. Some of these results are presented in Section 5.4.1. Both the number of harmonics and their respective magnitudes were peculiar. Adding to the fact that the microphone's sensitivity for higher frequencies is unaccounted for, but falls off as the frequency approaches 200 kHz, led to questions about the origin of these harmonics. Thus, the measurement amplifier and analog filter were electrically tested. The gain of said instruments was also verified to yield the expected amplifications.

A measure of the total harmonic distortion (THD) can serve as a useful tool in evaluating the measured electrical signals. The IEEE standard 519-2014 defines the THD

(for both voltage and current) as the ratio of harmonic content relative to the fundamental, considering harmonics up to the order of 50, as noted by the authors in [75]. A voltage THD thus yields [76, 75]

$$V_{\mathrm{THD}} = \sqrt{\sum_{h=2}^{H} \left(\frac{V_h}{V_1}\right)^2} = \frac{\sqrt{\sum_{h=2}^{H} V_h^2}}{V_1}, \tag{3.18}$$

where V_{THD} is the total voltage harmonic distortion, V_1 is the amplitude of the fundamental component, and V_h the amplitude of the h^{th} harmonic component.

The following tests of the receiving electronics were carried out using identical waveform characteristics, besides applied amplitude which naturally had to be varied. A burst of 60 periods for a frequency corresponding to the first radial mode (R1) of the 20x2 disc was used, and the input to the tested instrument(s) was measured at the oscilloscope to retain control of the original signal, denoted $V_{0\mathrm{m}}$ in Figure 3.8. The output signal of the last instrument was then terminated in the oscilloscope, denoted V_{OUT}, and both channels of the scope averaged 512 times before reading the registers.

Firstly, the Krohn-Hite filter was set up as depicted in Figure 3.8(a), with high-pass filtering at channel 1 using a cutoff frequency (f_{cut}) equal half the resonance frequency of R1 (f_{R1}), and the output of channel 1 terminated in the low-pass configured channel 2, with $f_{\mathrm{cut}} = 10 f_{\mathrm{R1}}$. The output of channel 2 was then terminated in the oscilloscope and measured. The filter was further configured to zero gain on both inputs. Measurements were conducted for a variety of amplitudes before the attenuator was connected in place of the filter, and measured similarly.

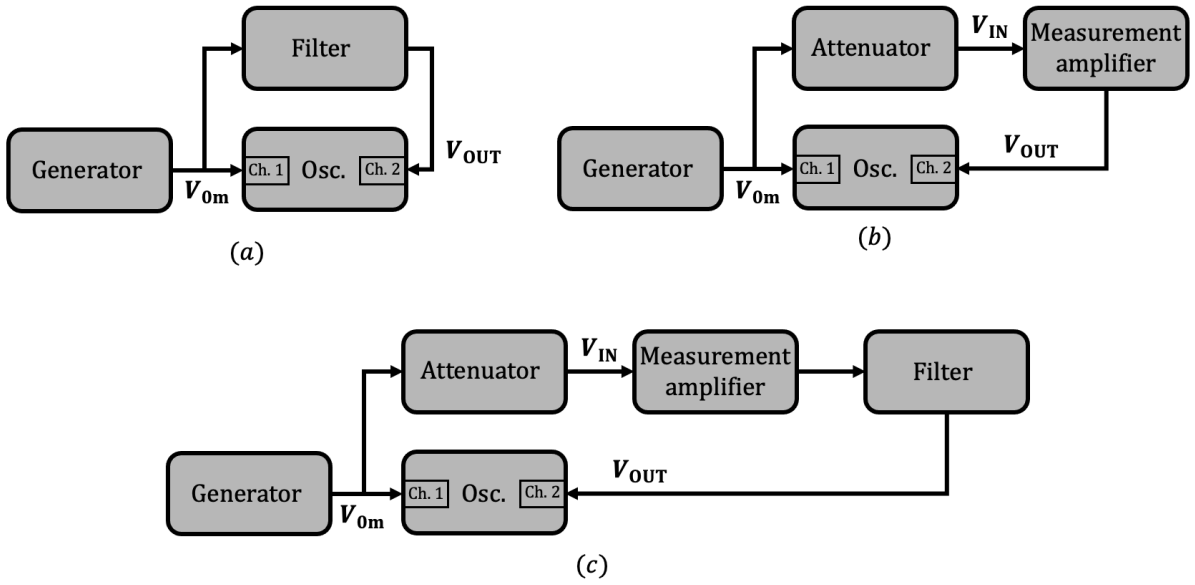

Figure 3.8: Block diagram of the instrument configurations tested for harmonic distortion. In figure (a): the Krohn-Hite filter, (b): an attenuator in cascade with the measurement amplifier, and (c) the attenuator, the measurement amplifier, and the Krohn-Hite filer in cascade.

Following these measurements, the attenuator was utilized to lower the amplitude of the generated waveform, so that it could be terminated into the measurement amplifier, denoted V_{IN}, and tested with amplitudes similar to those measured in the acoustic setup with a microphone. The setup illustrated in Figure 3.8(b) was wired up, and measured as the preceding instruments. The amplification configuration of the measurement amplifier most frequently used in the acoustic measurement setup, and the configuration used in the initial testing, has been a 40 dB input gain, and an additional 20 dB amplification of the output. Thus, those configurations were applied to the amplifier, to begin with.

To reach the complete configuration of the receiving electronics utilized in the measurement setup, the Krohn-Hite filter was connected in cascade with the amplifier and oscilloscope, as shown in Figure 3.8(c). The filter configuration initially remained the same as explained above, before altering the output gain setting on the amplifier to 10 dB and 0 dB, respectively.

Results from some of the measurements are presented later in Section 5.4.2, alongside a brief discussion of the findings.

3.3.9 Limitations of the measurement setup

There are two main limitations of the measurement setup presented above most relevant to this work. Firstly, the achievable distance between transmitter and receiver, and secondly the microphone response.

Nonlinear effects from acoustic radiation in a medium are usually described with regard to the Rayleigh distance r_0, and the far-field region of the radiation sound field is said to be reached beyond r_0 [30]. The first- and second radial mode (R1 and R2) and the thickness mode (TE1) of the 20x2 piezodisc have Rayleigh distances of about 92 mm, 233 mm, and 909 mm, respectively, when the measured physical radius of the disc is used in the computation of r_0. Limitations in the measurement setup concerning the distance between the transmitter and receiver mean that measurements at higher frequencies barely reach the far-field region. The transmitter can be moved about 870 mm along the sound propagation axis with the current setup. Thus, sound pressure measurements of TE1 are not possible in the far-field of the 20x2 disc. The latter is however possible for R1 and R2.

The same can not be said for the 13x2 disc, as its smaller radius puts the far-field well within the measuring distance of the three mentioned resonance modes. Even the thickness mode of the disc puts the transition to the far-field at about 370 mm from the disc, and thus within the boundaries of the setup. However, the microphone response constitutes a new obstacle.

The properties of the Brüel & Kjær 4138 pressure-field microphone are accounted for on the frequency interval 0-200 kHz. This means that pressure measurements of R2 and TE1 are problematic, as the response of the microphone sensitivity is unaccounted for. It also puts restraints on the interpretation of measured harmonics. The second harmonic of R1 of the 20x2 disc can be calculated using the respective microphone sensitivity. Other, higher harmonics have to be interpreted across measurement series as relative magnitudes with regard to the fundamental frequency.

In light of this, acoustic sound pressure measurements of the two discs were carried out only for R1, which are presented in Section 5.4.

3.3.10 Frequency analysis

To access the frequency content of the measured signals, a transform from the time domain to the frequency domain was carried out through Fourier transforms. In this work, the Fast Fourier transform (FFT) available through MATLABs fft() function has been used. The following describes the procedure of the Fourier transforms carried out.

A portion of the sampled signal in the steady state was extracted for a number of full periods of the fundamental carrier frequency. The indices of the signal were located in the time domain through calculations of the travel distance, in the case of acoustical measurements in air. Similarly, for the electrical measurements, a sampled reference time axis of the oscilloscope was used in order to get full periods of the fundamental frequency.

A Hanning window, whose coefficients were multiplied with two in order to retain signal amplitude through the transform, was then applied to the extracted part of the signal.

The windowed, extracted part of the signal was then (significantly) zero-padded to increase the total length of the signal, in order to get higher frequency resolution in the frequency domain (increased number of frequency bins). Following the transform to the frequency domain, the corresponding spectrum $S(f)$ was divided by the length of the extracted signal prior to the zero padding.

Chapter 4

Simulations

4.1 Finite element simulation

A finite element (FE) program was used to simulate the electrical characteristics of the piezodiscs. The FE program utilized was FEMP version 6.1.2 (Finite Element Modeling of Piezoelectric structures).

4.1.1 Critical distances and infinite elements

For simulations of a disc in a fluid, a critical distance R_{inf} designates the boundary where infinite elements take the place of regular fluid elements, and computations become sparse. Infinite elements are introduced to reduce the number of computations in the fluid. It is desirable to choose the smallest R_{inf} possible while retaining computational accuracy to reduce computational cost and time.

Defining a normalized variable S as the distance to the last axial pressure maximum of a plane piston radiator, as described in Section 2.3.1, so that $S = z/(a^2/\lambda)$. Then the critical distance is given by the relation [27]

$$\frac{R_{\text{inf}}}{a^2/\lambda} = S \quad \xrightarrow{v=\lambda f} \quad R_{\text{inf}} = \frac{Sa^2 f}{v}, \tag{4.1}$$

where a is the radius of the disk, and v is the speed of sound in the fluid. The critical distance for 10^{th} order infinite elements was found to be sufficient for $0.32S$, where further increasing R_{inf} does little to the error of the solution [27].

The two elements considered in this thesis are simulated around their 1st and 2nd radial mode (R1 and R2) and the fundamental thickness mode (TE1). The critical distances listed in Table 4.1 below are computed using the maximum frequency for each simulation, the measured radii of the discs, and the speed of sound in air, chosen to be $v = 343$ m/s for 1 atm and 20 °C following [29]. Due to the severely increased computational cost for simulations with higher frequencies, simulation of the thickness modes were carried out in a vacuum, and thus have no critical distances.

Table 4.1: Calculated critical distances for the infinite elements in the FE simulations for the two piezoelectric elements. The frequencies chosen are the upper limit of the simulated frequency area around the corresponding resonance modes.

Mode	**PZ27 20x2 mm**		**PZ27 13x2 mm**	
	f_{max} [kHz]	R_{inf} [mm]	f_{max} [kHz]	R_{inf} [mm]
R1	110	10.4	165	6.4
R2	260	24.6	395	15.3

4.1.2 Mesh

Presented in Figure 4.1 below is an illustration of the meshing used in the FE simulations. The green rectangular box is the piezoelectric disk. Only half the elements are present in the mesh presented, as the geometry of the FE computations is specified as rotationally symmetric [27]. The light blue area surrounding the disk is the finite elements of the fluid medium, whose size is determined by R_{inf} as discussed above. Lastly, the dark blue area contains the infinite elements. In the figure beneath, the number of elements per wavelength was heavily reduced for the purpose of visualization.

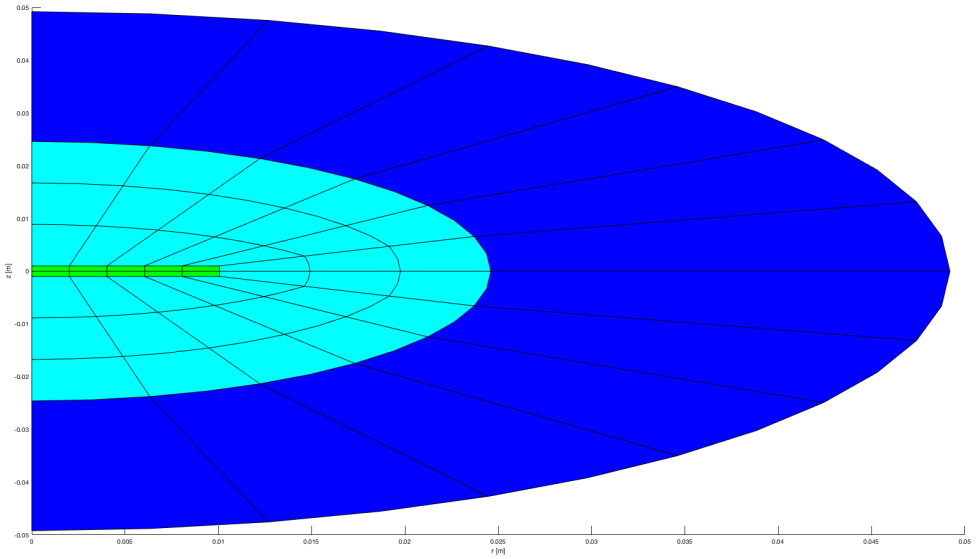

Figure 4.1: Simulation setup with R_{inf} corresponding to 260 kHz. Green area is the piezodisk, light blue is the fluid, and dark blue the infinite elements. The number of elements per wavelength were here heavily reduced for the purpose of the visualization.

4.1.3 Material data

Finite element simulations of a piezoelectric element require material data. Listed in Table 4.2 below are the material parameters in column one, the adjusted parameter values by Lohne/Knappskog [77] in column two, and the material data provided by the manufacturer [52] in column three. The latter has turned out to be far less accurate than what is desirable for precise simulations and characterization. Thus, an alternative data set has been established by earlier master students at the Department of Physics and Technology at UiB, amongst others, by the above-mentioned authors.

Table 4.2: Material coefficients for a PZ27 element used in the FE simulations. Adjusted parameters as reported in work done by Lohne and Knappskog. To the right, values listed by manufacturer Ferroperm.

Parameter	**Adjusted (Lohne/Knappskog)**	**Ferroperm**
c_{11}^E [10^{10} N/m^2]	$11.875(1+i/95.75)$	14.70
c_{12}^E [10^{10} N/m^2]	$7.430(1+i/71.24)$	10.50
c_{13}^E [10^{10} N/m^2]	$7.425(1+i/120.19)$	9.37
c_{33}^E [10^{10} N/m^2]	$11.205(1+i/177.99)$	11.30
c_{44}^E [10^{10} N/m^2]	$2.110(1+i/75)$	2.30
e_{31} [C/m^2]	$-5.40(1-i/166)$	-3.09
e_{33} [C/m^2]	$16.0389(1-i/323.77)$	16.00
e_{15} [C/m^2]	$11.20(1-i/200)$	11.60
ε_{11}^S [10^{-9} F/m]	$8.11043(1+i/50)$	10.0005
ε_{11}^S [10^{-9} F/m]	$8.14585(1+i/86.28)$	8.0927
ρ [kg/m^3]	7700	7700
Q_M	0	80
$\tan\delta$	0	0.017

4.2 Finite difference simulation

To assist acoustic pressure measurements, finite difference (FD) simulations were carried out using a Fortran program known as the Bergen Code. It solves the KZK equation (Eq. (2.51)) for directional sound beams, which takes the effects of nonlinearity, absorption, and diffraction into account. The Bergen Code was initiated by Jaqueline N. Tjøtta and Sigve Tjøtta at the University of Bergen in the 1980s [78].

The KZK equation, and thus the simulation, are valid within the parabolic approximation. "Sufficiently close to the sound beam axis, and sufficiently far from the source". Neglection of local effects is also a prerequisite for the KZK equation. Other assumptions regarding the source, which is assumed to behave as a uniform piston, is that it is defined in the plane $z = 0$, it has characteristic radius a and radiates at frequencies satisfying $ka \gg 1$, as mentioned in Section 2.4.4.

4.2.1 Coordinate system

Utilization of axisymmetry, assuming the piezoelectric element radiates as a uniform piston, reduces the problem of solving the KZK equation from three to two dimensions. More specifically, from (x, y, z) to (x, z), where the source is located perpendicular to the z-axis (in the xy-plane) at $z = 0$, with the z-axis the direction of propagation. An illustration of this coordinate system is presented in Figure 4.2 below.

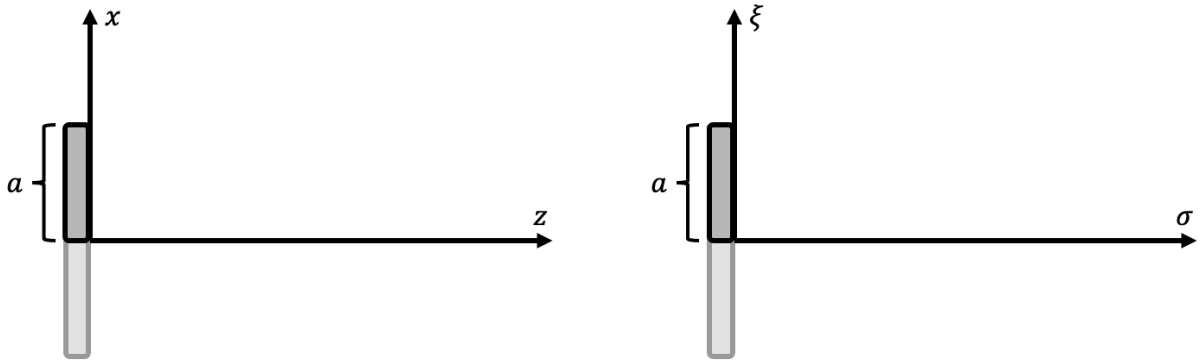

Figure 4.2: Coordinate system (x, z) to the left, and transformed (ξ, σ) to the right, of the finite difference simulation program.

The faded area below the z-axis illustrates the full size of the modeled piston. The xz-plane is further made dimensionless through the coordinate transformations [79]

$$x \to \xi = \frac{x}{a}, \qquad z \to \sigma = \frac{z}{r_0} \tag{4.2}$$

where a is the radius of the uniform piston, and $r_0 = \frac{1}{2}ka^2$ is the Rayleigh distance, also shown in the figure above. The source condition, at $\sigma = 0$, is that of a uniform piston and defined as

$$p(\xi, 0) = \begin{cases} p_0, & \text{if } \xi \leq 1 \\ 0, & \text{otherwise} \end{cases}, \tag{4.3}$$

where the acoustic pressure amplitude follows the plane wave impedance relation $p = \rho_0 c_0 u_z$, where u_z is the component of the particle velocity amplitude in the propagation direction.

4.2.2 Effective source radius

A piezodisc is modeled as a uniform circular piston in the simulation program. However, the physical behavior of a disc is rather different from that of a piston. It is, therefore, necessary to obtain the effective source radius of the disc for a given frequency, as input parameter to the simulation program. In other words, the radius needed to yield a similar performance between a uniform circular piston, and a piezodisc, under assumed linear conditions.

The effective source radius was determined through acoustic directivity measurements, compared to the theoretical expression of Eq. (2.17) given in [29], and solving for a. From tabulated values available in the appendix of [29], using $v = 1.6$ when $2J_1(v)/v = 0.7124$, Eq. (2.17) can be solved for a so that the effective source radius yields

$$v = ka_{\text{eff}} \sin(\theta) \quad \Longrightarrow \quad a_{\text{eff}} = \frac{v}{k \sin(\theta)}, \tag{4.4}$$

where θ is determined from directivity measurements of the disc.

4.2.3 Determination of the input parameter p_0

The input parameter p_0, which is the pressure amplitude at the face of the piston, i.e., $p_0 = |\boldsymbol{p}(r = 0)|$, was determined through measurements of the radiated acoustic pressure. The measured pressure amplitude along the acoustic sound axis was extracted at a chosen distance r_1 in the far-field. It was then assumed that the radiated sound field at r_1 had undergone losses due only to spherical spreading and absorption. In other words, losses due to nonlinear effects in the sound propagation were assumed to be sufficiently weak and thus neglected. Adding an absorption factor on the right-hand side of Eq. (2.14), and solving for the piston's particle velocity in the propagation direction u_z, then yields

$$u_z = \frac{|p_{\text{meas}}(r = r_1, \theta = 0)|}{2\rho_0 c_0 \left|\sin\left(\frac{1}{2}kr_1\left[\sqrt{1 + (a_{\text{eff}}/r_1)^2} - 1\right]\right)\right| e^{-\alpha r_1}}, \tag{4.5}$$

where a_{eff} is the effective radius of the source, and α is the absorption coefficient in Np/m discussed in Section 4.2.4 below. Within the approximation of the KZK equation, the acoustic sound pressure and the particle velocity in the propagation direction follow the plane wave impedance relation $p = \rho_0 c_o u_z$, so that the expression of p_0 becomes

$$p_0 = \frac{|p_{\text{meas}}(r = r_1, \theta = 0)|}{2\left|\sin\left(\frac{1}{2}kr_1\left[\sqrt{1 + (a_{\text{eff}}/r_1)^2} - 1\right]\right)\right| e^{-\alpha r_1}}. \tag{4.6}$$

The other parameters that go into Eq. (2.14), are direct dependencies to the simulation program, and have to be given as input. These parameters are attended in Section 4.2.4 below. A comparison of the theoretical expression, and a linear simulation ($\beta = 0$), is given in Section 4.2.6.

4.2.4 Simulation parameters

Environmental parameters of the medium, such as temperature, pressure, humidity, and carbon dioxide content, play a decisive role in the accurate determination of medium properties. Specifically, the speed of sound, density, and absorption varies greatly, and have to be determined based on the measured environmental parameters taken as the measurement series of the sound pressure were conducted, in order to produce simulations as close to the reality as possible. In the following, these medium properties and their calculation are explained.

The speed of sound in air was computed following approximate equations presented by Cramer [80]. Environmental parameters, such as temperature, pressure, relative humidity, and the molecular fraction of CO_2, are needed for the calculations. The three first parameters are measured in the lab, while the latter was assumed to be a reference value of 400 ppm typically found in laboratories [81], as it was not measured directly. As noted by the authors of [81], other experiments have reported values of the molecular fraction of CO_2 as high as 1000 ppm, while averages of the maximum reported values from various

laboratories were about 600 ppm. Altering the molecular fraction in this area, while leaving the other measured parameters unchanged, does little to the speed of sound, which was found to be approximately 347.5 m/s.

In addition to the approximate equations of the speed of sound, Cramer presented similar equations to calculate the ratio of specific heats γ. Using the measured parameters as above, γ was found to yield about 1.4009, which is in good correspondence with reported values of 1.4 by [30, 29, 36]. Thus, giving a nonlinear coefficient β equal to 1.2 for the simulations.

The density of the medium was calculated following a revised formula of the density of moist air (CIPM-2007) [81], based on the 1981/91 equation by R. Davis [82]. The formula calculates the density based on the above-mentioned parameters so that $\rho_{\text{air}} = \rho(t, P_0, RH, x_{\text{CO}_2})$, where t is the temperature in °C, P_0 is the ambient absolute pressure in Pa, RH the relative humidity in %, and x_{CO_2} the molecular fraction of carbon dioxide. The latter is assumed to be 400 ppm if left unspecified. The script used for the calculations can be found in Appendix C.2.1.

Absorption is calculated using Eq. (2.26) from the ANSI/ASA S1.26-2014 standard discussed in Section 2.3.5. The coefficient has dependencies on ambient temperature and pressure, as well as relative humidity. The MATLAB script used to compute the absorption coefficient can be found in Appendix C.2.2.

The absorption coefficient computed for a specified frequency is combined with relaxation frequencies of oxygen and nitrogen, and in other manners combined in expressions needed to yield the resulting value, as shown in Eqs. (2.23)-(2.26). Thus, the calculated coefficient in Np/m gives the most correct value for the specified frequency. However, the input absorption coefficient α_2 to the Bergen Code has the units of Np/m/Hz^2, and thus, the calculated value has to be divided by f^2. As the absorption coefficient is frequency dependent, the value fed to the Bergen Code becomes incorrect in computing losses for higher-order harmonics. The latter is illustrated in Figure 4.3 below as α_2, where the absorption coefficient as a function of frequency is presented. To the left in the figure using measured environmental parameters in the acoustic laboratory for measurements of the 20x2 disc, and similar for the 13x2 disc to the right. The absorption coefficient α in the figure was computed for every new frequency following the ANSI standard described above, and α_c corresponds to the classical absorption coefficient tabulated in [29] as $\alpha_c = 1.37 \times 10^{-11}$ [Np/m/Hz^2]. The two vertical dashed lines mark the frequency corresponding to the first radial mode of the 20x2 disc and 13x2 disc, to the left and right, respectively.

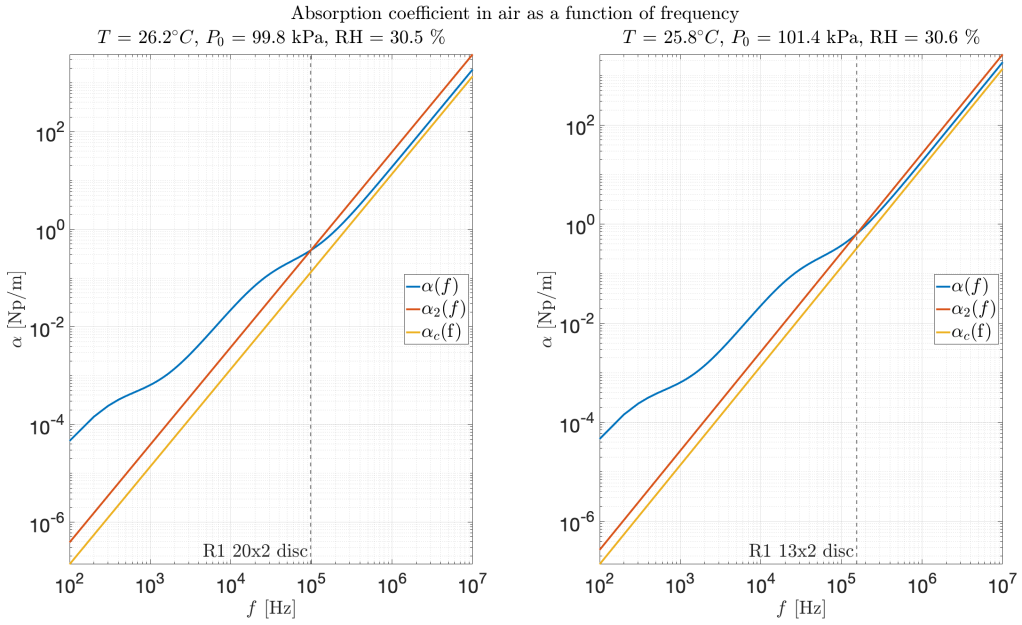

Figure 4.3: Calculated absorption coefficient as a function of frequency in Np/m.

The environmental properties have uncertainties to their measured values, as briefly mentioned in Section 3.3.3. To test the variation of the calculated medium parameters, temperature, relative humidity, and pressure was altered within the respective instrument uncertainties. The content of CO^2, assumed to be 400 ppm, was varied from 200 ppm to 600 ppm.

The greatest dependency was found in temperature, which altered the outcome of most parameters calculated. Here, both an uncertainty of 0.01°C and 0.2°C was tested, but the listed values in Table 4.4 were computed using the latter of the two. Relative humidity also played a sizeable part in the interval tested, especially concerning the absorption of sound.

Listed in Table 4.3 below are the values of temperature, barometric pressure, relative humidity, and molecular fraction of carbon dioxide, used to calculate the medium parameters. The value in the middle of each interval corresponds to the measured value during axial pressure measurements of the 20x2 disc for R1 ($f = 98.370$ kHz). About 195,000 (21^4) computations of each parameter go into Table 4.4, where the minimum- and maximum value, the mean, and the corresponding standard deviation are presented.

Table 4.3: Environmental properties used to compute medium parameters listed in Table 4.4 below. Each interval presented in column three corresponding to 21 values, with the increments listed in column four.

Parameter	**Symbol**	**Interval**	**Increments**	**Unit**
Temperature	T	[25.98, 26.38]	0.02	°C
Barometric pressure	P_0	[99683.5, 99703.4]	0.1	Pa
Relative humidity	RH	[30.6, 32.6]	0.1	%
Molecular fraction of CO_2	x_{CO_2}	[200, 600]	20	ppm

Table 4.4: Calculated variation in the medium parameters within uncertainties of the measured environmental properties. In column two and -three, the minimum and maximum value, respectively. Column four lists the mean of the computed values, and column five the corresponding standard deviation.

Parameter	**Min.**	**Max.**	μ	σ	**Unit**
$c(f, t, P_0, RH, x_{CO_2})$	347.38	347.70	347.54	0.08	m/s^2
$\gamma(f, t, P_0, RH, x_{CO_2})$	1.40081	1.40097	1.40089	0.00003	-
$\rho(t, P_0, RH, x_{CO_2})$	1.1547	1.1571	1.1559	0.0005	kg/m^3
$\alpha(f, P_0, RH, t)$	0.371	0.390	0.381	0.004	Np/m
$\alpha_2(f, P_0, RH, t)$	3.84×10^{-11}	4.03×10^{-11}	3.93×10^{-11}	0.04×10^{-11}	$Np/m/Hz^2$

4.2.5 Correction of the beam pattern

The beam patterns returned from the Bergen Code simulations are computed in a grid structure marching forward, and the Bergen Code outputs a transversal section of the propagated sound beam, i.e., the complex sound pressure $\boldsymbol{p}(z, \theta)$ along a vertical line perpendicular to the sound axis. The latter is illustrated in Figure 4.4 below as the red dashed line. A transversal beam pattern extracted from a simulation consists of sound pressure values $\boldsymbol{p}(z, \theta)$, which for every $\theta \neq 0$ is located a distance d from the origin (x, z)=(0,0).

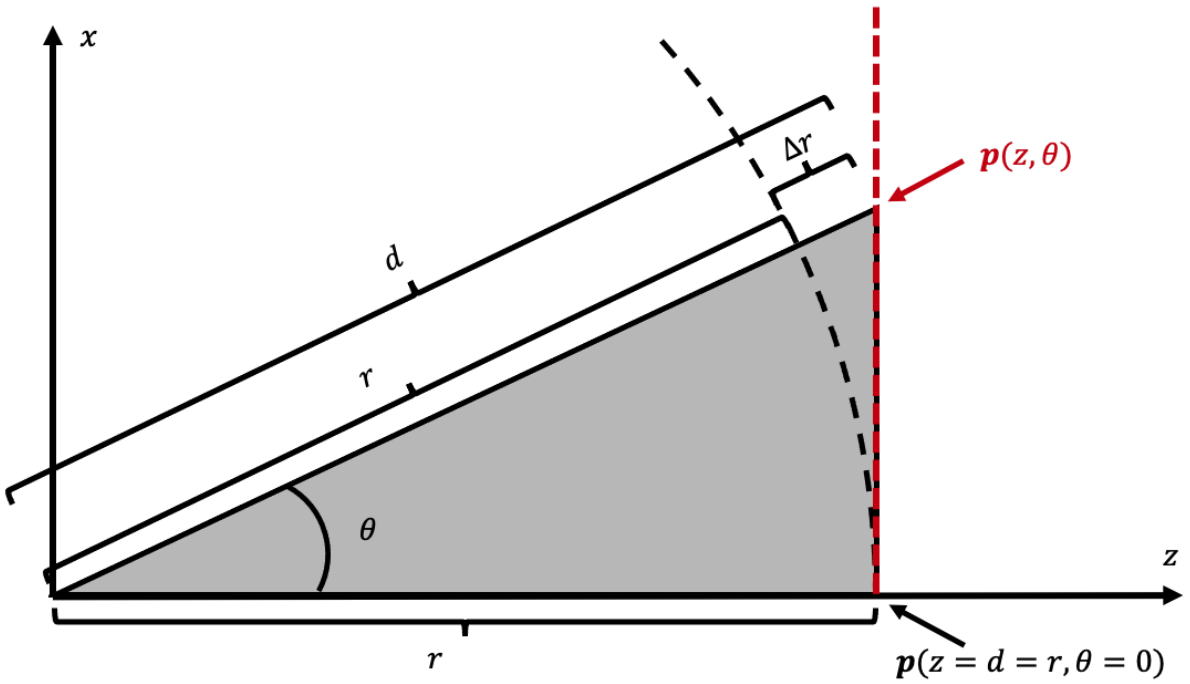

Figure 4.4: Illustration of the geometry of the transversal pressure values returned by the Bergen Code. The red dashed line indicates the extracted, transversal beam pattern from the Bergen Code, while the black dashed line indicates the effect of holding the distance to the source constant when θ is rotationally incremented.

However, unlike the beam pattern from the Bergen Code, directivity measurements conducted in the acoustic measurement setup are carried out by rotational increments of the piezodisc from its original position ($z = r, \theta = 0$), and the distance r between transmitter and microphone remains constant as θ is rotationally incremented. This is illustrated in Figure 4.5 above as the black dashed arc. As this is not the case for the simulated beam pattern, every sound pressure amplitude $p(z, \theta)$ on the transversal section has to be corrected for an extra propagation distance Δr. Assuming spherical spreading, and absorption, the sound pressure amplitude adjustment from $p(z, \theta)$ to $p(r, \theta)$ yields

$$p(r, \theta) = p(z, \theta) \left(\frac{d}{r} \right) e^{\alpha_2 \Delta r}, \tag{4.7}$$

where $d = r / \cos\theta$, and $\Delta r = d - r$, and α_2 is the absorption coefficient.

The effect of correcting the beam pattern due to propagation distance is illustrated in Figure 4.5 below, where the uncorrected beam pattern is plotted in a red dashed line, and the adjusted beam pattern in a solid blue line. It can be noted that it has a near-insignificant impact on the main lobe of the propagated sound beam, but becomes progressively more significant as θ increases, i.e., moving further away from the sound axis. The term (d/r) in Eq. (4.7) will, for a constant θ, remain constant for beam patterns further away from the source (increasing r). However, the latter part of Eq. (4.7), the absorption term, will have a more significant impact for greater distances, as shown in Figure 4.6. Here,

the complete adjustment term $\left(\frac{d}{r}\right) e^{\alpha \Delta r}$ is plotted as a function of distance r from the source, for four values of θ, and with an absorption coefficient corresponding to measured laboratory conditions and R1 of the 20x2 disc.

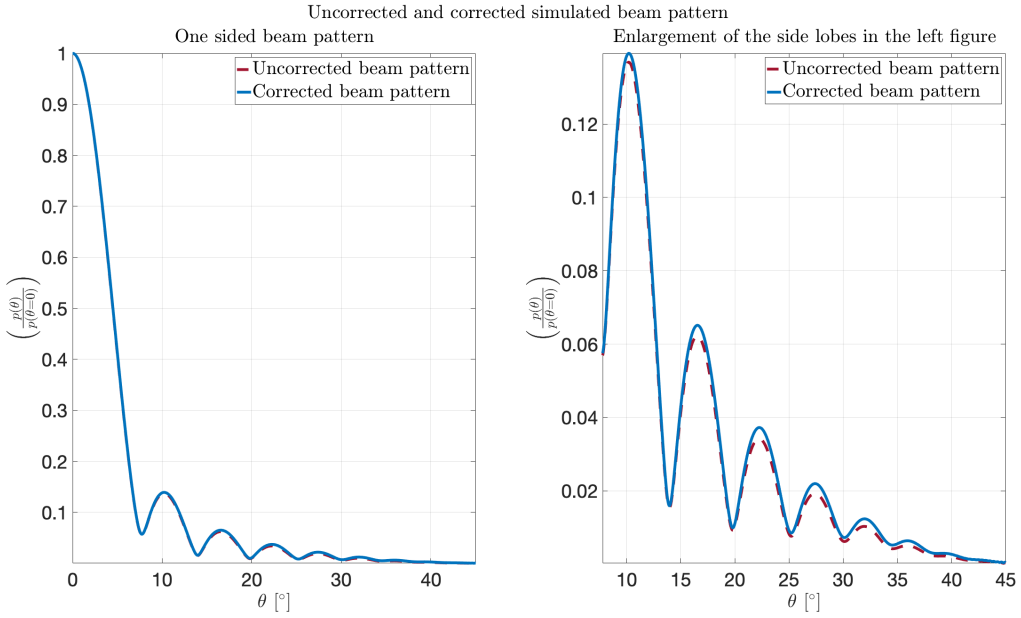

Figure 4.5: The effect of adjusting the Bergen Code beam pattern due to propagation distance from the source.

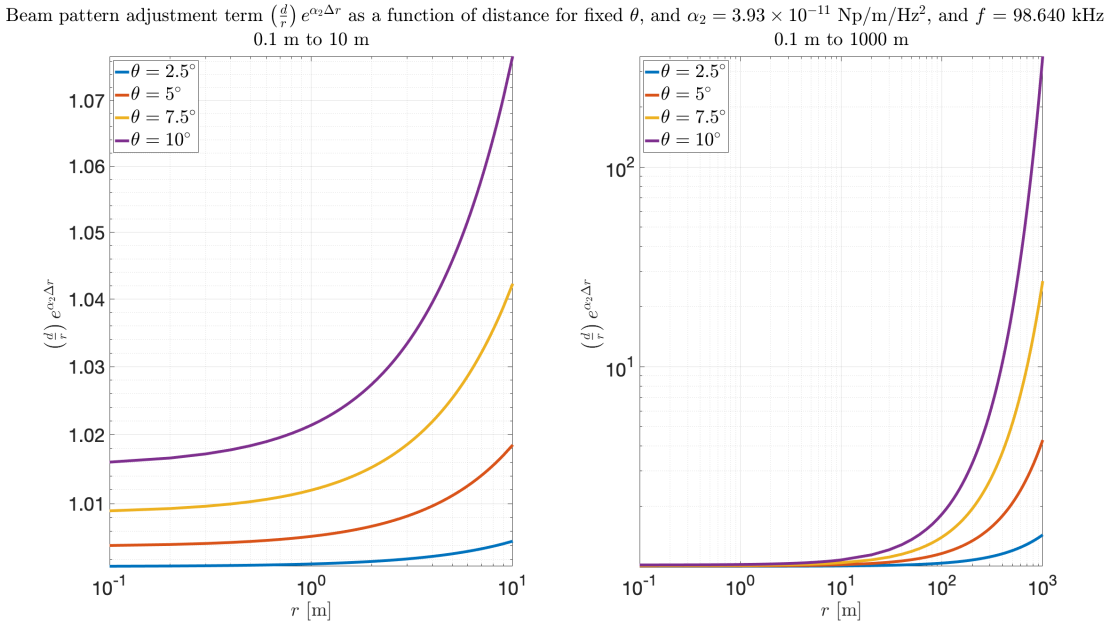

Figure 4.6: The adjustment factor $\left(\frac{d}{r}\right) e^{\alpha \Delta r}$ as a function of distance r from the source for fixed θ, an absorption coefficient equal $\alpha_2 = 3.93 \times 10^{-11}$ Np/m/Hz^2, and a frequency corresponding to R1 of the 20x2 disc.

4.2.6 Comparison of linear simulation to theoretical expression

Bergen Code simulations of linear sound propagation were carried out to compare the acoustic sound pressure amplitude along the sound axis to the theoretical expression given in [29] (Eq. (2.14)). Several mutual dependencies can be noted from the theoretical expression of Eq. (2.14), and the simulation parameters listed in the previous section. Both require an ambient (or unperturbed) fluid density, the speed of sound of the fluid, the wave number of the acoustic disturbance, and the radius of the disc. The simulation has an input source condition p_0, which relates to the particle velocity u_0 as noted above. The input p_0 was used to determine the particle velocity using the linear plane wave impedance relation as

$$u_z = \frac{p_0}{\rho_0 c_0}. \tag{4.8}$$

In addition, absorption in the fluid has to be added to the theoretical expression in order to yield comparable results. Absorption is added as an exponential factor, to a general expression of acoustic pressure, as

$$\boldsymbol{p} = P_0 e^{j(\omega t - kr)} e^{-\alpha_2 r}, \tag{4.9}$$

where α_2 is the absorption coefficient in Np/m/Hz^2, in other words, dependent on both distance and frequency squared. The values used both in the simulation and the computation of the theoretical expression, are listed in Table 4.5 below.

Table 4.5: Simulation parameters used as input in Bergen Code simulations of linear sound propagation for R1 of the 20x2 piezodisc.

Parameter	f_0	p_0	a	c_0	ρ_0	β	α_2
Value	98.640	1	10.0665	345	1.21	0	1.37×10^{-11}
Unit	kHz	Pa	mm	m/s	kg/m^3	-	Np/m/Hz^2

The resulting axial sound pressure amplitude for R1 are plotted in Figure 4.7 below. The upper of the two plots shows the logarithmic pressure in dB relative to 1 Pa, while the bottom plot shows the logarithmic amplitude ratio of the theoretical- and simulated values.

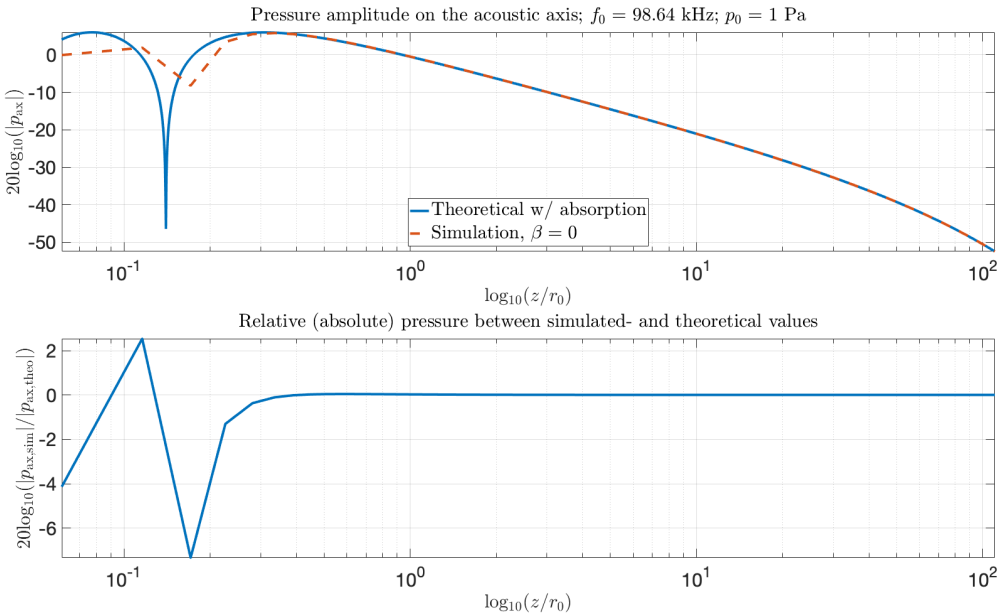

Figure 4.7: Upper plot: acoustic pressure amplitude on the sound axis from theoretical expression alongside values from a linear simulation using the Bergen Code, for the first radial mode. Lower plot: pressure amplitude ratio between theoretical expression and linear simulation.

Chapter 5

Results PZ27 20x2

5.1 Low voltage impedance measurements

Initially, FE simulations and measurements of the piezodiscs were carried out to establish the frequencies of interest. The impedance measurements were conducted using the HP 4192A impedance analyzer and were carried out at a modest excitation amplitude of 0.3 V_{rms}, assuming the behavior of the element to be fairly linear. The choice of amplitude to characterize the discs follows that of previous work [2, 68, 66], amongst others, in order to minimize nonlinear effects while still retaining measurement resolution. Plotted in Figure 5.1 below are the simulated- and measured values around frequencies corresponding to the two first radial modes (R1 and R2) and the thickness mode (TE1), for the 20x2 piezodisc.

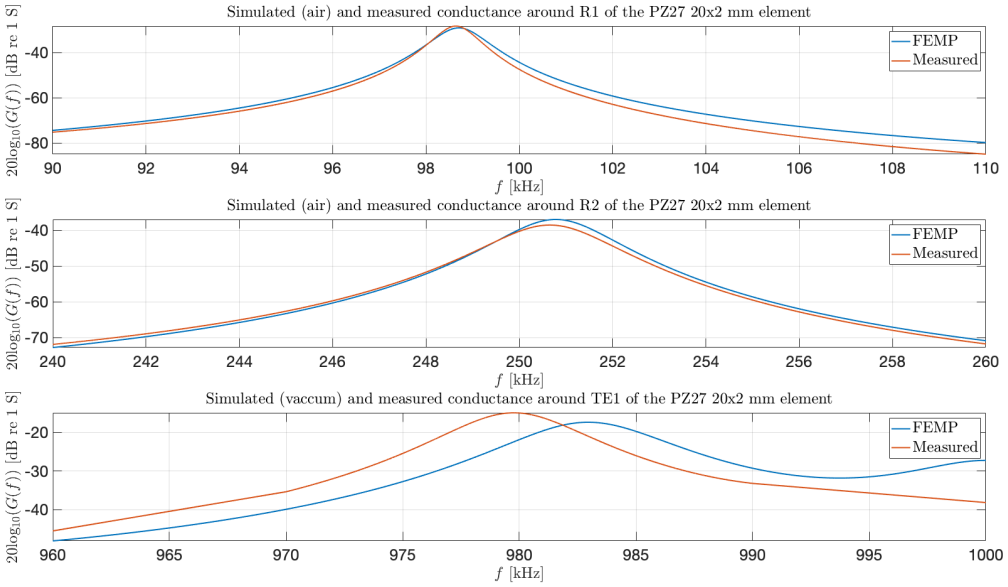

Figure 5.1: Measured and simulated values of conductance around R1, R2, and TE1 of the 20x2 disc.

Listed in Table 5.1 below are simulated- and measured values of the resonance frequencies of the two discs, extracted from the data depicted in the figure above, and similar for the 13x2 piezodisc. The resistances in column two were calculated through Eq. (2.4) in Section 2.1.1 from the admittance measurements of each resonance frequency.

Table 5.1: Resonances for R1, R2, and TE1, for the piezodiscs. Simulation values from FEMP, and admittance measurements using the HP 4192A impedance analyzer. Resistances of the discs at each resonance calculated from the measured values.

20x2 disc			
Mode	**Resistance**	**Measured**	**FEMP**
R1	25.9 Ω	98.640 kHz	98.700 kHz (air)
R2	81.4 Ω	250.650 kHz	250.780 kHz (air)
TE1	5.6 Ω	979.760 kHz	982.900 kHz (vacuum)
13x2 disc			
Mode	**Resistance**	**Measured**	**FEMP**
R1	42.4 Ω	155.650 kHz	153.290 kHz (air)
R2	132.4 Ω	382.970 kHz	377.420 kHz (air)
TE1	31.4 Ω	969.900 kHz	980.600 kHz (vacuum)

In Table 5.2, the -3 dB frequencies and corresponding bandwidths of the piezodiscs are presented. The values were calculated from the admittance measurements and simulated values described above, taking advantage of known characteristics of the conductance as described in Section 2.2.4.

Table 5.2: Calculated -3 dB frequencies and corresponding bandwidths of the piezodiscs from admittance measurements and simulations.

Measured							
	20x2 disc			**13x2 disc**			
Mode	$f^-_{-3\text{ dB}}$	$f^+_{-3\text{ dB}}$	Δf	$f^-_{-3\text{ dB}}$	$f^+_{-3\text{ dB}}$	Δf	**Unit**
R1	98.140	99.120	0.980	154.810	156.450	1.640	kHz
R2	249.250	252.000	2.750	380.700	385.250	4.550	kHz
TE1	976.640	982.840	6.200	966.010	973.910	7.900	kHz
Simulated							
	20x2 disc			**13x2 disc**			
Mode	$f^-_{-3\text{ dB}}$	$f^+_{-3\text{ dB}}$	Δf	$f^-_{-3\text{ dB}}$	$f^+_{-3\text{ dB}}$	Δf	**Unit**
R1	98.110	99.300	1.190	152.370	154.210	1.840	kHz
R2	249.520	252.040	2.520	375.610	379.230	3.620	kHz
TE1	979.400	986.700	7.300	976.300	984.900	8.600	kHz

Based on the measurements listed in the tables above, the frequency range of interest concerning impedance measurements with higher excitation amplitude was determined. Frequency ranges around each resonance mode were chosen to be finely sampled, and these frequency ranges were defined to be

$$[f_\text{l}, f_\text{u}] = \left[f_s - 5\left(\frac{\Delta f}{2}\right), f_s + 3\left(\frac{\Delta f}{2}\right) \right], \tag{5.1}$$

to cover the interval around each resonance in more detail. Here, f_s denotes the resonance frequency of interest, i.e., the first- or second radial mode, or the thickness mode. The left (lower) boundary f_l had to be increased from three- to five times $\Delta f/2$ to better capture the changes due to an increased excitation amplitude.

Quality factors for each resonance were calculated from the measured and simulated impedance measurements, using Eq. (2.11), and are presented in Table 5.3 below.

Q-factor				
	20x2 disc		**13x2 disc**	
Mode	**Measured**	**Simulated**	**Measured**	**Simulated**
R1	101	82	95	83
R2	91	99	84	104
TE1	158	134	123	114

Table 5.3: Quality factors for R1, R2 and TE1 of the two discs from impedance measurements and simulations.

5.2 High voltage measurements

Following these initial measurements, the I-V circuit described in Section 3.2 was configured, and its characteristics were tested before measurements of the two piezodiscs were initialized. In the following three sections, characteristics of the circuit and instruments are attended to before moving on to measurements of the piezodisc in Section 5.2.4. Section 5.2.5 attends measurements of the resonance frequencies and bandwidths of the discs, before moving onto an inspection of the current in the circuit in Section 5.2.6.

5.2.1 Noise readings of the measurement circuit without output from the signal generator

Measurements of the circuit with no applied signal were carried out to investigate the inherent noise in the circuit. Both channels of the oscilloscope were read, as displayed in the two uppermost plots in Figure 5.2 below. The two plots at the bottom show the related one-sided frequency spectra of each channel, whose magnitude is expressed in decibels relative to 1 V.

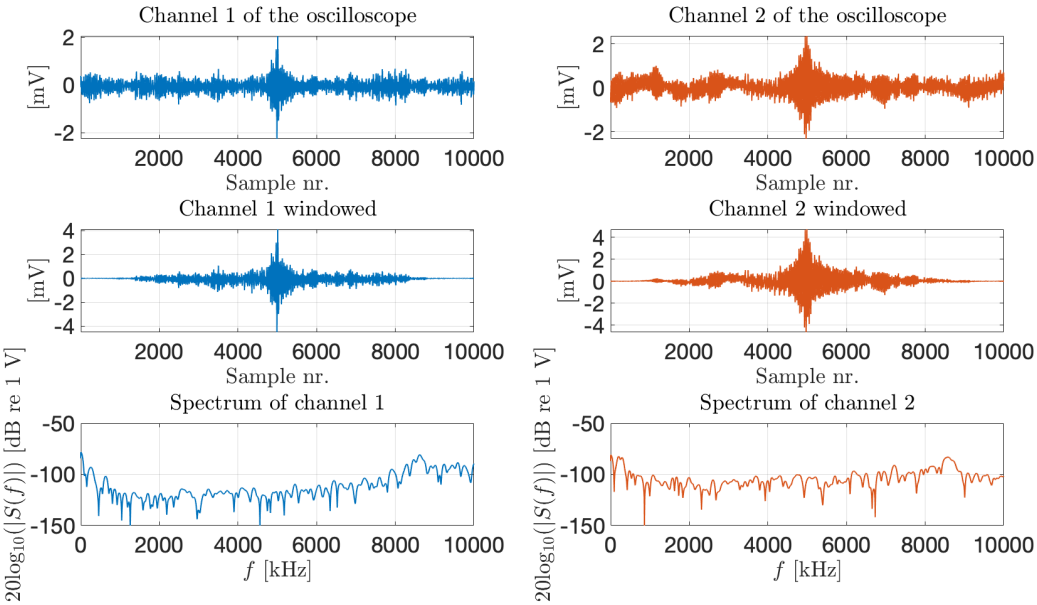

Figure 5.2: Noise readings on channels 1 and -2 of the Tektronix DPO3012 oscilloscope without output from the signal generator. Uppermost plot; raw data readings, middle plot; windowed readings of the oscilloscope, lowermost plot; Fourier spectra in decibel relative to 1 V.

5.2.2 Characteristics of the output signal of the signal generator

Following the measurements of the inherent noise in the circuit, the output of the signal generator was measured to characterize the signal. In general, signal generators exhibit harmonic features in the output signal, which are usually characterized in the datasheet [57].

Measurements of the first- and second radial mode, and the thickness mode were carried out for nominal applied voltages $V_{0,\mathrm{pp}}$ of 0.3-, 0.6-, 1.2-, 5-, 10- and 20 V. In Figure 5.3 below, two periods of the output signals can be seen in the upper left plot, for a frequency corresponding to R1. The upper right plot is the reading of the second channel of the oscilloscope when connected to the measurements circuit which, in turn, was not connected to the output signal. The two plots at the bottom of the figure show the one-sided Fourier transform of the six signals at channels 1 and 2 of the oscilloscope, respectively. Amplitudes of the spectrum of channel 1 are divided by their maximum value to yield 0 dB for what would be the frequency of the applied signal, i.e., the amplitudes are expressed in decibel relative to carrier (fundamental) level (dBc). The spectrum of channel 2 is divided by the corresponding maximum value of the spectrum of channel 1, for equal nominal applied voltage.

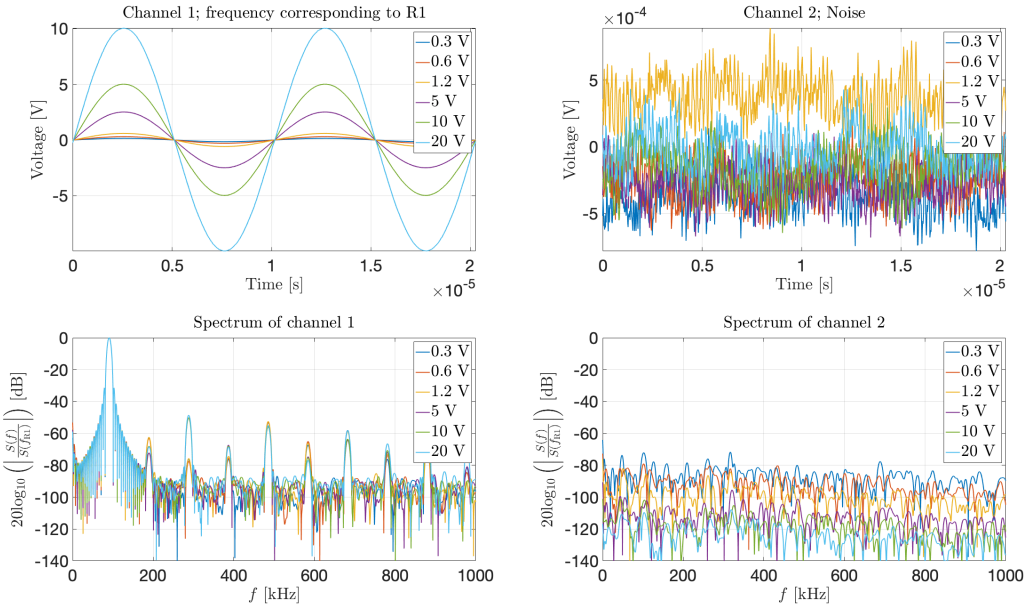

Figure 5.3: Parts of the measured readings of channel 1 and 2 of the oscilloscope (two upper plots), respectively, and their calculated spectrum below (two lower plots).

To simplify the comparison of the generated harmonics, as a function of applied voltage and across the different resonance frequencies, the harmonic amplitudes relative to the fundamental were extracted and plotted in Figure 5.4 below. Overtones of the fundamental frequencies corresponding to R1, R2, and TE1, are plotted in each column in the colors blue, red, and orange, respectively. The first three odd harmonics are displayed for each fundamental in Figure 5.4, but the three first even harmonics, and harmonics number seven, nine, and eleven can be found in Appendix B.1

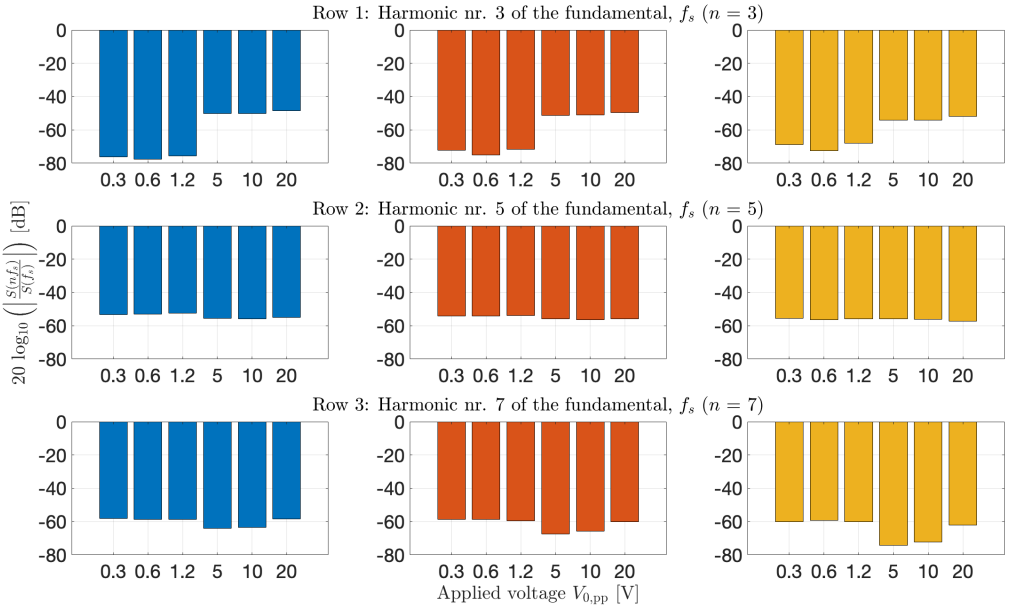

Figure 5.4: Harmonic amplitudes relative to the fundamental in the measured output of the signal generator for the fundamental frequencies corresponding to R1, R2, and TE1, plotted in blue, red, and orange colors, respectively. Here shown for the first three odd harmonics ($n = 3, 5, 7$).

5.2.3 Measurements of resistors in place of the piezodisc

A piezoelectric element has its characteristics altered with frequency. Other electrical components are typically assumed to be unaffected by changes in, e.g., the applied frequency or voltage, and thus have a constant value. This is however a simplification of reality as all components inherit dependencies to several parameters [54]. Resistors were placed in place of the piezodisc (one at a time), and measurements were carried out for frequencies corresponding to R1, R2, and TE1, of the disc, for different nominal applied voltages. Two resistors were utilized, one with a resistance around 5 Ω to best reflect the resistance of the disc around TE1, and one at about 55 Ω for the two radial modes.

Displayed in Figure 5.5 below are the results for a resistor of 55 Ω, and frequency corresponding to the first radial mode. Similar measurements were conducted successively for R2 and TE1, only changing the resistor for the latter. The measurements corresponding to R2 and TE1 are not shown here but can be found in Appendix B.2.

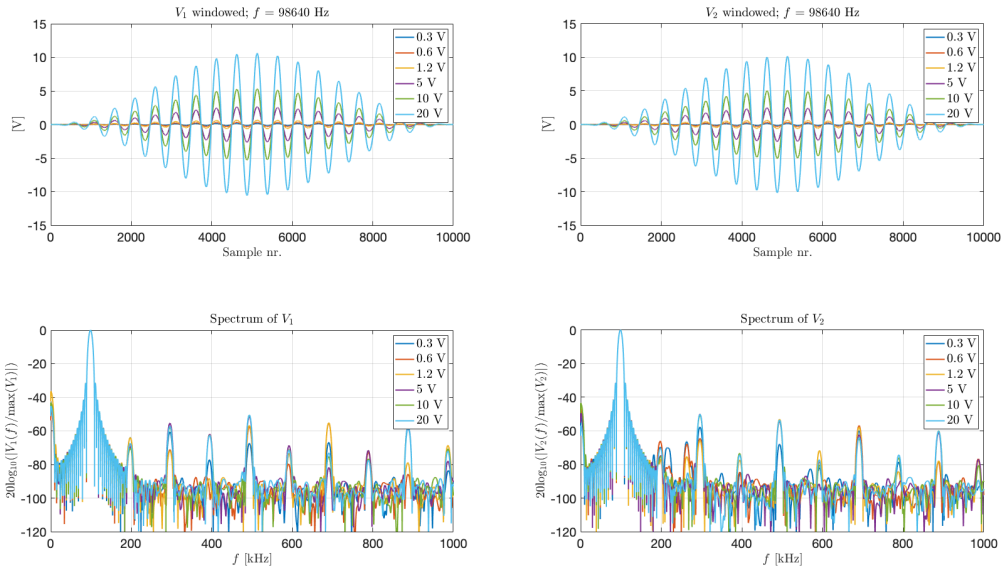

Figure 5.5: Windowed readings from the oscilloscope (upper plots) and Fourier transform (lower plots) for V_1 and V_2 with a resistor of 55 Ω in place of the piezodisc for R1. Multiple series with varying nominal applied voltage $V_{0,\text{pp}}$ displayed in each plot.

5.2.4 Measurements of the piezodisc

Finally, the piezodisc was mounted in the I-V circuit, and measurements were conducted around the three resonance modes. An inspection of the harmonics in the measured voltages V_1 and V_2 was carried out, for each mode, as can be seen for the frequency corresponding to R1 in Figure 5.6 below. Similar figures for R2 and TE1 can be found in Appendix B.3. A closer look at the frequency range 0 kHz to 300 kHz of the spectra of V_2 for fundamental frequency corresponding to R1, measured for the resistor and piezodisc mounted in the I-V circuit, separately, are presented in Figure 5.7.

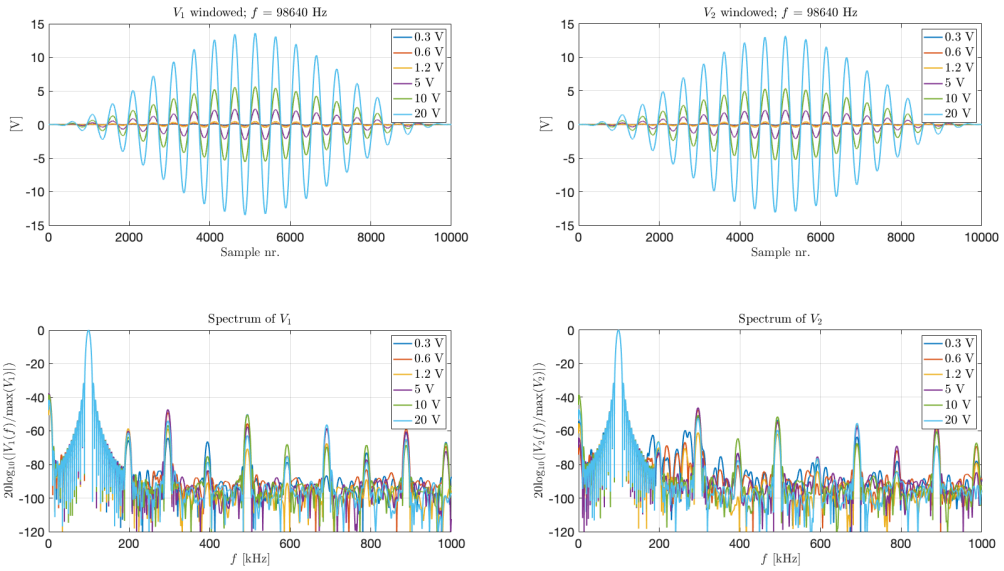

Figure 5.6: Windowed readings from the oscilloscope (upper plots) and Fourier transform (lower plots) for V_1 and V_2 for various excitation amplitudes $V_{0,\text{pp}}$ for R1. V_2 is here the voltage measured across the 20x2 mm piezodisc.

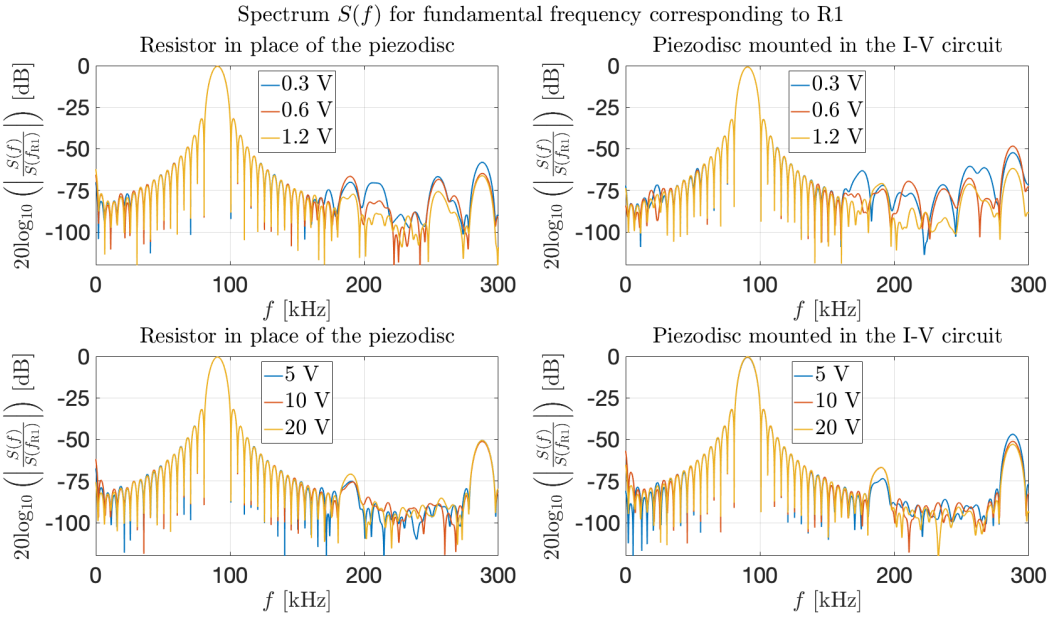

Figure 5.7: Spectra of the measured voltages V_2 from Figure 5.5 (resistor in place of the piezodisc) and Figure 5.6 (measurements of the piezodisc) above, here shown in the frequency range 0 kHz to 300 kHz.

The current in the circuit, calculated from the voltage measurements in Figure 5.5 and 5.6, for the 55 Ω resistor, and 20x2 piezodisc, respectively, are compared in Figure 5.8

below. The lower nominal applied voltages are separated into the two upper plots, and the higher ones to the bottom of the figure. Summarized in Table 5.4 below are the THD of the currents for frequencies corresponding to R1, R2, and TE1, of the piezodisc, for the measurements of the resistor, and piezodisc, mounted in the circuit separately.

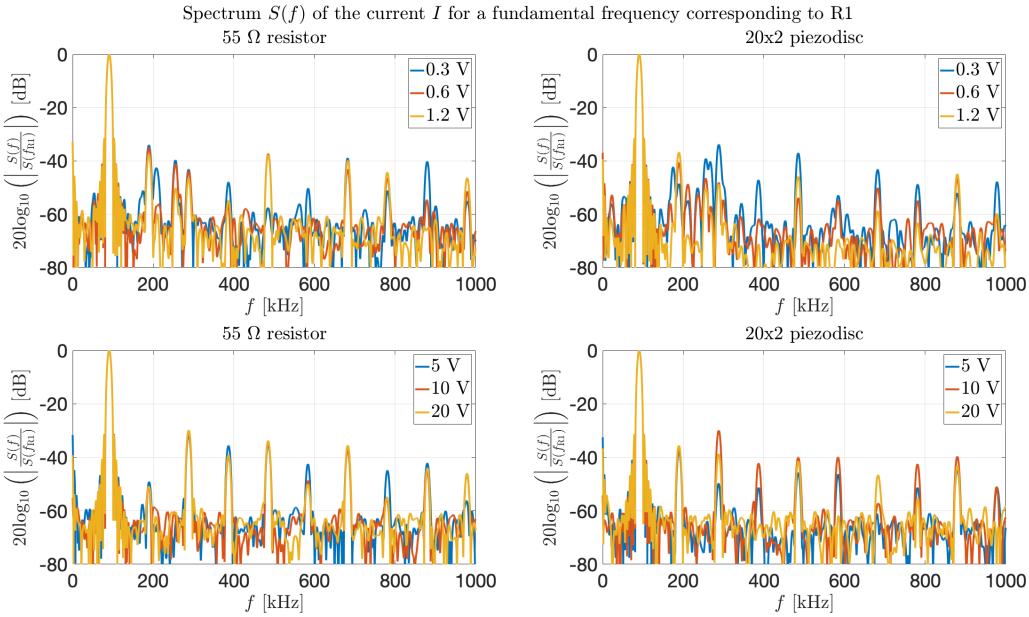

Figure 5.8: Comparison of the frequency spectra of measured currents with, in the left column, a 55 Ω resistor in the circuit, and to the right, the 20x2 piezodisc. Fundamental frequency corresponding to R1 of the piezodisc for all measurements.

Table 5.4: Calculated total harmonic distortion of the computed currents, for both resistors and the 20x2 piezodisc, for frequencies corresponding to the three resonance modes of the 20x2 disc, for different excitation amplitudes $V_{0,\mathrm{pp}}$, including the first 50 harmonic components.

Resistor							
$V_{0,\mathrm{pp}}$	0.3 V	0.6 V	1.2 V	5 V	10V	20 V	Unit
R1 (55 Ω)	3.09	3.64	3.51	4.69	4.54	5.04	[%]
R2 (55 Ω)	2.74	3.22	3.15	4.30	4.01	4.40	[%]
TE1 (5 Ω)	0.55	0.55	0.69	0.71	0.79	0.84	[%]
Piezodisc							
$V_{0,\mathrm{pp}}$	0.3 V	0.6 V	1.2 V	5 V	10V	20 V	Unit
R1	3.04	1.99	2.14	2.56	4.99	3.72	[%]
R2	12.4	3.37	3.17	4.06	4.06	6.21	[%]
TE1	0.65	0.55	0.64	0.61	0.69	0.83	[%]

5.2.5 Calculations based on measurements on the I-V circuit

Measurement series conducted over a limited frequency range around each resonance were used to calculate phase differences between the two measured voltages $\boldsymbol{V_1}$ and $\boldsymbol{V_2}$. The zero-crossing method was initially the chosen approach of the two discussed in Section 3.2.3. To begin with, the midpoint between the two samples of a zero crossing was used as the time of the zero crossing. This showed rather large fluctuations in the computed phase shifts, likely due to higher frequency noise in the measurements. Cubic spline interpolation was tested and reduced some of the noise seen previously. To further reduce deviations in computed zero crossings, another method was desirable and the cubic spline approximation was chosen. It is said to produce the smoothest possible approximation to the third degree, meaning that both the first and second derivative remains continuous [61]. By the use of cubic spline approximation, the fluctuations in the calculated values were further reduced.

In addition to the incorporation of a better interpolation method, lowpass filtering of the signals was applied before the zero-crossing calculation. The data collected from measurements around the resonances were filtered using a sixth-order Butterworth lowpass filter, whose filter coefficients were created using MATLABs built-in function butter() [83]. To further reduce noise in the waveforms, a finite impulse response (FIR) moving average filter of length $N = 25$ was applied to both waveforms locally in the zero-crossing method, as can be seen in Appendix C.3.1. Using equal filters in the filtering of both waveforms, and discarding the N first samples, removes unwanted and wrong values to be evaluated, and should thus yield a correct phase difference between the waveforms as it does not matter where in the waveform the search for zero-crossing starts. The latter is true as long as an even number of zero-crossings are computed, and the signals are fairly symmetric around zero.

From measurement series around R1, R2, and TE1, the impedance was calculated according to Eq. (3.7). The calculated phase shifts, conductance, and GB-plot are displayed for a frequency range around each of the resonance modes in Figures 5.10 to 5.12 below, for the 20x2 disc. Various nominal applied voltages were utilized, as highlighted by the labels in the figures, and the measurement series were processed separately. A continuous waveform was used as output from the signal generator for these measurements. Displayed in Figure 5.9 are GB-plots of around R1 and TE1 from the measurements.

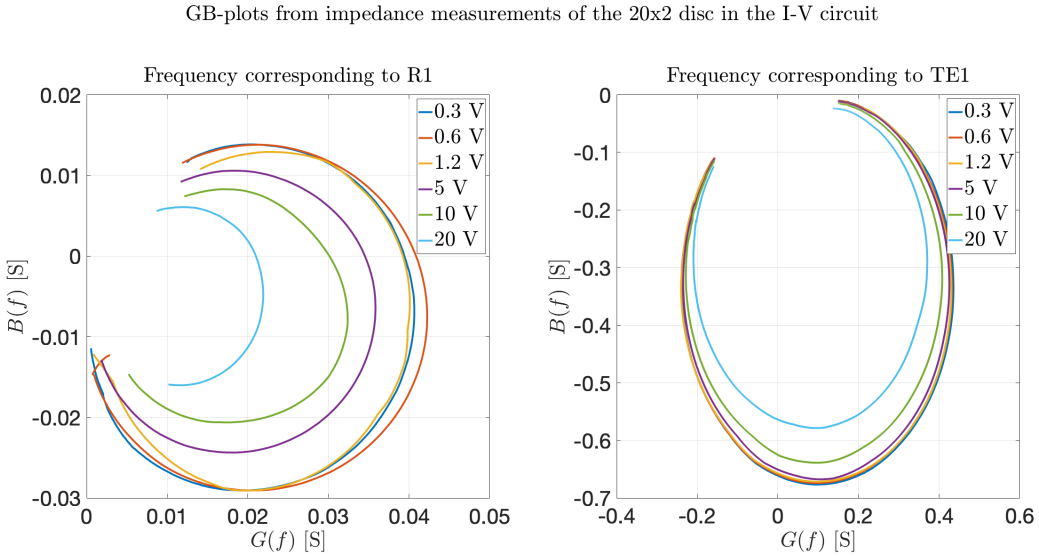

Figure 5.9: GB-plot of impedance measurements of the 20x2 disc in the I-V circuit, for a frequency range corresponding to R1 to the left, and TE1 to the right.

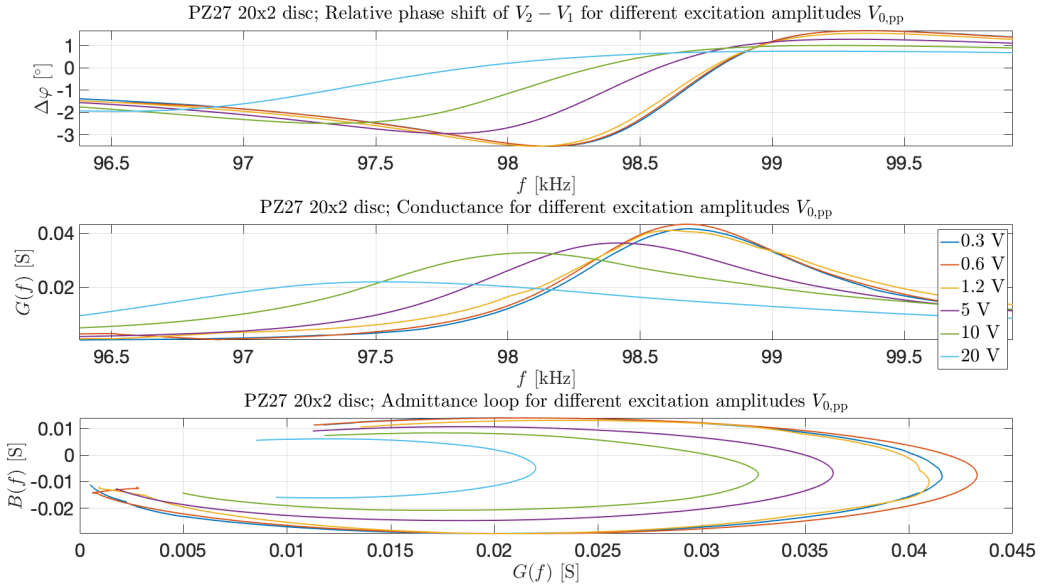

Figure 5.10: Calculations of phase shift between measured voltages $\boldsymbol{V_2}$ and $\boldsymbol{V_1}$, conductance, and a GB-plot in a frequency range around R1. Each curve corresponding to the nominal applied voltage $V_{0,pp}$ at the signal generator.

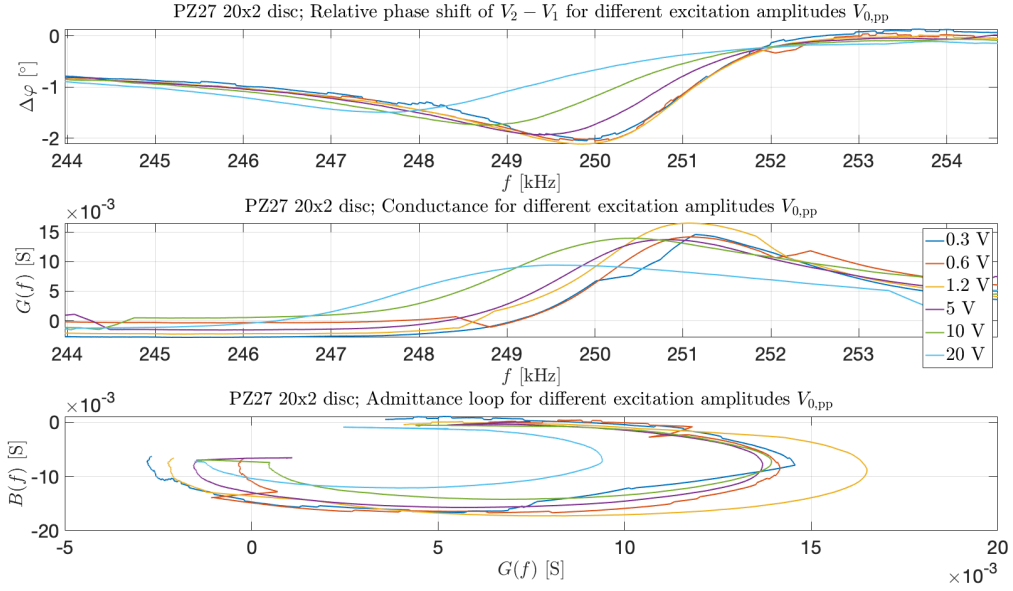

Figure 5.11: Same as Figure 5.10, but here around R2.

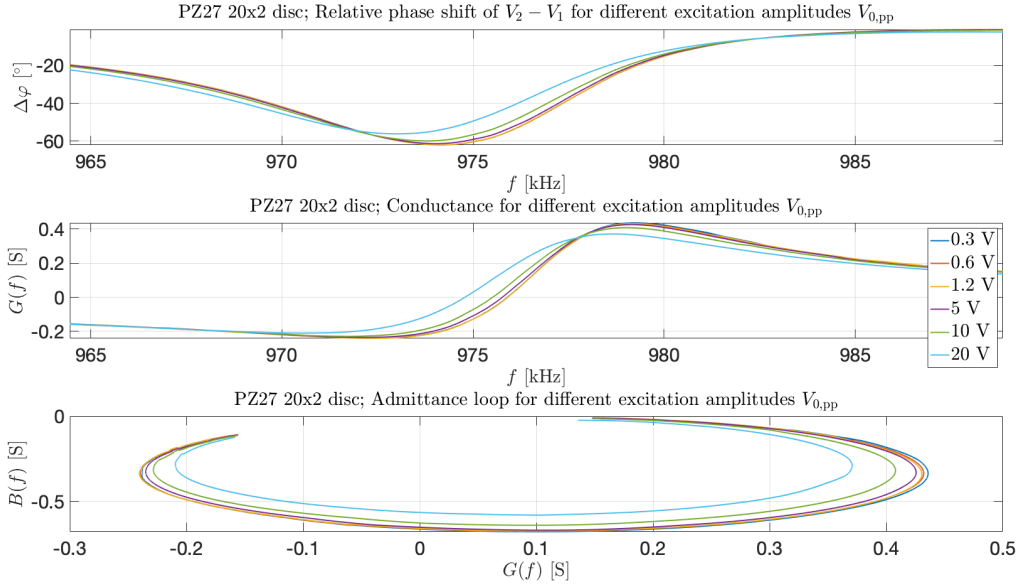

Figure 5.12: Same as Figure 5.10 and -5.11, but here around TE1.

In Table 5.5, computed resonance frequencies and bandwidths to the three different modes of the 20x2 disc are listed for the nominal excitation levels $V_{0,pp}$. Similar is presented for the 13x2 disc in Table 5.6 to the end of this section. Measurements of the thickness mode for transmitted burst signals showed odd phenomenon, and calculation of the impedance was unsuccessful.

Table 5.5: Calculated resonance and bandwidth for each mode for impedance measurements in the I-V circuit for the 20x2 disc. Both continuous waveform and burst excitation utilized.

Continuous waveform						
	R1		R2		TE1	
$V_{0,\mathrm{pp}}$ [V]	f_s [kHz]	Δf [kHz]	f_s [kHz]	Δf [kHz]	f_s [kHz]	Δf [kHz]
0.3	98.680	1.090	251.150	2.730	979.240	8.150
0.6	98.680	1.070	251.130	-	979.140	8.230
1.2	98.610	1.200	251.120	2.810	979.150	8.370
5	98.410	1.460	250.830	3.710	979.100	8.340
10	98.100	1.910	250.370	5.100	979.010	8.760
20	97.500	2.810	249.730	-	978.640	9.540
Burst excitation						
	R1		R2		TE1	
$V_{0,\mathrm{pp}}$ [V]	f_s [kHz]	Δf [kHz]	f_s [kHz]	Δf [kHz]	f_s [kHz]	Δf [kHz]
0.3	98.500	1.180	251.310	2.720	-	-
0.6	98.430	1.710	251.310	-	-	-
1.2	98.410	1.790	251.290	-	-	-
5	98.350	2.390	251.040	-	-	-
10	97.970	1.430	250.500	2.950	-	-
15	97.730	2.130	250.220	3.270	-	-
20	97.550	2.530	249.690	3.490	-	-

The measured values that go into Table 5.5 and 5.6 were found through the conductance as discussed in Section 2.2.3 and 2.2.4. Two examples of the calculated conductance based on the measurements of $\boldsymbol{V_2}$ and $\boldsymbol{V_1}$ in the I-V circuit are presented in Figure 5.13 and 5.14 below, for measurements of R1 of the 20x2 disc. Equal figures for other measurement series of R1, R2, and TE1, for the two discs, can be found in Figures B.10-B.66 in Appendix B.4. For these measurements, the frequency domain method discussed in Section 3.2.3, was utilized as the zero crossing method showed somewhat worse performance for some of the measurement series. As for the 20x2 disc, impedance calculations from the measurement series utilizing burst excitation was unsuccessful for TE1 of the 13x2 disc. Moreover, several of the measurement series, the bandwidths were not possible to determine accurately.

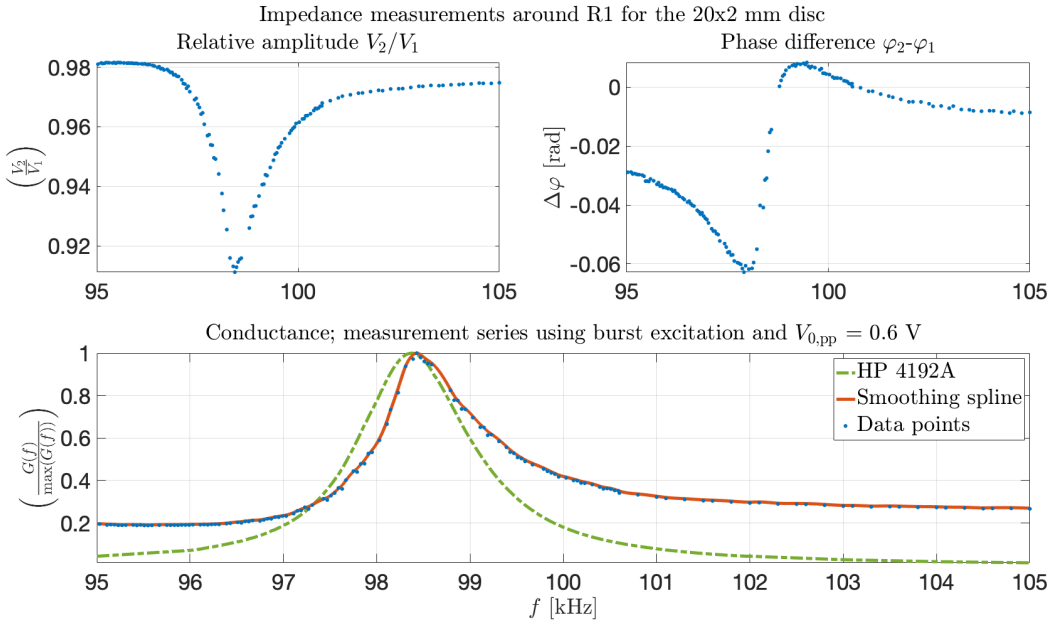

Figure 5.13: Example of the relative amplitudes V_2/V_1 and the phase difference $\Delta\varphi$, in the upper left and right part of the figure, respectively, measured in the I-V circuit, and used for computing the impedance. In the bottom part of the figure, the conductance measured in the I-V circuit is compared the measurements using the HP 4192A impedance analyzer. Here shown for the first radial mode of the 20x2 disc, with a nominal applied voltage $V_{0,\mathrm{pp}}$ equal 0.6 V.

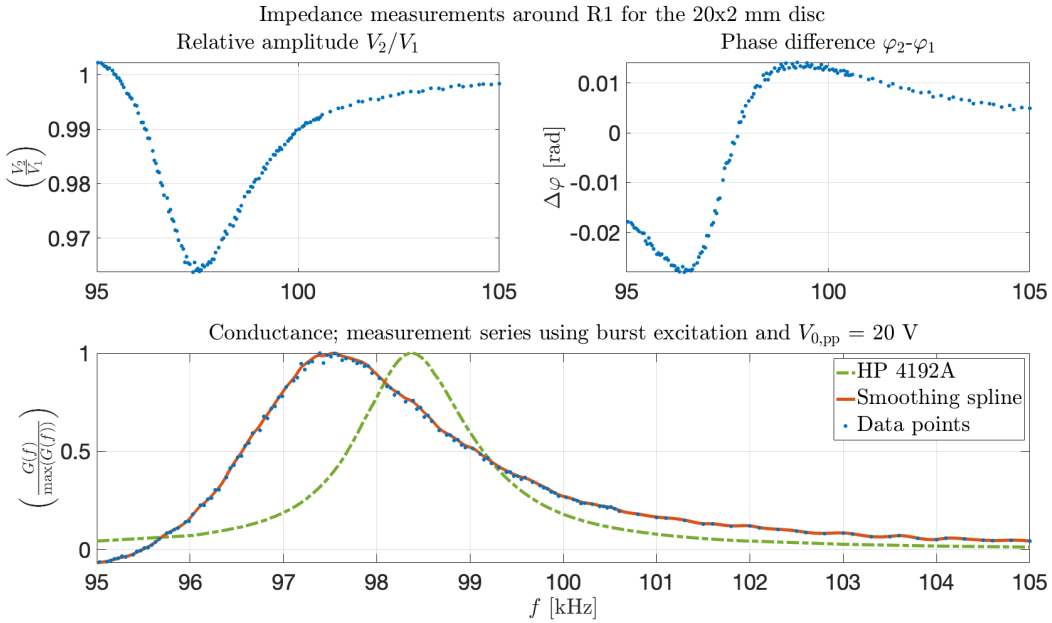

Figure 5.14: Same as Figure 5.13, but here for $V_{0,\mathrm{pp}} = 20$ V.

Table 5.6: Calculated resonance and bandwidth for each mode for impedance measurements in the I-V circuit for the 13x2 disc. Both continuous waveform and burst excitation utilized.

Continuous waveform						
	R1		R2		TE1	
$V_{0,\mathrm{pp}}$ [V]	f_s [kHz]	Δf [kHz]	f_s [kHz]	Δf [kHz]	f_s [kHz]	Δf [kHz]
0.3	154.440	2.380	382.630	3.470	976.180	7.320
0.6	154.410	-	382.640	-	976.080	-
1.2	154.300	-	382.570	-	975.880	-
5	154.130	-	382.170	-	975.710	-
10	153.470	-	381.950	-	975.000	7.980
20	153.200	-	381.870	-	974.380	8.120
Burst excitation						
	R1		R2		TE1	
$V_{0,\mathrm{pp}}$ [V]	f_s [kHz]	Δf [kHz]	f_s [kHz]	Δf [kHz]	f_s [kHz]	Δf [kHz]
0.3	155.020	3.250	382.270	3.350	-	-
0.6	155.030	-	382.520	-	-	-
1.2	154.980	-	382.310	-	-	-
5	154.720	-	382.520	-	-	-
10	154.210	3.540	381.820	3.920	-	-
15	153.750	3.640	381.490	3.760	-	-
20	153.320	4.160	381.090	4.140	-	-

5.2.6 Calculated current in the circuit

From the measurements conducted on the I-V circuit previously, calculations of the current through the discs were carried out. The current was computed from the voltage drop over the known resistor R in the circuit using the formula stated in Eq. (3.1) from Section 3.2. Filtering of any sort was not utilized, and a Fourier transform was computed for investigation of the frequency content in the current.

This was carried out for both discs, with both continuous waveform and bursts excitation output signals. The measurements with continuous waveform had 14 periods of the signal extracted. An example of this is shown for the 20x2 disc in Figure 5.15 below, where the frequency corresponds to the first radial mode. Measurement series utilizing bursts had 50 periods of the steady state part of the signal extracted before the current was calculated, and Fourier transformed. This is shown for R1 of the 20x2 disc in Figure 5.16 below. In the upper part of the figures, the windowed, extracted signal is plotted, while the associated Fourier spectra are displayed in the bottom half.

Similar measurements were carried out for frequencies corresponding to R2 and TE1, which can be found in Appendix B.5. Figure 5.17 displays the first six overtones of R1 for the current, as a function of nominal applied voltage, presented in a bar plot. Even

harmonics are presented in blue bars to the left and odd harmonics in red to the right in the figure. The THD for each measurement series were also calculated, including the first 50 harmonics, which are summarized in Table 5.7.

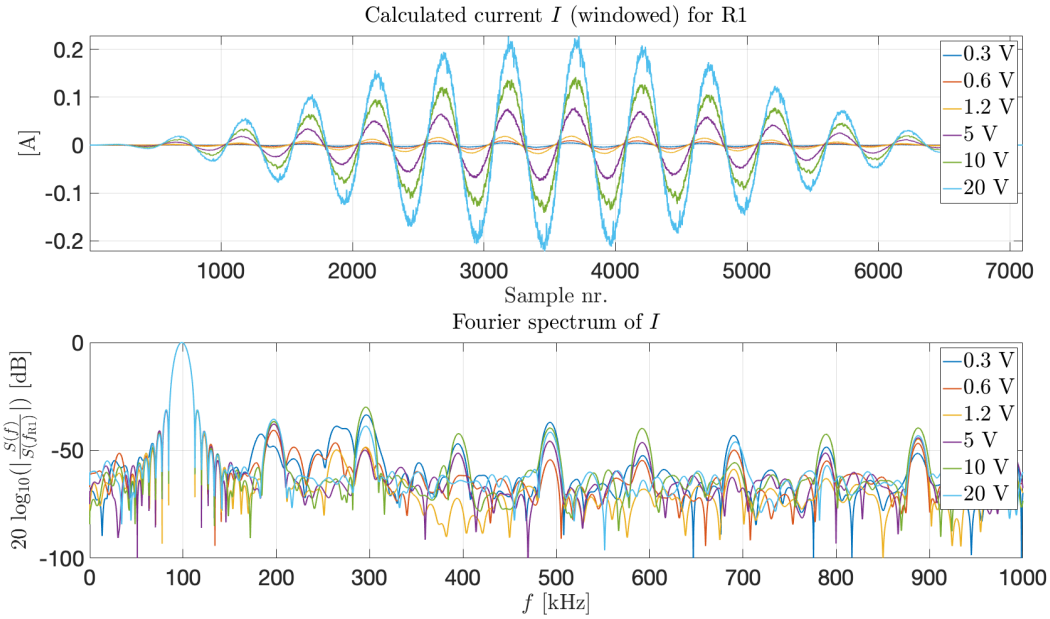

Figure 5.15: Calculated current through the 20x2 piezodisc from the voltage drop over the known resistor R (upper plot), and corresponding frequency spectrum (bottom plot), for R1.

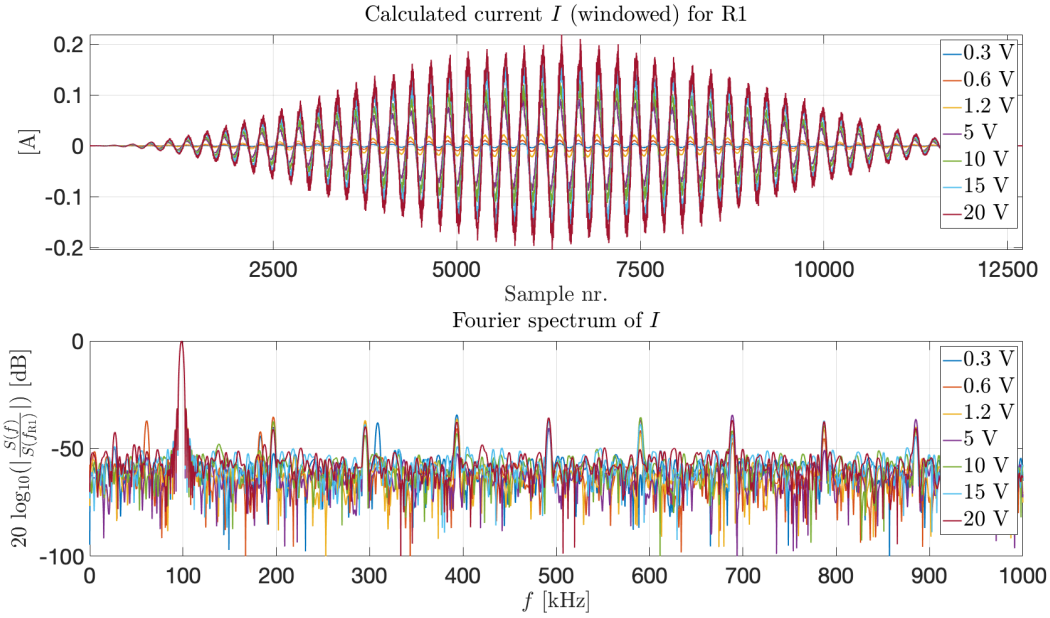

Figure 5.16: Calculated current through the piezodisc from the voltage drop over the known resistor R (upper plot), and corresponding frequency spectrum (bottom plot), for the first radial mode (R1).

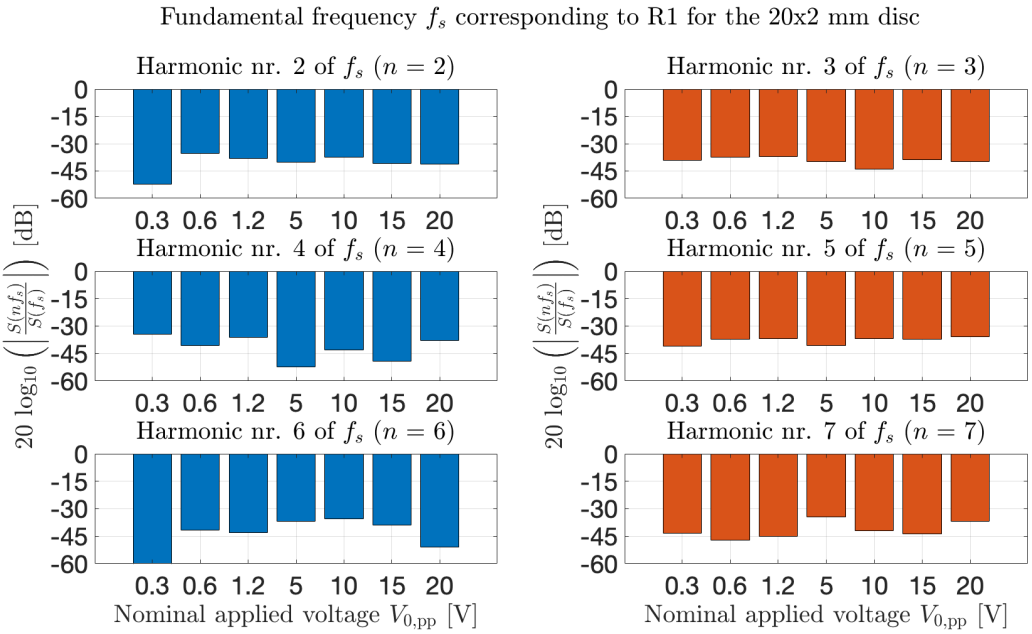

Figure 5.17: Relative harmonics amplitudes to the fundamental frequency corresponding to R1, for the first six overtones.

Table 5.7: Calculated total harmonic distortion in the computed currents of the three resonance modes for different excitation amplitudes $V_{0,\mathrm{pp}}$ including the first 50 harmonic components.

Continuous waveform								
$V_{0,\mathrm{pp}}$	0.3 V	0.6 V	1.2 V	5 V	10V	15 V	20 V	Unit
R1	3.04	1.99	2.14	2.56	4.99	-	3.72	[%]
R2	12.4	3.37	3.17	4.06	4.14	-	6.21	[%]
TE1	0.69	0.56	0.64	0.61	0.69	-	0.83	[%]
Burst excitation								
$V_{0,\mathrm{pp}}$	0.3 V	0.6 V	1.2 V	5 V	10V	15 V	20 V	Unit
R1	4.09	3.81	4.09	4.49	5.50	5.09	5.63	[%]
R2	5.64	3.26	3.33	3.36	7.62	10.5	10.4	[%]
TE1	2.45	2.43	2.53	2.59	2.63	2.57	2.47	[%]

As for the 20x2 disc, the current in the I-V circuit was calculated from voltage measurements across the 13x2 disc, for frequencies corresponding to R1, R2, and TE1. This is shown for R1 in Figure 5.18 and 5.19 below, and similar figures can be found for R2 and TE1 in Appendix B.5. The magnitude of the first six overtones of R1 and R2 can similarly be seen in Figure 5.20 and 5.21, and the THD for the resonances are presented in Table 5.8 below.

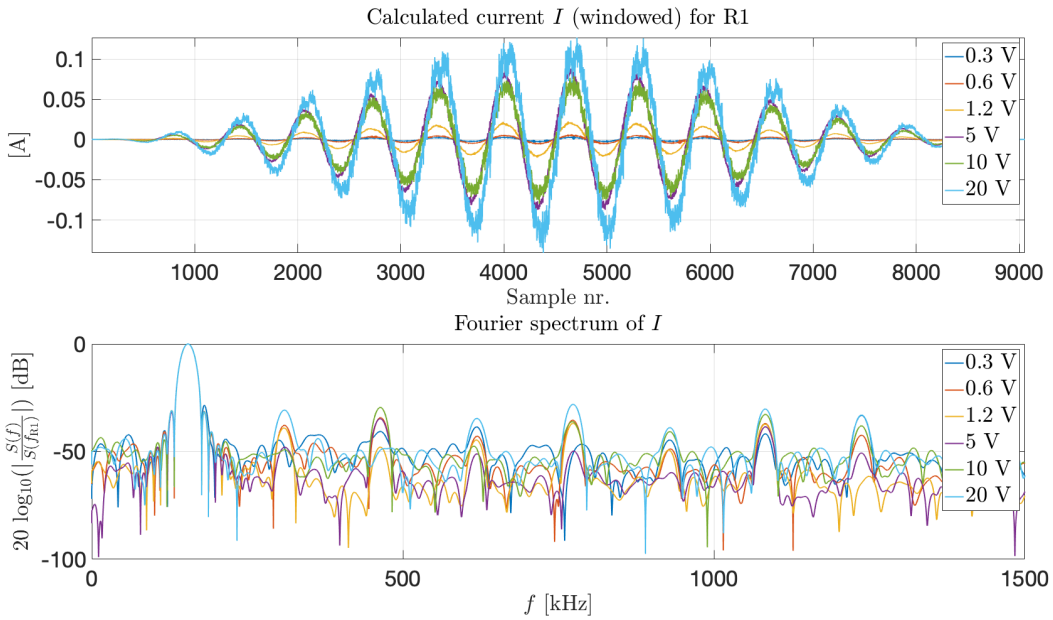

Figure 5.18: Calculated current through the 13x2 piezodisc from the voltage drop over the known resistor R (upper plot), and corresponding frequency spectrum (bottom plot), for R1.

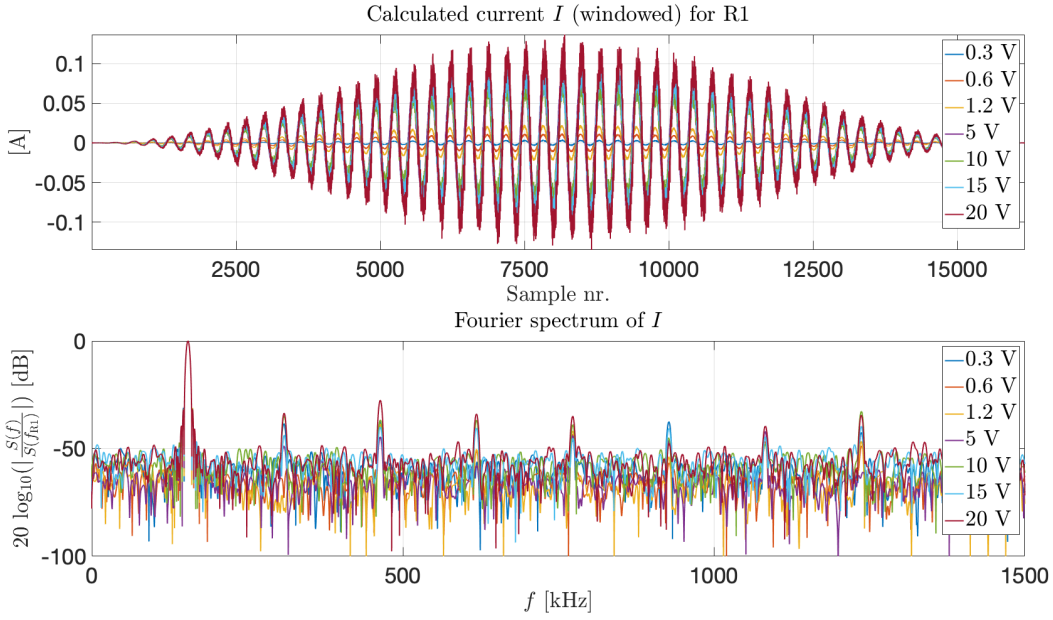

Figure 5.19: Calculated current through the 13x2 piezodisc from the voltage drop over the known resistor R (upper plot), and corresponding frequency spectrum (bottom plot), for the first radial mode (R1).

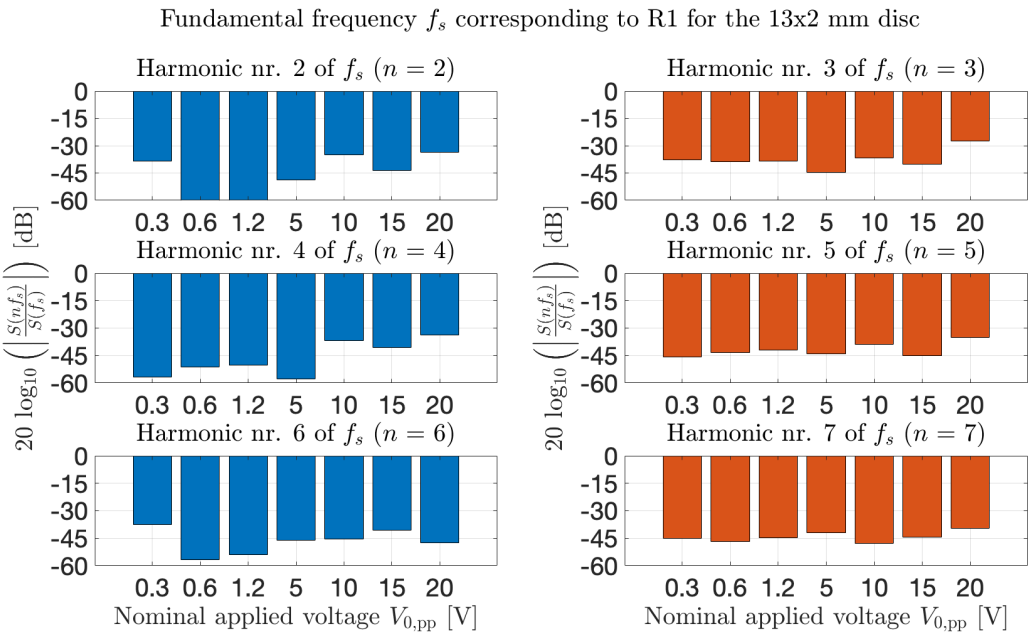

Figure 5.20: Relative harmonics amplitudes to the fundamental frequency corresponding to R1, for the first six overtones.

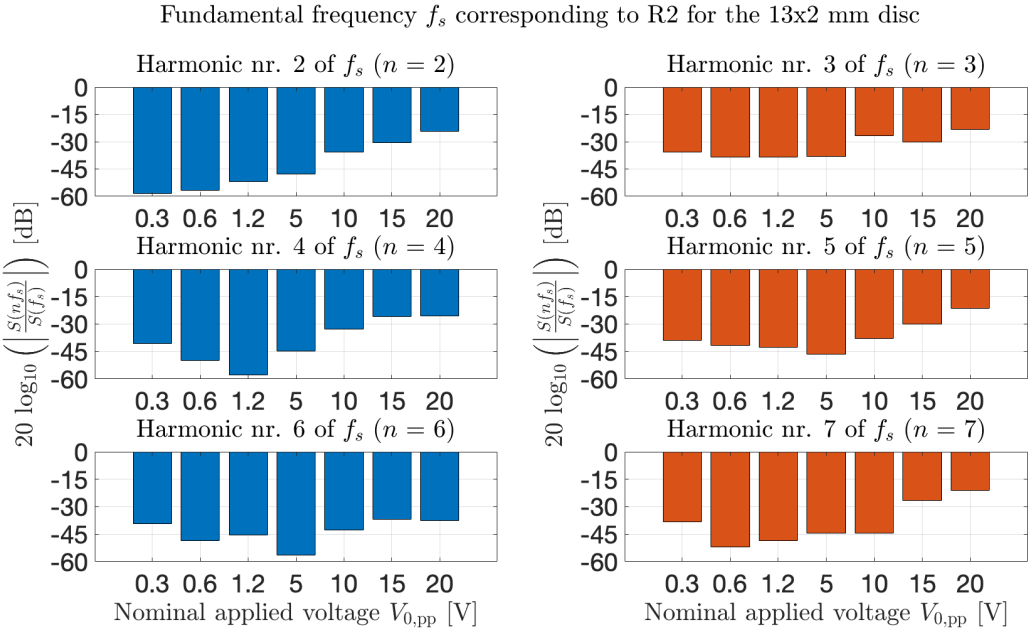

Figure 5.21: Relative harmonics amplitudes to the fundamental frequency corresponding to R2, for the first six overtones.

Table 5.8: Calculated total harmonic distortion in the currents of the three resonance modes for the 13x2 disc for different excitation amplitudes $V_{0,\mathrm{pp}}$, including the first 50 harmonic components.

Continuous waveform								
$V_{0,\mathrm{pp}}$	0.3 V	0.6 V	1.2 V	5 V	10V	15 V	20 V	Unit
R1	5.41	4.16	2.76	2.99	6.50	-	8.14	[%]
R2	10.0	4.48	3.40	3.14	8.51	-	24.6	[%]
TE1	2.62	2.62	2.08	2.32	2.75	-	3.03	[%]
Burst excitation								
$V_{0,\mathrm{pp}}$	0.3 V	0.6 V	1.2 V	5 V	10V	15 V	20 V	Unit
R1	4.70	2.95	3.08	3.17	7.40	6.89	8.99	[%]
R2	6.44	3.03	3.14	3.38	9.85	14.3	20.4	[%]
TE1	3.68	3.40	3.41	3.39	3.79	3.74	3.72	[%]

5.3 Soldering of the piezodisc

After electrical measurements of the piezodiscs in the I-V circuit, the two discs were soldered to a positive and negative connector, so that they could be integrated into the acoustical measurement setup discussed previously in Section 3.3. The soldering of the piezodiscs was carried out by chief engineer Bilal Hasan Qureshi in charge of the soldering- and assembly lab at the Department of Physics and Technology at the University of Bergen. A soldering temperature of 280 °C was used, which lies well beneath the Curie temperature, stated as > 350 °C by the manufacturer [52].

Afterward, new admittance measurements were carried out using the HP 4192A impedance analyzer. The measurements covered the frequency range 1-1300 kHz with increments of 1 kHz. Around R1, R2, and TE1, the frequency increments were lowered to 10 Hz, identical to the earliest admittance measurements presented alongside the new measurements in Figure 5.22 and 5.23, for the 20x2 disc and 13x2 disc, respectively.

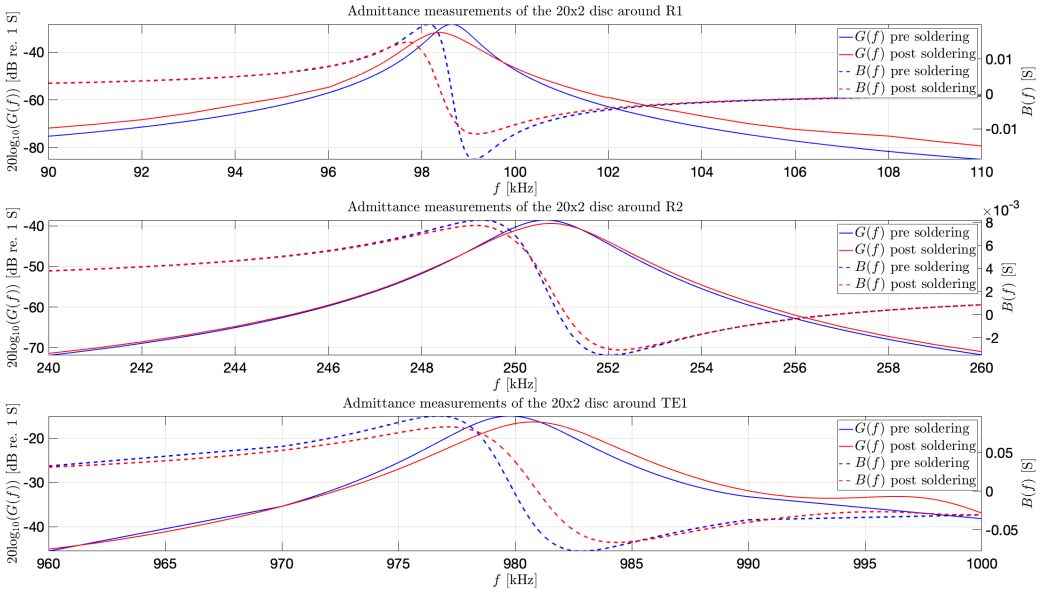

Figure 5.22: Measured conductance (solid lines) and susceptance (dashed lines) around R1, R2, and TE1, for the 20x2 disc, prior to (in blue) and after (in red) soldering of the connectors to the disc. Admittance measurements were conducted using the HP 4192A impedance analyzer.

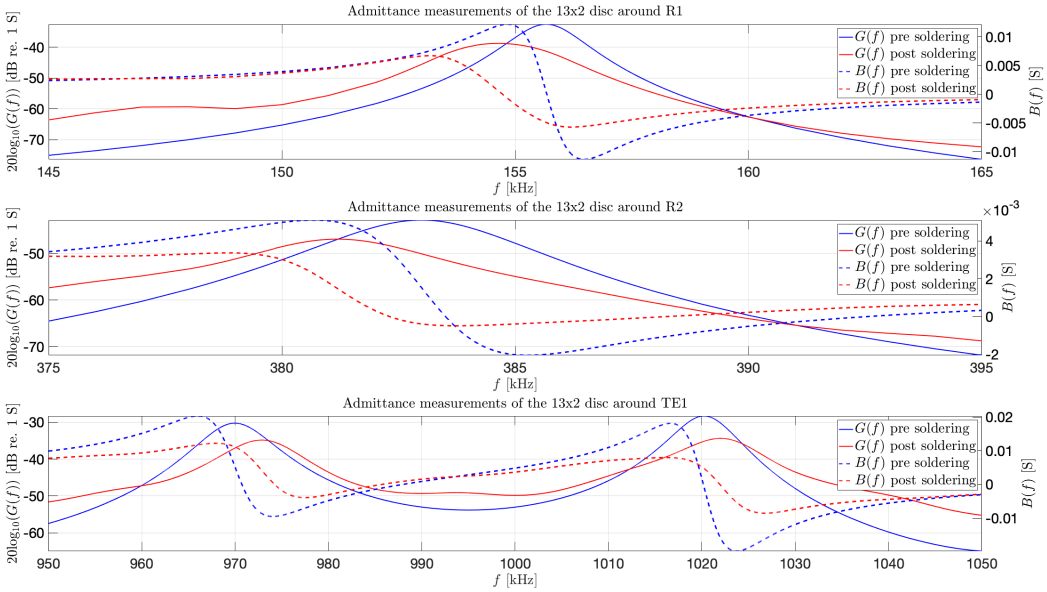

Figure 5.23: Measured conductance (solid lines) and susceptance (dashed lines) around R1, R2, and TE1, for the 13x2 disc, prior to (in blue) and after (in red) soldering of the connectors to the disc. Admittance measurements were conducted using the HP 4192A impedance analyzer.

Resonances and -3 dB bandwidths of the newly soldered piezodiscs were again determined from the new admittance measurements. The resonance frequencies before and after soldering are presented in Table 5.9 below. A relative frequency shift of the resonance Δf_s, as a result of the soldering, is shown in column four of the table. The bandwidths are presented below Table 5.9, in Table 5.10.

Table 5.9: Calculated resonance frequencies for the two discs, from admittance measurements using the HP 4192A impedance analyzer at 0.3 V_{rms}. Here Δf_s denotes a change in resonance frequency relative to before soldering of the disc.

20x2 disc				
Mode	**Pre soldering**	**Post soldering**	Δf_s	**Unit**
R1	98.640	98.370	-0.270	kHz
R2	250.650	250.790	0.140	kHz
TE1	979.760	980.690	0.930	kHz
13x2 disc				
Mode	**Pre soldering**	**Post soldering**	Δf_s	**Unit**
R1	155.650	154.640	-1.010	kHz
R2	382.970	381.180	-1.790	kHz
TE1	969.900	972.770	2.870	kHz

Table 5.10: Calculated -3 dB frequencies of the piezodisc after soldering, and corresponding -3 dB bandwidths Δf, from the admittance measurements described in Table 5.9.

20x2 disc							
	Pre soldering			**Post soldering**			
Mode	$f^-_{3\ \mathrm{dB}}$	$f^+_{3\ \mathrm{dB}}$	Δf	$f^-_{3\ \mathrm{dB}}$	$f^+_{3\ \mathrm{dB}}$	Δf	**Unit**
R1	98.140	99.120	0.980	97.690	99.170	1.480	kHz
R2	249.250	252.000	2.750	249.150	252.230	3.080	kHz
TE1	976.640	982.840	6.200	977.130	984.330	7.200	kHz
13x2 disc							
	Pre soldering			**Post soldering**			
Mode	$f^-_{3\ \mathrm{dB}}$	$f^+_{3\ \mathrm{dB}}$	Δf	$f^-_{3\ \mathrm{dB}}$	$f^+_{3\ \mathrm{dB}}$	Δf	**Unit**
R1	154.810	156.450	1.640	153.140	156.22	3.080	kHz
R2	380.700	385.250	4.550	378.810	383.700	4.890	kHz
TE1	966.010	973.910	7.900	967.870	977.490	9.620	kHz

The soldered 20x2 disc with connectors is shown in Figure 5.24a, and the same disc mounted to the rotation stage of the setup in Figure 5.24b. The wires connecting the disc were stretched out and taped to a thin 200x2 mm circular rod using electrical tape before the rod was fastened to the rotation arm. Aluminum foil was then wrapped around the rod and wires.

A summary of the changes to the resonance frequencies and bandwidths of the two discs is presented in Table 5.11 at the end of this section.

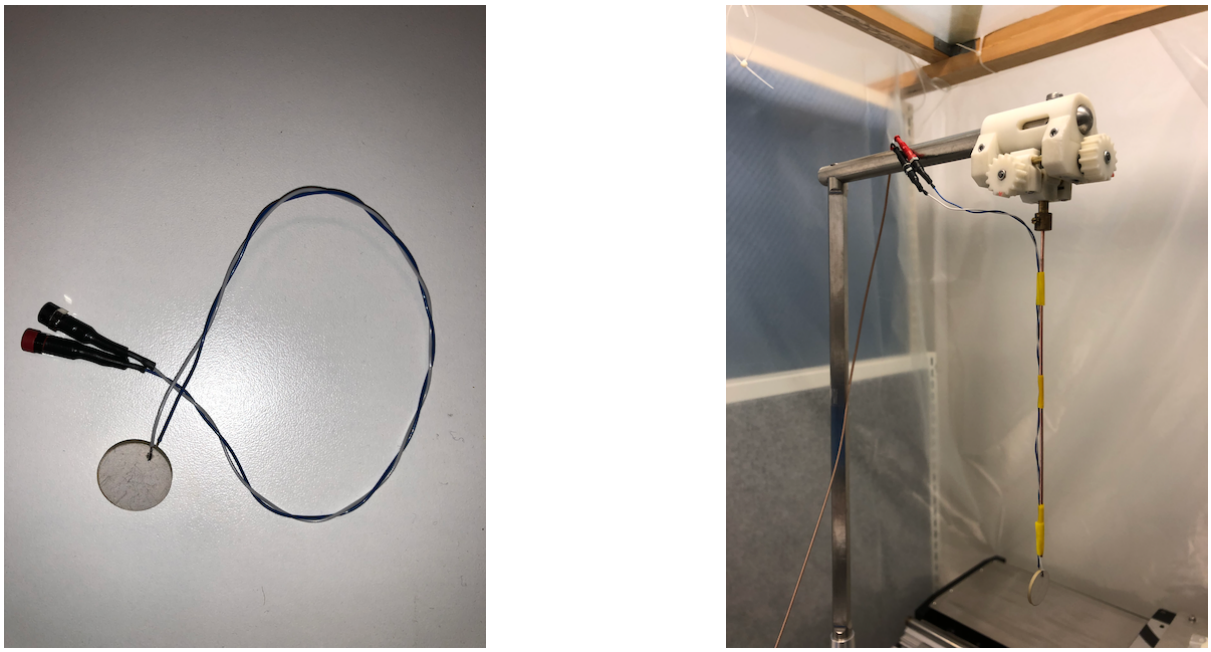

(a) (b)

Figure 5.24: Image of (a) the soldered 20x2 piezodisc, and (b) the same disc mounted to the rotation arm of the measurement setup.

20x2 disc					
20x2 disc	**Prior to soldering**		**After soldering**		
Mode	f_s	Δf	f_s	Δf	**Unit**
R1	98.640	0.980	98.370	1.480	[kHz]
R2	250.650	2.750	250.790	3.080	[kHz]
TE1	979.760	6.200	980.690	7.200	[kHz]
13x2 disc					
20x2 disc	**Prior to soldering**		**After soldering**		
Mode	f_s	Δf	f_s	Δf	**Unit**
R1	155.650	1.640	154.640	3.080	[kHz]
R2	382.970	4.550	381.180	4.890	[kHz]
TE1	969.900	7.900	972.770	9.620	[kHz]

Table 5.11: Summary of the changes to resonance frequencies, and corresponding bandwidths, as a result of soldering electrodes to the piezodiscs. Upper part belonging to the 20x2 disc, and the bottom part to the 13x2 disc.

5.4 Acoustical measurements in air

The preparatory measurements conducted as a test of the measurement setup, which revealed odd results for some of the measurement series, are first presented in Section 5.4.1. An investigation of the origin of the strange harmonic features was carried out in light of this and is presented in Section 5.4.2. Following the characterization of the receiving electronics, the piezodisc was mounted in the measurement setup. Sound pressure and directivity measurements were then conducted for the first radial mode for a variety of nominal applied voltage amplitudes $V_{0,\mathrm{pp}}$, and presented in Sections 5.4.3 and 5.4.4, respectively.

The sound pressure amplitude source condition p_0, and the effective radius a_{eff}, necessary for simulations with the Bergen Code, were calculated based on these measurements. Simulations of the sound pressure for each measurement series were then carried out, and compared to the measured sound pressure in Section 5.4.5.

5.4.1 Preparatory sound pressure measurements

A piezodisc already mounted in the acoustic setup equal to the 20x2 disc, was configured as described in Section 3.3.4 and 3.3.5, before measurements were conducted for various excitation amplitudes along the acoustic sound axis. Both near and far-field measurements were conducted for frequencies corresponding to R1 and R2 for the 20x2 disc, but only selected results in the far-field are presented in the following.

Fourier transforms of the steady state region of the measured responses for R1 at chosen distances of the transmitting piezodisc equal to $z = r_0$, $2r_0$, $4r_0$, and $8r_0$, were carried out to investigate the frequency content of the signals. In Figure 5.25, the calculated frequency spectra of the measured responses for six nominal applied voltages $V_{0,\mathrm{pp}}$ at $z = r_0$ are displayed. Three equal figures for the distances $z = 2r_0$, $4r_0$, and $8r_0$, can be found in Appendix B.6. The bandwidth of the filter in the measurement setup was for these series set to $[f_0/2,\ 10f_0]$, where f_0 corresponds to the carrier frequency of the transmitted bursts (R1 or R2). Special attention should be paid to the two bottom plots of Figure 5.25, but similar behavior can also be seen for $V_{0,\mathrm{pp}} = 20$ V at $z = 2r_0$ in the lower-right plot of Figure B.80 in Appendix B.6. Similar harmonic content was not found as the piezodisc were moved further away from the microphone (z increased), as can be seen in Figure B.81 and B.82 in Appendix B.6, for $z = 4r_0$ and $z = 8r_0$, respectively.

The prominent harmonic peaks in the bottom of Figure 5.25 led to the question of the origin of these harmonic components, as it seemed unlikely to originate from acoustical disturbances in the air. Thus, the need to test the receiving electronics, which was discussed in Section 3.3.8, and is further attended in Section 5.4.2.

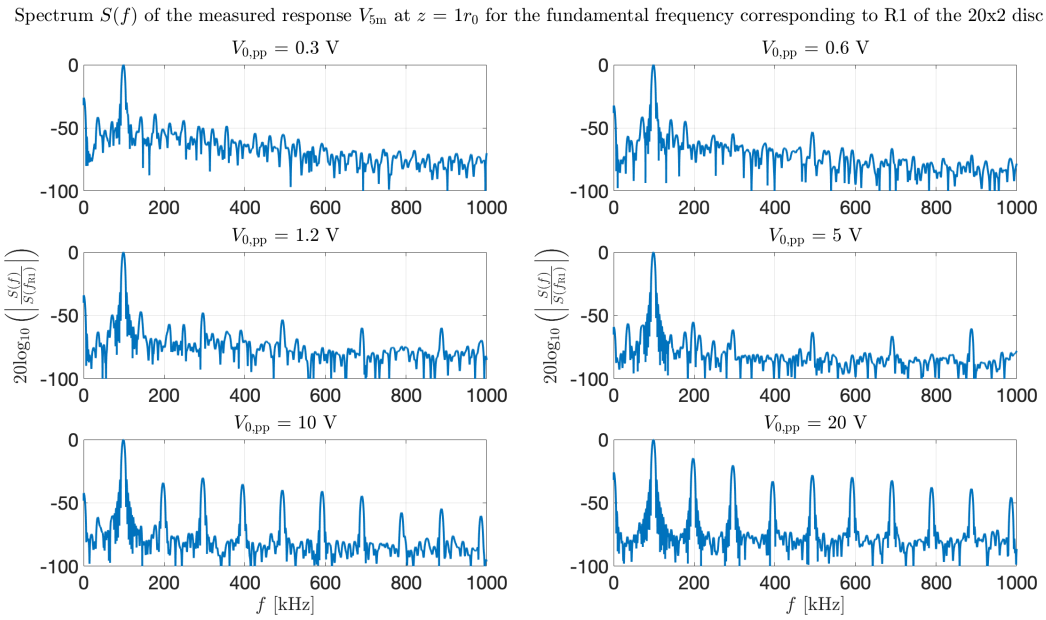

Figure 5.25: Frequency spectra of the steady state part of the received signal for various $V_{0,\mathrm{pp}}$ measured at $z = r_0$. Transmitted signal with carrier frequency corresponding to R1 of the 20x2 disc.

The data extracted in Figure 5.25 above was extracted for the steady state region of the received signal, as illustrated in Figure 5.26 below, wherever that was achievable. However, for greater and greater distances between transmitter and receiver and/or lower excitation amplitudes, the steady state region becomes progressively less well-defined and eventually vanishes.

In the latter case, the extracted values are dominated by fluctuations, random or not, as the propagated pulse no longer has a significant strength with regard to the noise. An example of this can be seen in Figure 5.27, in the case of lower nominal applied voltage $V_{0,\mathrm{pp}}$ (upper plots in the figure) for a fixed distance $z = 8r_0$. Thus, the selected values then become the latter part of the measured signal. Here, the first transient period of the signal is expected to have died out as much as possible, thereby giving the purest frequency content in the pulse achievable, before reaching the second transient period.

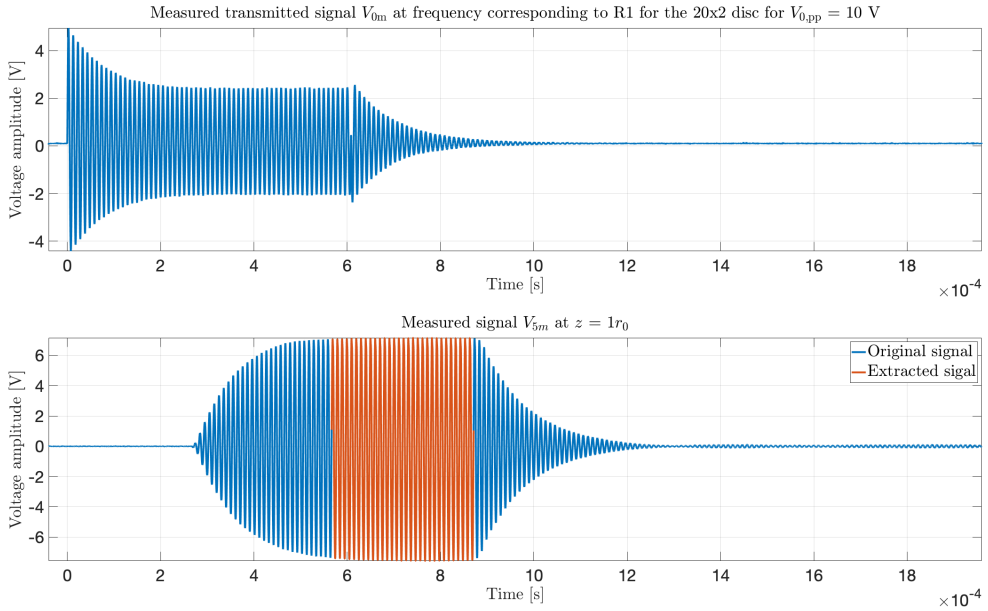

Figure 5.26: Transmitted and received signal for R1 of the 20x2 disc, and $V_{0,\text{pp}} = 10$ V, measured at a distance $z = r_0$. Red part of the bottom signal are the steady state region of the signal extracted for Fourier analysis.

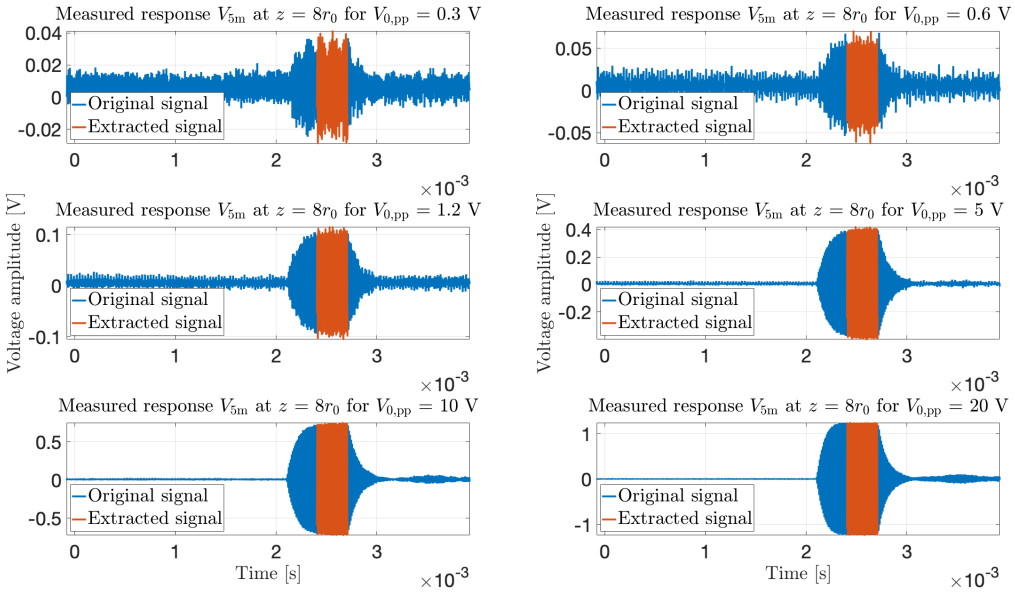

Figure 5.27: Measured response of a transmitted signal for R1 of the 20x2 disc for different nominal excitation amplitudes $V_{0,\text{pp}}$, at a distance $z = 8r_0$. The red region corresponds to the extracted parts of the signals, steady state or not, used for further calculations.

Similar to Figure 5.25 above, Fourier transforms of the measured responses of the excited piezodisc were conducted for the second radial mode (R2). The Rayleigh distance being

more than doubled for R2, again puts restraints on the possible distances between sender and receiver. In addition, the microphone sensitivity for R2 is unknown, and thus the actual magnitude of the transmitted response of the piezodisc around the second radial mode cannot be interpreted from these results.

In Figure 5.28 below, excitation of the 20x2 disc at a frequency corresponding to R2 is presented. To the left in the figure, the oscilloscope reading $V_{5\mathrm{m}}$, with the extracted part of the signal marked in red. The red part of the uppermost plot corresponds to the first 1/3 of the pulse, the middle plot to the second 1/3, and the bottom plot corresponds to the last 1/3 of the measured response. The red sections of the measured response were located through calculations based on the frequency, the speed of sound, and the distance between the piezodisc and the microphone. Column two in Figure 5.28 depict the spectrum of the corresponding red part of $V_{5\mathrm{m}}$, and column three, the spectra of the steady state part of the transmitted burst. The measurement was conducted at a distance $z = r_0$, for a nominal voltage amplitude of 10 V. It can be noted from the spectra in Figure 5.28, that the first radial mode is excited throughout the burst, even for a fundamental frequency corresponding to R2.

Similar figures for lower nominal applied voltages can be found in Appendix B.6. For the lowest nominal voltages depicted in Figures B.83-B.85, the transmitted bursts were completely buried in noise, and the second radial mode appears as a peak amongst other, higher peaks of lower frequency. The latter was not unexpected, as the microphone is designed, and accounted for, frequencies well below 150 kHz [74], as discussed in Section 3.3.9.

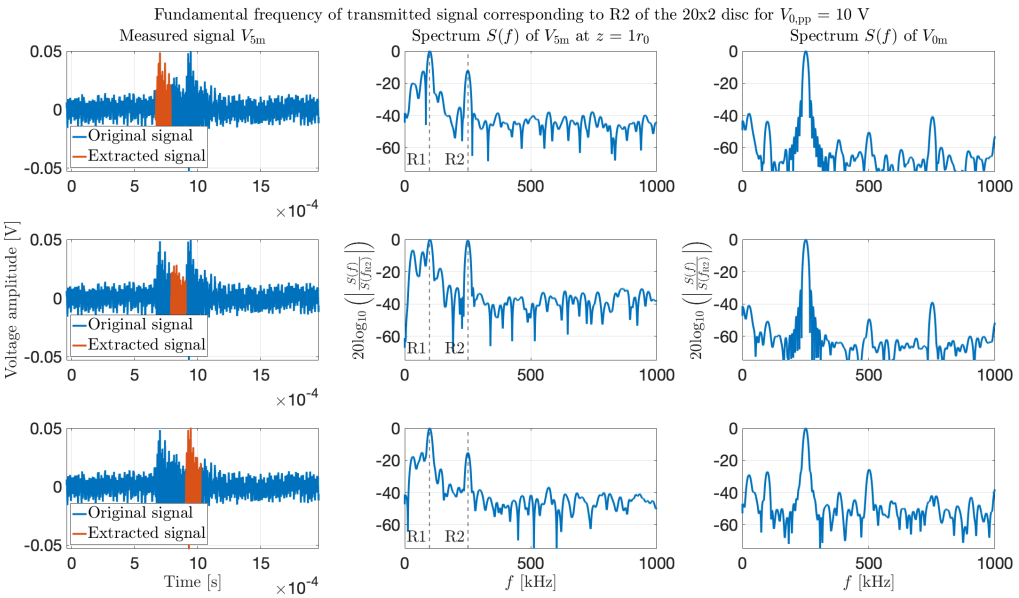

Figure 5.28: Measured response of the 20x2 disc transmitting at a frequency corresponding to R2 for $V_{0,\text{pp}} = 10$ V, measured at $z = r_0$. In the right column, the oscilloscope reading, and marked in red the extracted signal calculated based of the speed of sound and travel distance. In column two and three, the spectrum of the extracted measured response, and the steady state of the transmitted burst, respectively. First row corresponds to the first 1/3 of the burst, and the two next rows, to the next 1/3's.

5.4.2 Characteristics of the receiving electronics

Measurements of the receiving electronics described in Section 3.3.8 are presented in the following, alongside a brief discussion of the findings, as the significant distortion of the measured response discovered through the preparatory measurements presented in Section 5.4.1, had to be resolved prior to new sound pressure measurements.

The subsequent figures in this section show, in the left columns, the spectrum $S(f)$ of the Fourier transforms of the measured input and output pulses to the instrument(s), divided by the magnitude of the fundamental frequency f_0 of the transmitted signal. In the right columns, two periods of the corresponding waveforms are depicted, each extracted from the steady state of the signal. In the following figures, the blue curves correspond to the input signal, while the red curves are the measured output signal, denoted $V_{0\text{m}}$ and V_{OUT} in Figure 3.8 from Section 3.3.8.

Distortion in the analog filter

Measurements of the Krohn-Hite 3940 filter for nominal applied peak-to-peak voltage amplitudes $V_{0,\text{pp}}$ of 10 V, 15 V, and 20 V are presented in Figure 5.29 below. The signal generator output was here terminated directly into the filter, and the transmitted signals

measured across the output of the generator, as illustrated in Figure 3.8(a) in Section 3.3.8.

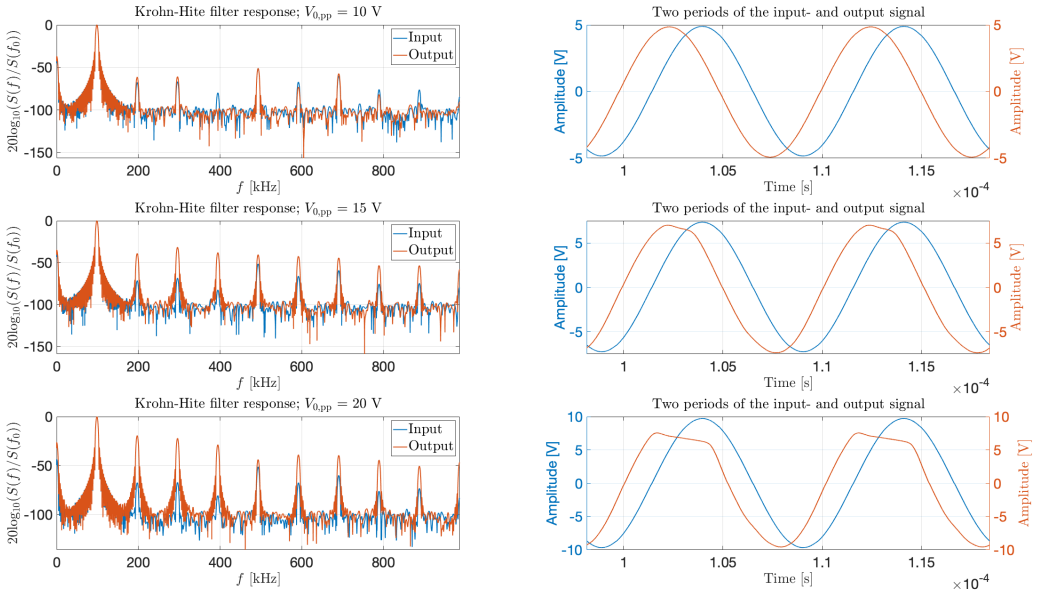

Figure 5.29: Fourier transforms of the measured response of the Krohn-Hite 3940 filter at R1 for three different amplitudes, and corresponding waveform of the signals extracted from the middle of the pulses.

As can be seen in Figure 5.29, the isolated Krohn-Hite filter revealed increasing harmonic distortion for input peak amplitudes greater than 5 V ($V_{0,\mathrm{pp}}/2$). The measured response carried significantly higher harmonic components than the measured input, suggesting that the analog filter itself distorts the signal in the passband. From the manufacturer's datasheet, the maximum input signal amplitude is stated as ± 4.5 V_p for carrier frequencies lower than 1 MHz. The distortion is further said to be <0.2 % when using an oscillator at 2.9 V_{rms} [84]. Thus, the measurements presented in Figure 5.29 are carried out under conditions not accounted for by the manufacturer.

Moreover, the THD calculated for the first row in Figure 5.29, where peak voltage amplitude to the input of the filter is about 5 V, yields 0.45 % for the generated signal, and 0.54 % for the filter output. Which remains in line with the manufacturer's declaration. The same calculations for an input amplitude of 7.5 V and 10 V gave 3.68 %, and 13.93 %, from the output signal, respectively. Whereas the THD in the input signal to the filter remained at about 0.22 % and 0.58 %, respectively, confirming that the filter indeed distorts the signal when the input amplitude exceeds certain levels.

The voltage amplitudes tested were significantly higher than what would be expected electrical response of a measured acoustic disturbance, but as the filter is connected in cascade with a measurement amplifier, it might put restraints on the latter.

Trimming of the waveforms in the measurement amplifier

The measurement amplifier, in cascade with a 40 dB attenuator to reduce the voltage amplitude of the input signal, was tested with gains of 40 dB and 20 dB on the input and output, respectively. An illustration of this can be found in Figure 3.8(b) from Section 3.3.8. With a 40 dB input gain, a maximum input voltage of 10 mV is marked on the instrument. Figure 5.30 shows measurements with input peak voltage, V_{IN}, less than or equal to this limit. In Figure 5.31 on the other hand, input amplitudes equal to or higher than the limit are presented. For input signals with amplitudes exceeding this value, the light indicating selected output gain on the instrument, flashed continuously while the measurements were conducted. The flashing light indicated an overload of the output amplifier stage of the instrument, and the resulting waveforms can be seen in the two lower plots in the right column of Figure 5.31 below.

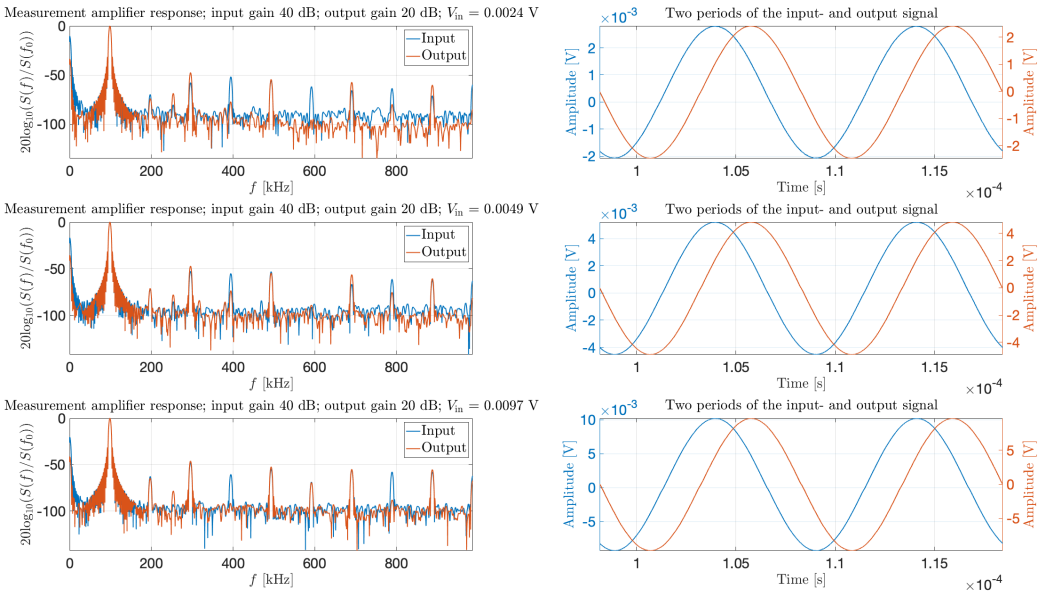

Figure 5.30: Fourier transforms of the measured response of the Brüel & Kjær 2636 measurement amplifier at R1 for three different input amplitudes lower than or equal the limit, and corresponding waveform of the signals extracted from the middle of the pulses.

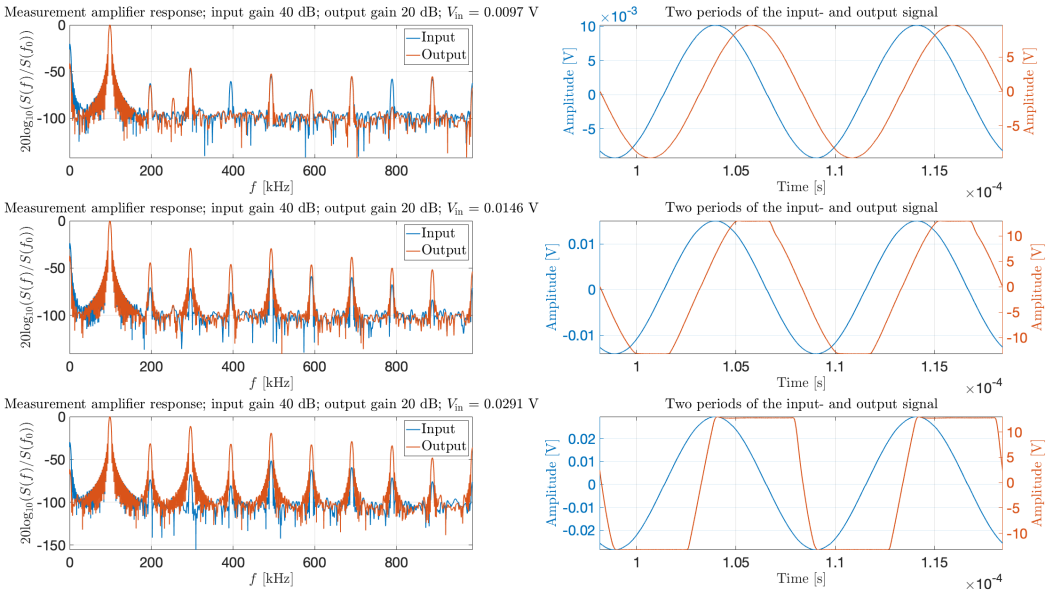

Figure 5.31: Same as for Figure 5.30, but with higher amplitudes.

A closer view of the wave tops of the measured signals, depicted in the plots to the right in Figure 5.31, are presented for each input voltage amplitude V_{in}, in Figure 5.32 below.

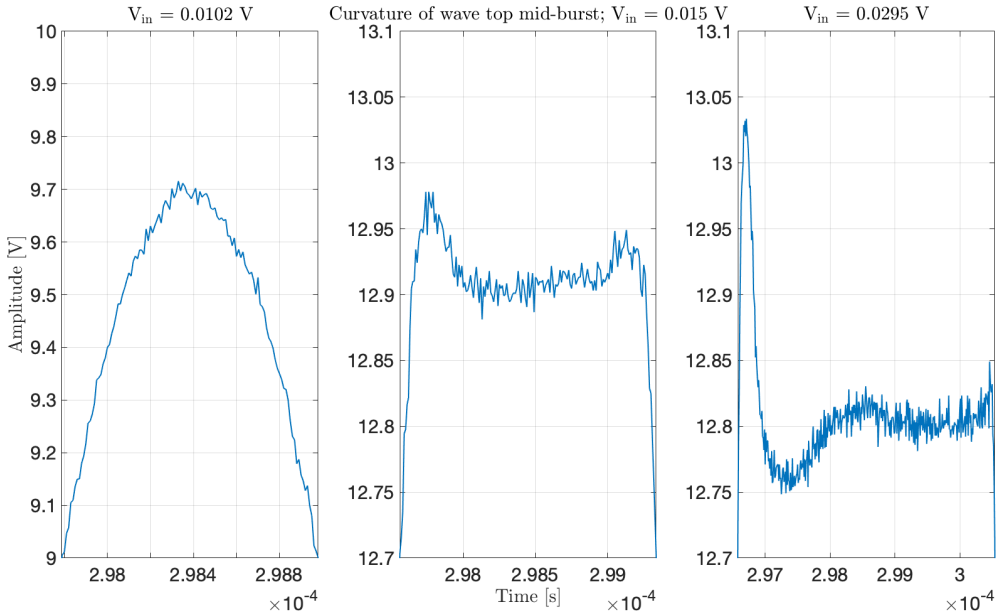

Figure 5.32: Closer view of the flat wave tops of the measured signal depicted in Figure 5.31.

In Figure 5.30, there is no noteworthy distortion of the signals. Figure 5.31 however, shows pruning of the waveform peaks due to an overload of the output channel of the

amplifier. The trimming of the peaks was further inspected in Figure 5.32, where the peaks were cut just below 13 V.

Combined effects of the cascaded receiving electronics

Lastly, the instruments on the receiving end of the acoustic measurement setup were configured as intended for acoustic pressure measurements. The filter with equal configuration as before was connected in cascade with the output of the measurement amplifier, as shown in Figure 3.8(c) from Section 3.3.8, and measurements similar to those above carried out. In Figure 5.33, the input signal amplitudes were kept under or at the threshold value, while equal measurements for higher amplitudes are presented in Figure 5.34.

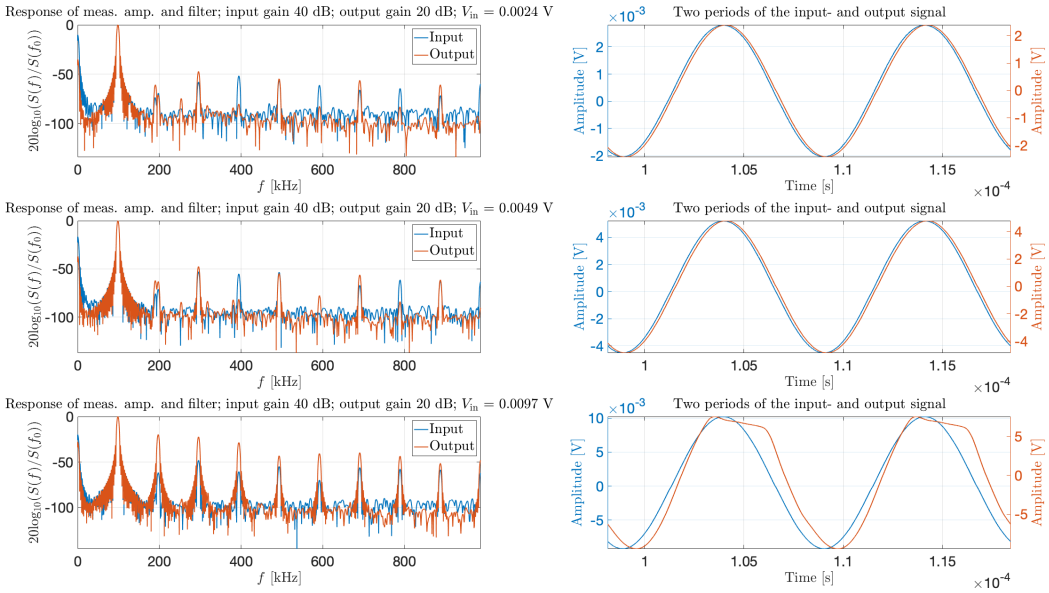

Figure 5.33: Fourier transforms of the measured response of the Brüel & Kjær 2636 measurement amplifier in cascade with the Krohn-Hite 3940 filter at R1 for three different input amplitudes lower than or equal the threshold value, and corresponding waveform of the signals extracted from the middle of the pulses.

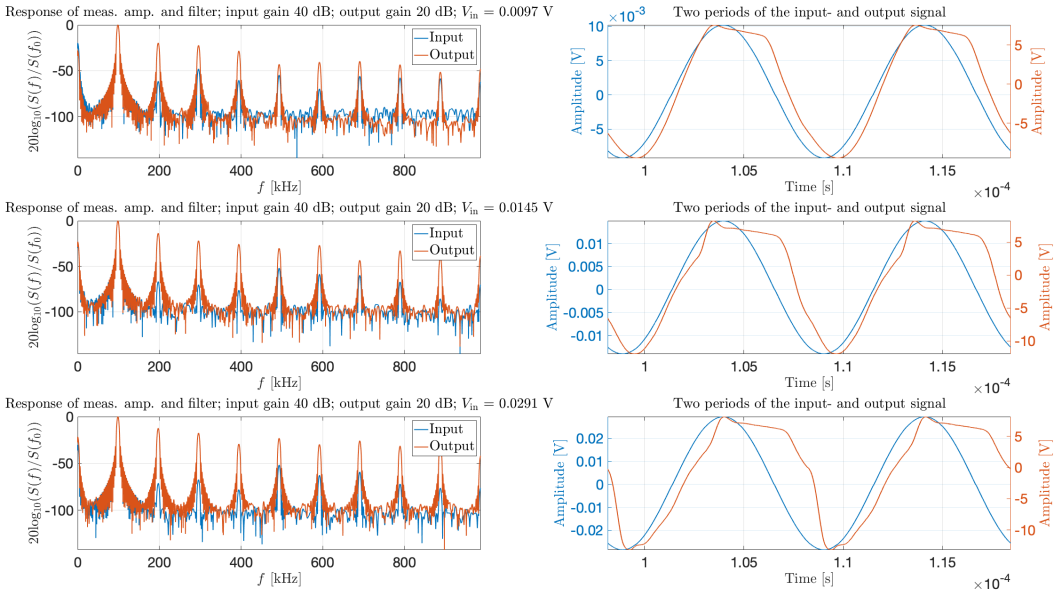

Figure 5.34: Same as for Figure 5.33, but here for input signals with higher amplitudes.

To investigate the impact of the output gain of the measurement amplifier, the gain was reduced to 10 dB, and identical measurements were conducted. Selected results are shown in Figure 5.35. Finally, the output gain was set to 0 dB, and the measurements were re-run. The distortion seen in previous measurements was not prominent for similar input signal amplitudes, and thus the input amplitude was increased further. Figure 5.36 below presents these results.

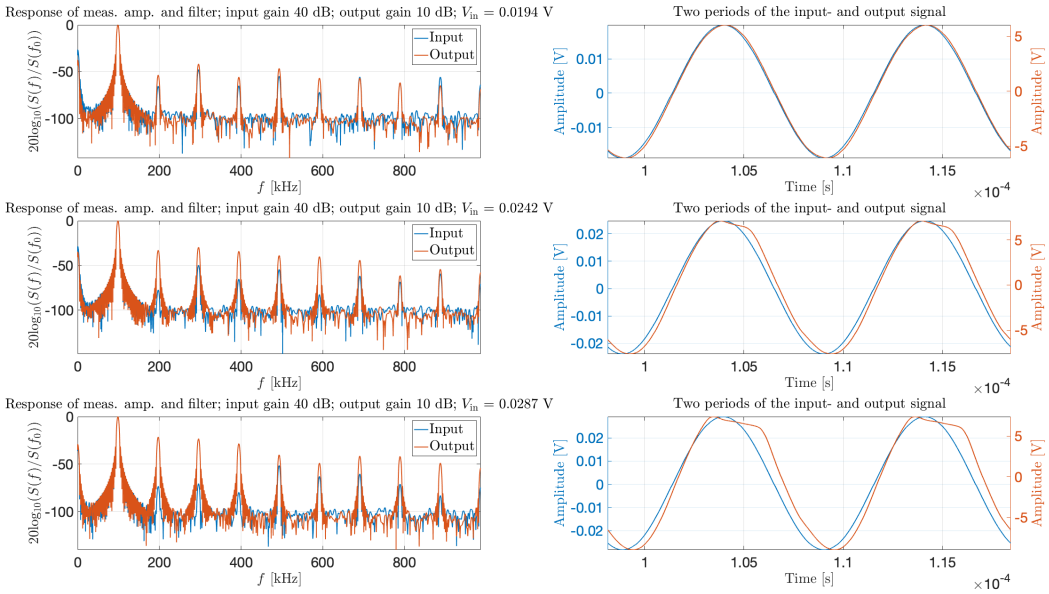

Figure 5.35: Same as for Figure 5.34, but reduced output gain configuration (10 dB). Input signal amplitudes are also somewhat different.

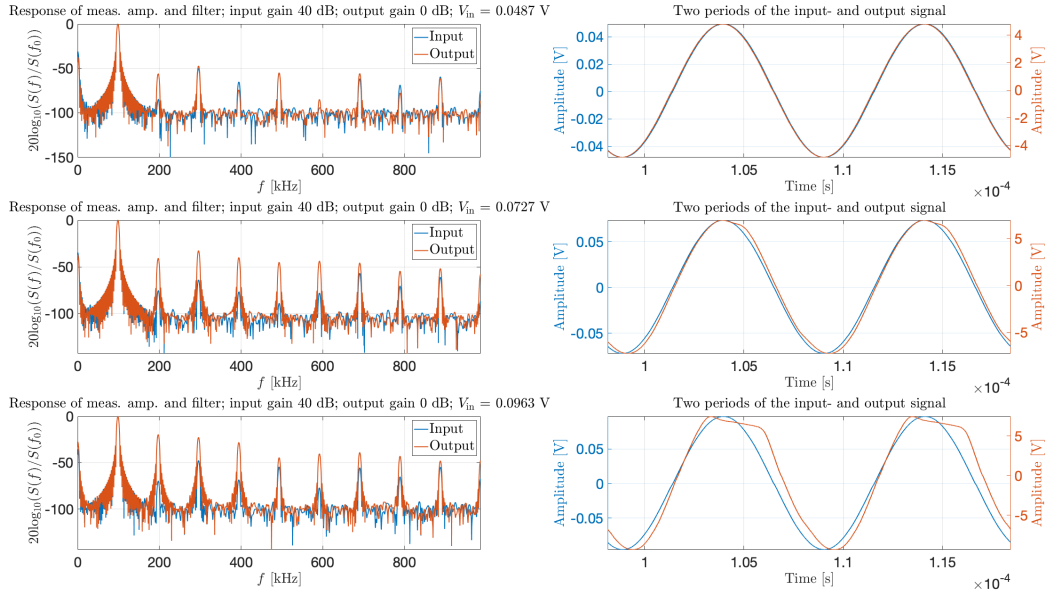

Figure 5.36: Same as for Figure 5.34, but reduced output gain configuration (0 dB). Input signal amplitudes significantly increased compared to earlier measurements depicted in above figures.

The measurement amplifier and filter in cascade show somewhat different output signal characteristics than seen in Figures 5.29-5.31. Distortion of the output signal is already

present in the bottom of Figure 5.33, where the input amplitude is equal to the measurement amplifier in isolation to the bottom of Figure 5.30. The problem thus seemed to lie with the Krohn-Hite filter, identified to be due to input peak voltage amplitudes greater than 4.5 V [84], and thereby subject to distortion locally in the filter. The trimming of the peaks depicted in Figure 5.31 and 5.32, are further altered and distorted when terminated into the filter, as depicted in the two bottom plots of Figure 5.34.

Figures 5.35 and 5.36 show the effect of lowering the output gain setting of the measurement amplifier. Here the input amplitudes to the measurement amplifier are significantly increased to yield similar results to that of Figure 5.34.

The preceding results highlight two major limitations of the receiving electronics. Firstly, the output channel of the measurement amplifier is susceptible to trimming of the waveform when the amplitudes reach a certain limit, and the output (and/or input) gain setting thus has to be changed accordingly. Secondly, the Krohn-Hite filter's input must be restricted so that it does not exceed 4.5 V peak amplitude. Thus, for measurements where the transmitter and microphone are in close vicinity of each other, and the excitation amplitudes to the transmitter are high, the gain settings of the measurement amplifier have to be altered accordingly to accompany this.

It is also noted in the manual to the measurement amplifier <0.1 % distortion at 50 kHz on the input section and <0.3 % at 50 kHz at the output section [85]. Adding the likelihood of some distortion of the signal in the analog filter, the measured response at the oscilloscope is likely to contain harmonics of the fundamental of some magnitude even when appropriate gain settings are utilized.

5.4.3 On-axis sound pressure measurements

Axial sound pressure measurements of the disc at R1 were carried out as discussed in Section 3.3.9. Voltage amplitude settings of $V_{0,\mathrm{pp}}$ of multiples of 0.3 V and 5 V, up to 2.4 V and 20 V, were applied at the signal generator. The near field was measured with range increments of $r_0/10$ out to $z = r_0$ (approximately 0.09 m), and beyond $z = r_0$, with increments of $r_0/2$ along the axis out to $z = 9.5r_0$. An example of a transmitted and measured burst, and the corresponding spectra of the signals are presented in Figure 5.37. The SPL were computed for the measurements series, which are shown in the upper part of Figure 5.38 below.

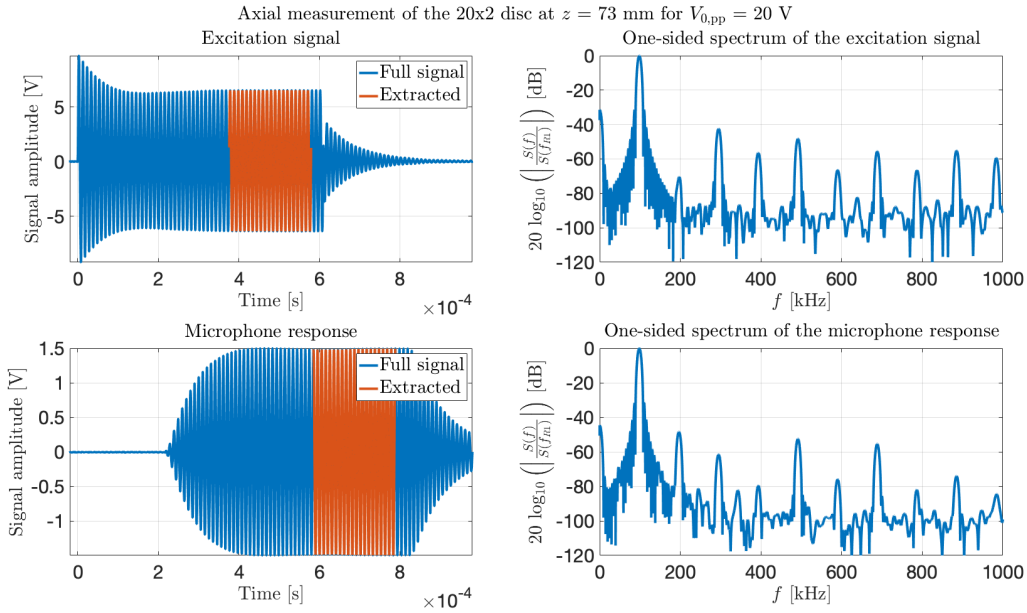

Figure 5.37: Example of the transmitted and received (left) and spectra of the signals to the right, for a axial sound pressure measurement in the vicinity of r_0 with $V_{0,\mathrm{pp}} = 20$ V for the 20x2 disc.

The effective axial sound pressure amplitudes of each series were then extrapolated to 1.1 m from the last known values. Voltage source sensitivities were then calculated using Eq. (2.3.3), from the extrapolated sound pressure amplitudes at 1 m for each measurement series, and the corresponding effective voltage amplitudes, calculated from the associated measured transmitted signals from the signal generator. The voltage source sensitivities were then plotted as a function of nominal applied voltage amplitudes at the signal generator, which is shown in the bottom part of Figure 5.38. The circular blue dots in the figure designate the calculated voltage source sensitivities, whereas the dashed blue line connecting the dots is a linear interpolation.

The SPL second harmonic component of the fundamental frequency were also computed for the measurement series. This is presented in Figure 5.39, where the solid lines mark the fundamental frequency component, and the dashed lines for equal color are the respective second harmonic component of R1. For the second harmonic component, a new microphone sensitivity had to be utilized, which was computed using a curve fit of the microphone response explained in Section 3.3.6.

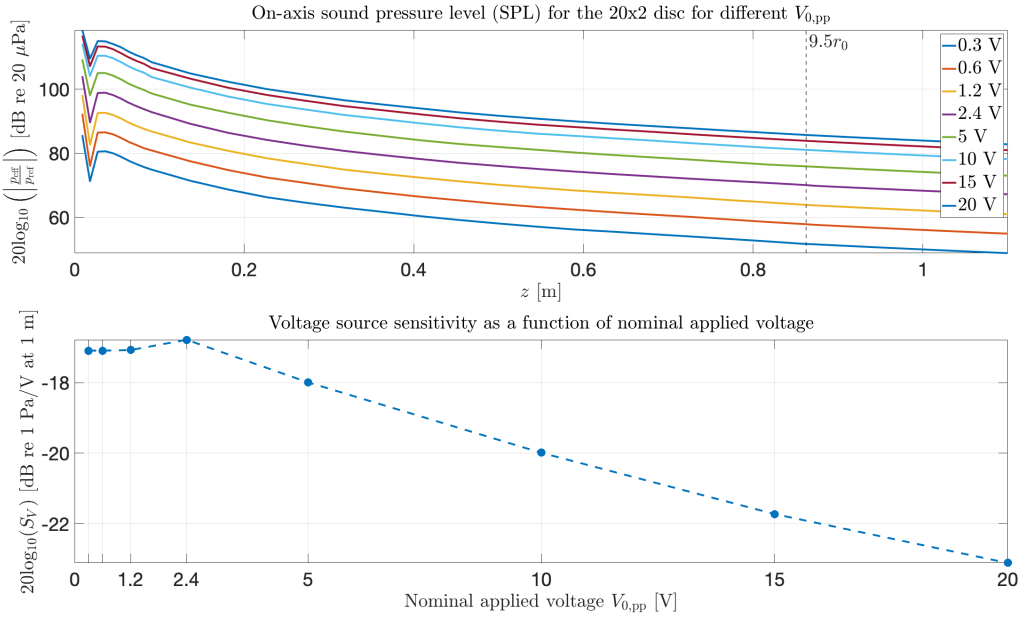

Figure 5.38: Sound pressure level on the acoustic sound axis for the 20x2 disc as a function of distance, and nominal applied voltage amplitude $V_{0,\mathrm{pp}}$, extrapolated from $z = 9.5r_0$ out to 1.1 m, in the upper part of the figure. Calculated voltage source sensitivity S_V (bottom plot) of the 20x2 disc as a function of nominal applied voltage $V_{0,\mathrm{pp}}$. Effective sound pressure taken from the extrapolated value at 1 m.

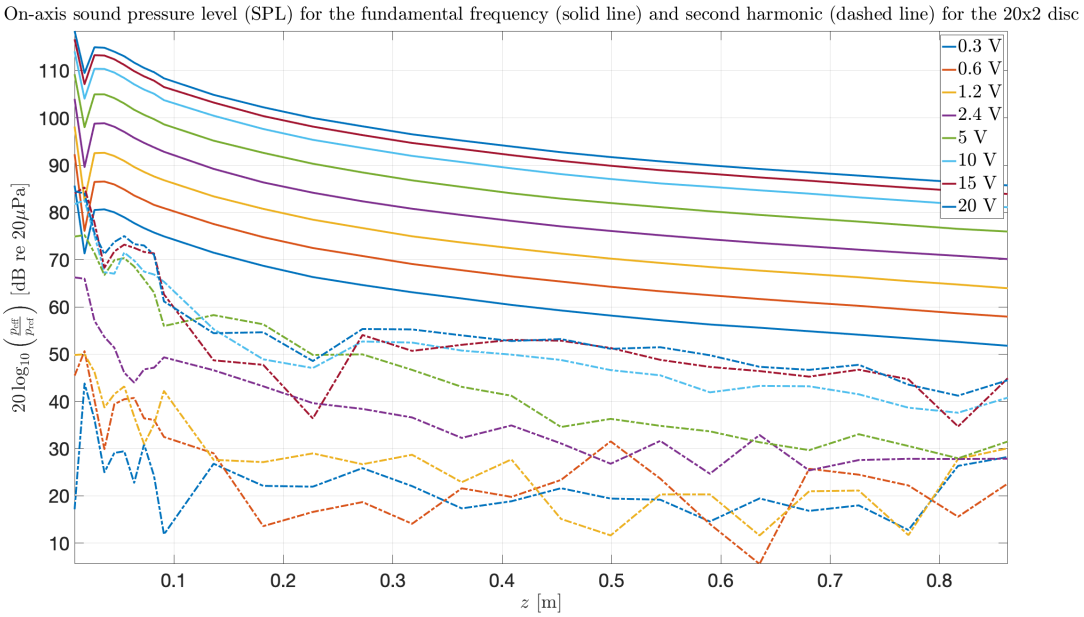

Figure 5.39: Sound pressure level on the acoustic sound axis for the 20x2 disc as a function of distance, and nominal applied voltage amplitude $V_{0,\mathrm{pp}}$. Here shown for the fundamental frequency in solid lines, and the respective second harmonics in dashed lines (colors for respective series are identical).

Axial sound pressure measurements, similar to that of the 20x2 disc displayed in Figure 5.38 above, were carried out for the 13x2 piezodisc for a frequency corresponding to R1. Range increments for the axial measurements were equal to that of the 20x2 disc, but the Rayleigh distance r_0 of the 13x2 disc is shorter, and was approximated to about 0.06 m when the measurements were taken. The sound pressure levels calculated from the measurements are displayed in the upper part of Figure 5.40 below. Extrapolation of the last measured axial sound pressure amplitudes out to 1.1 m was again used to calculate the voltage source sensitivities, shown at the bottom of Figure 5.40.

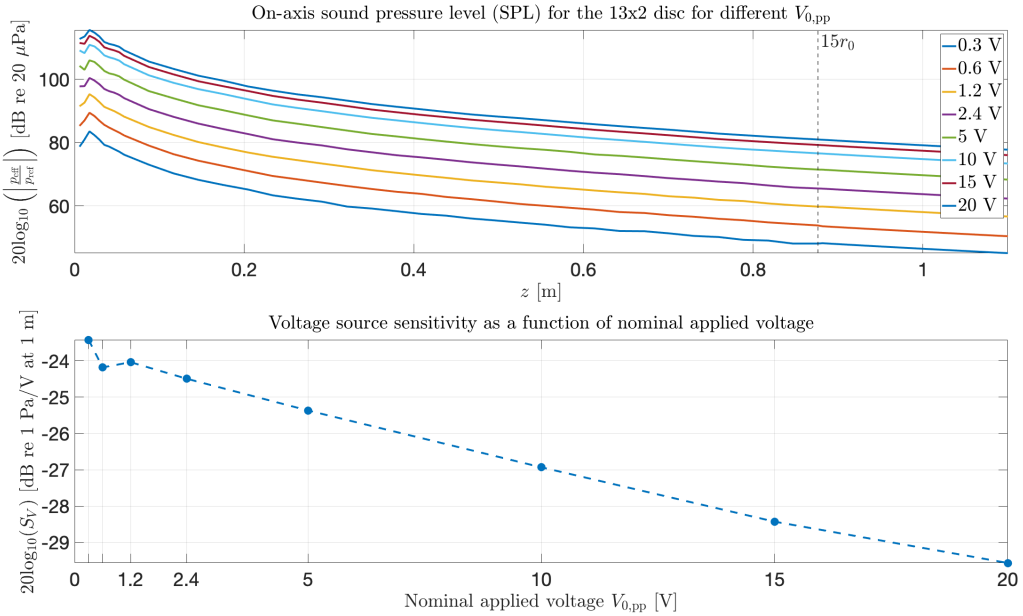

Figure 5.40: Sound pressure level on the acoustic sound axis for the 13x2 disc as a function of distance, and nominal applied voltage amplitude $V_{0,pp}$, extrapolated from $z = 15r_0$ out to 1.1 m, in the upper part of the figure. Calculated voltage source sensitivity S_V (bottom plot) of the 20x2 disc as a function of nominal applied voltage $V_{0,pp}$. Effective sound pressure taken from the extrapolated value at 1 m.

5.4.4 Directivity

Measurements of the directivity function of the radiated sound beam for the frequency corresponding to R1 were conducted at a distance $z = 2r_0$ from the microphone. The piezodisc was rotated with increments of 0.2° relative to its initial position in both directions, with a total rotation of 10° to each side of the sound beam axis. Seven different voltage amplitudes were applied at the signal generator. The resulting directivity plot is presented in Figure 5.41, to the left in the figure as effective pressure amplitude, and to the right normalized to maximum pressure amplitude for the corresponding applied voltage amplitude. Figure 5.42 shows the directivity measurements of the 20x2 disc, compared to the Bessel directivity $D(\theta)$ (Eq. (2.17) from Section 2.3). The latter was computed with the effective source radius calculated from the directivity measurements

and is plotted in a black dashed line. Lower nominal applied voltages are grouped to the left in the figure and higher voltages to the right.

In Figure 5.43, enlarged plots of the directivity function on the interval [-1.2°, 1.2°] are shown. The measurements to the left in the figure were carried out using positive rotational increments in θ, i.e., from -1.2° to 1.2°, and to the right in the figure, the other way around (negative increments).

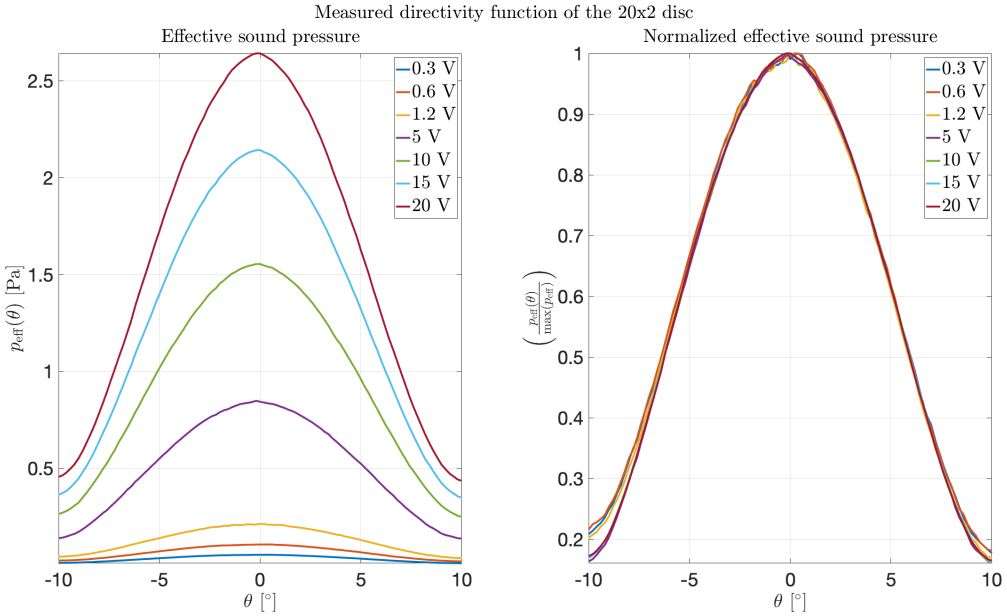

Figure 5.41: Directivity measurements for R1 of the 20x2 disc for different nominal applied voltage amplitudes at the signal generator. To the left plotted as effective pressure, and to the right normalized to maximum measured pressure amplitude as a function of θ, for each measurement series.

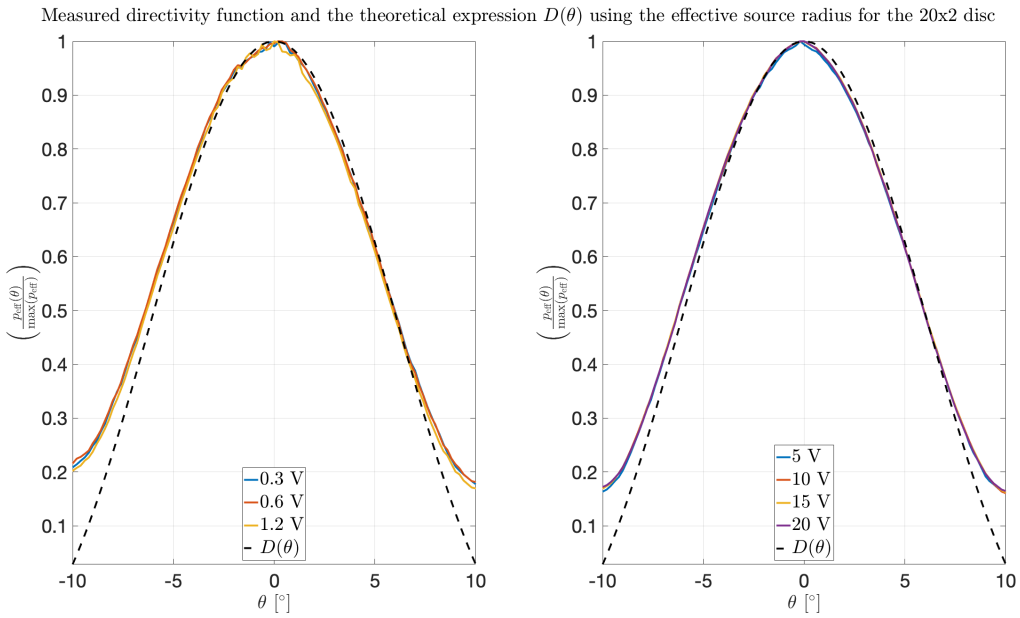

Figure 5.42: Normalized measured directivity function for R1 of the 20x2 disc compared to the theoretical expression of the directivity function $D(\theta)$, using the calculated effective source radius of the disc.

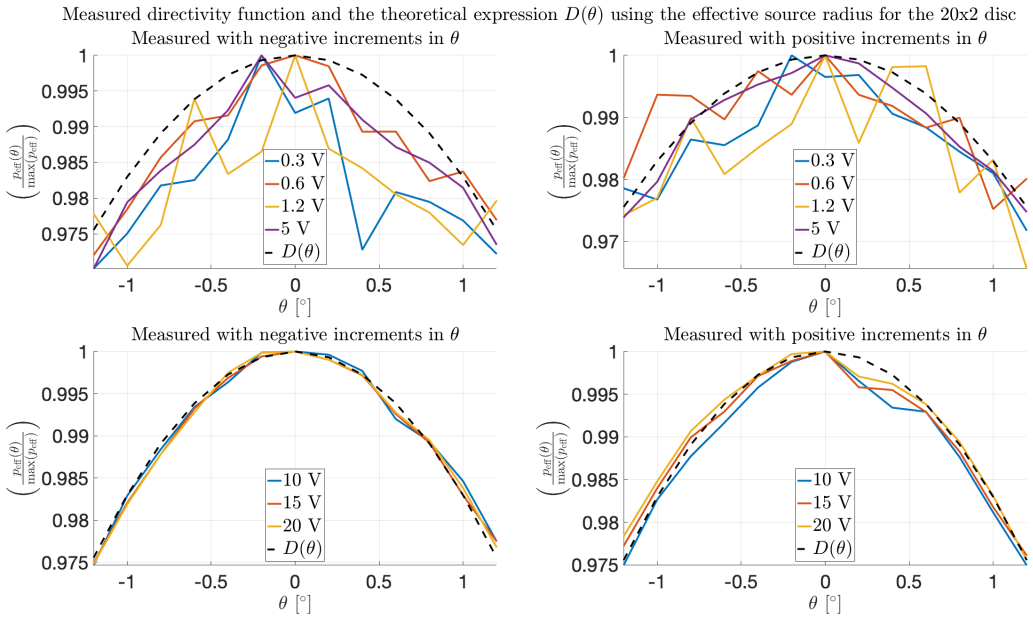

Figure 5.43: Similar directivity measurements as presented in Figure 5.41, but on a smaller interval around the sound beam axis. Measurement series separated due to more noisy results for the low amplitude settings, as seen in the upper two plots. Measurement series to the left carried out with negative rotational increments in θ, i.e., from +1 to -1. Opposite (positive rotational increments) for the measurements series to the right.

Measurements of the directivity function/beam pattern of R1 for the 13x2 disc were carried out on the interval [-10°, 10°] relative to its original alignment to the sound axis, with increments of 0.25°. The resulting directivity function is presented in Figure 5.44 below. In Figure 5.45, the measured directivity function of the 13x2 disc is compared to the theoretical Bessel directivity given in Eq. (2.17), using the effective source radius of the disc. The three lowest $V_{0,\mathrm{pp}}$ are shown to the left in the figure, and the four higher nominal voltages, to the right.

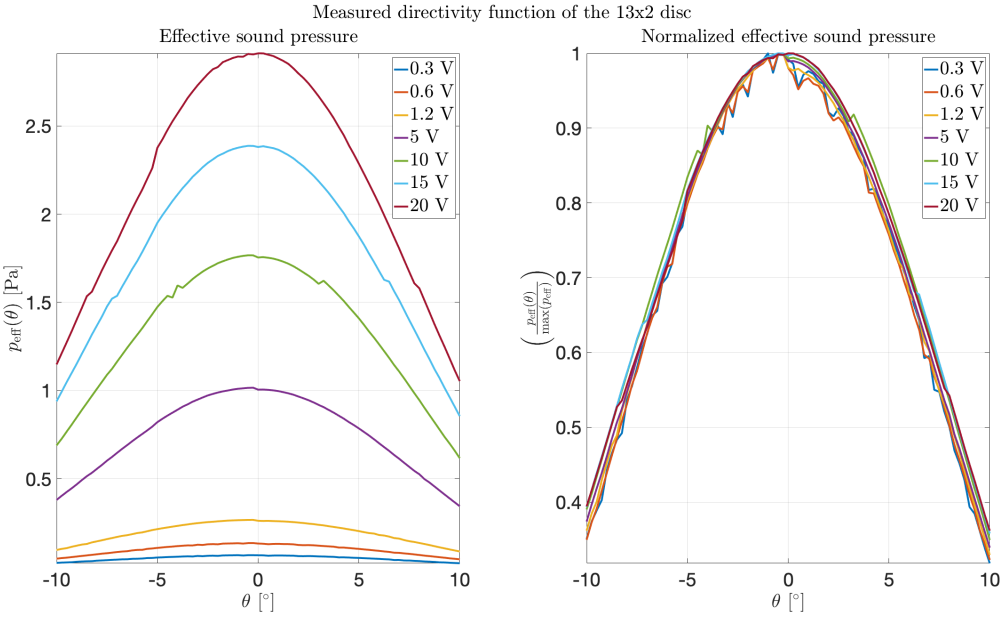

Figure 5.44: Directivity measurements for R1 of the 13x2 disc for different nominal applied voltage amplitudes at the signal generator. To the left plotted as effective pressure, and to the right normalized to maximum measured pressure amplitude as a function of θ, for each measurement series.

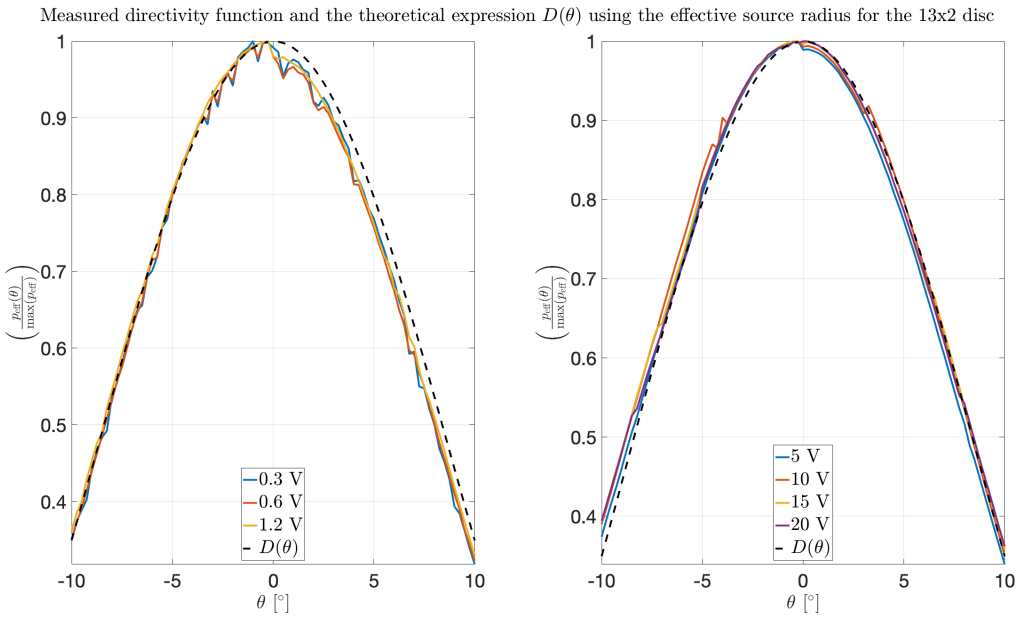

Figure 5.45: Normalized measured directivity function for R1 of the 13x2 disc compared to the theoretical expression of the directivity function $D(\theta)$, using the calculated effective source radius of the disc.

5.4.5 Simulations

The effective source radius of the piezodisc for R1 was determined based on the measurements above. Two approaches were attempted. Firstly, the angle θ needed in Eq. (4.4) was found as the angle of minimum deviation between normalized pressure relative to maximum pressure as a function of θ, and a tabulated value of Eq. (2.17), as described in Section 4.2.2. The angle was located on both sides of $\theta = 0$, and the mean was used in Eq. (4.4). This showed rather poor results, especially for lower nominal applied voltage amplitudes, and varied greatly when different measurement series were tested.

A second approach, using curve fits on the measured data to calculate θ showed more repeatable results. Firstly, MATLABs curveFitter application was used to visualize and test different fit types, and order, to the data. An example of this can be found in Appendix B.7. The resulting fit type was chosen to be a polynomial fit, where an order of nine gave the best results.

In the end, polynomial approximations to the measurement series of $V_{0,\mathrm{pp}}$ nominally equal to 5 V, 10 V, 15 V, and 20 V, were used to determine the effective source radius. A radius was calculated for each measurement series. Deviations between the computed effective source radii were of arbitrary behavior, and less than ± 0.3 % of the following presented value. Thus, the mean value of the four was utilized, which was found to be 11.9023 mm, which is in agreement with the effective source radius found for an equal disc by the author of [2] using FEMP. In comparison, the first approach gave an effective

source radius equal to 11.9857 mm. The effective source radius calculated was then used as an input parameter to the Bergen Code simulations for the R1 of the 20x2 disc. A similar procedure was carried out for the 13x2 disc and the directivity measurements presented in Figure 5.44, which gave an effective source radius of 5.3886 mm and 5.4157 mm, from curve fits, and raw measurements, respectively.

Simulations with effective source radii

Bergen Code simulations were carried out for both piezodiscs for every measurement series. Effective source radius was determined for both discs as described above and in Section 4.2.2. The source condition pressure amplitude p_0 was calculated for each measurement series as described in Section 4.2.3, based on the measured sound pressure amplitude at a distance $z = r_1$ in the far-field. The latter was chosen to be $r_1 = 5r_0$ and $r_1 = 8r_0$, for the 20x2 and 13x2 disc, respectively, as these distances showed better overall agreement in the far-field, which are attended to later in this section.

The resulting SPL of the simulations are plotted in dashed lines in the upper part of Figures 5.46 and 5.47 below, for the 20x2 and 13x2 disc, respectively. Measured SPL for the discs are plotted in solid lines with equal color. The bottom plot in both figures shows the discrepancy between simulated and measured values, and the dashed vertical line marks the transition from the near field to the far-field (at the Rayleigh distance r_0). Table 5.12 lists the remaining input parameters used for the two discs. The listed values are representative for all eight of the measurement series carried out for each disc, but small deviations between the actual values per measurement series, to the one listed exist, but are not presented here.

Deviations between linear ($\beta = 0$) and nonlinear ($\beta = 1.2$) simulated axial sound pressure amplitudes were also computed for the measurements series of the 20x2 disc and 13x2 disc, and are presented in Figure 5.48.

Table 5.12: Simulation parameters used as input to the Bergen Code for the 20x2 disc and 13x2 disc. Source condition p_0 computed from sound pressure amplitudes at $r_1 = 5r_0$ and $r_1 = 8r_0$, respectively, but are not shown here.

20x2 disc								
Parameter	f_0	p_0	a	c_0	ρ_0	β	α_2	T
Value	98.370	-	11.9023	347.51	1.156	1.2	3.89×10^{-11}	26.18
Unit	kHz	Pa	mm	m/s	kg/m^3	-	Np/m/Hz^2	°C
13x2 disc								
Parameter	f_0	p_0	a	c_0	ρ_0	β	α_2	T
Value	154.640	-	5.3886	347.23	1.178	1.2	2.67×10^{-11}	25.71
Unit	kHz	Pa	mm	m/s	kg/m^3	-	Np/m/Hz^2	°C

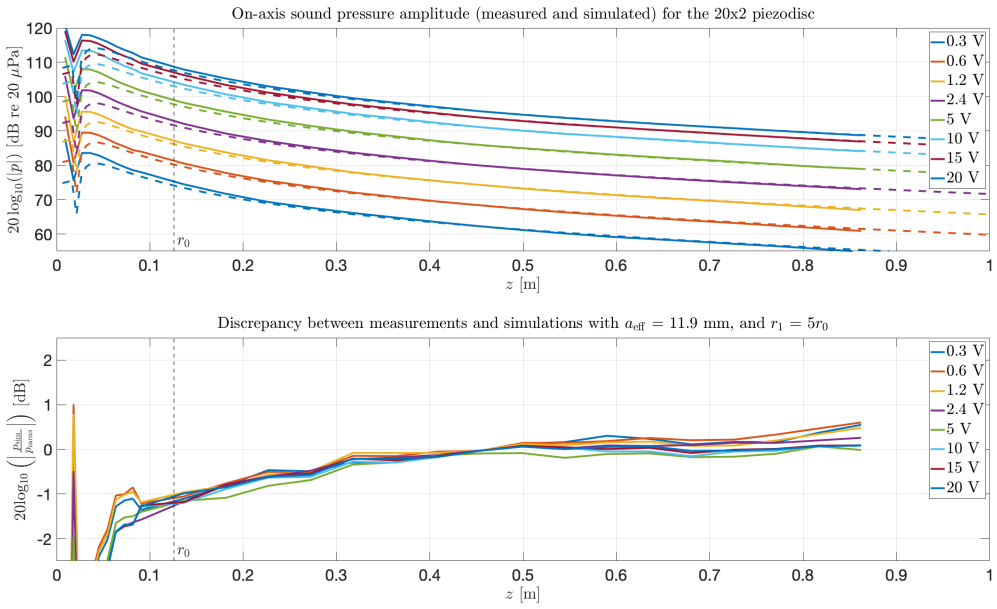

Figure 5.46: Simulated and measured axial sound pressure levels for the 20x2 disc in the upper plot. Dashed graphs correspond to the simulated values for each measured pressure series. In the bottom plot, the relative difference of the simulated and measured pressure amplitudes. Pressure source condition p_0 to the Bergen Code determined from measured pressure values at $z = r_1 = 5r_0$. Effective source radius $a_{\text{eff}} = 11.90$ mm used.

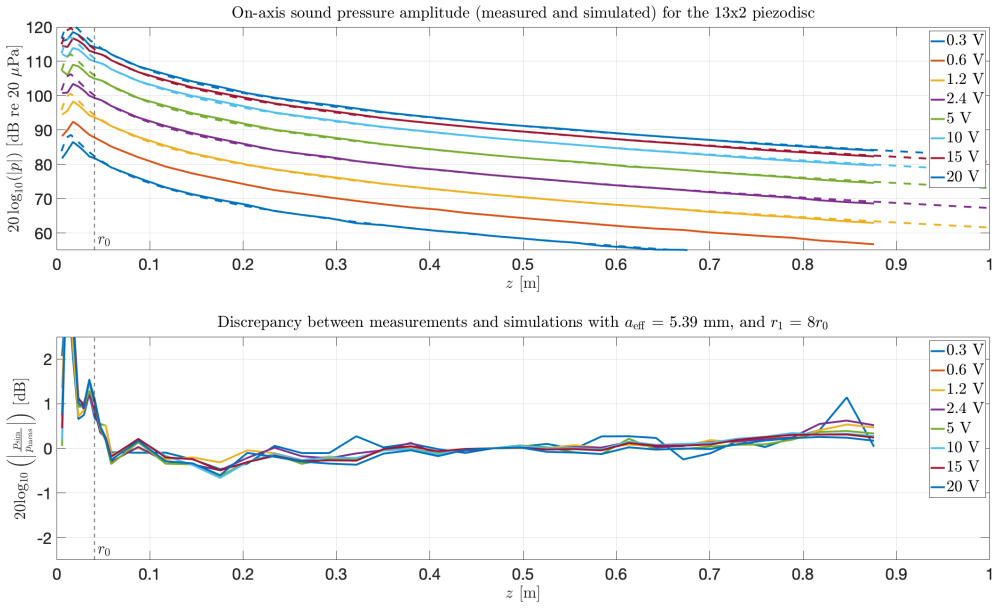

Figure 5.47: Same as Figure 5.46, but here for the 13x2 disc. Pressure source condition p_0 to the Bergen Code determined from measured pressure values at $z = r_1 = 8r_0$. Effective source radius $a_{\text{eff}} = 5.39$ mm used.

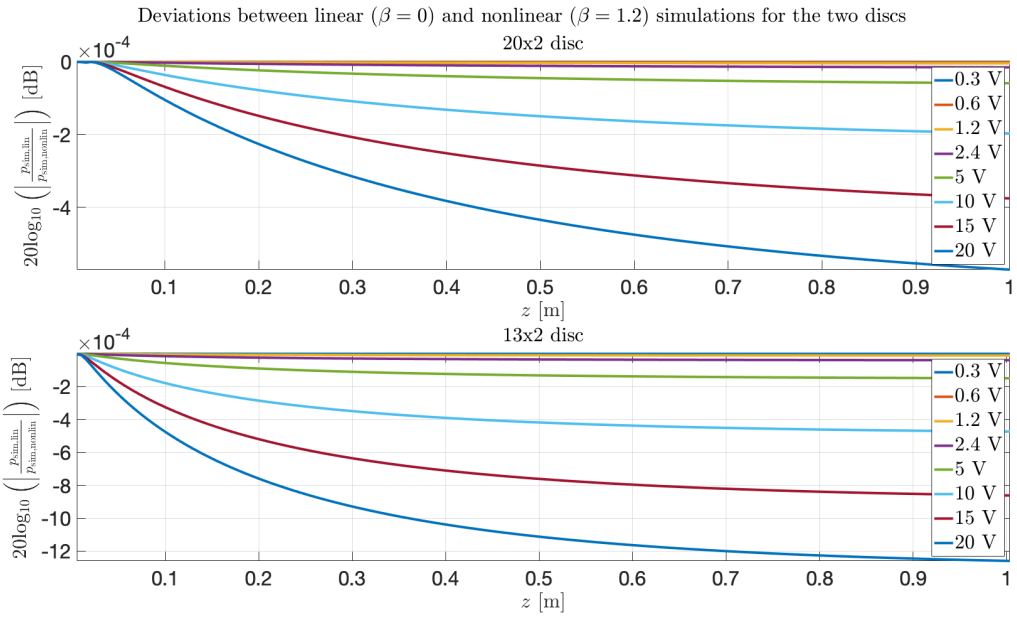

Figure 5.48: Discrepancy between the linear ($\beta = 0$) and nonlinear ($\beta = 1.2$) simulations of the axial sound pressure amplitudes of the 20x2 disc (upper plot) and 13x2 disc (lower plot).

Second harmonic component

The second harmonic component of the measured and simulated sound pressure amplitudes for the 20x2 disc was investigated for the data presented in Figure 5.46. Figure 5.49 displays the measured (solid lines), and corresponding simulated (dotted lines) SPL of the second harmonic component. The lower nominal voltages $V_{0,\mathrm{pp}}$ are grouped in the upper part of the figure, and higher $V_{0,\mathrm{pp}}$ in the bottom part.

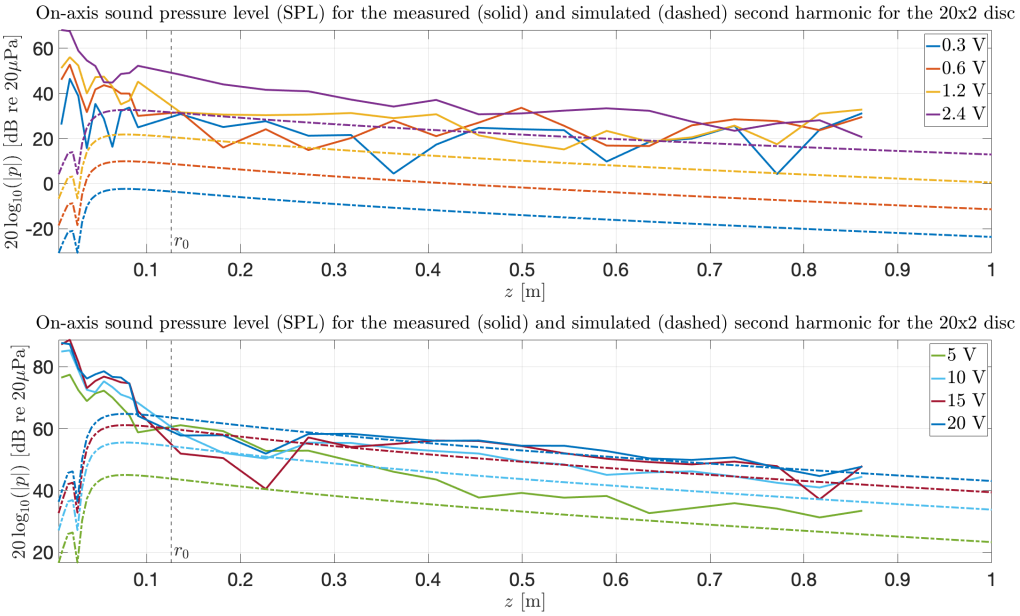

Figure 5.49: Comparison of the sound pressure level of the measured (solid lines) and simulated (dotted lines) second harmonic component, for the 20x2 disc. Simulations with $a_{\text{eff}} = 11.90$ mm, and $r_1 = 5r_0$. The measurement series with lower nominal applied voltage amplitudes $V_{0,\text{pp}}$ in the upper part of the figure, and higher $V_{0,\text{pp}}$ in the bottom part.

Impact of r_1 for the simulations

The impact of the chosen distance r_1 for the calculation of the source condition p_0 was modeled with the theoretical expression of a plane piston radiator, as in Eq. (4.9) from Section 4.2.6. Distances $z = r_1$ along the sound axis were tested for $r_1 = 2r_0$, where the directivity measurements were carried out, $r_1 = 9.5r_0$ which was the last measured point along the axis, and $r_1 = 5r_0$ which lies in between the two prior, for the 20x2 disc. The effect is presented in Figure 5.50 below. As can be seen from the figure, adjusting r_1 shifts the intersection of the 0 dB line (where the measured and theoretical amplitudes are equal), and thus induces an increasing deviation in the opposite direction to the adjustment of r_1. On this basis, the distances $r_1 = 5r_0$ and $r_1 = 8r_0$ were chosen for the 20x2 disc and 13x2 disc, respectively.

A comparison of simulated and measured sound pressure values can be found for the three cases of r_1 in Figures B.91-B.93 in Appendix B.9.1. An equal approach, to that shown in Figure 5.50, to the measurement series of the 13x2 disc, can also be found in Figure B.94 in Appendix B.9.1.

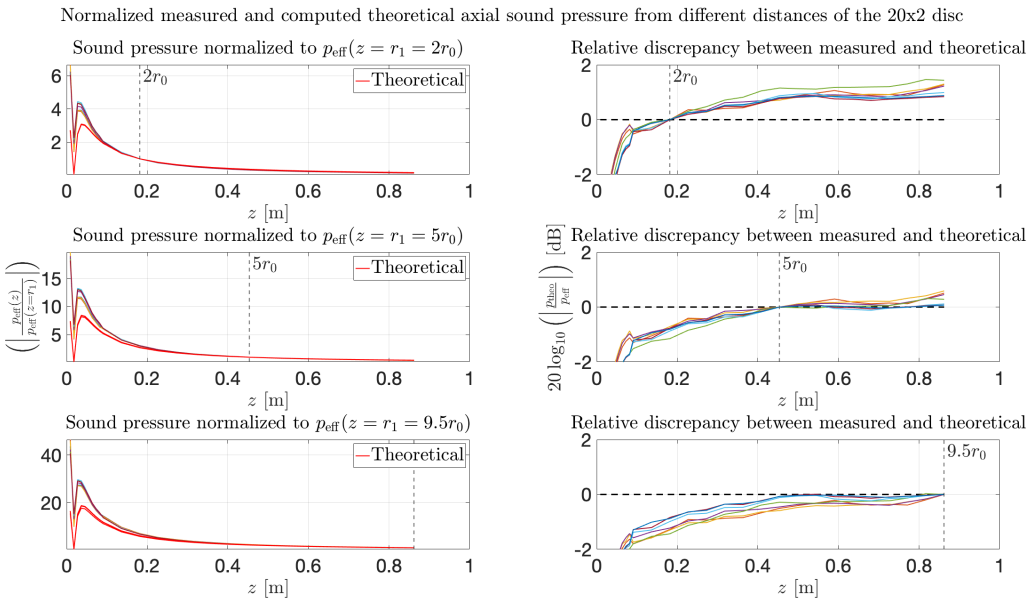

Figure 5.50: To the left in the figure; measurement series of the sound pressure amplitude of the 20x2 disc normalized to the pressure amplitudes $p(r_1 = 2r_0)$, $p(r_1 = 5r_0)$, and $p(r_1 = 9.5r_0)$, for each corresponding series. The theoretical expression of a plane piston radiator modeled with equal parameters as the simulations for each series, calculated for the same axial distance, and normalized, before being extrapolated on the interval. To the right in the figure; relative discrepancy between the normalized measured and theoretical sound pressure amplitudes, for the three cases of r_1.

Reducing the effective source radius of the 20x2 disc

The effect of reducing the effective source radius in the simulations was found to yield an increased source condition p_0, and similarly increased sound pressure amplitudes along the axis. The 0 dB intersection (equal amplitude) between measured and simulated values, was still determined by r_1. Simulations where the effective source radius was decreased, were only carried out for a fixed distance of $r_1 = 9.5r_0$ for the 20x2 disc. This is shown for effective source radii $a_{\text{eff}} = 10.07$ mm (the measured radius of the 20x2 disc), and $a_{\text{eff}} = 8.42$ mm, in Figures B.95-B.97 in Appendix B.9.2. The latter effective source radius was, somewhat arbitrary, chosen to be the radio of the effective and measured source radius of the 13x2 disc, multiplied by the measured radius of the 20x2 disc. The resulting simulated pressure amplitudes along the axis for $z < r_0$ were seen to slightly increase close to the transmitting source, but had less significant effect in the far-field ($z > r_0$).

However, for a r_1 closer to the transmitting source the effect of reducing the effective source radius could be less controlled, as the resulting discrepancy discussed above could induce increased deviations in the other end. In addition, the approach elaborated in Section 4.2.3 was based on the assumption that nonlinear effects in the sound radiation can be neglected. Thus, for significant nonlinear sound radiation, the effects of moving r_1 along the axis can be more considerable.

Chapter 6

Discussion

6.1 Low voltage impedance measurements

Admittance measurements carried out with the impedance analyzer were in agreement with the simulated values for the 20x2 disc. The first- and second radial modes were found to be reasonably equal, but the thickness mode showed a slight downshift of about 2 kHz. Bandwidths found from the simulations were somewhat wider for R1 and TE1, while R2 had a slightly sharper peak compared to the measurements.

The smaller disc displayed a poorer fit to the simulated values. Both R1 and R2 were measured some kilo hertz higher, whereas TE1 was found 10 kHz lower than the simulated mode. The bandwidths displayed similar traits to that of the 20x2 disc, where both R1 and TE1 were found to be wider in the simulations and R2 was more narrow. The preceding was summarized in Table 5.3 in Section 5.1, where the Q-factors were presented.

6.2 High voltage impedance measurements

6.2.1 Noise readings of the measurement circuit without output from the signal generator

The Fourier transform of the noise readings depicted in Figure 5.2 in section 5.2.1 show relatively similar noise characteristics. A comparison of the sum of the spectra yields about a 38 % higher value for channel 2. This could suggest that channel 2 might be more prone to noise than channel 1, and/or the connected measurement circuit contributes to a more noisy picture. However, the values are low, and for the most part well below -100 dB relative to 1 V, and thus assumed to be negligible in the measurements that followed.

6.2.2 Inherent characteristics of the output signal of the signal generator

Harmonic components are always present in electronic instruments and appear at multiples of the fundamental carrier frequency. Signal imperfections seen in the measurements of the output of the signal generator depicted in Figure 5.3, are claimed by the manufacturer to mainly be created in the digital to analog converter (DAC) [57]. Other elements of the signal path may also contribute to the imperfections. Current leakage from the cable connected to the generator's 'Sync' output connector can contribute to harmonic distortion at lower frequencies and amplitudes [57]. The waveform DAC is however proclaimed the biggest source of non-harmonic spurious components (called spurs), where harmonics are aliased, or folded back, into the passband of the signal generator, due to nonlinearity in the DAC [57].

The manufacturer proclaims harmonic distortion to be -60 dBc for peak-to-peak voltages of less than 3 V, and -55 dBc for $V_{0,\mathrm{pp}} > 3$ V [57], for carrier frequencies less than 1 MHz. From Figure 5.4 it is clear that most of the harmonics lie at amplitudes in good compliance with the manufacturer's listed values. However, the 5^{th} harmonic can be seen to lie somewhere between -50 dBc and -55 dBc for peak-to-peak voltages less than 3 V. The same can be said for the 3^{rd} harmonic of the signals with higher nominal applied voltages (more than 3 $\mathrm{V_{pp}}$), which are close to -50 dBc.

It should also be noted that increasing the nominal applied voltage $V_{0,\mathrm{pp}}$ seems to affect the 2^{nd}- and 3^{rd} harmonic component for all three frequencies. The 2^{nd} harmonic components seem to be less significant as the amplitude of the signal generator is increased, dropping about 10 dBc. The 3^{rd} harmonic, initially around -70 dBc for $V_{0,\mathrm{pp}}$ of 0.3 V, 0.6 V, and 1.2 V, jumps to about -50 dBc when the applied voltage is increased to 5 V, 10 V, and 20 V.

An ideal square wave consists of odd multiples of the carrier frequency. A reduction of the even harmonics, and a corresponding increase in the odd ones, could indicate that the above-mentioned effects on the 2^{nd} and 3^{rd} harmonics in the signals are due to the output signal acquiring square wave characteristics. Harmonic components in the measured signal can thus be interpreted as impurities and wave tops differing from that of a pure sine wave [19]. The amplitudes of the harmonics were however very small, and no distinct distortion in the output signals was observed during measurements.

6.2.3 Measurements of resistors in place of the piezodisc

The measurement conducted on the I-V circuit with a resistor in lieu of the piezodisc displayed some peculiar features for the first radial mode (R1) of the 20x2 mm disc. The frequency spectra of V_2 in Figure 5.5 shows peaks arising in between the 2^{nd}- and 3^{rd} harmonics. The even harmonics in general seem to be somewhat reduced for the calculated spectra based on the measurements for V_2, as opposed to the measured output of the signal generator, V_1.

The suppression of even harmonics seems also to be the case for R2, but perhaps to a lesser degree than for R1. In the case of TE1 in Figure B.6 in Appendix B.2, the harmonics for the measured signals with lower excitation amplitudes seem to be buried in noise, and thus less prominent. However, increasing the excitation amplitude seems to elevate the harmonics from the noise floor and make them stand out, both the even- and odd harmonics. It was also found, from the measurements of TE1, that the noise floor seemed to grow as a function of frequency for the lower nominal applied voltages.

6.2.4 Measurements of the piezodisc

In the case of the first radial mode, the characteristics of the measured voltage over the piezodisc in Figure 5.6 resembles that of the resistor in Figure 5.5. This may suggest

that the characteristics displayed in the Fourier transform are a result of the measurement circuit, and not that of the piezodisc placed in the circuit. A closer look at the frequency range 0 kHz to 300 kHz in Figure 5.7 reveals that the somewhat turbulent area between the 2^{nd} and 3^{rd} harmonic of the fundamental is supposedly suppressed as the nominal applied voltage amplitude is increased, for both cases (resistor and piezodisc). This might however be an effect of the relative amplitudes of the fundamental frequency, and an increase in the corresponding side lobes.

Looking at the Fourier transform of the second radial mode in Figure B.8, there seems to be less harmonic activity in the spectrum for V_2. Both the 2^{nd} and 3^{rd} harmonic are less prominent than that of the output of the signal generator. The transform of the measurements of the thickness mode seen in Figure B.9, displays similar traits to that of the 5 Ω resistor replacement. The harmonics of the output signal are far more visible (left plot) than that of the piezodisc. However, the 2^{nd} and 3^{rd} remain prominent, while the 5^{th} and 7^{th} are barely or not at all distinguishable from the noise for lower excitation levels. In general, most of the harmonic peaks have amplitudes less than -55 dB to -60 dB, which lies around the impurities found in the signal generator output.

In Figure 5.8, the frequency spectra of the currents in the circuit for the 55 Ω resistor were compared to the currents when the 20x2 piezodisc was placed in the circuit. Harmonic peaks of the fundamental were found to be similarly prominent in both cases, indicating that the frequency content seen was a result of the circuit itself and not the behavior of the disc. This was further summarized in Table 5.4, where the THD was computed for all three resonances. The values presented in the table indicate that the harmonic distortion seen in Figures 5.5-5.8, mainly varies due to the load impedance placed in the circuit, and the carrier frequency of the output signal, rather than the applied voltage amplitude.

6.2.5 Calculations based on measurements on the I-V circuit

From the measurements of the 20x2 disc utilizing continuous waveform in Figures 5.10-5.12, the relative phase shifts were achievable with the zero crossing method. It was however noticeable more noise in the measurements corresponding to R2, as shown in Figure 5.11. One reason for this can be the choice of the shunt resistor R with a resistance as low as 2.175 Ω. These measurement series were carried out before soldering.

Later measurements using bursts, and corresponding measurements for the 13x2 disc displayed a more noisy picture, and processing the data using the zero-crossing technique was cumbersome. Thus, the frequency domain method discussed in Section 3.2.3 was utilized to extract the phase and magnitude of the two voltage signals. However, new measurements in the I-V circuit showed more pronounced noise and jump phenomenon sporadically on the frequency intervals measured after testing, as can be seen from some of the figures attached in Appendix B.4.

Table 5.5 and 5.6 show the effect of higher applied voltages on the resonances of the discs. Both elements displayed downshifts of the respective resonances for each of the three modes and a widening of the bandwidth. A reduction in the conductance level and a downshift of the resonances for increased excitation amplitudes agree well with other findings [2].

The applied voltage is usually dependent on frequency, and it tends to decrease around resonance (f_s) [44]. The impedance measurements displayed a relative voltage drop around resonance, as depicted in the upper left plot as V_2/V_1 in Figure 5.13 and 5.14, and similarly in Figures B.10-B.66 in Appendix B.4. The voltage drop can from the figures be seen to move in line with the corresponding maximum in conductance, which marks the resonance frequency.

The resonance shifting found in the electrical impedance measurements in the I-V circuit is said to mainly originate from the SE term in Eq. (2.59), whereas an amplitude reduction is due to the S^2 term [9]. The strain squared, and cross term of the strain and electric field, are also present in Eq. (2.57), which serves as the base for additional voltage sources in the nonlinear Mason model presented by [6].

6.2.6 Calculated current in the circuit

The THD presented in Table 5.7 for the 20x2 disc showed little change in distortion of the currents as the amplitudes were increased. Somewhat higher values were seen for the first and second radial modes for $V_{0,\mathrm{pp}}$ of 10 V, 15 V, and 20 V, for both continuous and burst excitation. For TE1, no noteworthy increase was found.

For the 13x2 disc, distortion of the current signals was, in general, higher than for the 20x2 disc. A more significant increase in the distortion was also seen for R1 and R2, and especially the latter, for increased nominal voltage amplitudes, as presented in Table 5.8. The magnitudes of the first seven harmonics of R1 in Figure 5.20, showed an increase for the 2^{nd} and 4^{th} harmonics for higher $V_{0,\mathrm{pp}}$, but the magnitudes were low ($<$ -30 dB). The overtones of R2 were however seen to increase as the applied voltage was increased.

A distinct distortion of the current, as reported for high voltage drive levels (65 V to 150 V peak voltage amplitude) by [9], was not prominent in the measurements conducted in the I-V circuit. For about all of the resonance modes tested for the discs, the respective current harmonics were found to be less than -30 dB relative to the fundamentals. An exception was found for the second radial mode of the 13x2 disc, where current harmonics displayed amplitudes in the range of -20 dB and -30 dB relative to the fundamental, for the higher nominal voltages of 10 V, 15 V, and 20 V. The values are however significantly lower than the reported values in [9]. There is, however, a considerable voltage amplitude drive level difference between the reported values in [9] and the work carried out in this thesis.

Significant distortion of the measured voltage signals, and especially, high 2^{nd} and 3^{rd} harmonic components as reported in [50], were not observed. Pronounced harmonic amplitudes of the first overtones were found in [50] for measured voltages in the range 2 V to 25 V peak-to-peak voltage amplitude, as a function of current density, when the piezoelectric sample was driven at its resonance frequency. The effective voltage amplitudes of the measurements conducted in this work fall in the lower limit of this voltage range, and less harmonic activity could be a result of insufficient excitation amplitudes of the piezodiscs.

6.2.7 I-V circuit

The I-V circuit was the chosen approach to measure the impedance of the piezodisc. More sophisticated circuits include bridge, resonant, RF I-V, network analysis, and auto-balancing bridge method [54, 55], and could have served as alternative approaches. The methods mentioned typically have an upper frequency range limit of 70 MHz to 300 MHz [54], which is well within the frequency range of interest.

The bridge method yields high accuracy but needs to be manually balanced. The resonant method gives good results for high Q devices, but has to be tuned to resonance, and is also said to give low impedance accuracy [54]. The I-V method ideally requires a differential voltage probe to accurately measure the current in the circuit [54]. Such a probe could potentially have reduced noise, and given higher measurement resolution in the circuit, but was unfortunately not available. The RF I-V circuit is suited for measurements of frequencies in the range 1 MHz to 3 GHz, and thus unsuited for this work. The network analysis method's main disadvantage is a narrow impedance measurement range and besides requires recalibration when the measurement frequency is changed. The auto-balancing bridge method is however promising but typically requires an LCR meter as a part of the measurement setup [54]. Other methods include the constant voltage method, used in impedance analyzers, the constant current method, and the pulse drive method [32].

6.3 Acoustical measurements in air

6.3.1 Preparatory sound pressure measurements

The spectra of the measured responses of the preparatory sound pressure measurements in Figure 5.25 in Section 5.4.1, and Figures B.80-B.82 in Appendix B.6, revealed strange harmonic behavior for shorter distances between the transmitting 20x2 piezodisc and microphone. Especially for the higher nominal applied voltages $V_{0,\mathrm{pp}}$, both even and odd harmonics of the fundamental were of substantial magnitudes, beyond what seemed reasonable to origin from acoustic disturbances, i.e., a significant radiated nonlinear sound

field.

The fact that the salient harmonics could seem to die out as the piezodisc was moved farther away from the microphone, was in itself not unexpected, as harmonic components are attenuated more quickly than the fundamental [29], due to increased absorption in line with the squared frequency dependency. In addition, the majority of the harmonic generation happens within the near field ($z < r_0$) of the transmitting source [30, 29], and thus, as the distance z between the transmitter and receiver were increased, the harmonic components would be expected to progressively die out. However, the odd harmonics in Figures B.80-B.82 for higher $V_{0,\mathrm{pp}}$ remained distinguishable from the noise floor, but their magnitudes were somewhat arbitrary, thus likely to be of electrical origin rather than from the radiated sound field.

The inspection of the receiving electronics that followed in Section 5.4.2 did confirm the suspicion of the harmonics found in the preparatory sound pressure measurements, especially in Figure 5.25, were in fact due to the receiving electronics, and unfortunate gain settings of the measurement amplifier, combined with a voltage amplitude limitation in the analog filter.

Measurements of the 20x2 disc for a transmitted burst with a fundamental frequency corresponding to R2, presented in Figure 5.28, showed excitation of the discs first radial mode (R1). The excitation of R1 was prominent throughout the burst. As the transient periods of a burst contain a range of frequencies besides the (fundamental) carrier frequency, these might excite other (in this case, unwanted) resonance modes of the disc as well. This is in line with [86], where the authors found that a piezodisc's surface motion will tend towards the first radial mode after the initial stage of a transient period, as R1 is the last mode to be damped out. The magnitude of the radiated sound pressure for R1, however, cannot be compared to the amplitude of R2, due to the insufficient knowledge of the microphone response for the latter frequency.

In addition to the excitation of R1, multiples of some 30 kHz were also present in the spectra. The latter was more prominent for the lower nominal voltages applied, as can be seen from Figures B.83-B.86 in Appendix B.6. These peaks are likely due to resonances in components of the receiving electronic [87].

6.3.2 Axial sound pressure

The axial sound pressure measurements carried out displayed similar traits across the nominal applied voltages for the fundamental frequency, as can be seen from Figure 5.38 and 5.40, for the 20x2 disc and 13x2 disc, respectively. Significant nonlinear effects in the medium would have been expected to cause the generation of higher harmonic components, primarily in the near field [30], and thus decrease the amplitude in the fundamental due to energy conversion [88]. This effect was not prominent for the measurements carried out, and the sound pressure amplitudes seemed to decrease equally for the different

measurement series, due to spherical spreading and absorption.

Figure 5.37 showed an example of a transmitted and measured burst, and the corresponding frequency spectra, for an axial sound pressure measurement of the 20x2 disc. The excitation signal in the upper part shows harmonic multiples characteristic for all the measurements carried out. Harmonic peaks are salient on the interval 0 kHz to 1000 kHz, with the magnitude of the 3$^{\text{rd}}$ harmonic in the vicinity of -40 dB relative to the fundamental. The harmonic values are higher than what was found in the output of an equal signal generator in Figure 5.4, but was consistent across the nominal voltages applied and showed little effect of changes to the drive level.

Discrepancies between the measured and simulated sound pressure amplitudes increased for both discs for shorter distances to the transmitting source, as seen in Figure 5.46 and 5.47. For both discs and all eight corresponding measurement series, the discrepancy at $z = r_0$, which marks the transition from the near field ($z < r_0$) to the far-field ($z > r_0$), was found to be around -1 dB. The deviation remained less than ± 0.5 dB in the far field, and 0 dB for the distance $z = r_1$ used to calculate the source condition p_0 for the series. The minor differences seen in Figures 5.46 and 5.47 between the corresponding eight measurement series, for the 20x2 disc, and 13x2 disc, respectively, are more likely to origin from noise and uncertainties in the measurement setup and signal processing, rather than the acoustic radiation from the transmitting piezodiscs.

Second harmonic components of the sound pressure for the higher nominal applied voltages, $V_{0,\text{pp}} = 10$ V, 15 V, and 20 V, showed a similar decline to their respective simulated values in the far-field, as can be seen in the lower part of Figure 5.49 for the 20x2 disc. As the nominal applied voltages were reduced, the respective second harmonic amplitudes showed increased discrepancy to the simulated values, as can be seen in the bottom part of Figure 5.49. Especially for $V_{0\text{pp}} = 0.3$ V, 0.6 V, and 1.2 V, the sound pressure amplitude of the second harmonic components had fluctuating amplitude, and were indistinguishable from one another, leading to the belief that their magnitude was not of physical behavior, but rather the result of electrical impurities in the instruments and insufficient resolution. In general, the measured second harmonics amplitudes displayed significant noise and fluctuations, which could indicate that for the nominal voltages utilized, the resulting sound pressure amplitude of the second harmonics is small enough to be dominated by impurities in the receiving electronic.

A linear simulation of the sound pressure, using the same parameters as the ones used in the nonlinear simulations depicted in Figure 5.46 and 5.47, were carried out to quantify the nonlinear loss in the medium for the sound propagation. The loss showed at most -0.0006 dB and -0.0013 dB deviation at $z = 1$ m for the 20x2 disc and 13x2 disc, respectively, as depicted in Figure 5.48. Thus, the neglection of nonlinear effects due to the sound propagation in Section 4.2.3 was reasonable, for the nominal applied voltages utilized and the measuring distance in this work.

The voltage source sensitivities presented at the bottom of Figure 5.38 and 5.40, were found to be decreasing as the effective voltage amplitude got higher. In the strict linear

case, the computed voltage source sensitivities should have remained at a constant level, where an increased excitation voltage amplitude was accompanied by increased pressure values. This was not the case, as the measured sound pressure amplitude did not increase similarly to the applied voltage, and the efficiency declined.

Using the analogy of additional voltage sources V_c, from Eq. (2.58) in Section 2.5.3, in an equivalent circuit, the decreased performance on the mechanical side with regard to the increase on the electrical side, might be assigned dielectric losses. The dielectric permittivity coefficient ε, which typically is assigned a constant value, has gotten significant attention in [4, 48, 49], amongst others. In [48], near linear relations between the dielectric coefficient and the nominal electric field strength was found in the vicinity of the threshold field level, which for the soft piezoceramics tested was about 5-10 V/mm. It is however a complex picture, as can be interpreted from the nonlinear constitutive equations presented in 2.5.3, and the additions of Eqs. (2.53)-(2.57), which require a deliberate approach to the problem.

6.3.3 Directivity measurements

Measurements of the directivity were conducted at a distance $z = 2r_0$, which lies beyond the near field but is still not too far out in the far-field. Different excitation amplitudes were utilized, but with the low efficiency in air, it is unlikely that nonlinear effects due to sound propagation in the medium were significant. The directivity function for R1 displays similar traits across the different amplitudes for both discs. Significant nonlinear effects would be expected to alter the beam pattern, by a flattening of the main lobe of the fundamental [89, 90, 30], i.e., reduce the peak amplitude, as energy would have been transferred to higher harmonic components [88, 30]. A resulting broadening of the main lobe of the fundamental would then have been expected [89, 90]. Such effects would have altered the calculations of the effective source radius, but were not the case for the measurements conducted, as using either one of the measurement series gave similar results.

The directivity measurements of the 13x2 disc, displayed in Figure 5.44 (and Figure 5.45, but here less prominent due to the normalization), showed indentation for several of the series. Fluctuations between the rotational increments were also present. This was likely related to the measurement system itself, specifically the switching of analog gain settings in the oscilloscope [19], and not the radiated sound field.

6.4 Comparison of the two discs

A difference in the position of the electrodes clamped against the discs during the electrical measurements might have caused unwanted effects. The 20x2 disc had the electrodes clamped towards the center of the disc, as is the desired form [91]. Whereas the 13x2 disc, being significantly smaller and put in the same styrofoam slit, had the electrodes clamped

against the outer rim of the disc, which can cause a downshift of the resonance frequency and a higher impedance at resonance [91]. This has however remained constant throughout the work, and should therefore serve as a constant source of error for the smallest disc.

Soldering of electrodes to the discs had distinct effects on the frequency response of the elements. As summarized in Table 5.11, the resonances experienced relative shifts, and the corresponding bandwidths were widened, with regard to before the soldering process. For the 20x2 disc, the first radial mode was moved down, while R2 and TE1 shifted upwards. The soldering processes seemed to have a considerably bigger impact on the 13x2 disc. Both R1 and R2 were shifted downwards to a greater extent than what was seen for the 20x2 disc. The movement of R2 for the 13x2 disc was also in the opposite direction to that found for the 20x2 disc. The thickness mode was however moved upwards, as for the 20x2 disc.

A widening of the bandwidths was also evident, and the most significant increase was found for the smallest element (13x2). Common for both discs, was the relatively greater widening of the bandwidth for the first radial mode, which was close to doubled for the smallest disc. The widening of the bandwidths was more similar for R2 and TE1 between the two discs.

As shown in [91], increasing the solder mass used to connect the electrodes to the disc will increase the change in frequency correspondingly. Thus, the larger frequency shifts found for the smallest element (13x2) might be the result of adding a relatively greater solder mass, compared to the mass of the disc itself, to the face of the disc. The downshift of the second radial mode for the 13x2 disc also yields good agreement with [91], which showed that the effect of increasing the thickness of a 10 mm disc yields a downshift in resonance for R2.

Chapter 7

Conclusion and further work

7.1 Conclusion

In this thesis, a measurement circuit was utilized to measure the impedance of piezodiscs with higher excitation amplitude, and to investigate the frequency content of the current and voltage signals across the discs. The discs were further used for acoustic measurements in air to examine the nature of the radiated sound field of said discs, and the results were compared to simulations of nonlinear sound propagation with the Bergen Code.

A modified I-V circuit was configured in order to carry out impedance measurements of the piezodiscs with higher excitation amplitude. The impedance measurements showed a clear resonance frequency downshift and a widening of the bandwidth, which is a typical behavior nonlinearity in piezoceramics. Inspection of the harmonic distortion of the voltage and current signals in the circuit revealed little harmonic activity. The discrepancies found across resonance modes and excitation levels were more likely to differ from one another due to the load impedance of the two discs placed in the circuit.

Measurements of the axial sound pressure amplitude and the radiated sound beam did not show prominent nonlinear effects in the radiated sound field. A second harmonic component was, however, measurable for the measurement series with higher excitation amplitudes. Nevertheless, the magnitude of the 2^{nd} harmonic components was minuscule.

A nonlinear relation between the applied excitation voltage and the axial far-field pressure amplitude, expressed through the voltage source sensitivity, indicated losses in either the piezodisc or the medium, or a combination of the two. The drift from a linear relation was prominent for nominal applied peak-to-peak voltages above 2.4 V.

The nonlinear loss in the medium was quantified through linear and nonlinear simulations of the sound pressure with the Bergen Code and was found to be insignificant. Thus, the radiated sound field was established to be primarily of linear behavior across

the drive levels tested. In light of this, the nonlinear behavior of the two discs for increased drive levels should be attributed primarily to nonlinearity in the piezoelectric ceramic discs for the nominal voltage levels tested.

7.2 Further work

In light of the work conducted in this thesis, several ideas for further work come to mind. The measurements, both electrical and acoustic, have utilized the same signal generator with its inherent voltage limitation. It would be most interesting to conduct similar experiments with a higher applied voltage using an appropriate amplifier. Amplification of the output of the signal generator should be easily achieved for both the I-V circuit, or equivalent circuits, and in the acoustic setup for air measurements. Investigation of the vibration of the transducer surface could further be investigated by the use of precise displacement measurements as the authors of [3] studied.

Looking at other fluids, measurements with higher amplitudes in water, with a possible incorporation of an I-V circuit, or similar, would be highly exciting. Combined with simulations of a disc in water, it could perhaps be possible to further examine the behavior of piezoelectric elements in the influence of higher amplitudes when the impedance mismatch is less severe.

A nonlinear Mason model was introduced by [6] as an extension of the widely known linear Mason model, used to characterize the behavior of piezoelectric elements. Methods and means to develop an appropriate model incorporating the nonlinear behavior of an element could be an angle of attack. Such a model requires the determination of, an adequate number of nonlinear coefficients, but could serve useful in the search for accurate modeling of high-power transducers, as highlighted in [6].

List of Acronyms and Abbreviations

ADC analog to digital converter.
DAC digital to analog converter.
dBc decibel relative to carrier (fundamental) level.
DFT discrete Fourier transform.
DUT device under test.
FD finite difference.
FE finite element.
FFT Fast Fourier transform.
FIR finite impulse response.
KZK Khokhlov-Zabolotskaya-Kuznetsov.
RMS root mean square.
SNR signal-to-noise ratio.
SPL sound pressure level.
THD total harmonic distortion.

Bibliography

[1] P. Norli, *Sound velocity cell for gas characterization.* PhD thesis, University of Bergen, Aug. 2007.

[2] E. Mosland, "Reciprocity calibration method for ultrasonic piezoelectric transducers in air," Master's thesis, Department of Physics and Technology, University of Bergen, Jun. 2013.

[3] Y. Liu, R. Ozaki, and T. Morita, "Investigation of nonlinearity in piezoelectric transducers," *Sensors and Actuators A: Physical*, vol. 227, pp. 31–38, May 2015.

[4] D. A. Hall, "Review nonlinearity in piezoelectric ceramics," *Journal of Materials Science*, vol. 36, pp. 4575–4601, 2001.

[5] S. Takahashi, Y. Sasaki, M. Umeda, K. Nakamura, and S. Ueha, "Nonlinear behavior in piezoelectric ceramic transducers," *IEEE International Symposium on Applications of Ferroelectrics*, vol. 1, pp. 11–16, 2000.

[6] D. S. Shim and D. A. Feld, "A general nonlinear mason model of arbitrary nonlinearities in a piezoelectric film," *Proceedings - IEEE Ultrasonics Symposium*, pp. 295–300, 2010.

[7] D. A. Feld, D. S. Shim, S. Fouladi, and F. Bayatpur, "Advances in nonlinear measurement & modeling of bulk acoustic wave resonators (invited)," *IEEE International Ultrasonics Symposium, IUS*, pp. 264–272, Oct. 2014.

[8] C. Kirkendall, P. L. Yu, D. Shim, S. Fouladi, and C. Liu, "A 3d finite element model of h2 emissions in apodized baw devices," *IEEE MTT-S International Conference on Microwave Acoustics and Mechanics, IC-MAM 2022*, pp. 45–48, 2022.

[9] N. Aurelle, D. Guyomar, C. Richard, P. Gonnard, and L. Eyraud, "Nonlinear behavior of an ultrasonic transducer," *Ultrasonics*, vol. 34, pp. 187–191, Jun. 1996.

[10] Y. Wu, H. Ji, J. Qiu, and L. Han, "A 2-degree-of-freedom cubic nonlinear piezoelectric harvester intended for practical low-frequency vibration," *Sensors and Actuators A: Physical*, vol. 264, pp. 1–10, Sep. 2017.

[11] Z. Yang and J. Zu, "Toward harvesting vibration energy from multiple directions by a nonlinear compressive-mode piezoelectric transducer," *IEEE/ASME Transactions on Mechatronics*, vol. 21, pp. 1787–1791, Jun. 2016.

[12] H. F. Hu, W. J. Staszewski, N. Q. Hu, R. B. Jenal, and G. J. Qin, "Crack detection using nonlinear acoustics and piezoceramic transducers-instantaneous amplitude and frequency analysis," *Smart Materials and Structures*, vol. 19, 2010.

[13] Z. K. Peng, Z. Q. Lang, and S. A. Billings, "Crack detection using nonlinear output frequency response functions," *Journal of Sound and Vibration*, vol. 301, pp. 777–788, Apr. 2007.

[14] Z. Parsons and W. J. Staszewski, "Nonlinear acoustics with low-profile piezoceramic excitation for crack detection in metallic structures," *Smart Materials and Structures*, vol. 15, p. 1110, Jul. 2006.

[15] P. C. Pedersen, O. Tretiak, and P. He, "Impedance-matching properties of an inhomogeneous matching layer with continuously changing acoustic impedance," *The Journal of the Acoustical Society of America*, vol. 72, pp. 327–336, Aug. 1982.

[16] A. L. Song, T. N. Chen, X. P. Wang, and L. L. Wan, "Waveform-preserved unidirectional acoustic transmission based on impedance-matched acoustic metasurface and phononic crystal," *Journal of Applied Physics*, vol. 120, Aug. 2016.

[17] J. Mei and Y. Wu, "Controllable transmission and total reflection through an impedance-matched acoustic metasurface," *New Journal of Physics*, vol. 16, p. 123007, Dec. 2014.

[18] R. A. Jahdali and Y. Wu, "High transmission acoustic focusing by impedance-matched acoustic meta-surfaces," *Applied Physics Letters*, vol. 108, p. 31902, Jan. 2016.

[19] A. O. Pedersen , private communication, May 2023.

[20] X. Lurton, *An Introduction to Underwater Acoustics: Principles and Applications*. Springer-Verlag Berlin Heidelberg, 2nd ed., 2010.

[21] M. Vesterheim, "Kapittel 2: Kretsbeskrivelse (chapter 2: Circuit description)." Syllabus in course 'PHYS272: Acoustic transducers' held at the Department of Physics and Technology at the University of Bergen, unpublished, 2013.

[22] M. Vesterheim, "Kapitttel 4: Piezoelektriske materialer (chapter 4: Piezoelectric materials)." Syllabus in course 'PHYS272: Acoustic transducers' held at the Department of Physics and Technology at the University of Bergen, unpublished, 2003.

[23] M. Vesterheim, "Kapittel 5: Piezoelektriske resonatorer (chapter 5: Piezoelectric resonators)." Syllabus in course 'PHYS272: Acoustic transducers' held at the Department of Physics and Technology at the University of Bergen, unpublished, 2008.

[24] Anon., "IEEE standard on piezoelectricity," *ANSI/IEEE Std 176-1987*, 1988.

[25] E. A. Shaw, "On the resonant vibrations of thick barium titanate disks," *Journal of the Acoustical Society of America*, vol. 28, pp. 38–50, 1956.

[26] N. Guo, P. Cawley, and D. Hitchings, "The finite element analysis of the vibration characteristics of piezoelectric discs," *Journal of Sound and Vibration*, vol. 159, pp. 115–138, Nov. 1992.

[27] J. Kocbach, *Finite Element Modeling of Ultrasonic Piezoelectric Transducers*. PhD thesis, University of Bergen, Sep. 2000.

[28] H. Hatano and J. Oosumi, "Effect of bevelling on the thickness vibration of high-frequency pb(zrti)o3 ceramic transducers," *Ultrasonics*, vol. 21, pp. 205–210, Sep. 1983.

[29] L. E. Kinsler, A. R. Frey, A. B. Coppens, and J. V. Sanders, *Fundamentals of Acoustics*. John Wiley & Sons, Inc., 4th ed., 2000.

[30] M. F. Hamilton and D. T. Blackstock, *Nonlinear Acoustics*. Acoustical Society of America, 2008.

[31] Y. Chen, S. Wang, H. Zhou, Q. Xu, Q. Wang, and J. Zhu, "A systematic analysis of the radial resonance frequency spectra of the pzt-based (zr/ti = 52/48) piezoceramic thin disks," *Journal of Advanced Ceramics*, vol. 9, pp. 380–392, 2020.

[32] K. Uchino, J. Zheng, A. Joshi, Y. H. Chen, S. Yoshikawa, S. Hirose, S. Takahashi, and J. W. D. Vries, "High power characterization of piezoelectric materials," *Journal of Electroceramics*, vol. 2, pp. 33–40, 1998.

[33] R. E. Newnham, L. J. Bowen, K. A. Klicker, and L. E. Cross, "Composite piezoelectric transducers," *Materials & Design*, vol. 2, pp. 93–106, Dec. 1980.

[34] M. Vesterheim, "Kapittel 7: Kalibrering (chapter 7: Calibration)." Syllabus in course 'PHYS272: Acoustic transducers' held at the Department of Physics and Technology at the University of Bergen, unpublished, 2013.

[35] W. Chen, J. Fu, Q. Wu, Y. Kang, N. Li, al, T. Tsuchiya, Y. Teshima, S. Hiryu, and M. F. Kazan, "Sensitivity and directivity measurement of ultrasonic transducer with polymer-powder matching layer," *Journal of Physics: Conference Series*, vol. 1038, p. 012109, Jun. 2018.

[36] P. K. Kundu, I. M. Cohen, and D. R. Dowling, *Fluid Mechanics*. Academic Press, an imprint of Elsevier, 6 ed., 2016.

[37] L. D. Landau and E. M. Lifshitz, *Fluid Mechanics*, vol. 6. 2 ed., 1987.

[38] D. Ćirić and A. Pantić, "Numerical compensation of air absorption of sound in scale model measurements," *Archives of Acoustics*, vol. vol. 37, pp. 219–225, 2012.

[39] Anon., "ANSI/ASA S1.26-2014 - methods for calculation of the absorption of sound by the atmosphere," tech. rep., Standards Secretariat Acoustical Society of America, Melville, NY 11747, 2014.

[40] F. E. Fox and W. A. Wallace, "Absorption of finite amplitude sound waves," *The Journal of the Acoustical Society of America*, vol. 26, pp. 994–1006, 1954.

[41] M. F. Hamilton and D. T. Blackstock, "On the coefficient of nonlinearity β in nonlinear acoustics," *The Journal of the Acoustical Society of America*, vol. 83, pp. 74–77, 1988.

[42] R. A. Alfons and Pérez, "Non-linear behaviour of piezoelectric ceramics," 2011.

[43] T. Zawada, T. Bove, K. Astafiev, E. Ringgaard, and R. Lou-Moeller, "Lead-free hifu transducers," *Ultrasound in Medicine & Biology*, vol. 48, pp. 2530–2543, Dec. 2022.

[44] A. Albareda, P. Gonnard, V. Perrin, R. Briot, and D. Guyomar, "Characterization of the mechanical nonlinear behavior of piezoelectric ceramics," *IEEE Transactions on Ultrasonics, Ferroelectrics, and Frequency Control*, vol. 47, pp. 844–853, Jul. 2000.

[45] A. Albareda, R. Pérez, J. A. Casals, J. E. García, and D. A. Ochoa, "Optimization of elastic nonlinear behavior measurements of ceramic piezoelectric resonators with burst excitation," *IEEE Transactions on Ultrasonics, Ferroelectrics, and Frequency Control*, vol. 54, pp. 2175–2188, Oct. 2007.

[46] A. Albareda, J. H. Kayombo, and J. A. Gorri, "Nonlinear direct and indirect third harmonic generation in piezoelectric resonators by the intermodulation method," *Review of Scientific Instruments*, vol. 72, pp. 2742–2749, 6 2001.

[47] B. Lewis, "Energy loss processes in ferroelectric ceramics," *Proceedings of the Physical Society*, vol. 73, p. 17, 1959.

[48] D. A. Hall, "Rayleigh behaviour and the threshold field in ferroelectric ceramics," *Ferroelectrics*, vol. 223, pp. 319–328, 1999.

[49] D. A. Hall and P. J. Stevenson, "High field dielectric behaviour of ferroelectric ceramics," *Ferroelectrics*, vol. 228, pp. 139–158, 1999.

[50] K. Ishii, N. Akimoto, S. Tashiro, and H. Igarashi, "Analysis of nonlinear phenomena in piezoelectric ceramics under high-power vibration," *Journal of the Ceramic Society of Japan*, vol. 106, pp. 555–558, 1998.

[51] R. Perez, A. Albareda, E. Minguella, and J. L. Villar, "Electrical model for a nonlinear piezoelectric transducer," *IEEE*, p. 4, 1996.

[52] Anon., "High quality components and materials for the electronic industry," tech. rep., Ferroperm Piezoceramics A/S (now a member of Meggitt´s Sensing Systems division), Kvistgård, Denmark, 2012.

[53] Anon., "JCGM - evaluation of measurement data - Guide to the expression of uncertainty in measurement Évaluation des données de mesure - Guide pour l'expression de l'incertitude de mesure," 2008.

[54] Anon., "Impedance measurement handbook a guide to measurement technology and techniques 6th edition," tech. rep., Keysight Technologies, n.d.

[55] V. Dumbrava and L. Svilainis, "The automated complex impedance measurement system," *Electronics and Electrical Engineering*, vol. 76, pp. 59–62, Apr. 2007.

[56] Anon., "Oscilloscope measurement lab: Measuring impedance and capacitance," tech. rep., Tektronix, Apr. 2013.

[57] Anon., "Agilent 33250A 80 MHz function/arbitrary waveform generator — User's guide," tech. rep., Agilent Technologies, Inc. 2000, Mar. 2003.

[58] Anon., "MSO3000 and DPO3000 series digital phosphor oscilloscopes - Programmer manual," tech. rep., Tektronix, Inc., Beaverton, OR 97077, USA, n.d.

[59] R. Wall, "Simple methods for detecting zero crossing," in *IECON'03. 29th Annual Conference of the IEEE Industrial Electronics Society (IEEE Cat. No.03CH37468)*, vol. 3, pp. 2477–2481 Vol.3, 2003.

[60] L. Mažeika and L. Draudvilienė, "Analysis of the zero-crossing technique in relation to measurements of phase velocities of the lamb waves," *Ultragarsas / Ultrasound*, vol. 65, pp. 7–12, Jun. 2010.

[61] R. J. Aliaga, "Real-time estimation of zero crossings of sampled signals for timing using cubic spline interpolation," *IEEE Transactions on Nuclear Science*, vol. 64, pp. 2414–2422, Aug. 2017.

[62] J. H. McClellan, R. W. Schafter, and M. A. Yoder, *DSP First*. Pearson Education Limited, second edition ed., 2017.

[63] S. Mahata, S. K. Saha, R. Kar, and D. Mandal, "Optimal design of fractional order low pass butterworth filter with accurate magnitude response," *Digital Signal Processing*, vol. 72, pp. 96–114, Jan. 2018.

[64] J. Karki, "Active low-pass filter design," tech. rep., Texas Instruments Incorporated, Feb. 2023.

[65] I. W. Selesnick and C. S. Burrus, "Generalized digital butterworth filter design," *IEEE Transactions on Signal Processing*, vol. 46, pp. 1688–1694, 1998.

[66] E. Fosse, "Finite element modeling and experimental characterization of piezoelectric ceramic disk in air," Master's thesis, Department of Physics and Technology, University of Bergen, Jun. 2022.

[67] V. Knappskog, "Radiellmode svingninger i piezoelektriske ultralydtransdusere for luft : målinger og endelig element analyser," Master's thesis, University of Bergen, 2007.

[68] R. Hauge, "Finite element modeling of ultrasound measurement systems for gas. comparison with experiments in air.," Master's thesis, Department of Physics and Technology, University of Bergen, 2013.

[69] Anon., "HMT310 humidity and temperature transmitter," tech. rep., Vaisala Oyj, 2019.

[70] Anon., "ASL F250 MK II Precision thermometer," tech. rep., ISOTECH, Willston, VT, n.d.

[71] Anon., "Digiquartz intelligent barometers and barometric standards," tech. rep., Paroscientific, Inc., Redmond, WA, 1997.

[72] Anon., "High-speed, high-accuracy CCD laser displacement sensor LK-G series user's manual LK-G series user's manual 96M1327," tech. rep., Keyence Corporation, Osaka, Japan, Jan. 2014.

[73] F. Expert, S. Viollet, and F. Ruffier, "Outdoor field performances of insect-based visual motion sensors," *Journal of Field Robotics*, vol. 28, pp. 529–541, 2011.

[74] Anon., "1/8-inch pressure-field microphone type 4138," tech. rep., Hottinger Brüel & Kjær A/S, Nærum, Denmark, Sep. 2021.

[75] P. Sivaraman and C. Sharmeela, "Power system harmonics," *Power Quality in Modern Power Systems*, pp. 61–103, Jan. 2020.

[76] H. Zumbahlen, "The op amp," *Linear Circuit Design Handbook*, pp. 1–82, 2008.

[77] V. Knappskog, "Radielle svingninger i piezoelektriske ultralydstransdusere for luft. målinger og endelig element analyse," Master's thesis, Department of Physics and Technology, University of Bergen, Bergen, Norway, 2007.

[78] A. O. Pedersen, *Effects of nonlinear sound propagation in fisheries research.* PhD thesis, University of Bergen, Oct. 2006.

[79] J. Berntsen, "The numerical calculation of the khokhlov-zabolotzkaya-kuznetsov equation for piston sources," Sep. 1989.

[80] O. Cramer, "The variation of the specific heat ratio and the speed of sound in air with temperature, pressure, humidity, and co2 concentration," *The Journal of the Acoustical Society of America*, vol. 93, pp. 2510–2516, May 1993.

[81] A. Picard, R. S. Davis, M. Gläser, and K. Fujii, "Revised formula for the density of moist air (CIPM-2007)," *Metrologia*, vol. 45, p. 149, Feb. 2008.

[82] R. S. Davis, "Equation for the determination of the density of moist air (1981/91)," *Metrologia*, vol. 29, Jan. 1992.

[83] Anon., "Butterworth filter design - MATLAB butter R2023a," tech. rep., 1994-2023 The Mathworks, Inc., 2022.

[84] Anon., "Operating and maintenance manual - model 3940/3944," tech. rep., Krohn-Hite Corporation, 2014.

[85] Anon., "Wide range measuring amplifiers - types 2610 and 2636," tech. rep., Brüel & Kjær A/S, Nærum, Denmark, n.d.

[86] N. Guo and P. Cawley, "Transient response of piezoelectric discs to applied voltage pulses," *Ultrasonics*, vol. 29, pp. 208–217, May 1991.

[87] E. N. Mosland , private communication, Apr 2023.

[88] T. S. Harta and M. F. Hamilton, "Nonlinear effects in focused sound beams," *Journal of the Acoustical Society of America*, vol. 84, pp. 1488–1496, 1988.

[89] A. O. Pedersen, P. Lunde, F. Tichy, and R. Korneliussen, "Finite-amplitude sound propagation effects in volume backscattering measurements for fish abundance estimation," 2022.

[90] P. T. Christopher and K. J. Parker, "New approaches to nonlinear diffractive field propagation," *Journal of the Acoustical Society of America*, vol. 90, pp. 488–499, 1991.

[91] M. G. Cain and M. Stewart, "Piezoelectric resonance," pp. 15–35, 2014.

Appendix A

A.1 Absorption coefficient

The subsequent elaboration (the entirety of Appendix A.1) follows the ANSI/ASA S1.26-2014 Methods for Calculation of the Absorption of Sound by the Atmosphere, where the equations, relations and numerical values are given [39].

The absorption coefficient α can be expressed as the sum of four individual absorption terms

$$\alpha = \alpha_{\mathrm{c}} + \alpha_{\mathrm{rot}} + \alpha_{\mathrm{vib,O}} + \alpha_{\mathrm{vib,N}}, \tag{A.1}$$

where α_{c} is the classical absorption coefficient, α_{rot} is an absorption term due to molecular rotation relaxation, and $\alpha_{\mathrm{vib,O}}$ and $\alpha_{\mathrm{vib,N}}$ denotes absorption as a result of molecular vibration relaxation of oxygen and nitrogen, respectively. The sum of the classical- and rotational absorption coefficient can be written as

$$\alpha_{\mathrm{c}} + \alpha_{rot} = \left[1.60 \times 10^{-10} \left(\frac{T}{T_{\mathrm{r}}}\right)^{\frac{1}{2}} f^2\right] \left(\frac{p_{\mathrm{a}}}{p_{\mathrm{r}}}\right)^{-1}, \tag{A.2}$$

where T is the ambient temperature in kelvins, T_{r} is a reference temperature at 20 °C of 293.15 K, p_{a} the ambient atmospheric pressure in kPa, p_{r} the reference pressure of 1 atm equal 101.325 kPa, and f the frequency in hertz. The coefficients introduced in Eq. (2.23) in Section 2.3.5, a_T and b_T, correspond to the values $1.60 \times 10^{-10}(T/T_{\mathrm{r}})^{0.5}$ and $(p_{\mathrm{a}}/p_{\mathrm{r}})^{-1}$ in Eq. (A.2), respectively.

The absorption coefficients due to vibrational relaxation of oxygen and nitrogen, respectively, are given as

$$\alpha_{\mathrm{vib,O}} = [(a\lambda)_{\mathrm{max,O}}] \left(\frac{f}{c}\right) \left(\frac{2 f_{\mathrm{rO}} f}{f_{\mathrm{rO}}^2 + f^2}\right), \tag{A.3}$$

$$\alpha_{\mathrm{vib,N}} = [(a\lambda)_{\mathrm{max,N}}] \left(\frac{f}{c}\right) \left(\frac{2 f_{\mathrm{rN}} f}{f_{\mathrm{rN}}^2 + f^2}\right), \tag{A.4}$$

where $(a\lambda)_{\max}$ is the maximum absorption per wavelength due to vibrational relaxation, and f_{r} is the relaxation frequency, for the respective gases.

The maximum absorption per wavelength are calculated, for oxygen and nitrogen respectively, as

$$(a\lambda)_{\max,\mathrm{O}} = \left(\frac{2\pi}{35}\right)[10\log_{10}(e^2)]X_{\mathrm{O}}\left(\frac{\Theta_{\mathrm{O}}}{T}\right)^2 \exp\left(\frac{-\Theta_{\mathrm{O}}}{T}\right), \tag{A.5}$$

$$(a\lambda)_{\max,\mathrm{N}} = \left(\frac{2\pi}{35}\right)[10\log_{10}(e^2)]X_{\mathrm{N}}\left(\frac{\Theta_{\mathrm{N}}}{T}\right)^2 \exp\left(\frac{-\Theta_{\mathrm{N}}}{T}\right), \tag{A.6}$$

where Θ is the characteristic vibrational temperature (K), and X is the fractional molar concentration in dry air (dimensionless). They have the values $\Theta = 2239.1$ K and $X = 0.209$ for oxygen, and $\Theta = 3352.0$ K and $X = 0.781$ for nitrogen.

The relaxation frequencies of oxygen and nitrogen, respectively, are given as

$$f_{\mathrm{rO}} = \left(\frac{p_{\mathrm{a}}}{p_{\mathrm{r}}}\right)\left\{24 + \left[\frac{(4.04\times10^4 h)(0.02+h)}{0.391+h}\right]\right\}, \tag{A.7}$$

$$f_{\mathrm{rN}} = \left(\frac{p_{\mathrm{a}}}{p_{\mathrm{r}}}\right)\left(\frac{T}{T_{\mathrm{r}}}\right)^{-\frac{1}{2}} \times \left(9 + 280h\exp\left\{-4.170\left[\left(\frac{T}{T_{\mathrm{r}}}\right)^{-\frac{1}{3}} - 1\right]\right\}\right), \tag{A.8}$$

where h is the molar concentration of water vapor in percent, which have the following relation to pressure

$$h = h_{\mathrm{rel}}\left(\frac{p_{\mathrm{sat}}}{p_{\mathrm{r}}}\right)\left(\frac{p_{\mathrm{a}}}{p_{\mathrm{r}}}\right)^{-1}. \tag{A.9}$$

Here, h_{rel} is the specified relative humidity in percent, and p_{sat} the saturation vapor pressure. The fraction $p_{\mathrm{sat}}/p_{\mathrm{r}}$ can be determined from the expression

$$\left(\frac{p_{\mathrm{sat}}}{p_{\mathrm{r}}}\right) = 10^{\mathrm{V}}, \tag{A.10}$$

where the purely temperature dependent exponent V are determined through

$$\begin{aligned} V = {} & 10.79586\left[1 - \left(\frac{T_{01}}{T}\right)\right] - 5.02808\log_{10}\left(\frac{T}{T_{01}}\right) \\ & + 1.50474\times10^{-4}\{1 - \times10^{-8.29692[(T/T_{01})-1]}\} \\ & + 0.42873\times10^{-3}\{-1 + \times10^{4.76955[1-(T_{01}/T)]}\} - 2.2195983, \end{aligned} \tag{A.11}$$

where T_{01} is the triple-point isotherm temperature equal to 273.16 K (0.01 °C). The equations (A.9)-(A.11) are calculated with respect to a plane surface of liquid water for the same temperature and pressure as that of the moist air.

Appendix B

Supplementary figures

B.1 Characteristics of the output signal of the signal generator

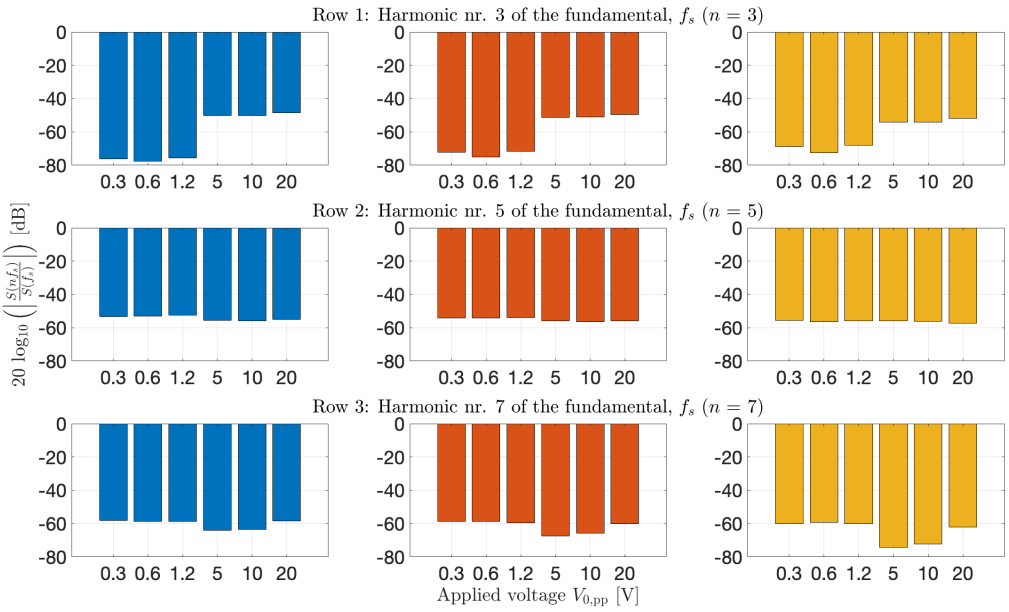

Figure B.1: Harmonic amplitudes relative to the fundamental in the measured output of the signal generator for the fundamental frequencies corresponding to R1, R2, and TE1, plotted in blue, red, and orange colors, respectively. Here shown for the first three odd harmonics ($n = 3, 5, 7$).

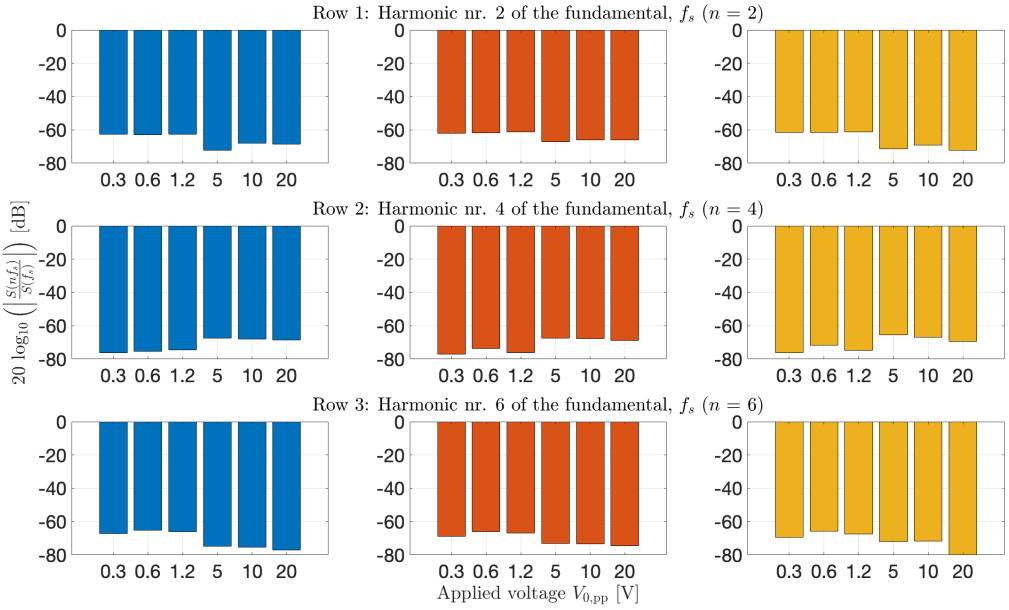

Figure B.2: Same as for Figure B.1, but here shown for the first three even harmonics (n = 2, 4, 6).

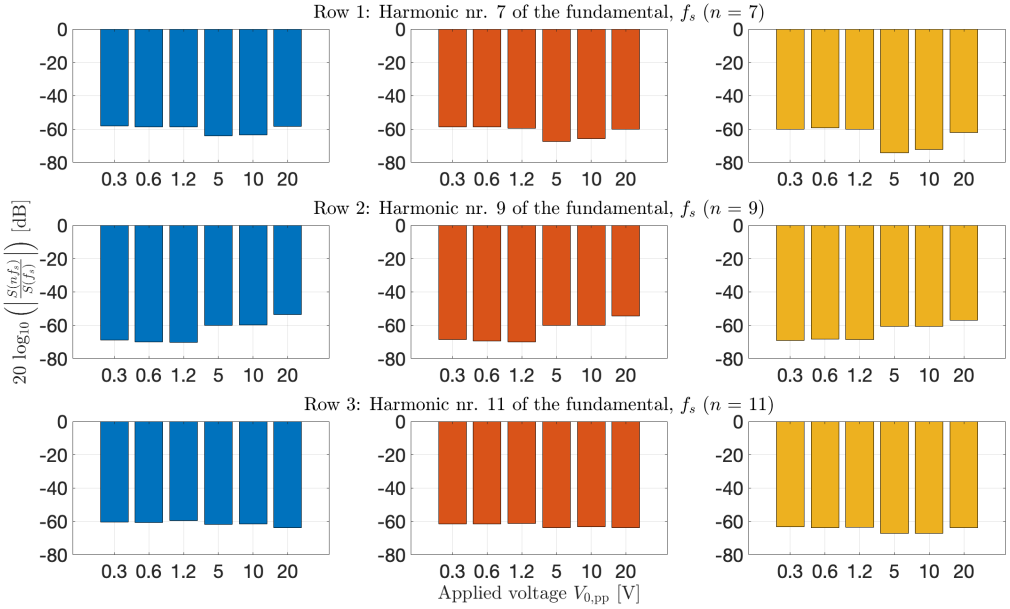

Figure B.3: Same as for Figures B.1 and B.2, but here shown for the first three even harmonics (n = 7, 9, 11).

B.2 Measurements of resistors in place of the piezodisc

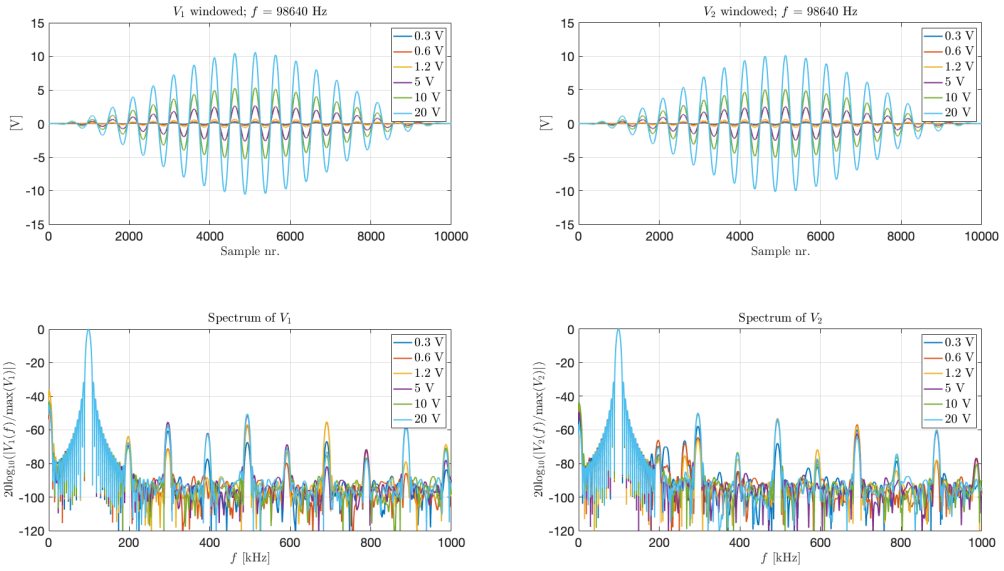

Figure B.4: Windowed readings from the oscilloscope (upper plots) and Fourier transform (lower plots) for V_1 and V_2 with a resistor of 55 Ω in place of the piezodisc for R1. Multiple series with varying applied voltage $V_{0,\mathrm{pp}}$ displayed in each plot.

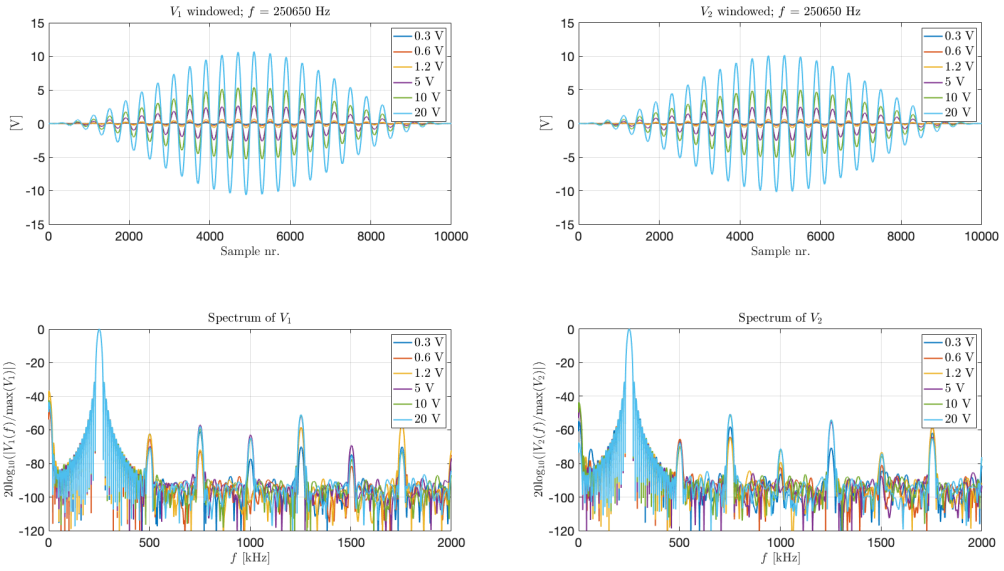

Figure B.5: Same as for Figure B.4, but for R2.

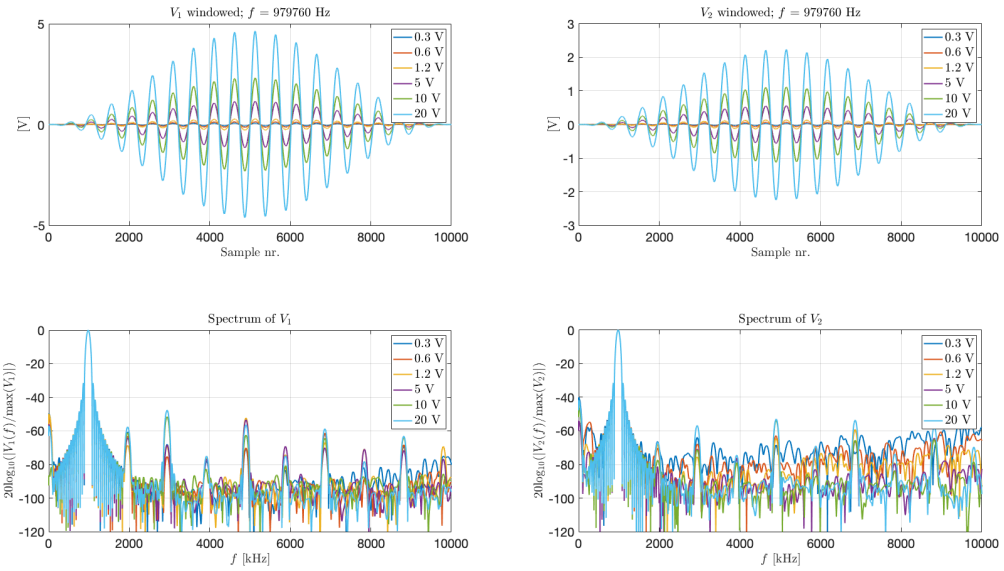

Figure B.6: Similar to Figures B.4 and B.5, but with a 5 Ω resistor for TE1.

B.3 Measurements of the piezodisc

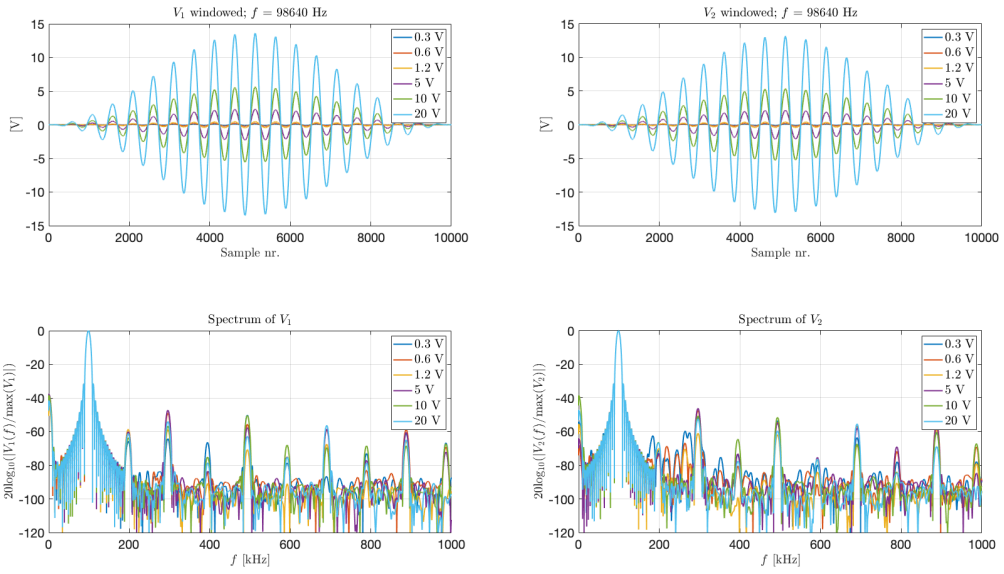

Figure B.7: Windowed readings from the oscilloscope (upper plots) and Fourier transform (lower plots) for V_1 and V_2 for various nominal applied voltage amplitudes $V_{0,\mathrm{pp}}$ for a frequency corresponding R1. V_2 is here the voltage measured across the 20x2 mm piezodisc.

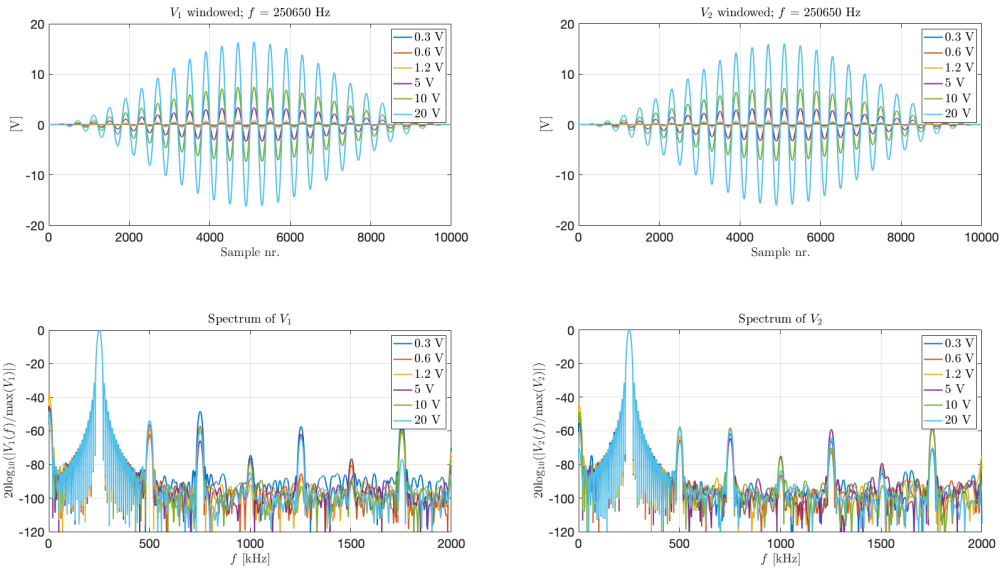

Figure B.8: Same as for Figure B.7, but for R2.

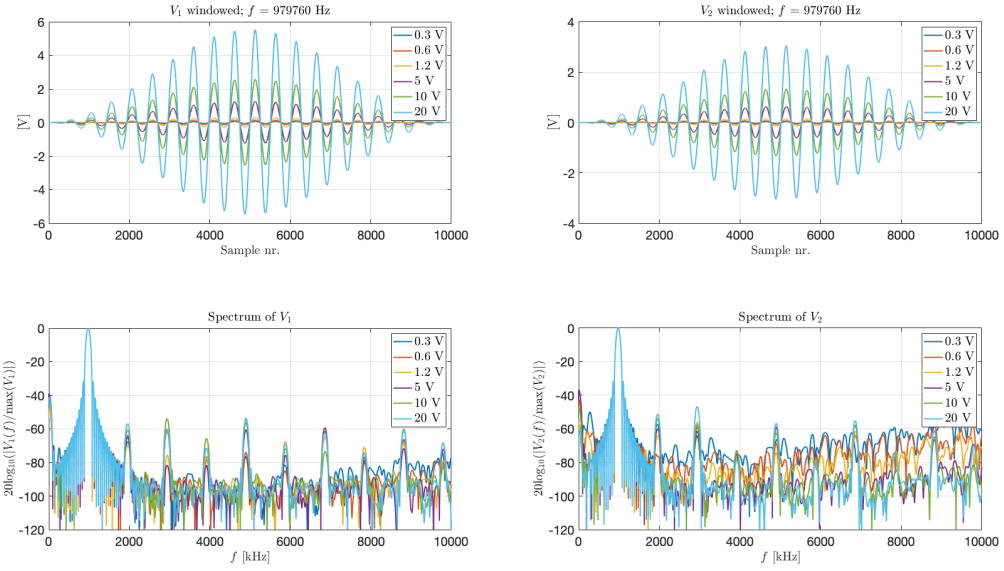

Figure B.9: Same as for Figures B.7 and B.8, but for TE1.

B.4 Calculations based on measurements on the I-V ciruit

B.4.1 20x2 disc measured with continuous waveform for R1

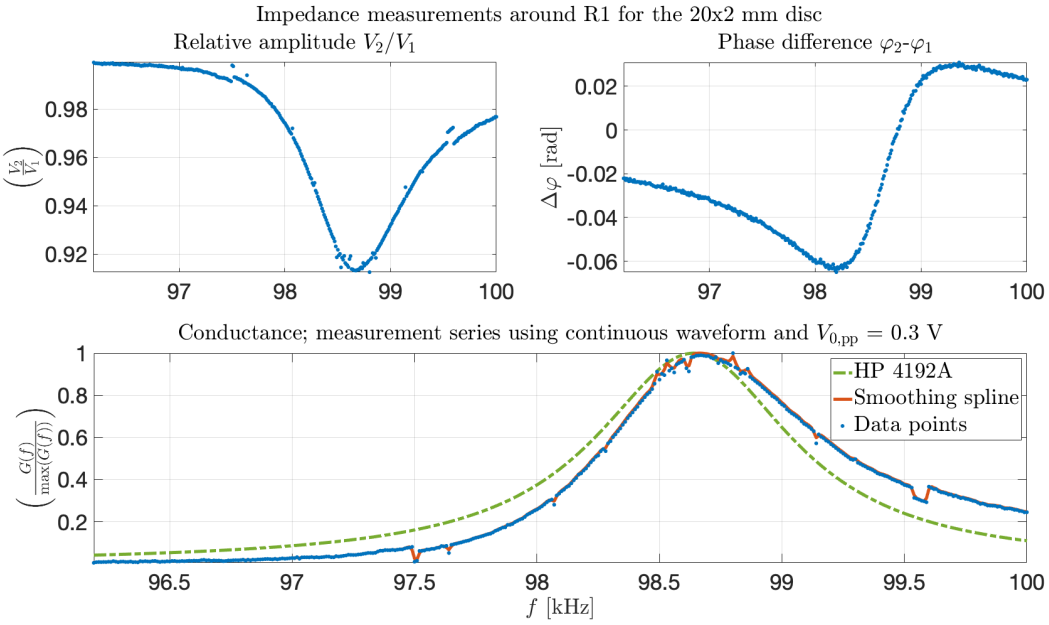

Figure B.10: Measured voltages V_1 and V_2 in the I-V circuit used to compute the impedance through Eq. (3.7). The relative voltage amplitude V_2/V_1, and phase shift $\Delta\varphi$ between the two measured voltages, are here shown in the upper two plots, and the computed conductance (real part of the impedance) in the bottom plot. Here shown for the 20x2 disc, for a frequency corresponding to R1, and with a nominal applied voltage $V_{0,\mathrm{pp}}$ of 0.3 V. Continuous waveform transmitted from the signal generator. Blue dots corresponds to measured values, and the red curve and dotted green curve in the bottom plot corresponds to a smoothing spline of the data points, and conductance measurement using the HP 4192A impedance analyser.

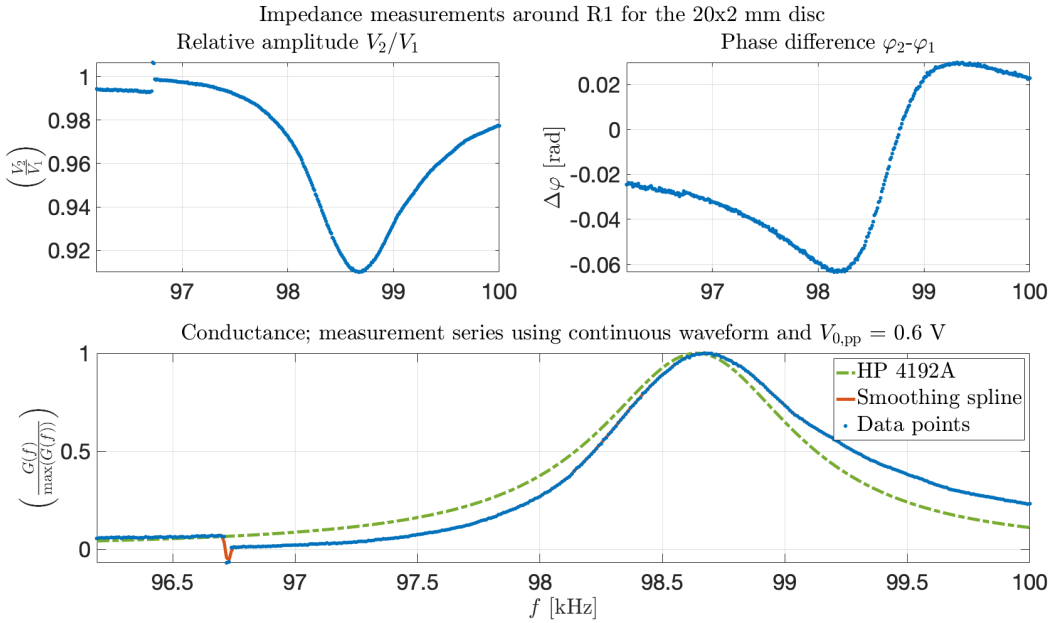

Figure B.11: Same as for Figure B.10, but here with $V_{0,\mathrm{pp}} = 0.6$ V.

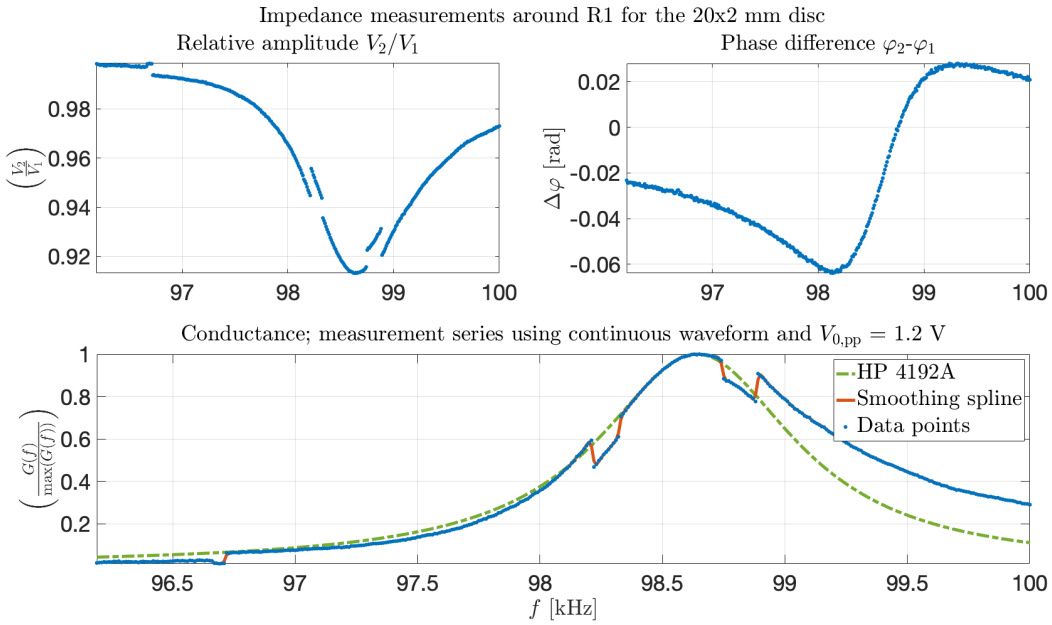

Figure B.12: Same as for Figure B.10, but here with $V_{0,\mathrm{pp}} = 1.2$ V.

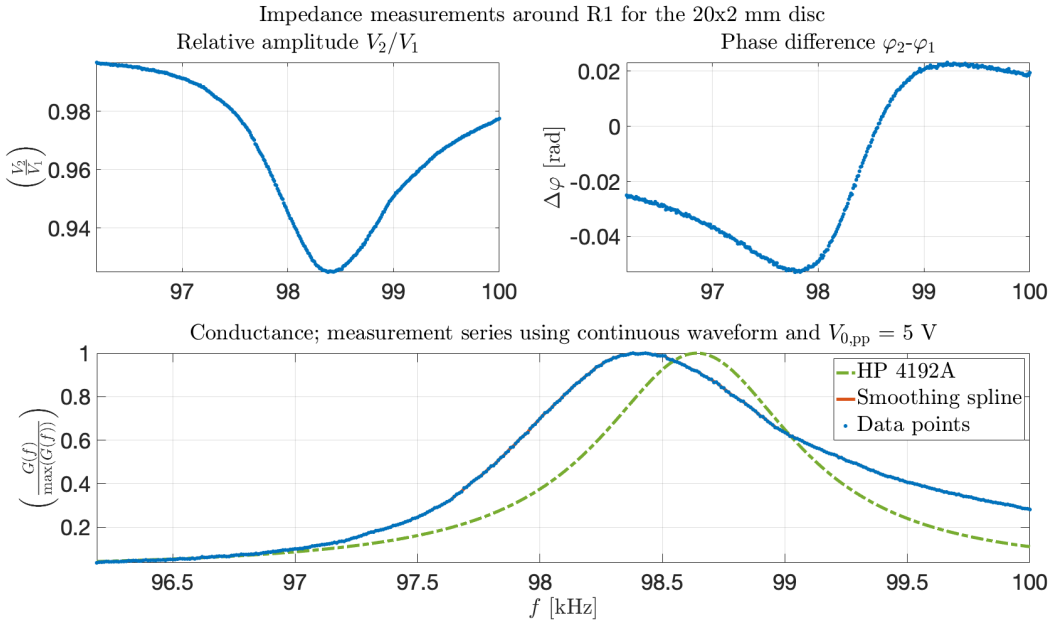

Figure B.13: Same as for Figure B.10, but here with $V_{0,\mathrm{pp}} = 5$ V.

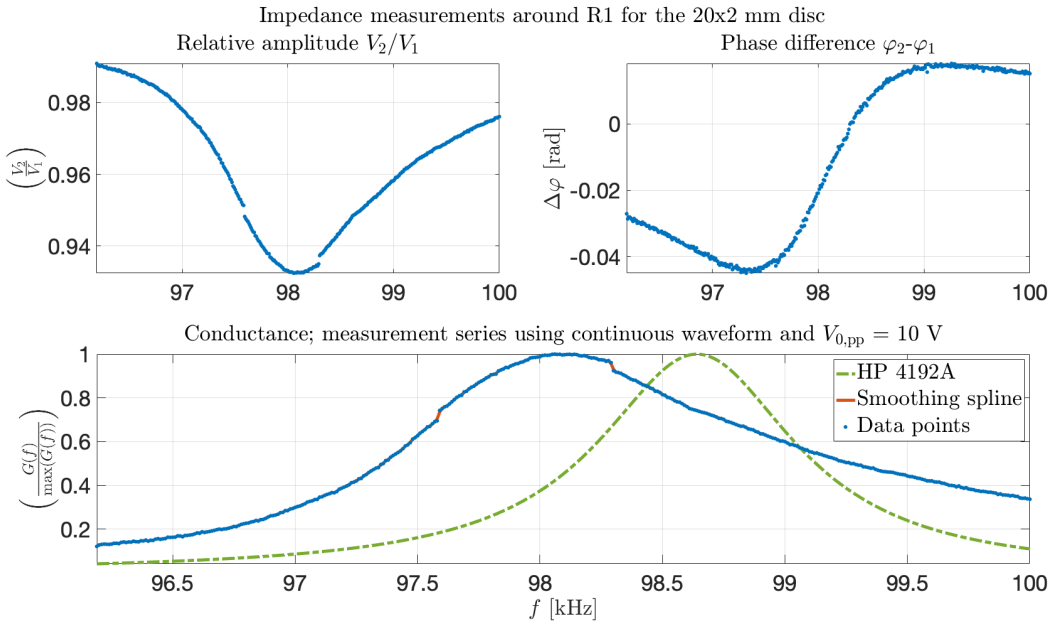

Figure B.14: Same as for Figure B.10, but here with $V_{0,\mathrm{pp}} = 10$ V.

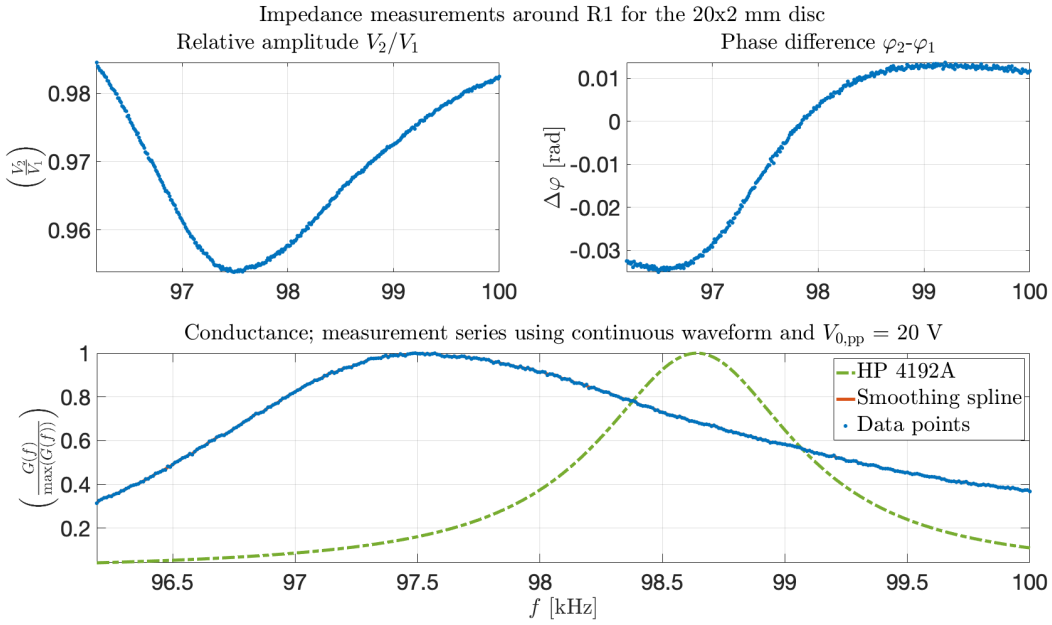

Figure B.15: Same as for Figure B.10, but here with $V_{0,\mathrm{pp}} = 20$ V.

B.4.2 20x2 disc measured with continuous waveform for R2

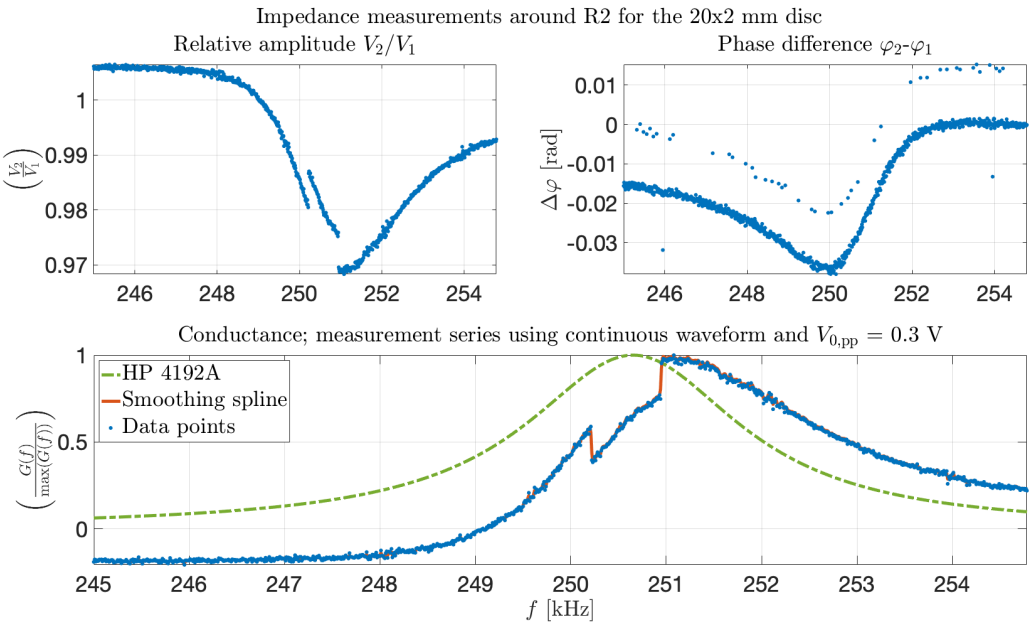

Figure B.16: Measured voltages V_1 and V_2 in the I-V circuit used to compute the impedance through Eq. (3.7). The relative voltage amplitude V_2/V_1, and phase shift $\Delta\varphi$ between the two measured voltages, are here shown in the upper two plots, and the computed conductance (real part of the impedance) in the bottom plot. Here shown for the 20x2 disc, for a frequency corresponding to R2, and with a nominal applied voltage $V_{0,\mathrm{pp}}$ of 0.3 V. Continuous waveform transmitted from the signal generator. Blue dots corresponds to measured values, and the red curve and dotted green curve in the bottom plot corresponds to a smoothing spline of the data points, and conductance measurement using the HP 4192A impedance analyser.

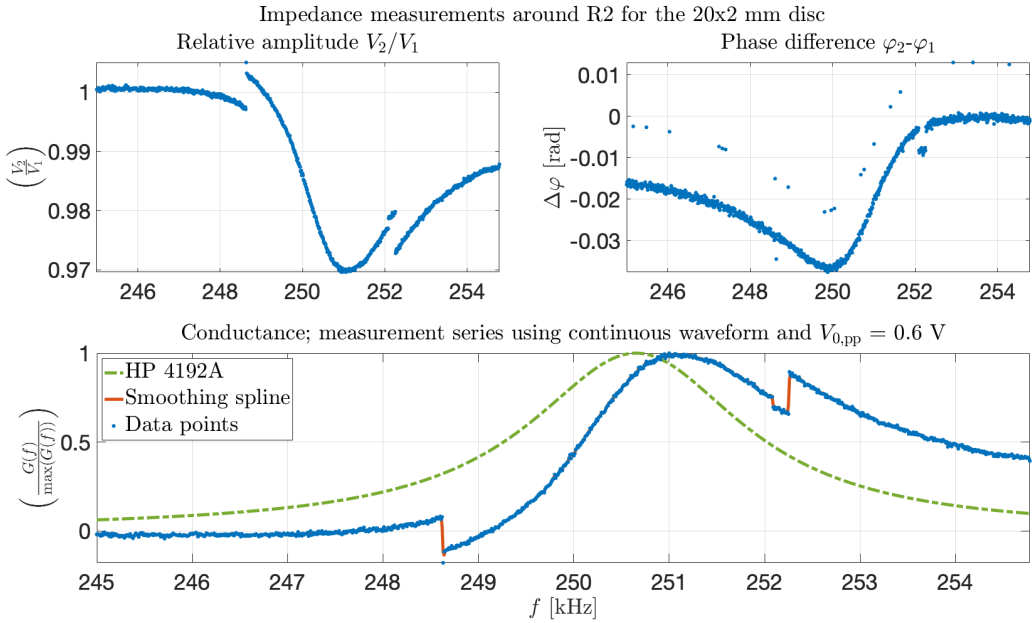

Figure B.17: Same as for Figure B.16, but here with $V_{0,\mathrm{pp}} = 0.6$ V.

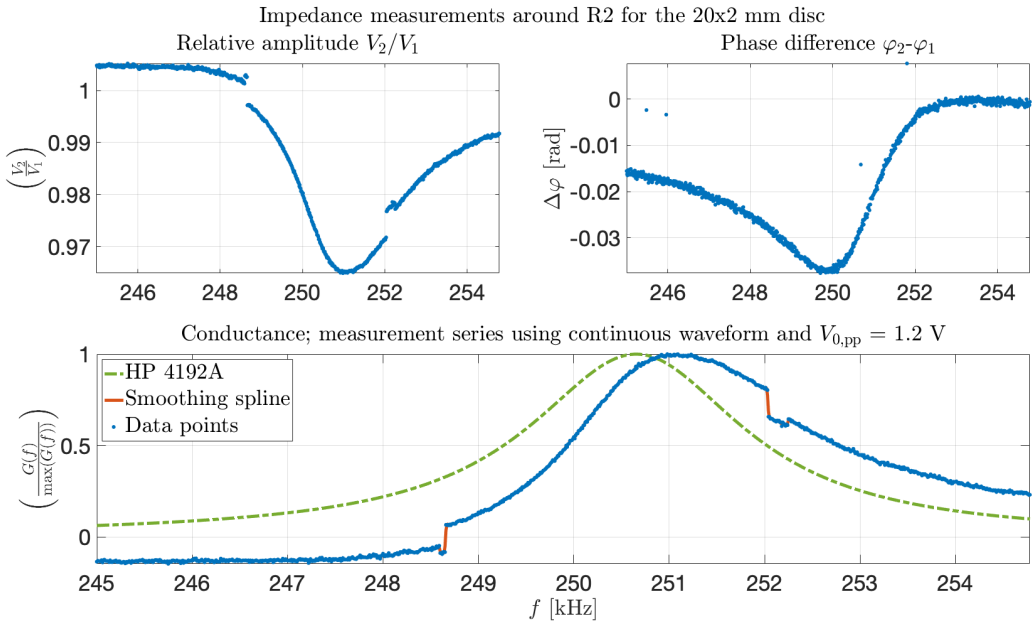

Figure B.18: Same as for Figure B.16, but here with $V_{0,\mathrm{pp}} = 1.2$ V.

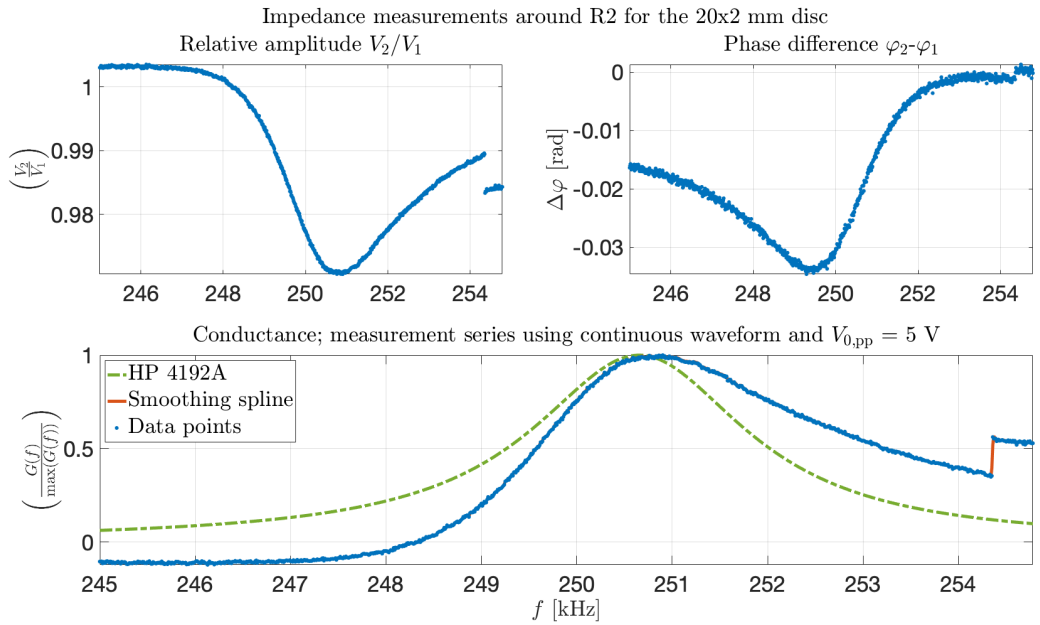

Figure B.19: Same as for Figure B.16, but here with $V_{0,\mathrm{pp}} = 5$ V.

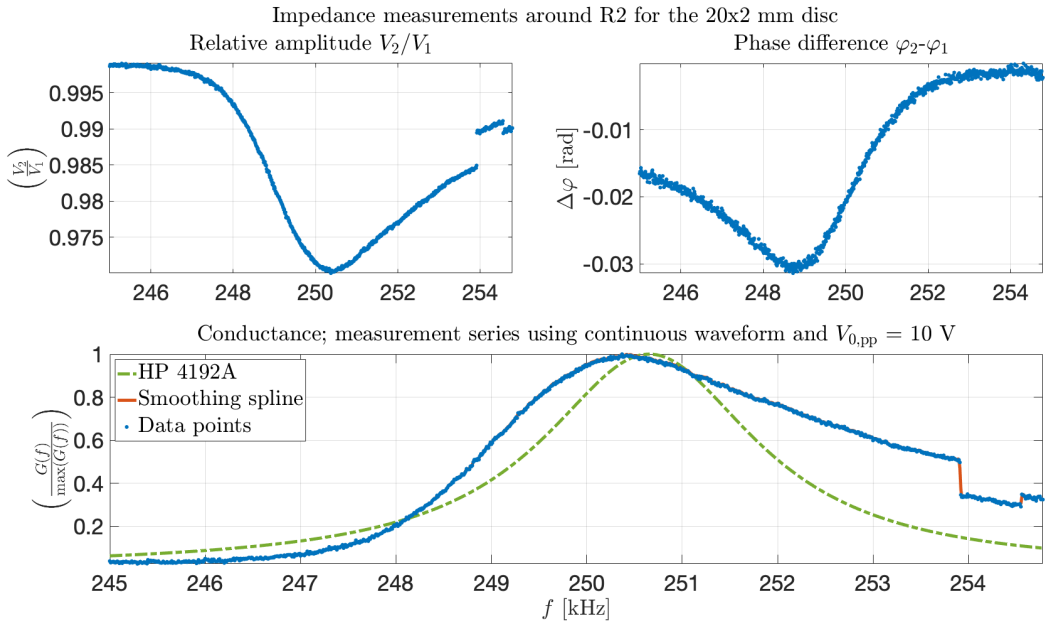

Figure B.20: Same as for Figure B.16, but here with $V_{0,\mathrm{pp}} = 10$ V.

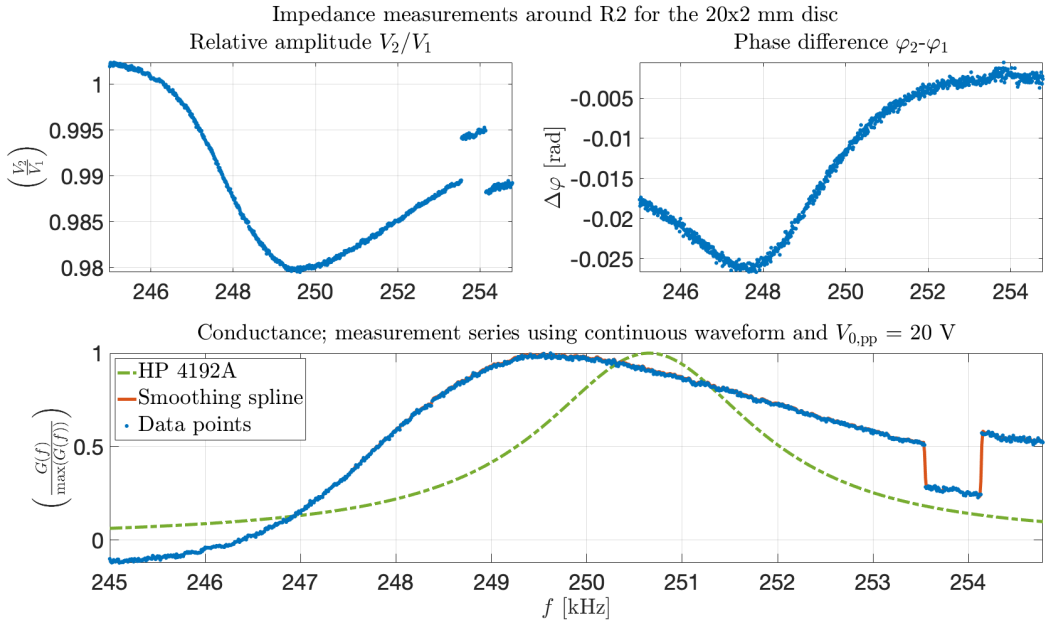

Figure B.21: Same as for Figure B.16, but here with $V_{0,\mathrm{pp}} = 20$ V.

B.4.3 20x2 disc measured with continuous waveform for TE1

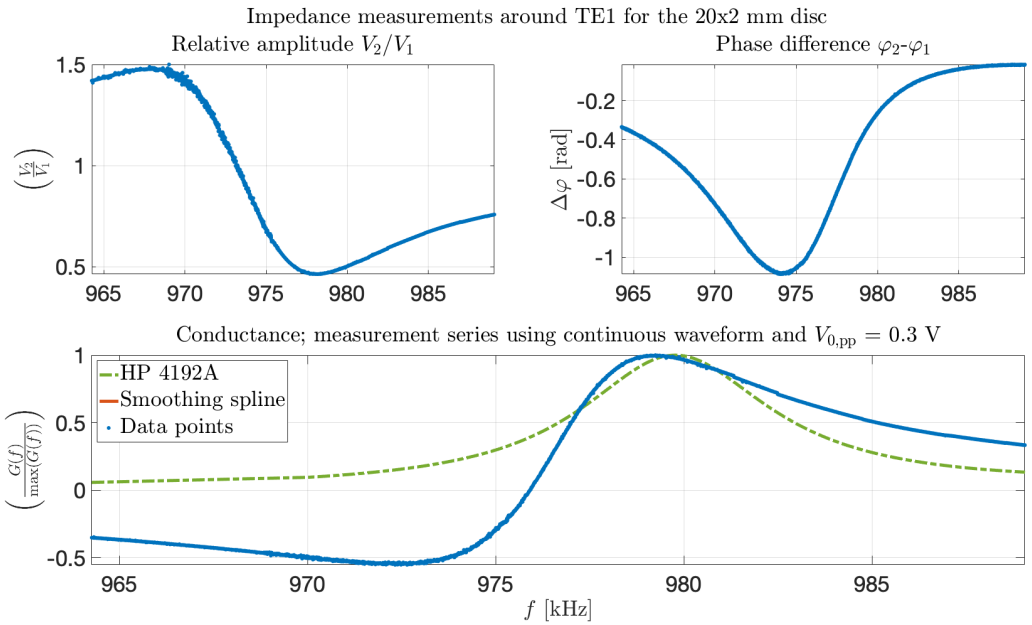

Figure B.22: Measured voltages V_1 and V_2 in the I-V circuit used to compute the impedance through Eq. (3.7). The relative voltage amplitude V_2/V_1, and phase shift $\Delta\varphi$ between the two measured voltages, are here shown in the upper two plots, and the computed conductance (real part of the impedance) in the bottom plot. Here shown for the 20x2 disc, for a frequency corresponding to R2, and with a nominal applied voltage $V_{0,\mathrm{pp}}$ of 0.3 V. Continuous waveform transmitted from the signal generator. Blue dots corresponds to measured values, and the red curve and dotted green curve in the bottom plot corresponds to a smoothing spline of the data points, and conductance measurement using the HP 4192A impedance analyser.

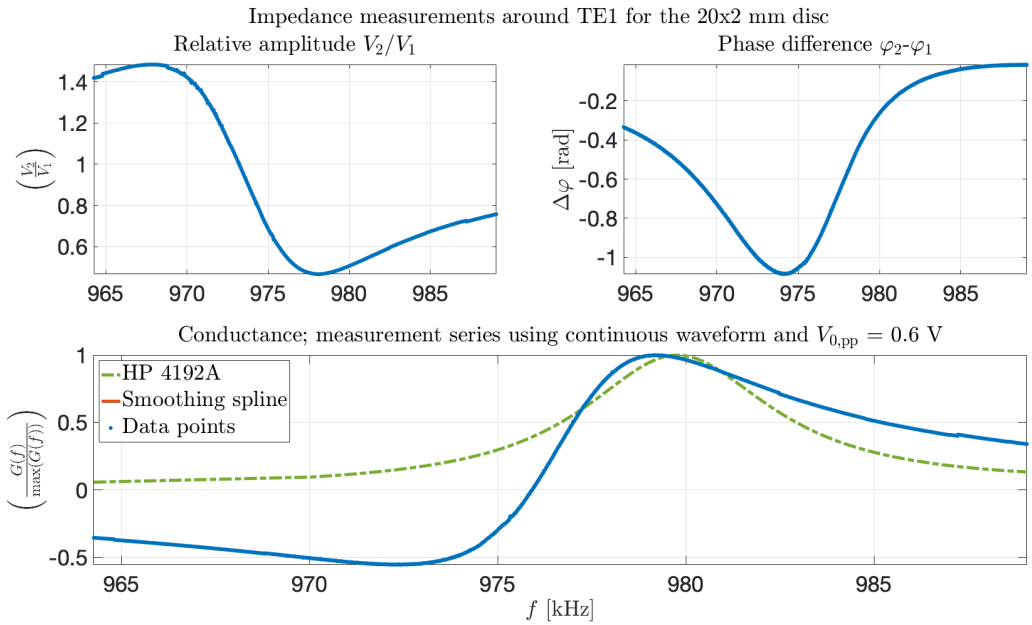

Figure B.23: Same as for Figure B.22, but here with $V_{0,\mathrm{pp}} = 0.6$ V.

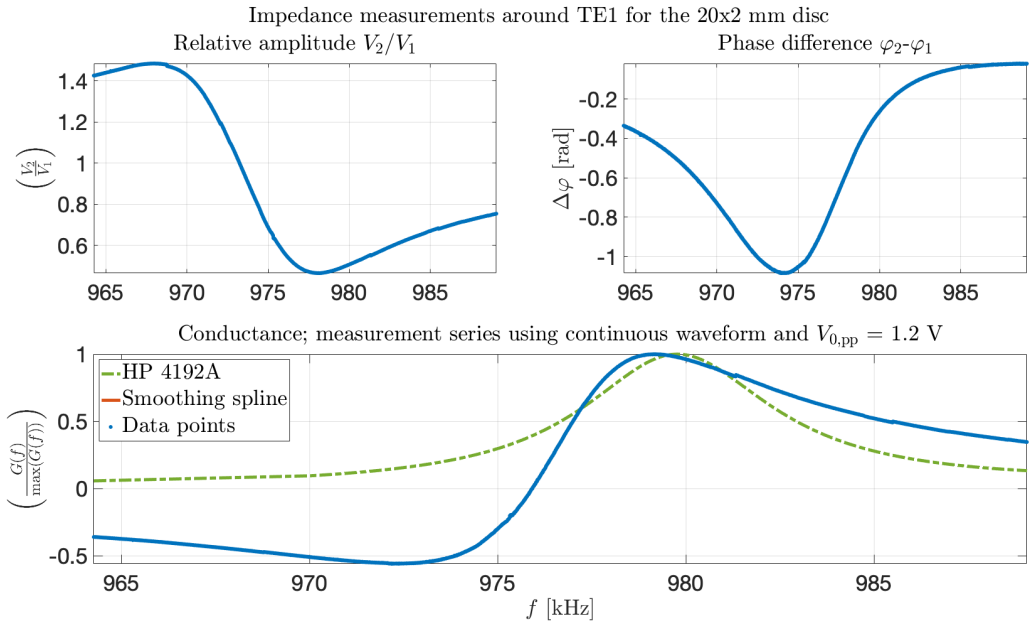

Figure B.24: Same as for Figure B.22, but here with $V_{0,\mathrm{pp}} = 1.2$ V.

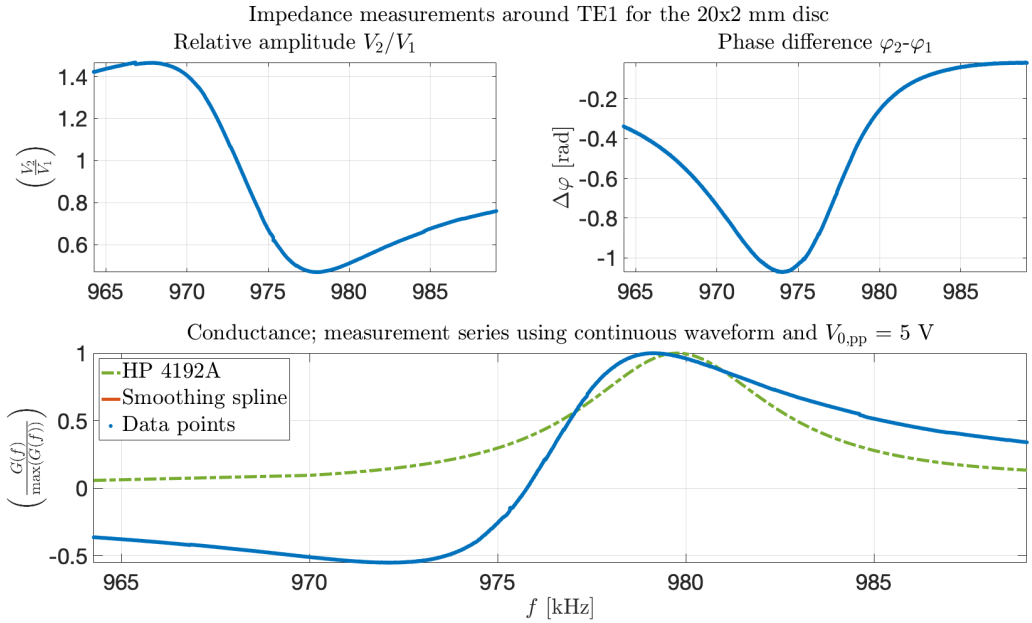

Figure B.25: Same as for Figure B.22, but here with $V_{0,\mathrm{pp}} = 5$ V.

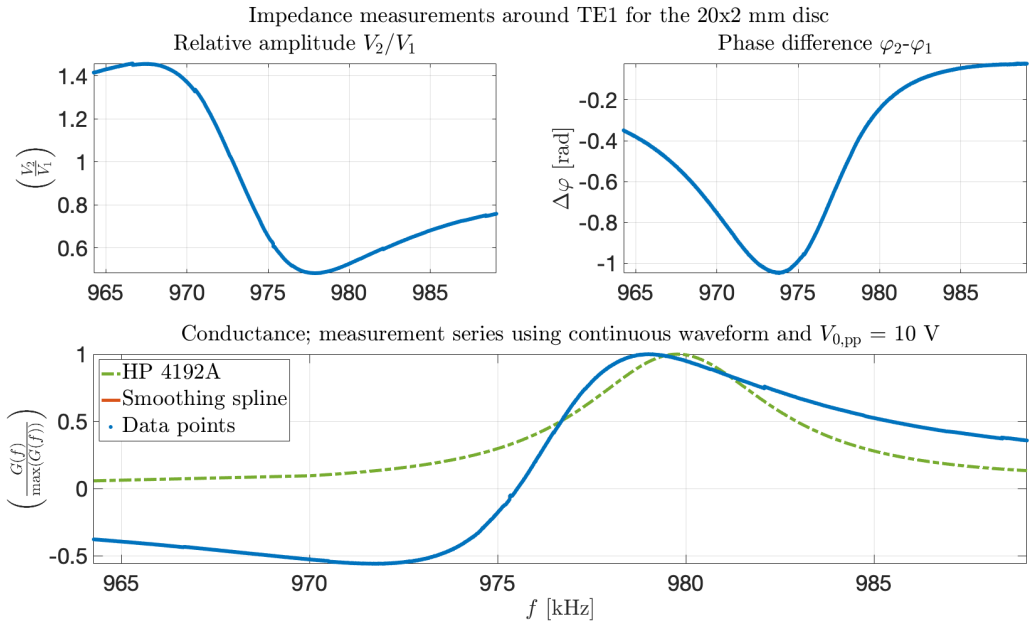

Figure B.26: Same as for Figure B.22, but here with $V_{0,\mathrm{pp}} = 10$ V.

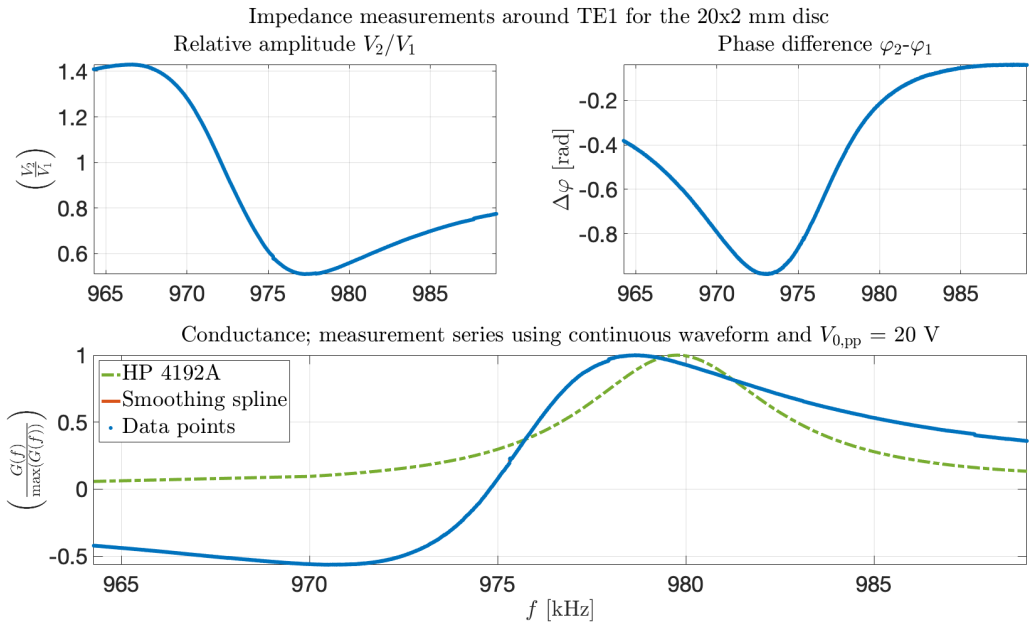

Figure B.27: Same as for Figure B.22, but here with $V_{0,\mathrm{pp}} = 20$ V.

B.4.4 20x2 disc measured with burst excitation for R1

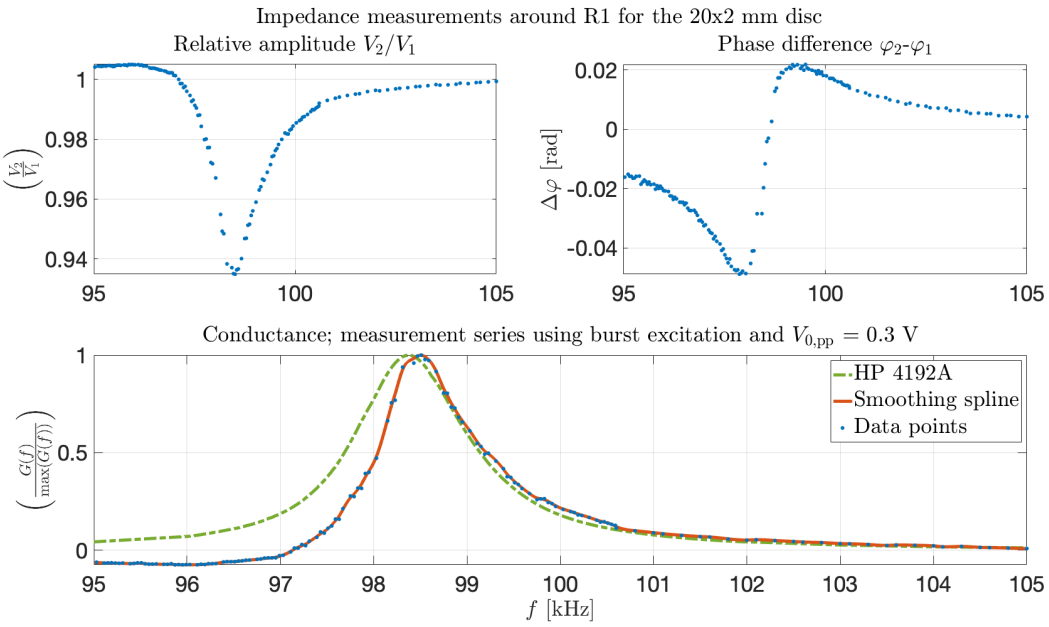

Figure B.28: Measured voltages V_1 and V_2 in the I-V circuit used to compute the impedance through Eq. (3.7). The relative voltage amplitude V_2/V_1, and phase shift $\Delta\varphi$ between the two measured voltages, are here shown in the upper two plots, and the computed conductance (real part of the impedance) in the bottom plot. Here shown for the 20x2 disc, for a frequency corresponding to R1, and with a nominal applied voltage $V_{0,\mathrm{pp}}$ of 0.3 V. Burst excitation transmitted from the signal generator. Blue dots corresponds to measured values, and the red curve and dotted green curve in the bottom plot corresponds to a smoothing spline of the data points, and conductance measurement using the HP 4192A impedance analyser.

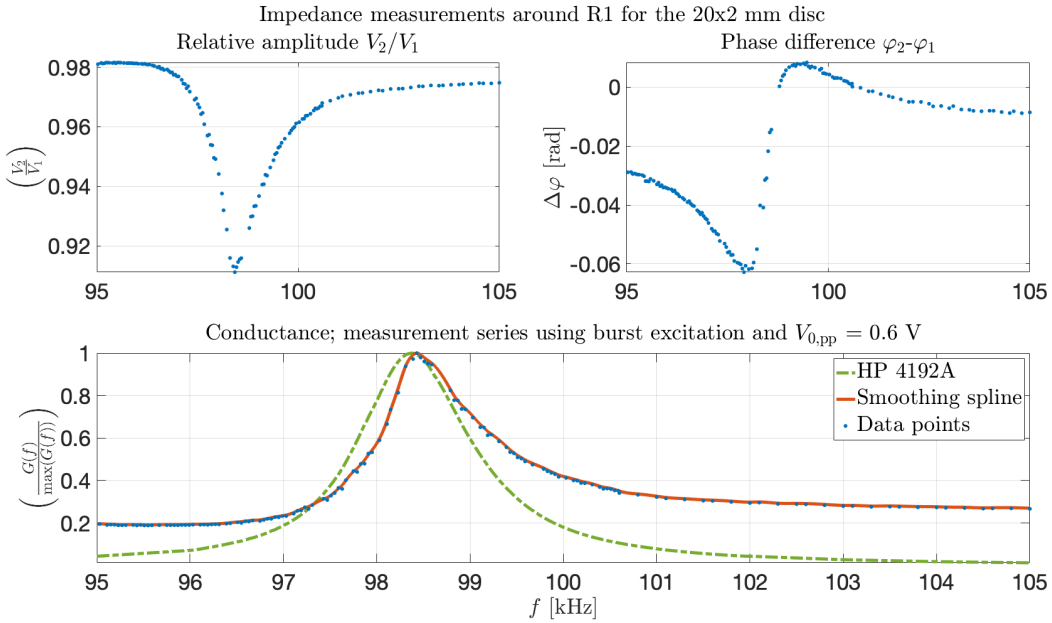

Figure B.29: Same as for Figure B.28, but here with $V_{0,\mathrm{pp}} = 0.6$ V.

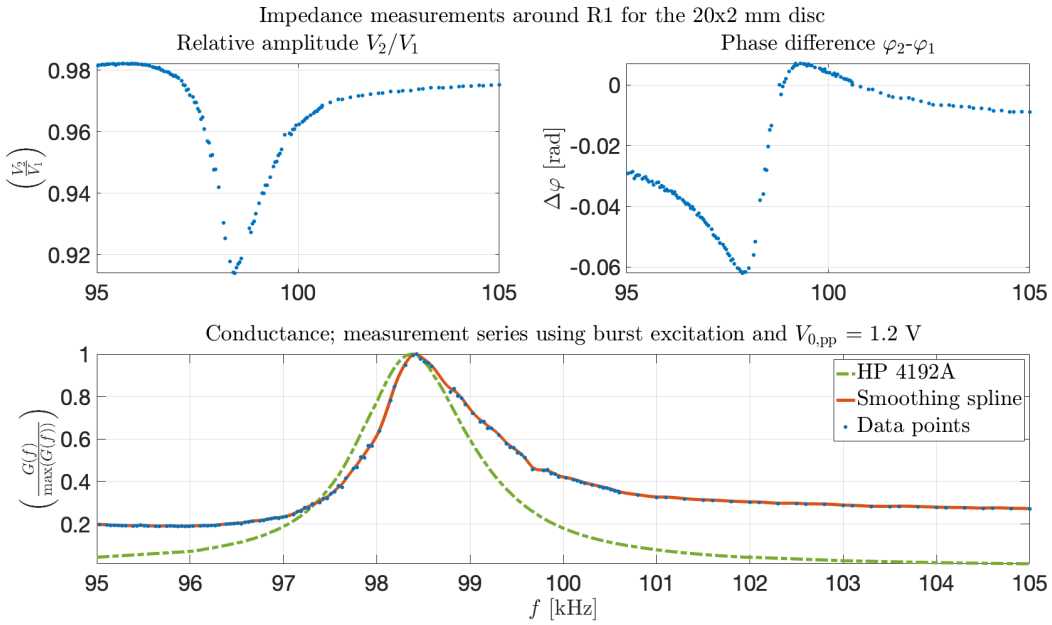

Figure B.30: Same as for Figure B.28, but here with $V_{0,\mathrm{pp}} = 1.2$ V.

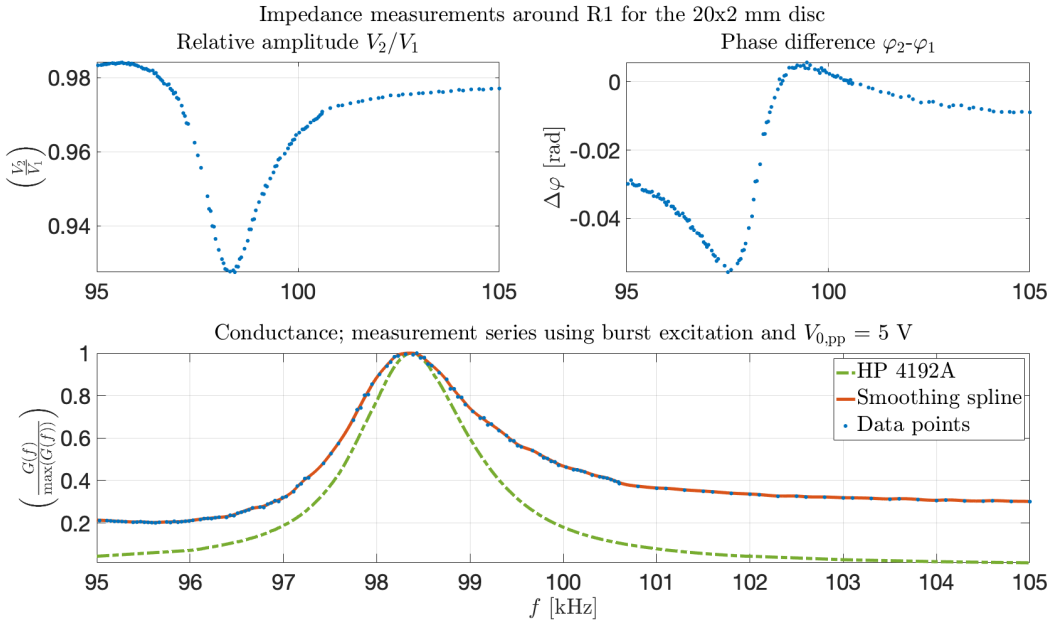

Figure B.31: Same as for Figure B.28, but here with $V_{0,\mathrm{pp}} = 5$ V.

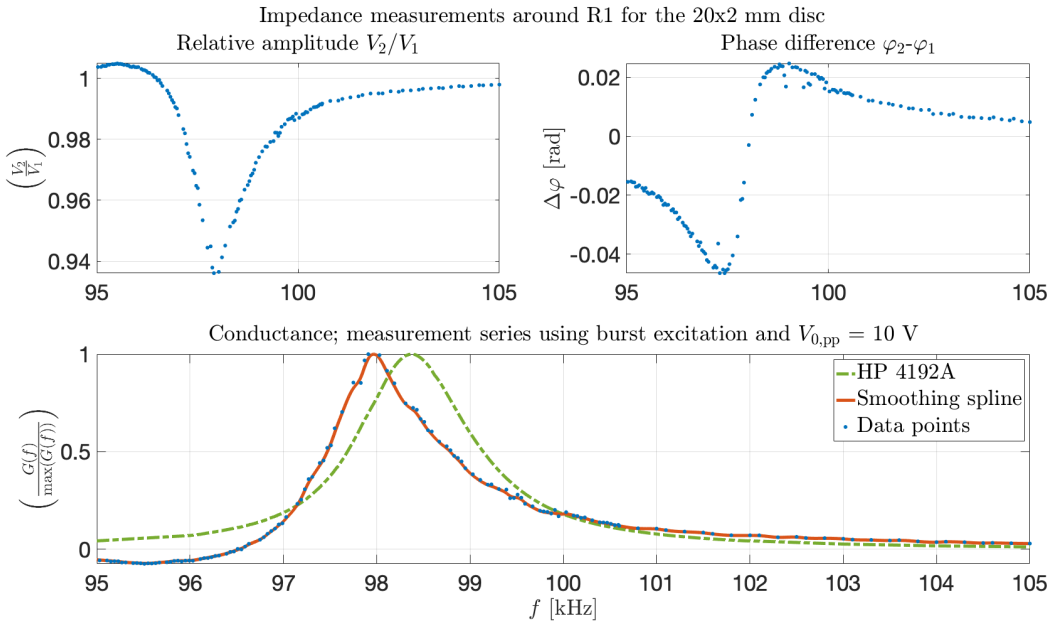

Figure B.32: Same as for Figure B.28, but here with $V_{0,\mathrm{pp}} = 10$ V.

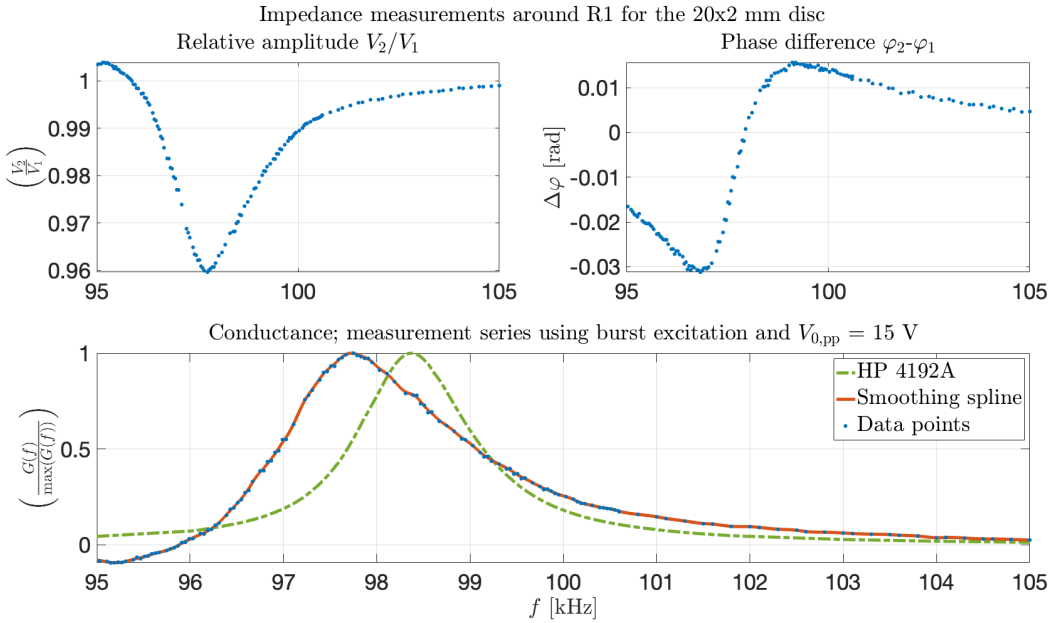

Figure B.33: Same as for Figure B.28, but here with $V_{0,\mathrm{pp}} = 15$ V.

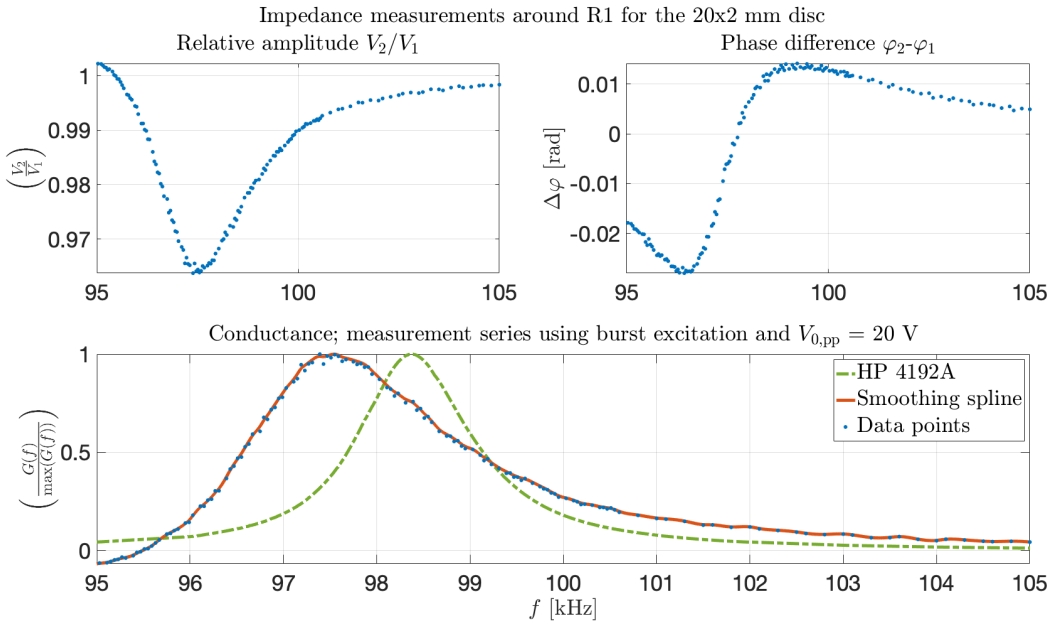

Figure B.34: Same as for Figure B.28, but here with $V_{0,\mathrm{pp}} = 20$ V.

B.4.5 20x2 disc measured with burst excitation for R2

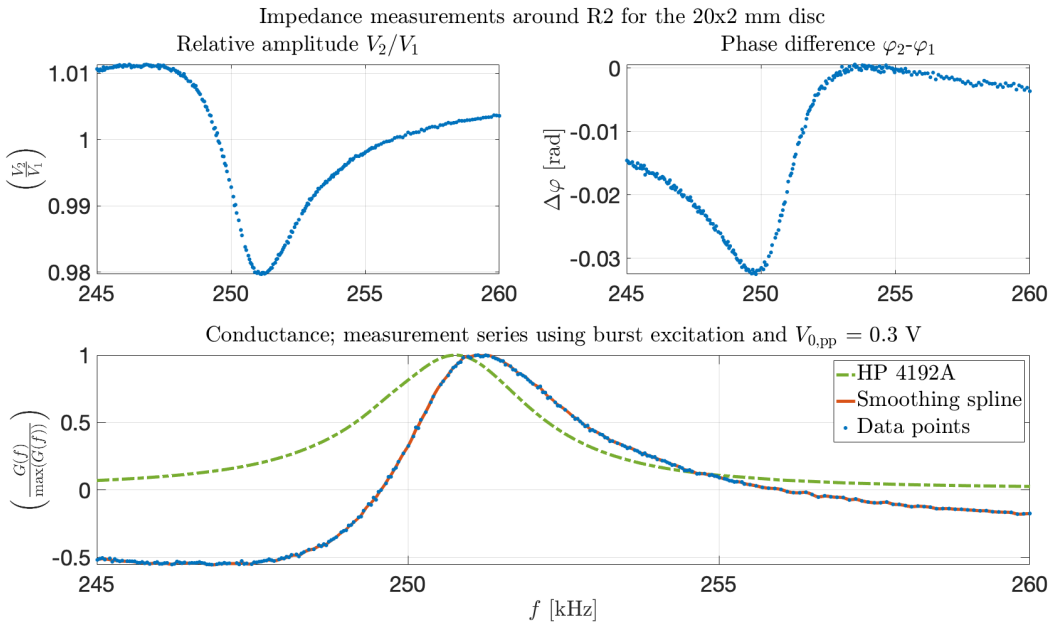

Figure B.35: Measured voltages V_1 and V_2 in the I-V circuit used to compute the impedance through Eq. (3.7). The relative voltage amplitude V_2/V_1, and phase shift $\Delta\varphi$ between the two measured voltages, are here shown in the upper two plots, and the computed conductance (real part of the impedance) in the bottom plot. Here shown for the 20x2 disc, for a frequency corresponding to R2, and with a nominal applied voltage $V_{0,\mathrm{pp}}$ of 0.3 V. Burst excitation transmitted from the signal generator. Blue dots corresponds to measured values, and the red curve and dotted green curve in the bottom plot corresponds to a smoothing spline of the data points, and conductance measurement using the HP 4192A impedance analyser.

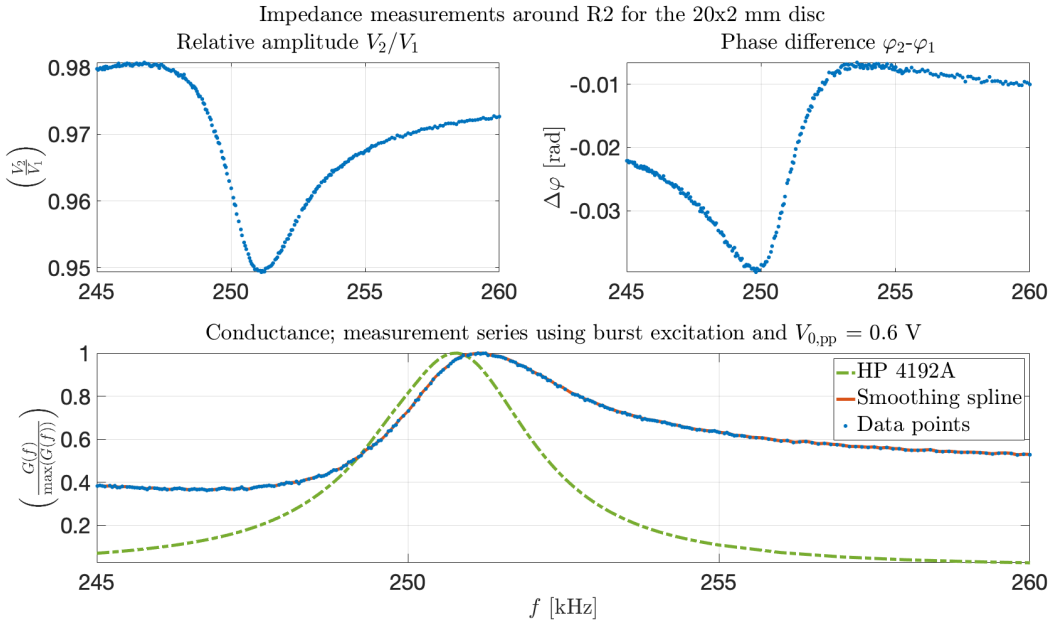

Figure B.36: Same as for Figure B.35, but here with $V_{0,\mathrm{pp}} = 0.6$ V.

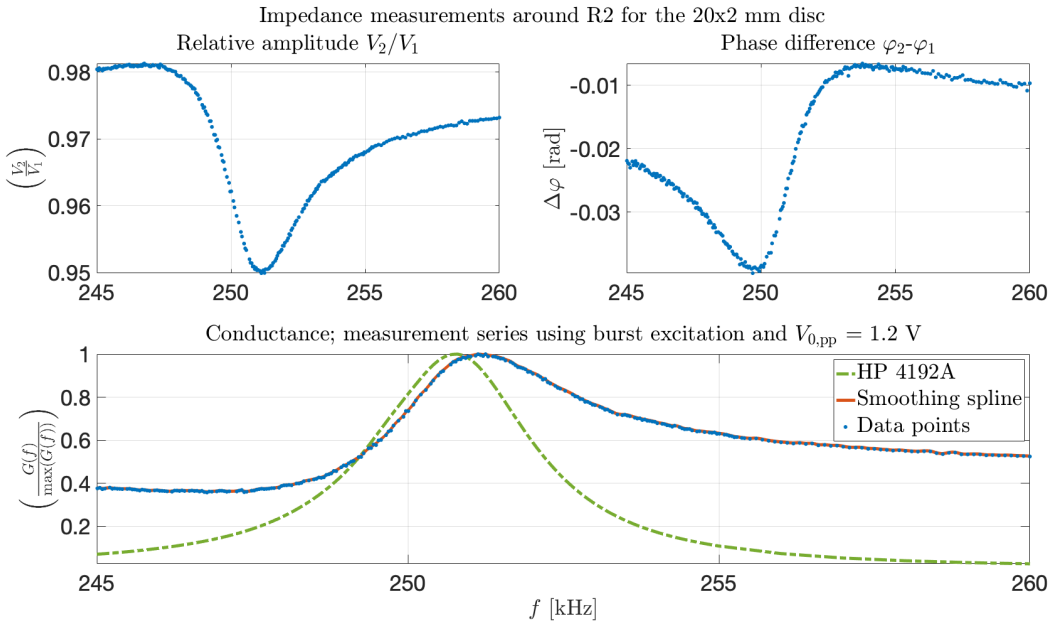

Figure B.37: Same as for Figure B.35, but here with $V_{0,\mathrm{pp}} = 1.2$ V.

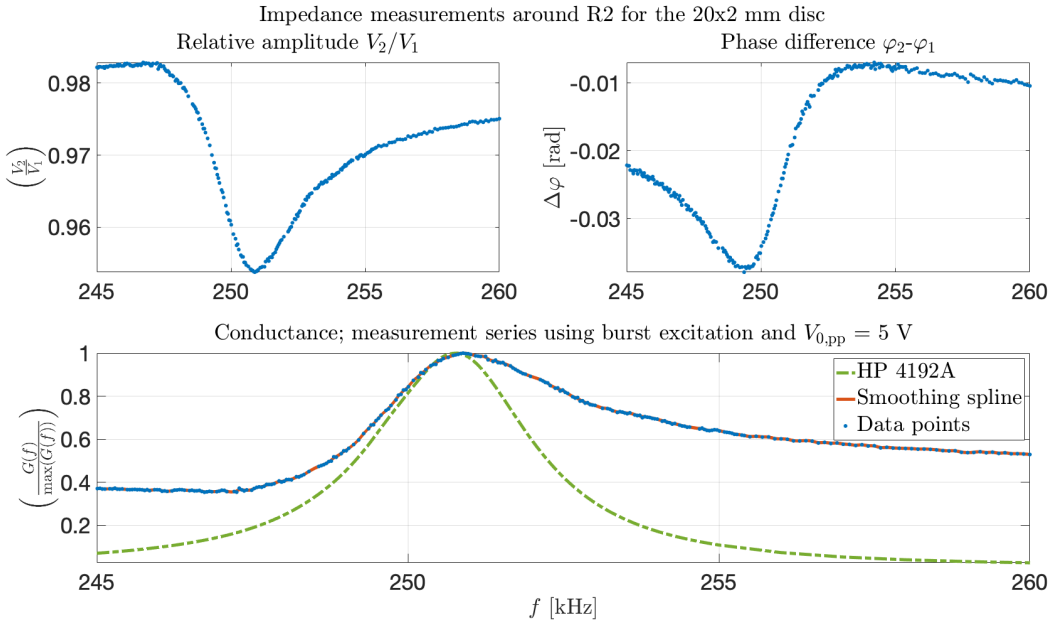

Figure B.38: Same as for Figure B.35, but here with $V_{0,\mathrm{pp}} = 5$ V.

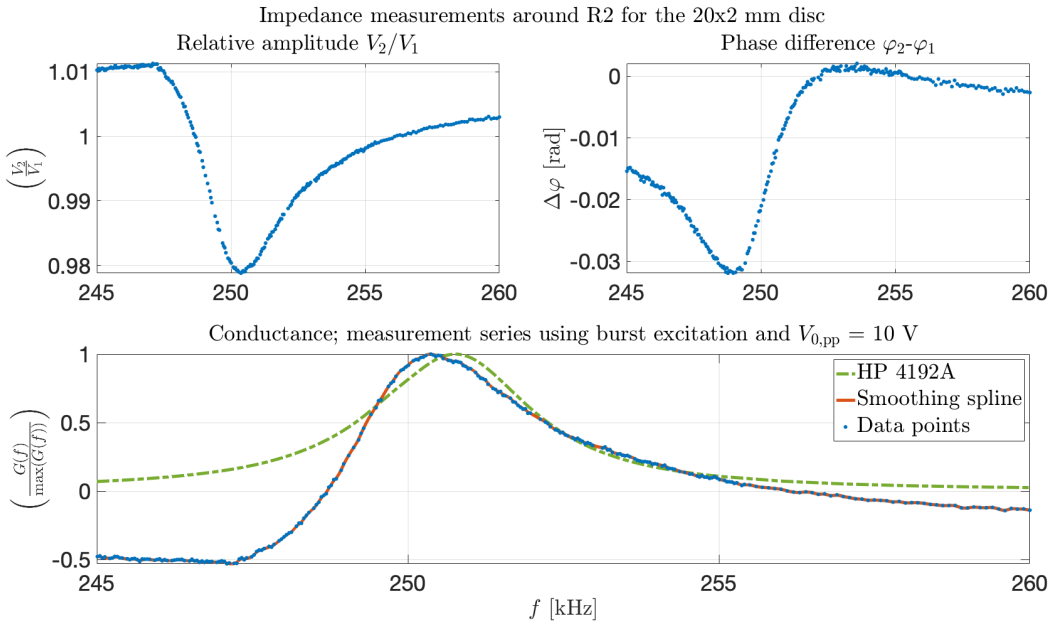

Figure B.39: Same as for Figure B.35, but here with $V_{0,\mathrm{pp}} = 10$ V.

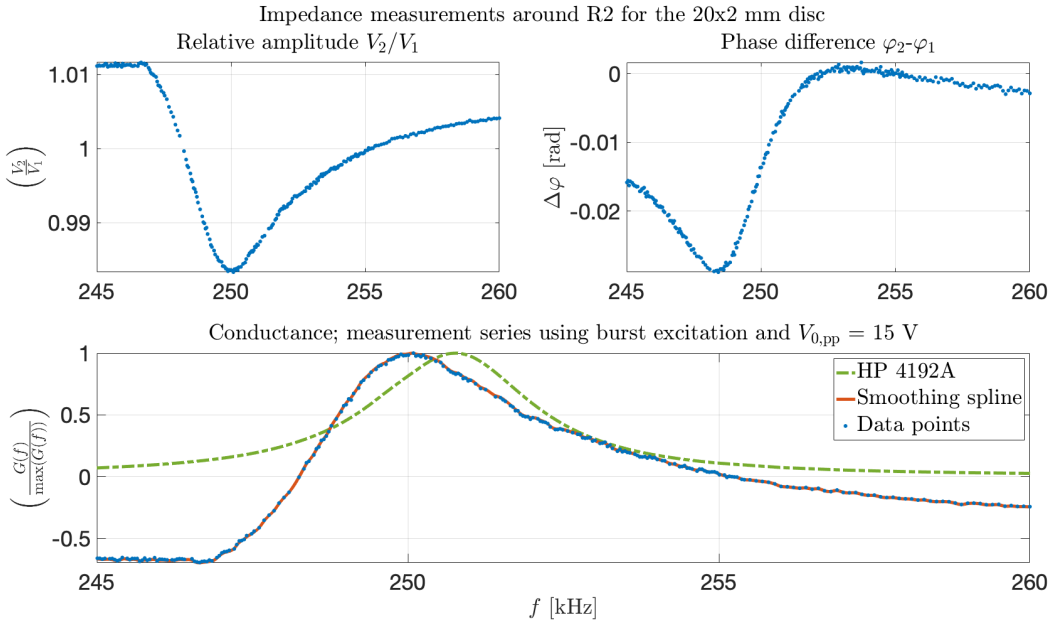

Figure B.40: Same as for Figure B.35, but here with $V_{0,\mathrm{pp}} = 15$ V.

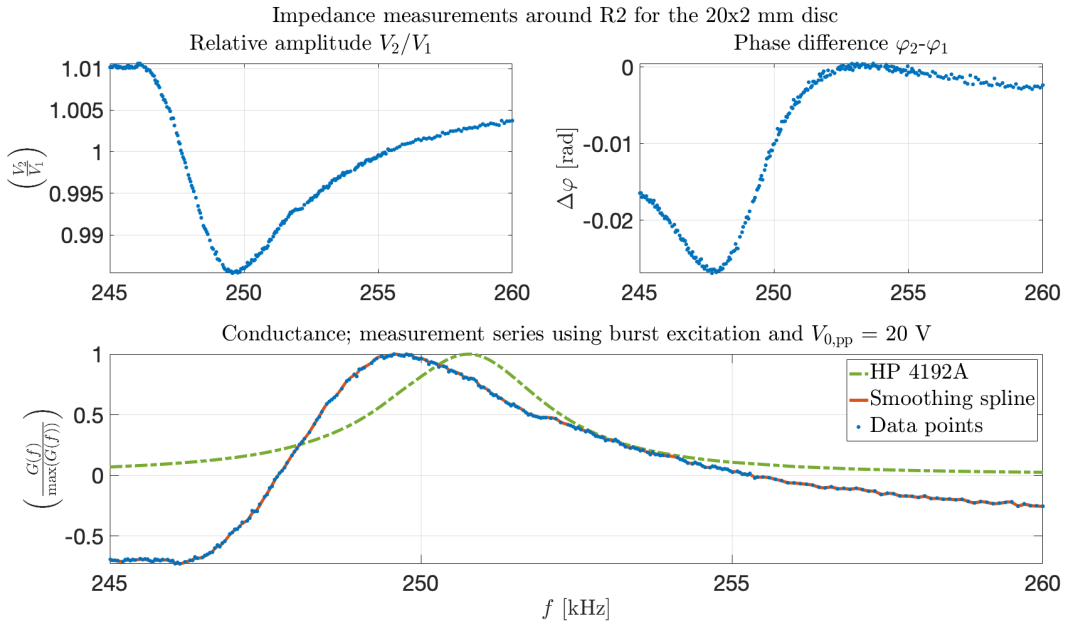

Figure B.41: Same as for Figure B.35, but here with $V_{0,\mathrm{pp}} = 20$ V.

B.4.6 13x2 disc measured with continuous waveform for R1

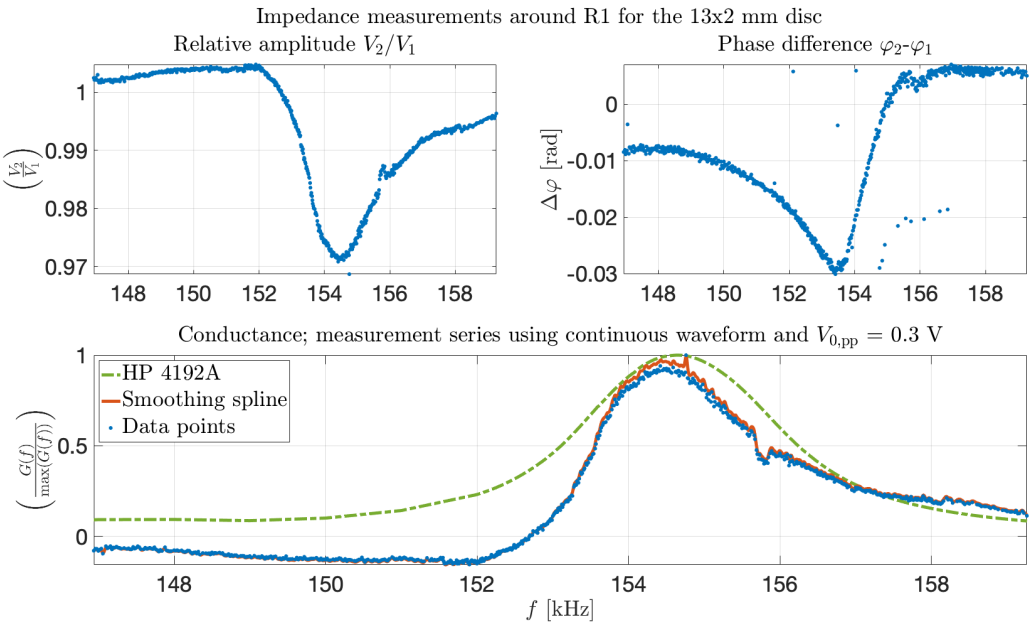

Figure B.42: Measured voltages V_1 and V_2 in the I-V circuit used to compute the impedance through Eq. (3.7). The relative voltage amplitude V_2/V_1, and phase shift $\Delta\varphi$ between the two measured voltages, are here shown in the upper two plots, and the computed conductance (real part of the impedance) in the bottom plot. Here shown for the 13x2 disc, for a frequency corresponding to R1, and with a nominal applied voltage $V_{0,\mathrm{pp}}$ of 0.3 V. Continuous waveform transmitted from the signal generator. Blue dots corresponds to measured values, and the red curve and dotted green curve in the bottom plot corresponds to a smoothing spline of the data points, and conductance measurement using the HP 4192A impedance analyser.

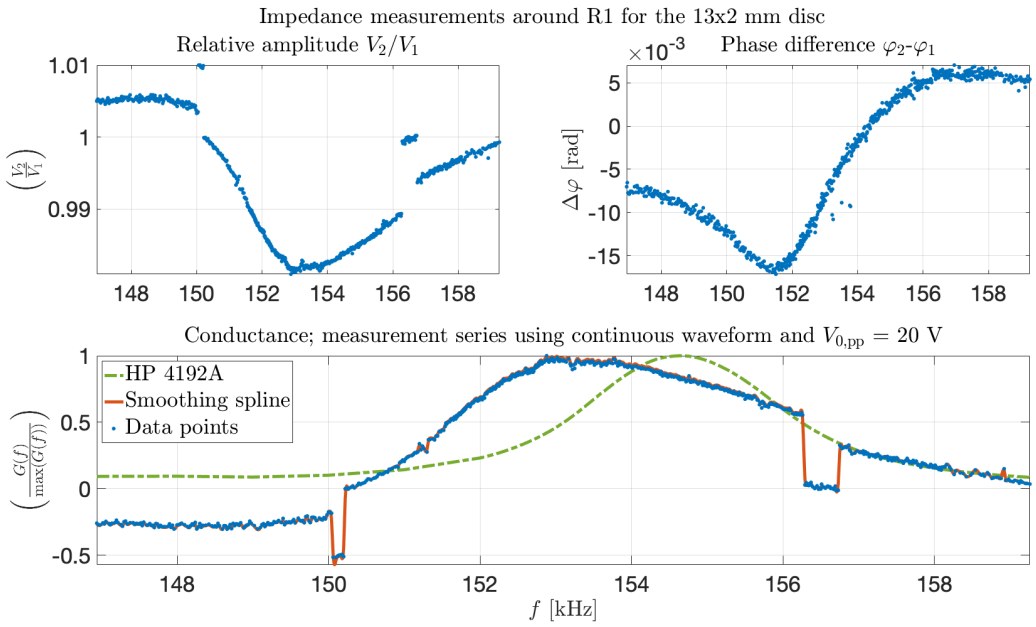

Figure B.43: Same as for Figure B.42, but here with $V_{0,\mathrm{pp}} = 20$ V.

B.4.7 13x2 disc measured with continuous waveform for R2

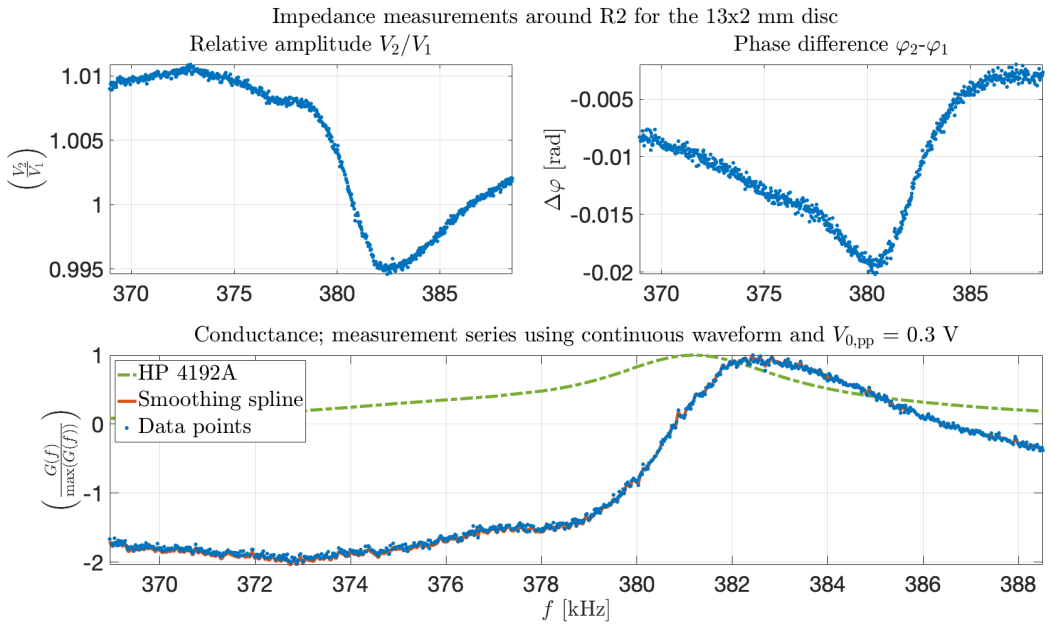

Figure B.44: Measured voltages V_1 and V_2 in the I-V circuit used to compute the impedance through Eq. (3.7). The relative voltage amplitude V_2/V_1, and phase shift $\Delta\varphi$ between the two measured voltages, are here shown in the upper two plots, and the computed conductance (real part of the impedance) in the bottom plot. Here shown for the 13x2 disc, for a frequency corresponding to R2, and with a nominal applied voltage $V_{0,\mathrm{pp}}$ of 0.3 V. Continuous waveform transmitted from the signal generator. Blue dots corresponds to measured values, and the red curve and dotted green curve in the bottom plot corresponds to a smoothing spline of the data points, and conductance measurement using the HP 4192A impedance analyser.

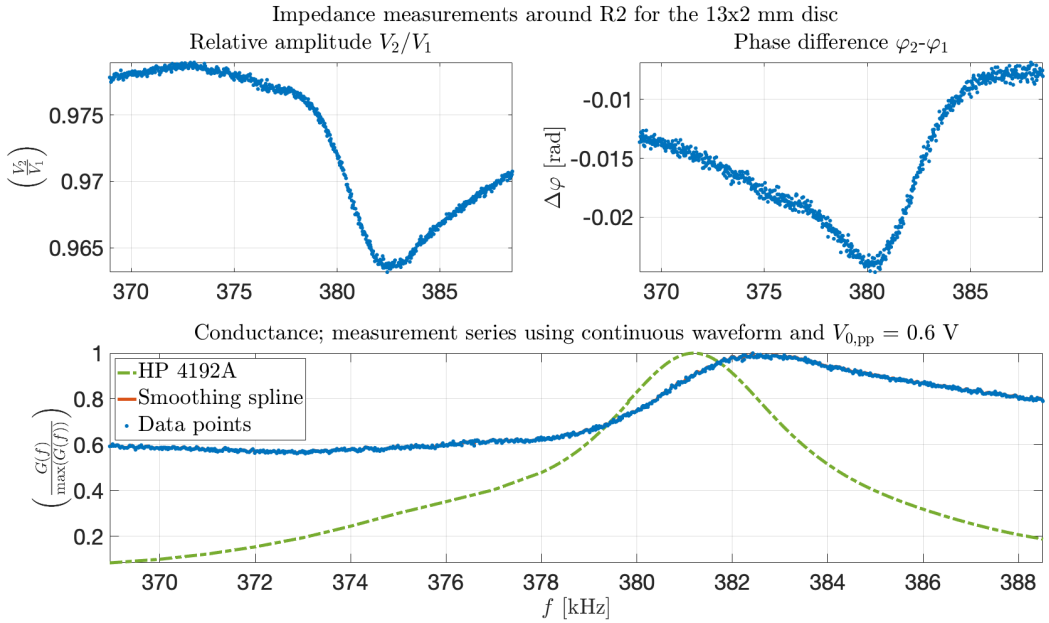

Figure B.45: Same as for Figure B.44, but here with $V_{0,\mathrm{pp}} = 0.6$ V.

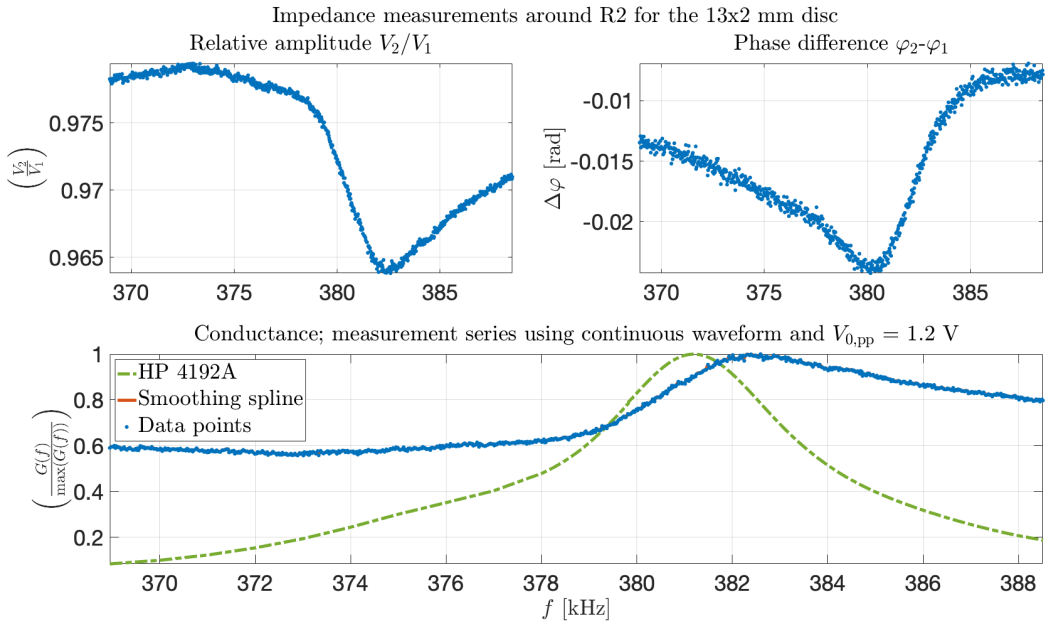

Figure B.46: Same as for Figure B.44, but here with $V_{0,\mathrm{pp}} = 1.2$ V.

B.4.8 13x2 disc measured with continuous waveform for TE1

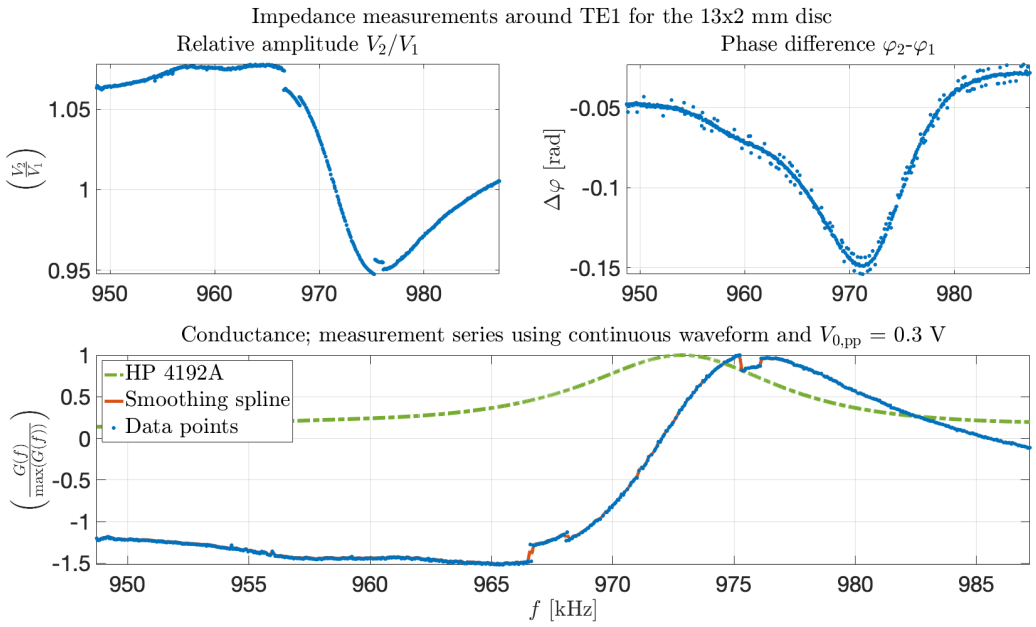

Figure B.47: Measured voltages V_1 and V_2 in the I-V circuit used to compute the impedance through Eq. (3.7). The relative voltage amplitude V_2/V_1, and phase shift $\Delta\varphi$ between the two measured voltages, are here shown in the upper two plots, and the computed conductance (real part of the impedance) in the bottom plot. Here shown for the 13x2 disc, for a frequency corresponding to R2, and with a nominal applied voltage $V_{0,\mathrm{pp}}$ of 0.3 V. Continuous waveform transmitted from the signal generator. Blue dots corresponds to measured values, and the red curve and dotted green curve in the bottom plot corresponds to a smoothing spline of the data points, and conductance measurement using the HP 4192A impedance analyser.

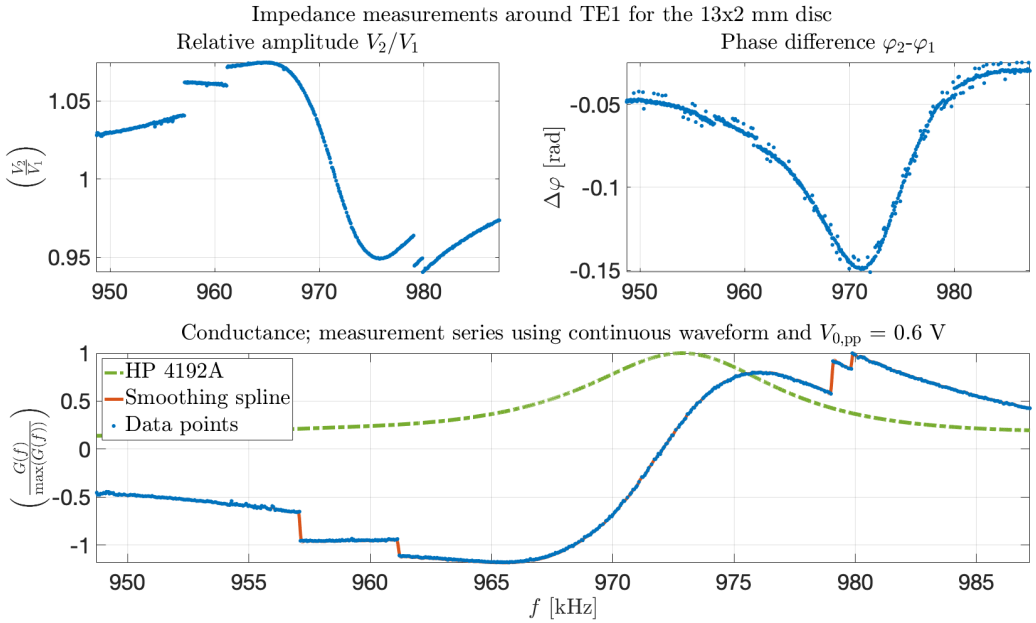

Figure B.48: Same as for Figure B.47, but here with $V_{0,\mathrm{pp}} = 0.6$ V.

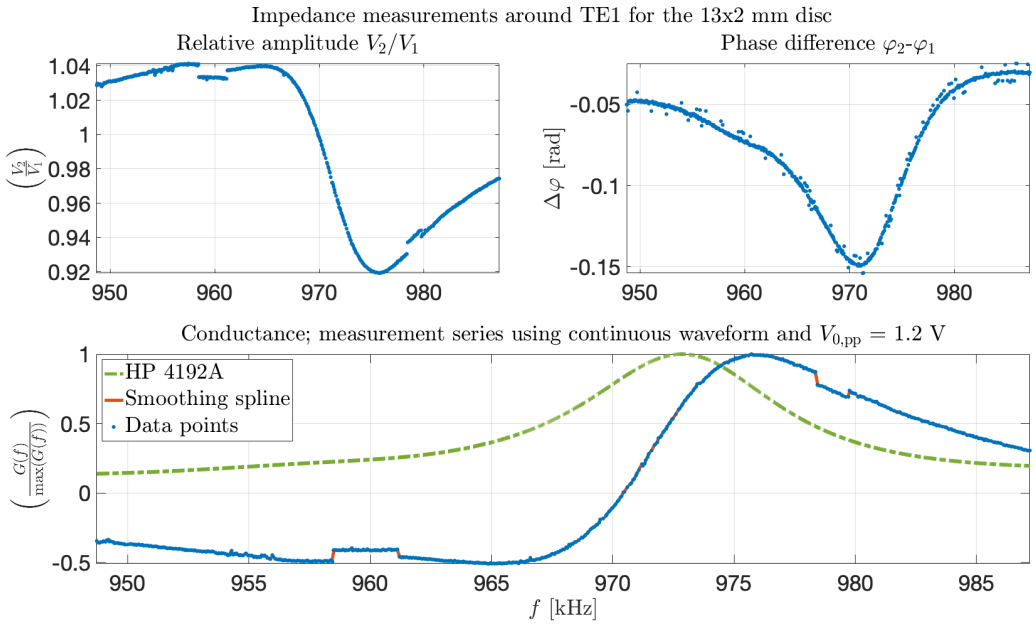

Figure B.49: Same as for Figure B.47, but here with $V_{0,\mathrm{pp}} = 1.2$ V.

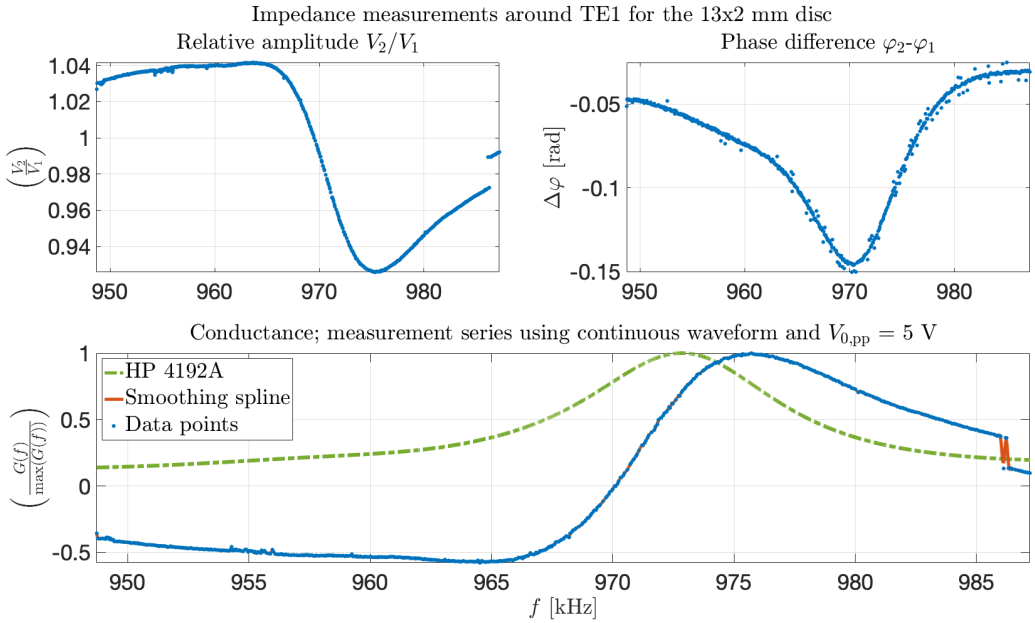

Figure B.50: Same as for Figure B.47, but here with $V_{0,\mathrm{pp}} = 5$ V.

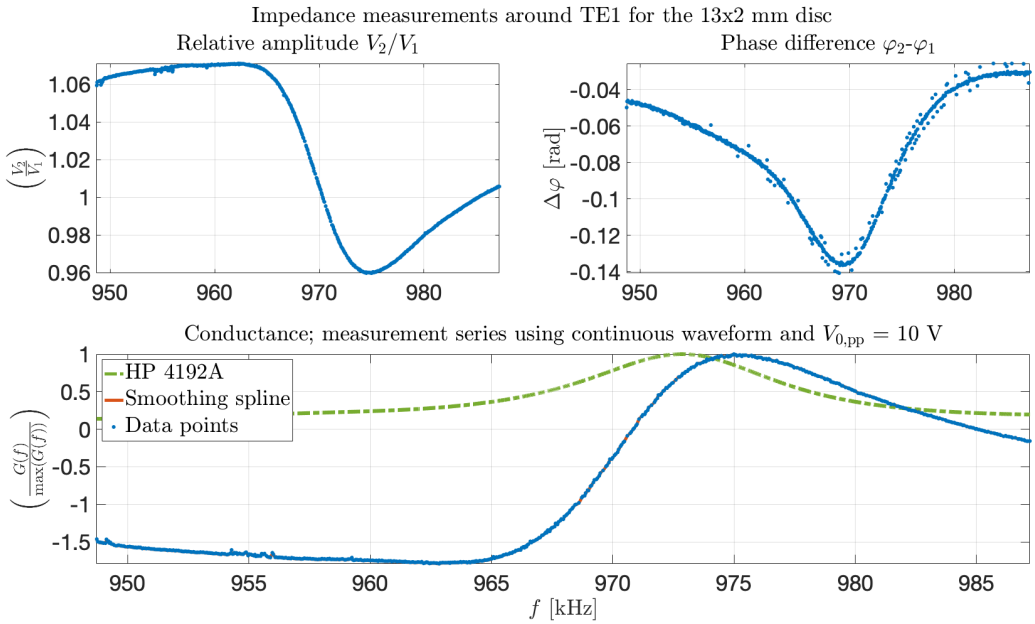

Figure B.51: Same as for Figure B.47, but here with $V_{0,\mathrm{pp}} = 10$ V.

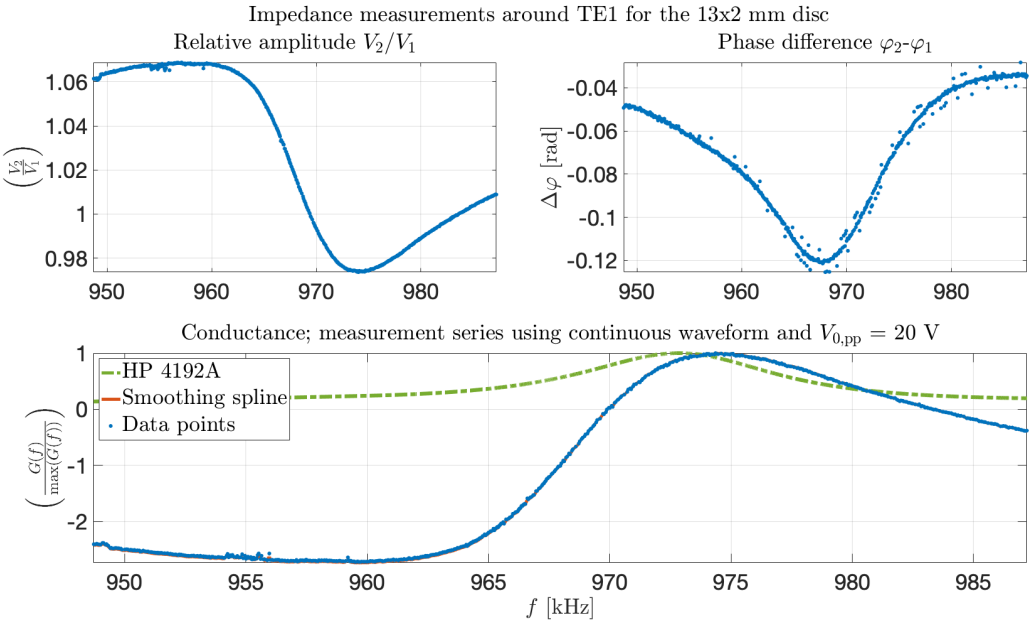

Figure B.52: Same as for Figure B.47, but here with $V_{0,\mathrm{pp}} = 20$ V.

B.4.9 13x2 disc measured with burst excitation for R1

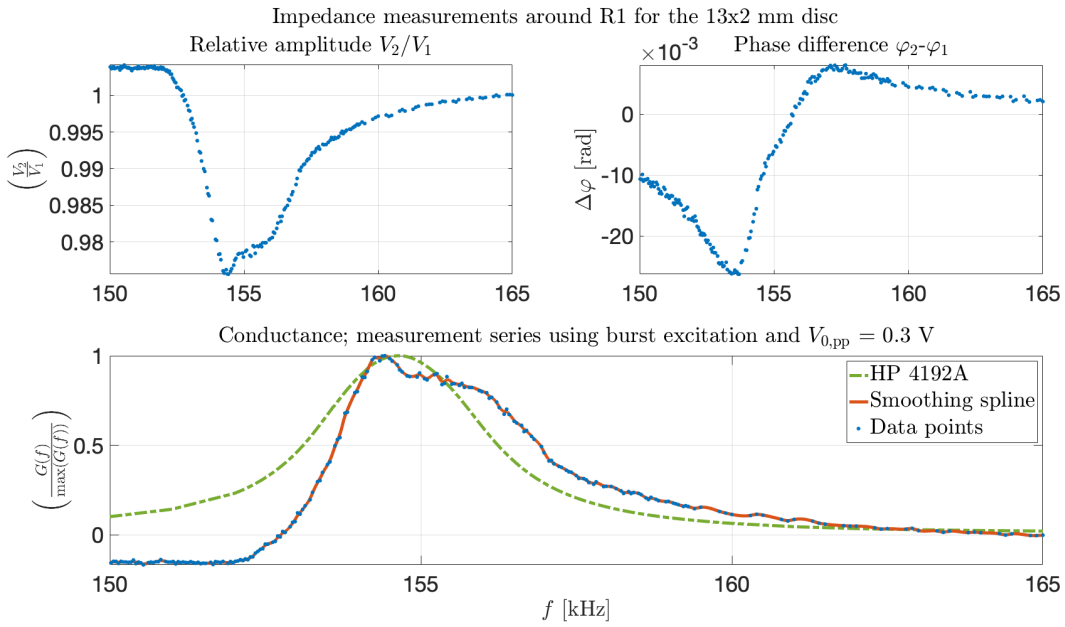

Figure B.53: Measured voltages V_1 and V_2 in the I-V circuit used to compute the impedance through Eq. (3.7). The relative voltage amplitude V_2/V_1, and phase shift $\Delta\varphi$ between the two measured voltages, are here shown in the upper two plots, and the computed conductance (real part of the impedance) in the bottom plot. Here shown for the 13x2 disc, for a frequency corresponding to R1, and with a nominal applied voltage $V_{0,\mathrm{pp}}$ of 0.3 V. Burst excitation transmitted from the signal generator. Blue dots corresponds to measured values, and the red curve and dotted green curve in the bottom plot corresponds to a smoothing spline of the data points, and conductance measurement using the HP 4192A impedance analyser.

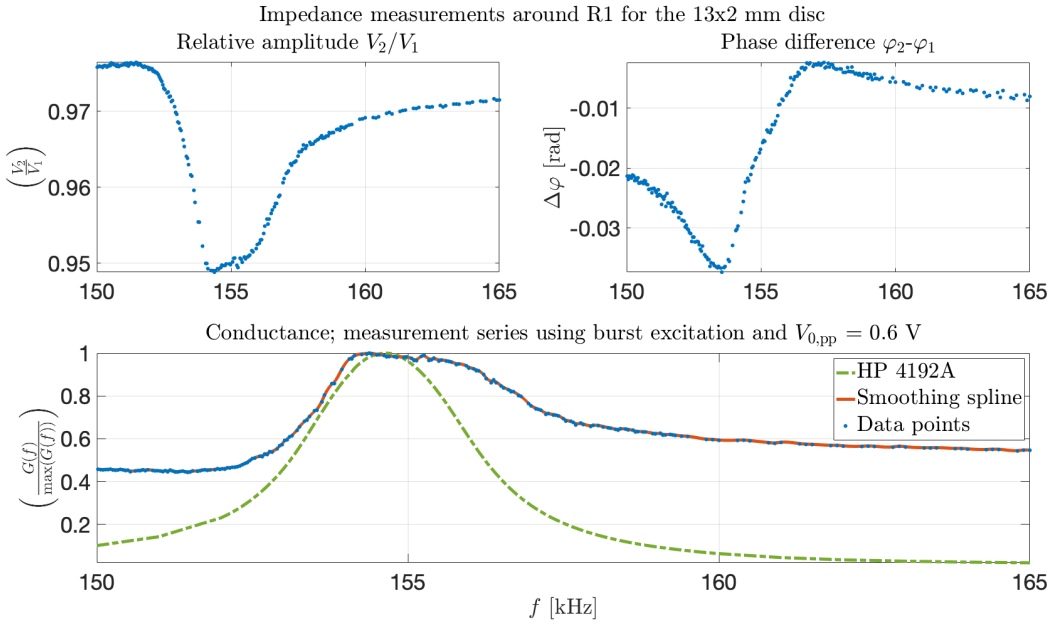

Figure B.54: Same as for Figure B.53, but here with $V_{0,\mathrm{pp}} = 0.6$ V.

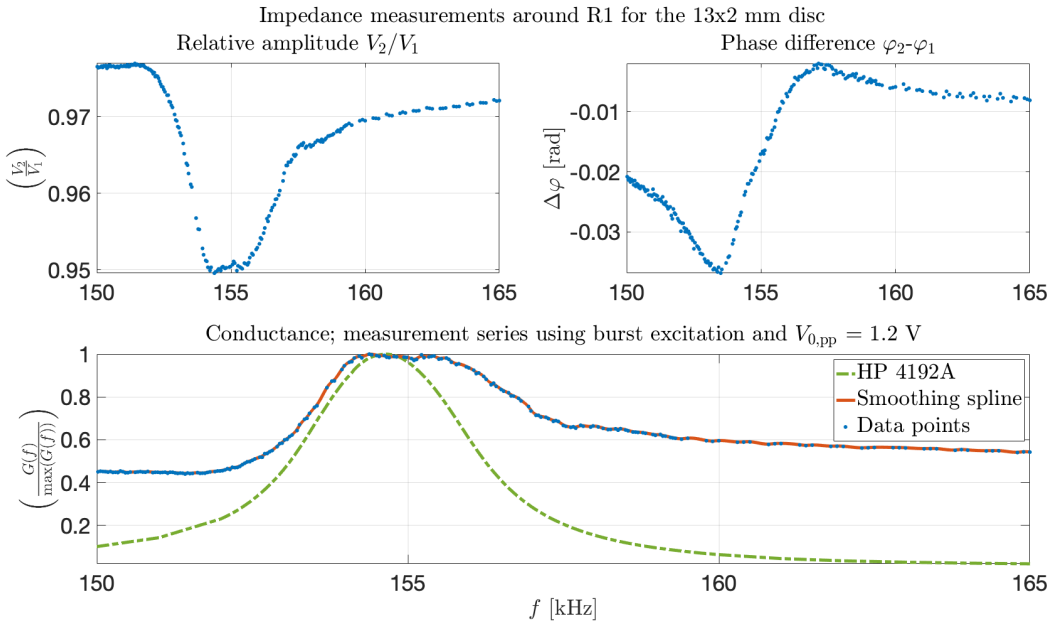

Figure B.55: Same as for Figure B.53, but here with $V_{0,\mathrm{pp}} = 1.2$ V.

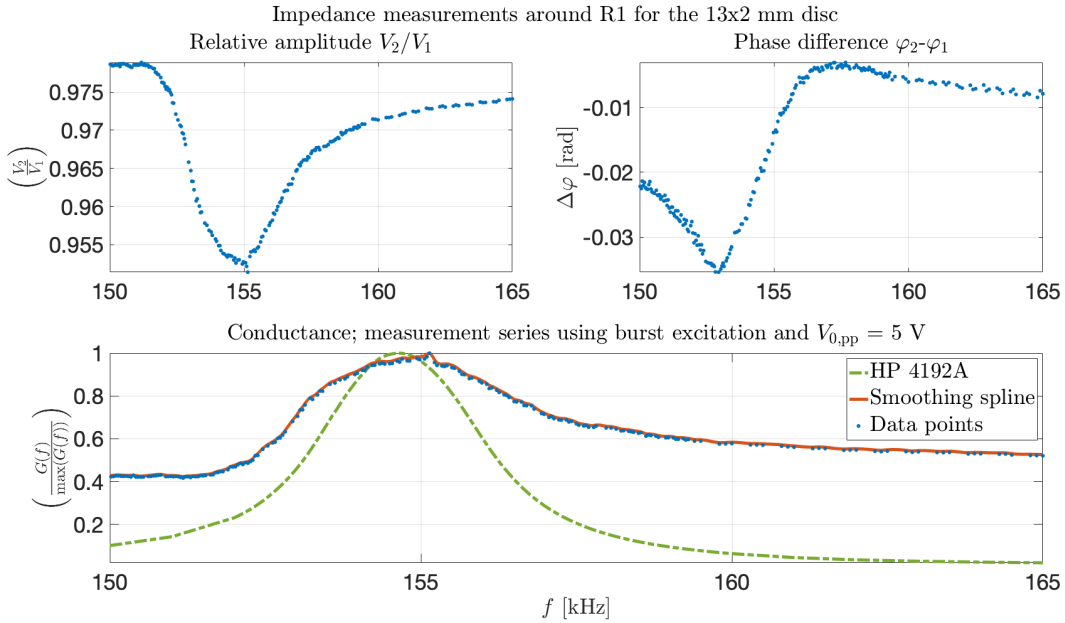

Figure B.56: Same as for Figure B.53, but here with $V_{0,\mathrm{pp}} = 5$ V.

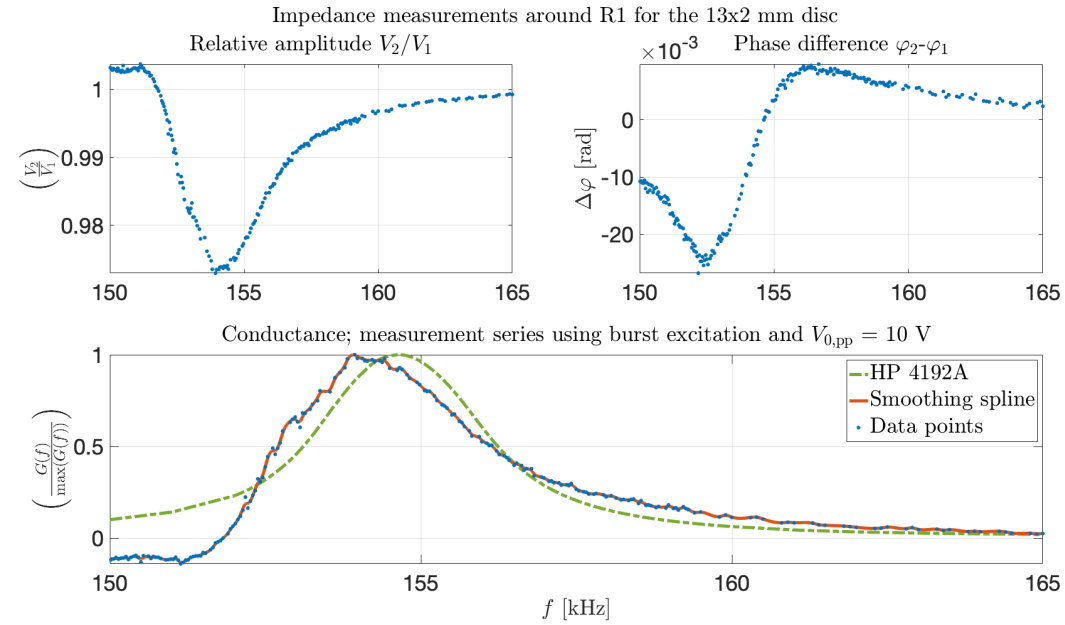

Figure B.57: Same as for Figure B.53, but here with $V_{0,\mathrm{pp}} = 10$ V.

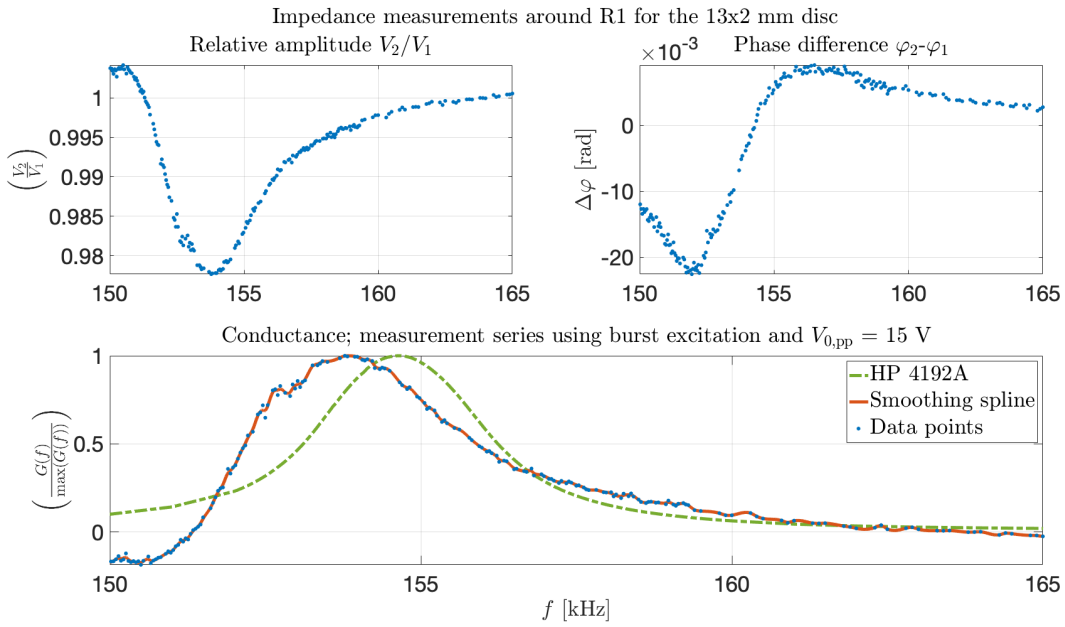

Figure B.58: Same as for Figure B.53, but here with $V_{0,\mathrm{pp}} = 15$ V.

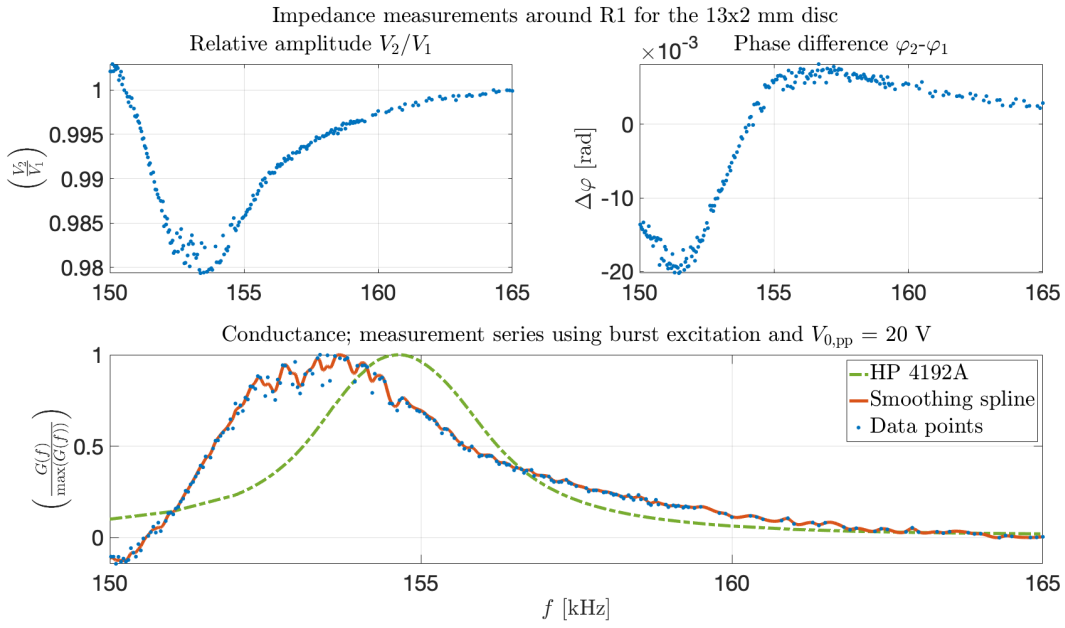

Figure B.59: Same as for Figure B.53, but here with $V_{0,\mathrm{pp}} = 20$ V.

B.4.10 13x2 disc measured with burst excitation for R2

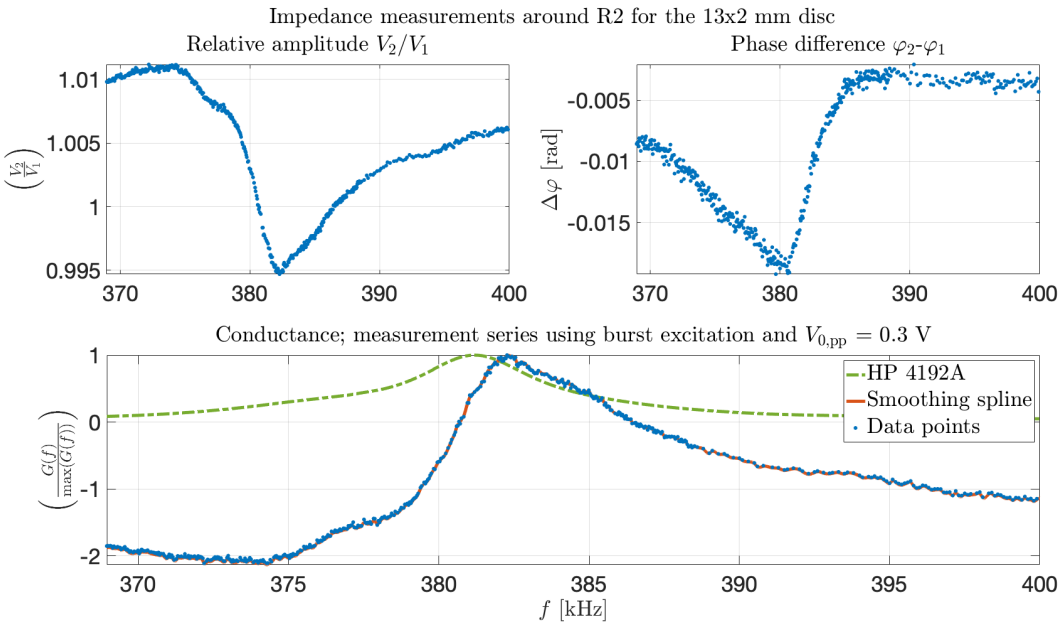

Figure B.60: Measured voltages V_1 and V_2 in the I-V circuit used to compute the impedance through Eq. (3.7). The relative voltage amplitude V_2/V_1, and phase shift $\Delta\varphi$ between the two measured voltages, are here shown in the upper two plots, and the computed conductance (real part of the impedance) in the bottom plot. Here shown for the 13x2 disc, for a frequency corresponding to R2, and with a nominal applied voltage $V_{0,\mathrm{pp}}$ of 0.3 V. Burst excitation transmitted from the signal generator. Blue dots corresponds to measured values, and the red curve and dotted green curve in the bottom plot corresponds to a smoothing spline of the data points, and conductance measurement using the HP 4192A impedance analyser.

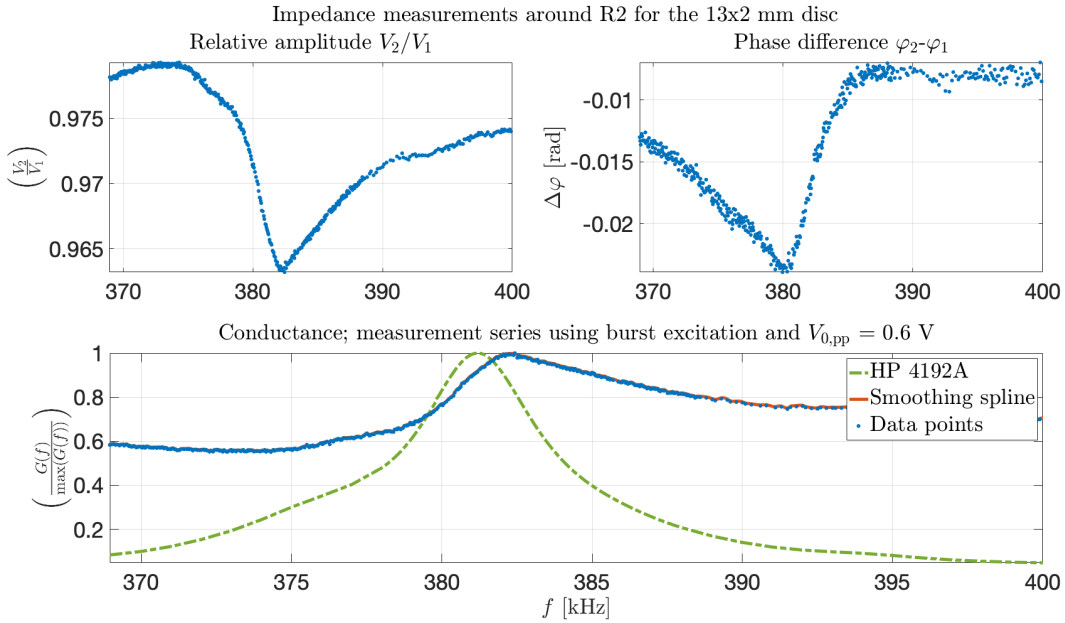

Figure B.61: Same as for Figure B.60, but here with $V_{0,\mathrm{pp}} = 0.6$ V.

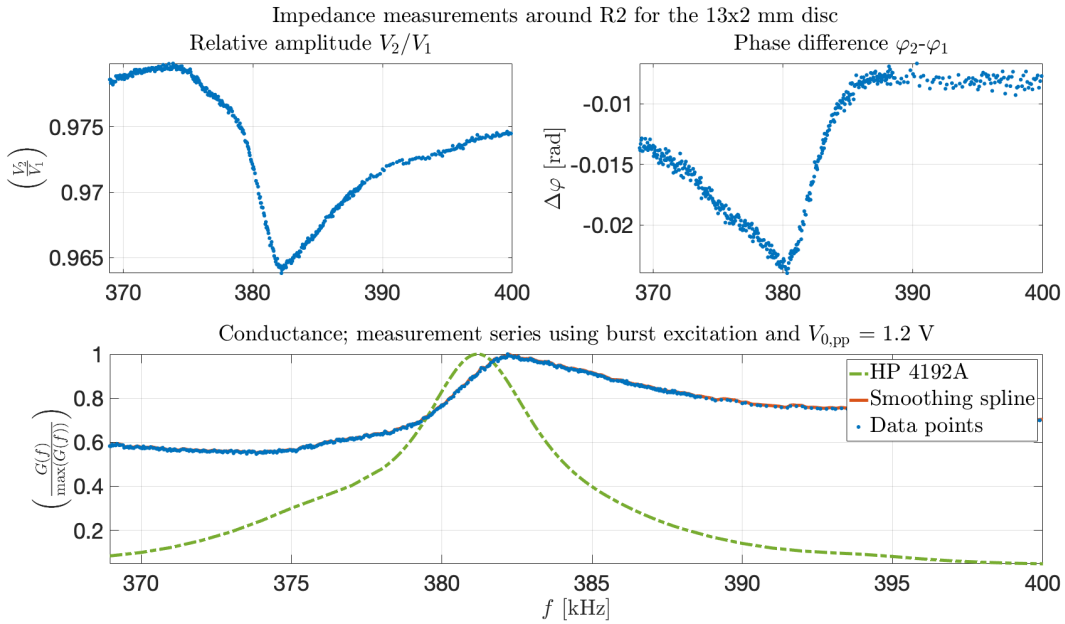

Figure B.62: Same as for Figure B.60, but here with $V_{0,\mathrm{pp}} = 1.2$ V.

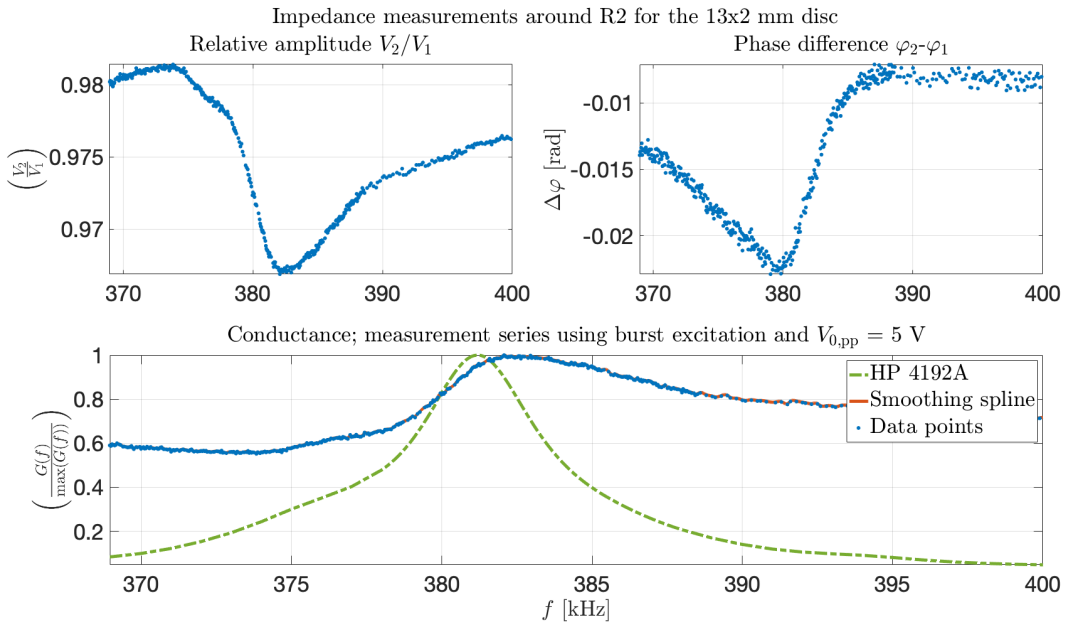

Figure B.63: Same as for Figure B.60, but here with $V_{0,\mathrm{pp}} = 5$ V.

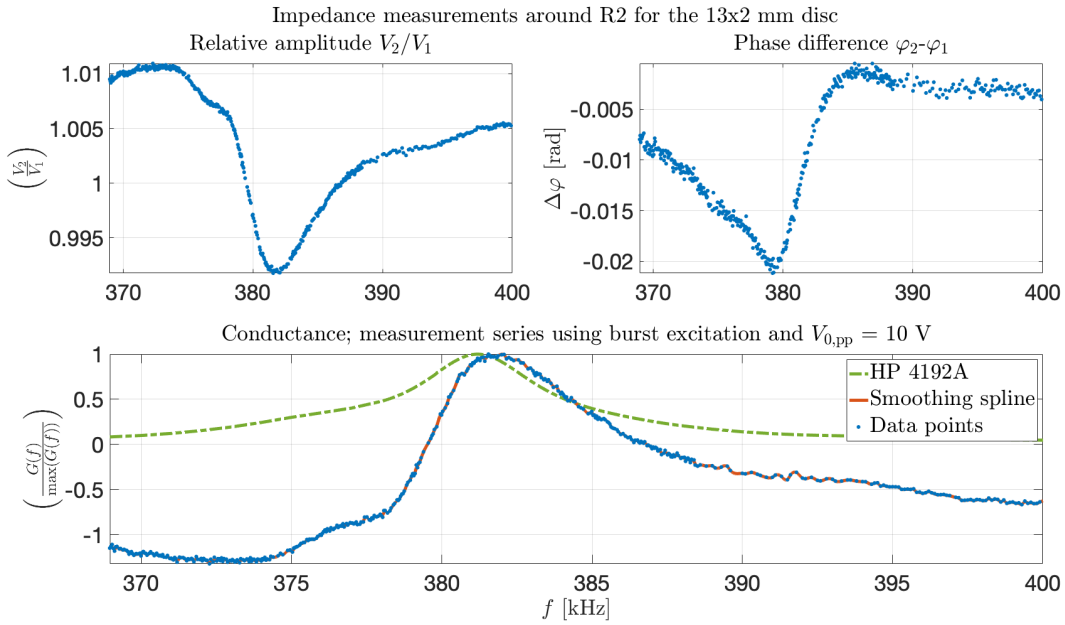

Figure B.64: Same as for Figure B.60, but here with $V_{0,\mathrm{pp}} = 10$ V.

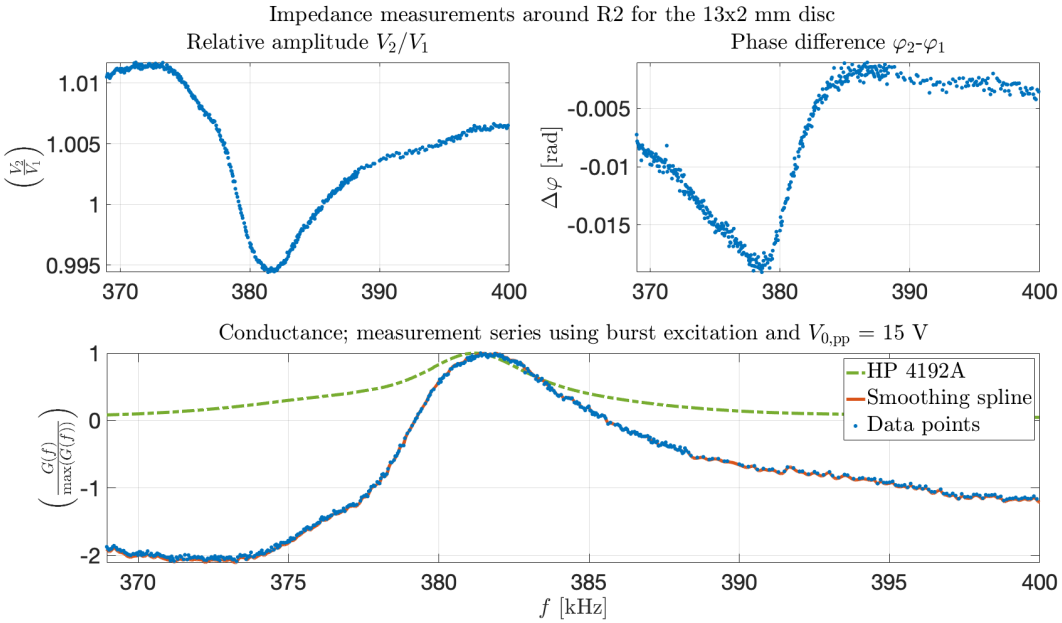

Figure B.65: Same as for Figure B.60, but here with $V_{0,\mathrm{pp}} = 15$ V.

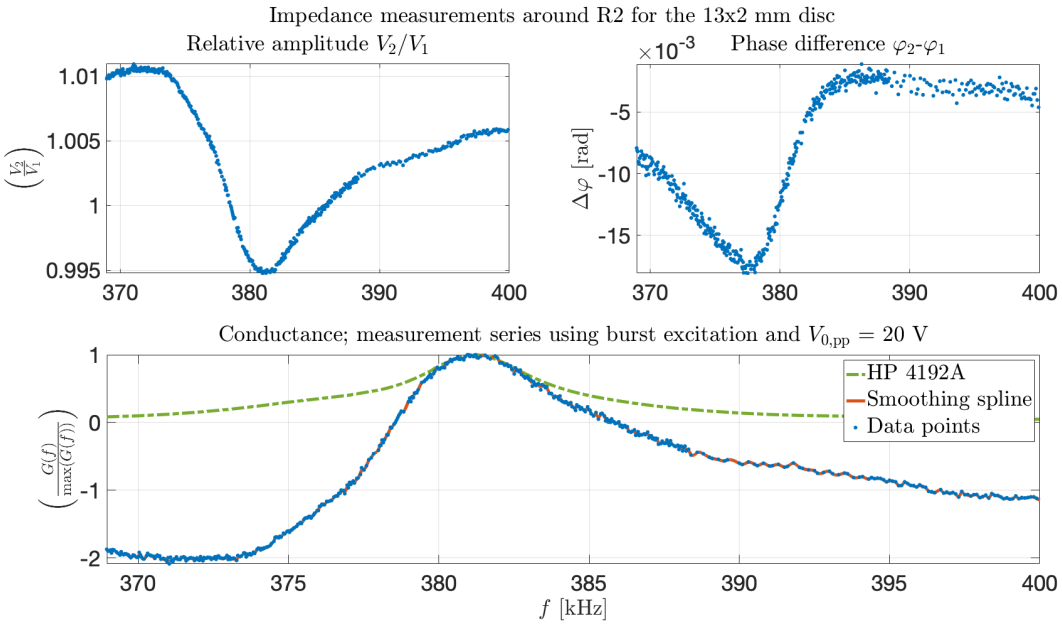

Figure B.66: Same as for Figure B.60, but here with $V_{0,\mathrm{pp}} = 20$ V.

B.5 Calculated current in the circuit

B.5.1 20x2 disc continuous waveform

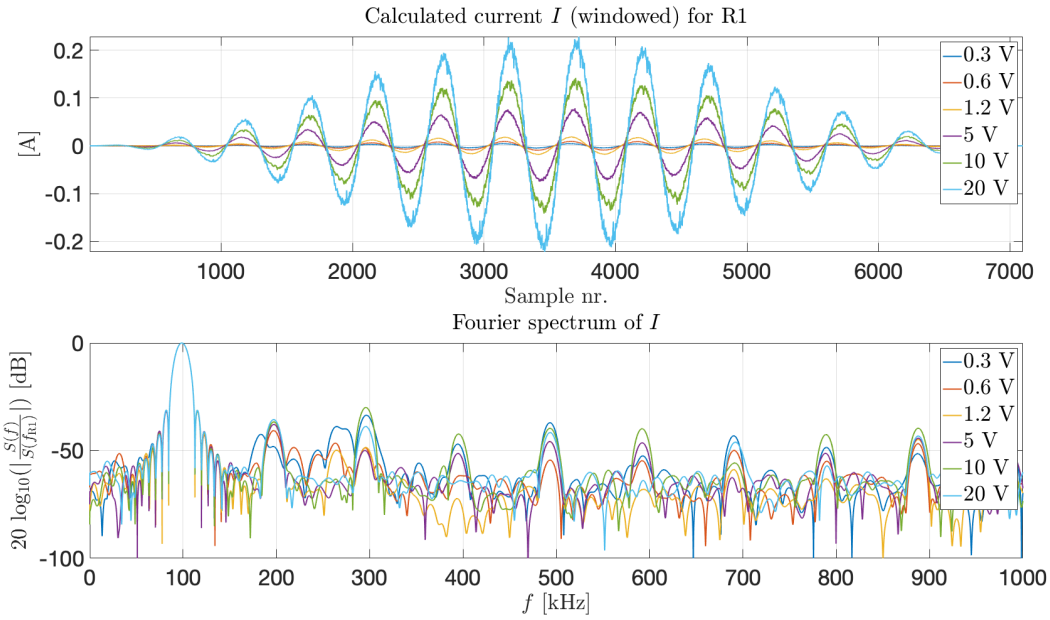

Figure B.67: Calculated current through the 20x2 piezodisc from the voltage drop over the known resistor R (upper plot), and corresponding frequency spectrum (bottom plot), for R1.

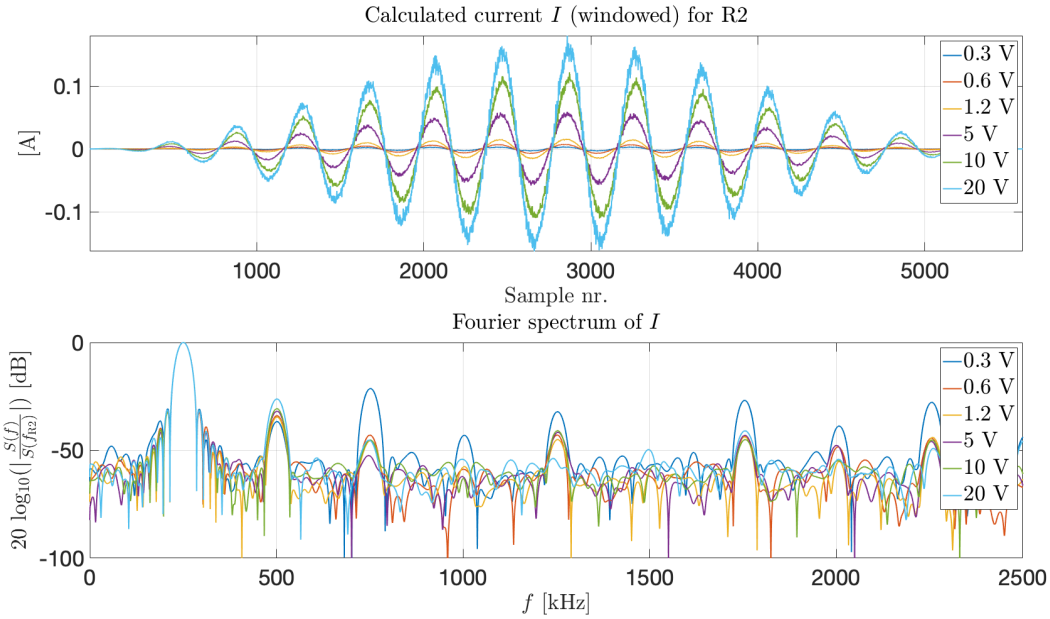

Figure B.68: Same as for Figure B.67, but for R2.

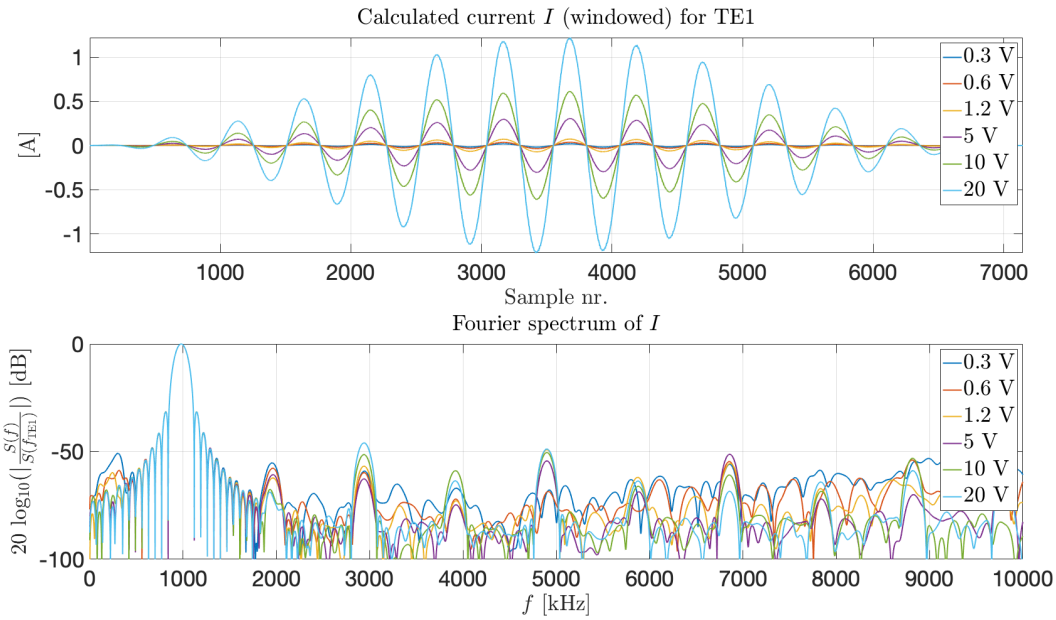

Figure B.69: Same as for Figures B.67 and B.68, but for TE1.

B.5.2 20x2 disc bursts excitation

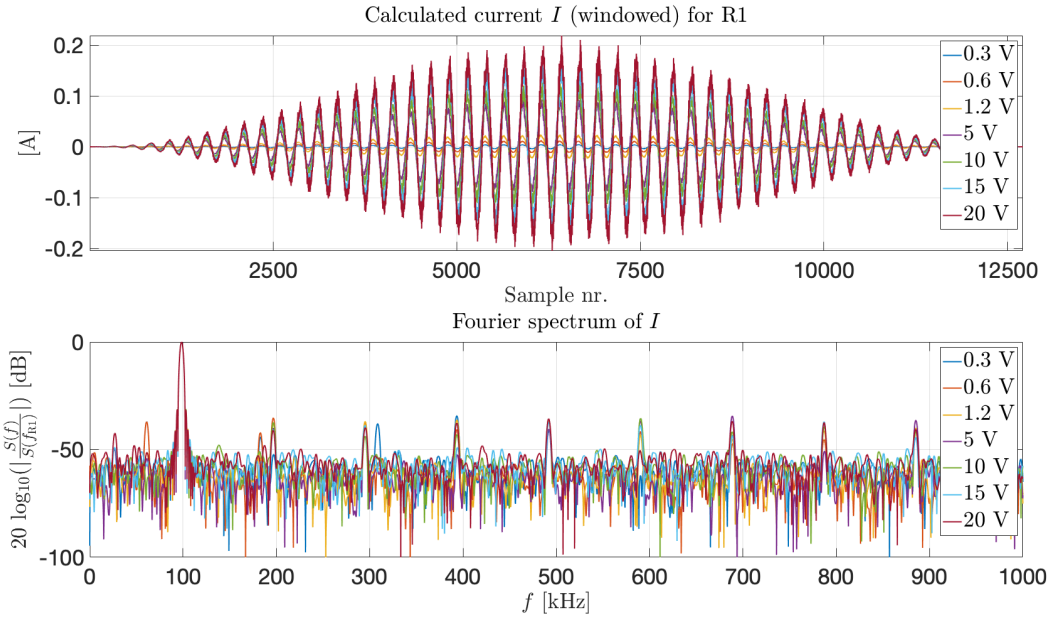

Figure B.70: Calculated current through the piezodisc from the voltage drop over the known resistor R (upper plot), and corresponding frequency spectrum (bottom plot), for the first radial mode (R1).

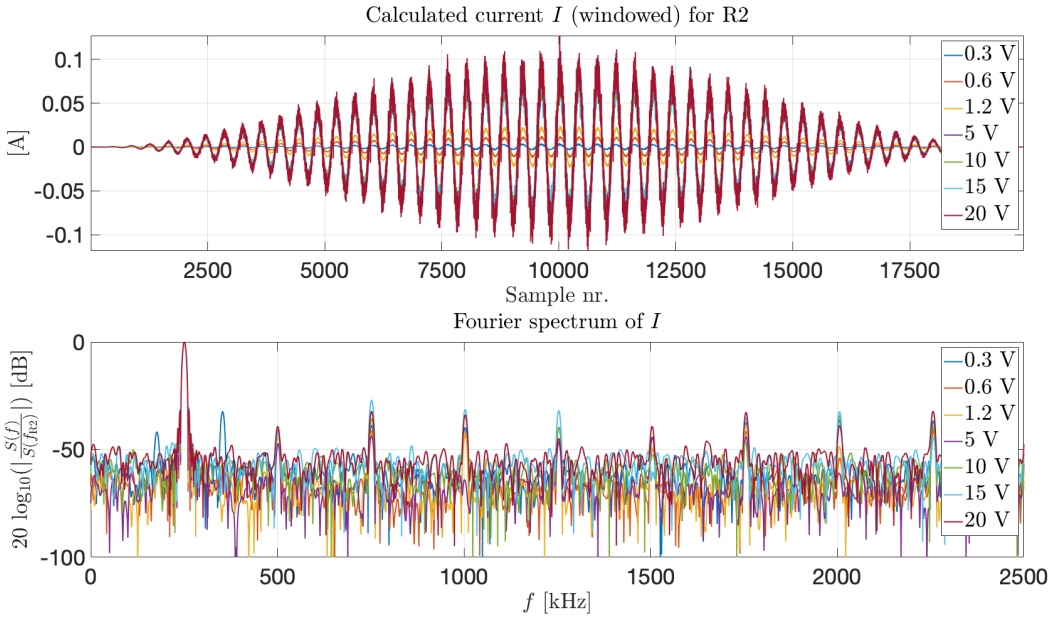

Figure B.71: Same as for Figure B.70, but for R2.

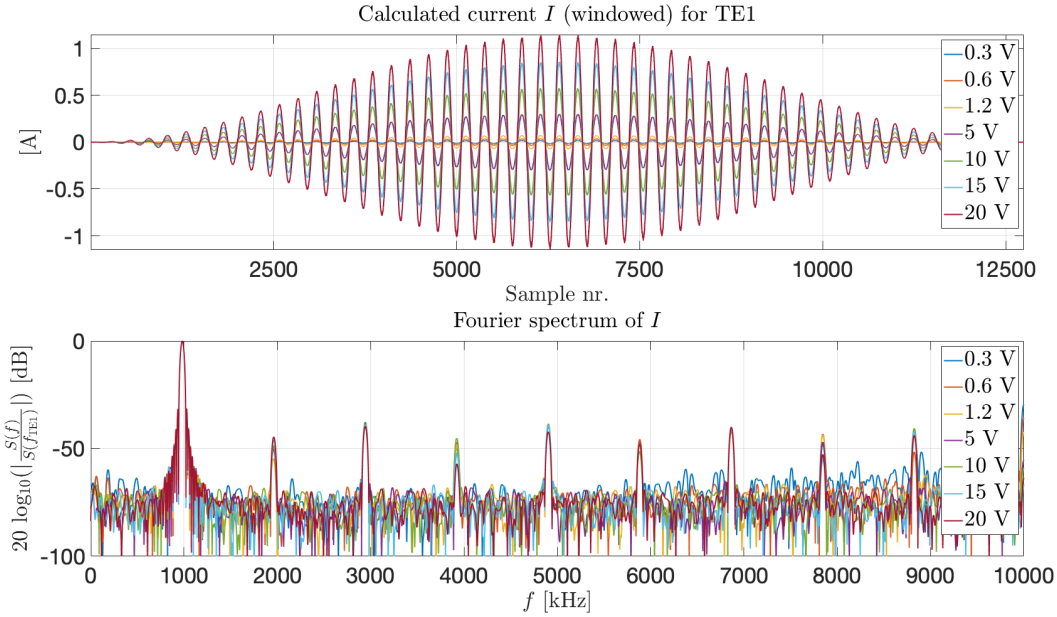

Figure B.72: Same as for Figures B.70 and B.71, but for TE1.

B.5.3 13x2 continuous waveform

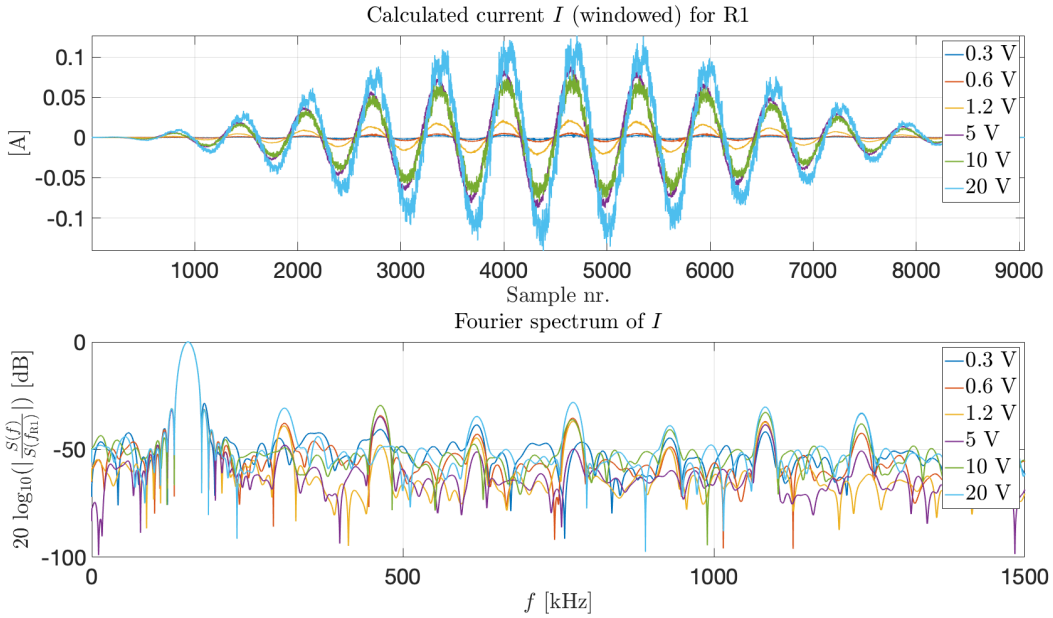

Figure B.73: Calculated current through the 13x2 piezodisc from the voltage drop over the known resistor R (upper plot), and corresponding frequency spectrum (bottom plot), for R1.

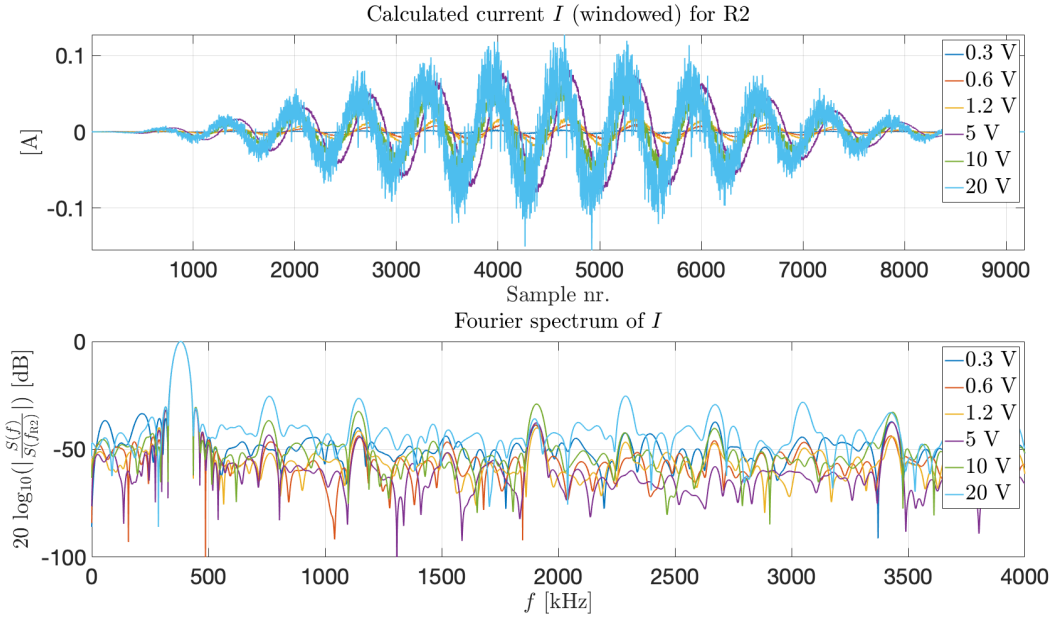

Figure B.74: Same as for Figure B.73, but for R2.

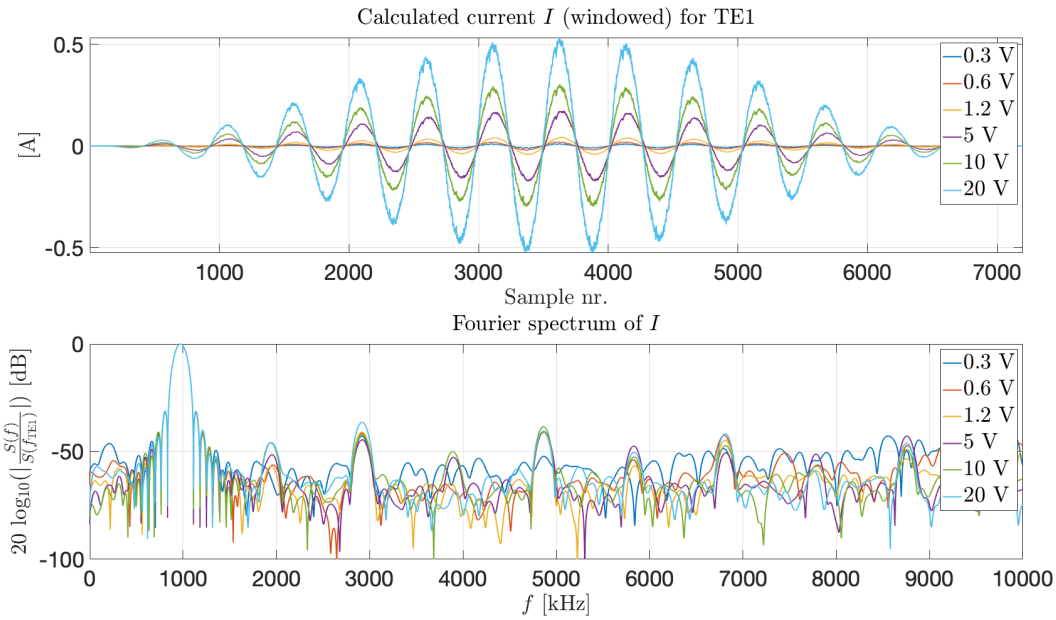

Figure B.75: Same as for Figures B.73 and B.74, but for TE1.

B.5.4 13x2 burst excitation

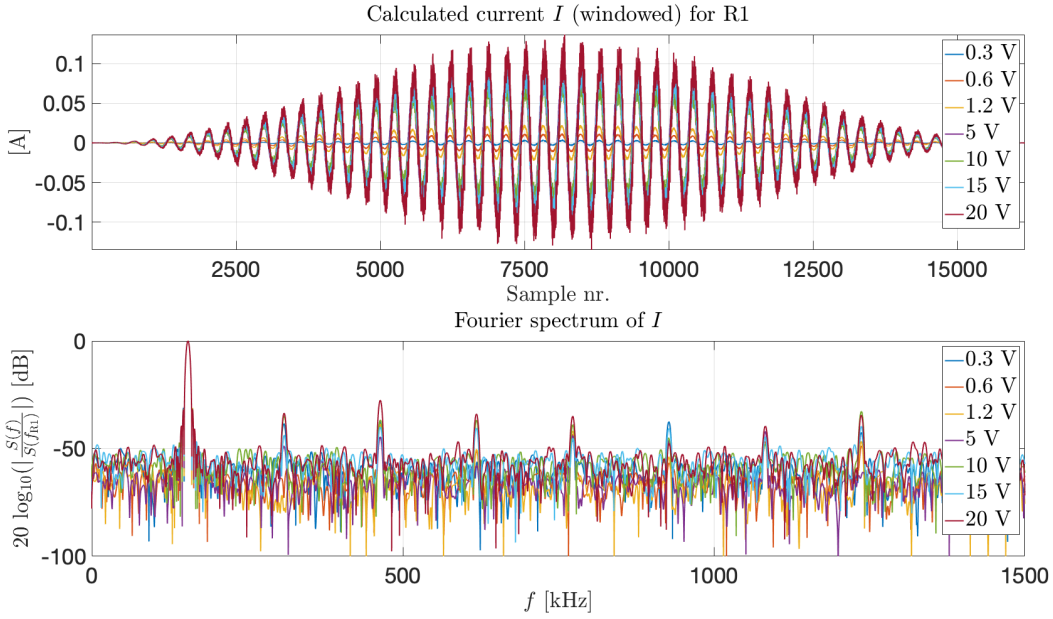

Figure B.76: Calculated current through the piezodisc from the voltage drop over the known resistor R (upper plot), and corresponding frequency spectrum (bottom plot), for the first radial mode (R1).

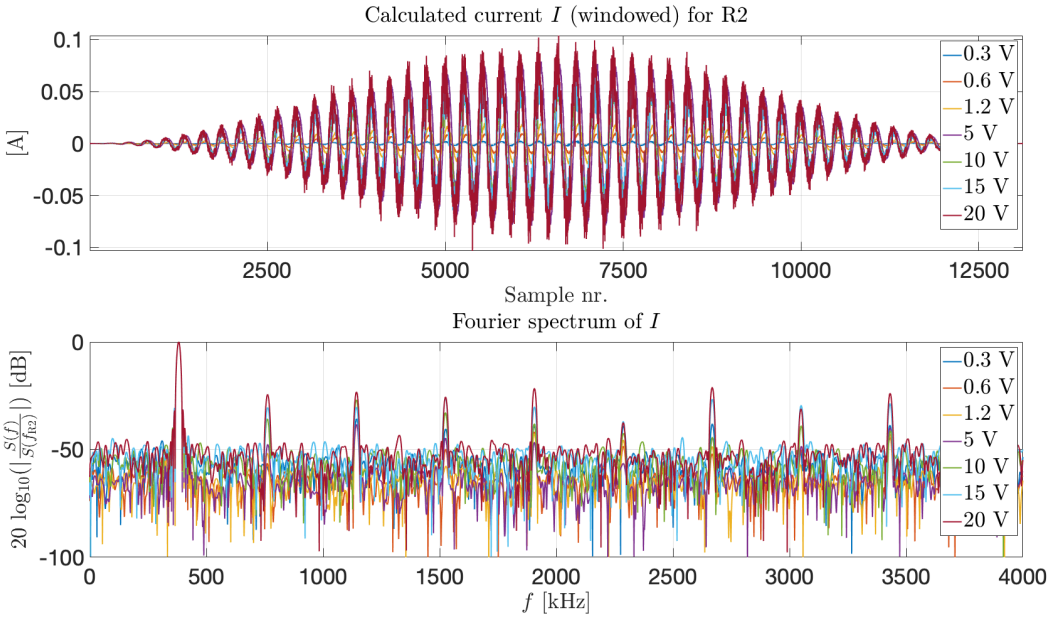

Figure B.77: Same as for Figure B.76, but for R2.

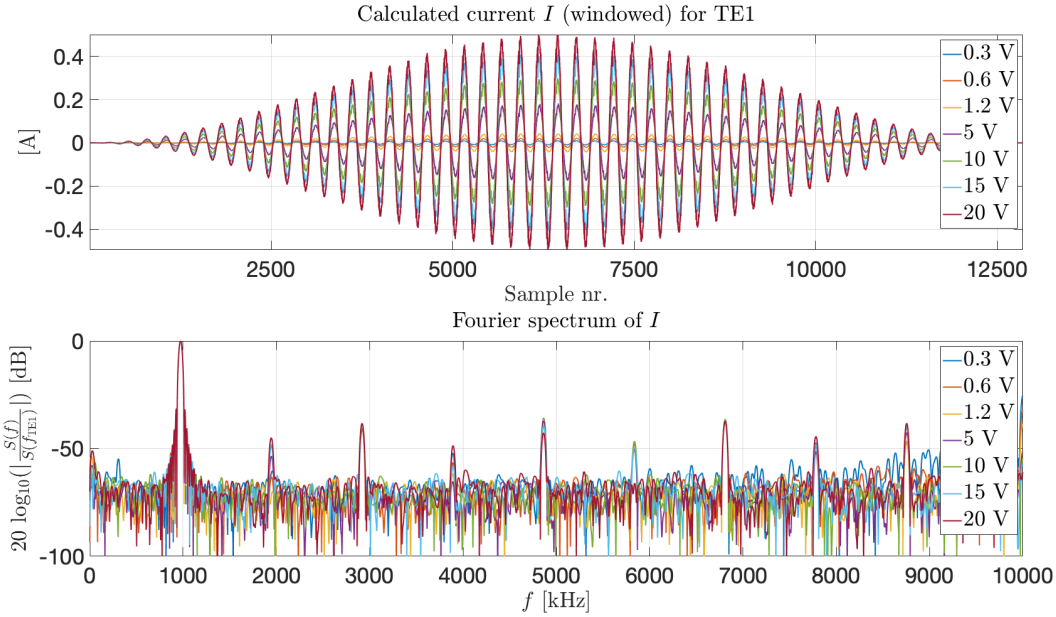

Figure B.78: Same as for Figures B.76 and B.77, but for TE1.

B.6 Preparatory sound pressure measurements

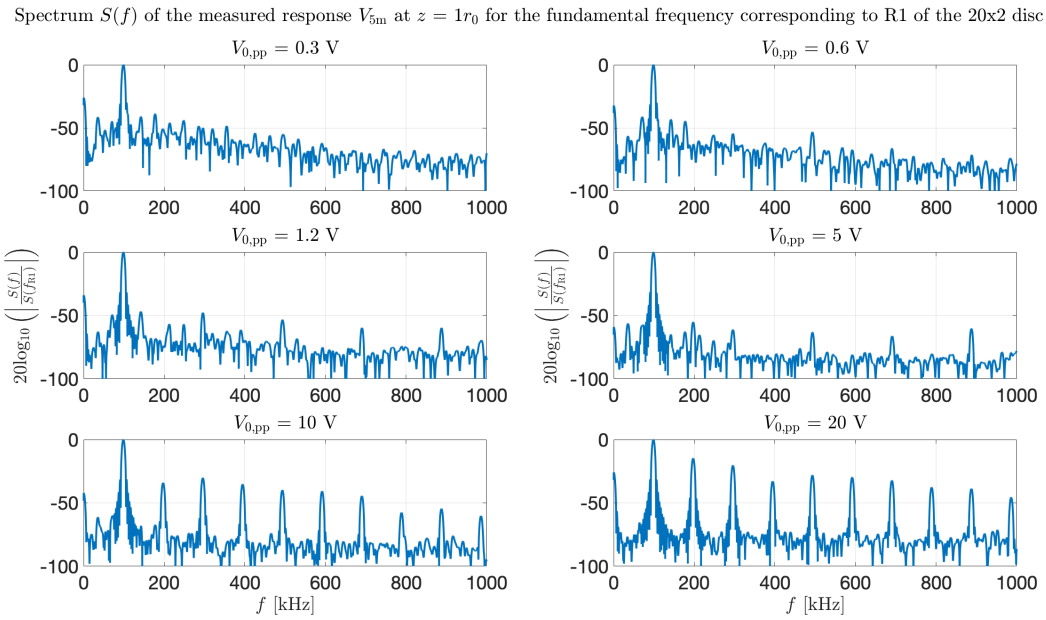

Figure B.79: Frequency spectra of the steady state part of the received signal for various $V_{0,\mathrm{pp}}$ measured at $z = r_0$. Transmitted signal with carrier frequency corresponding to R1 of the 20x2 disc.

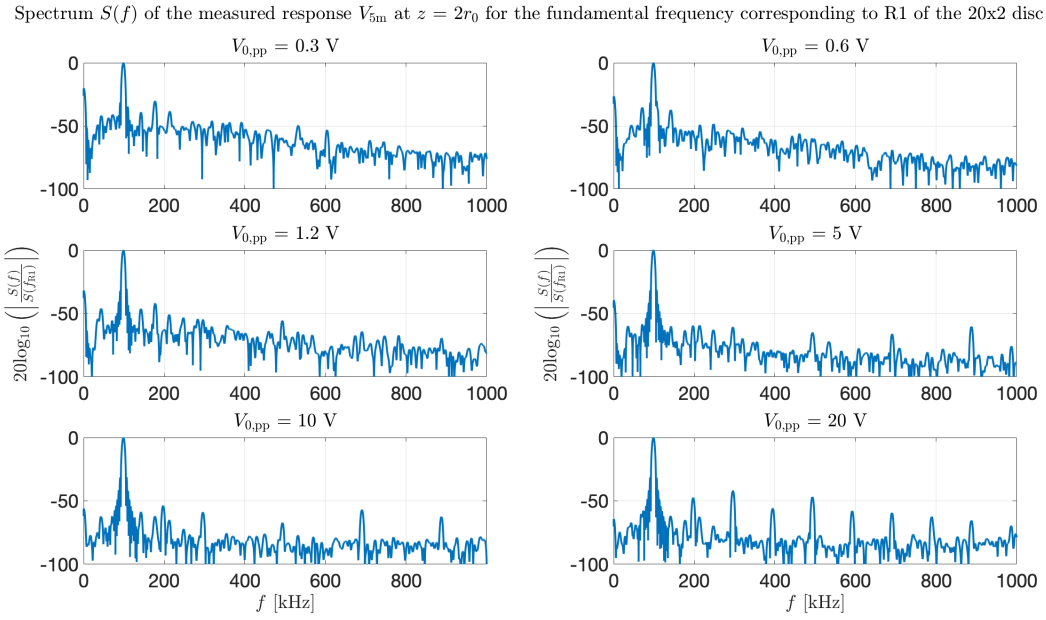

Figure B.80: Same as for Figure B.79, but here for $z = 2r_0$.

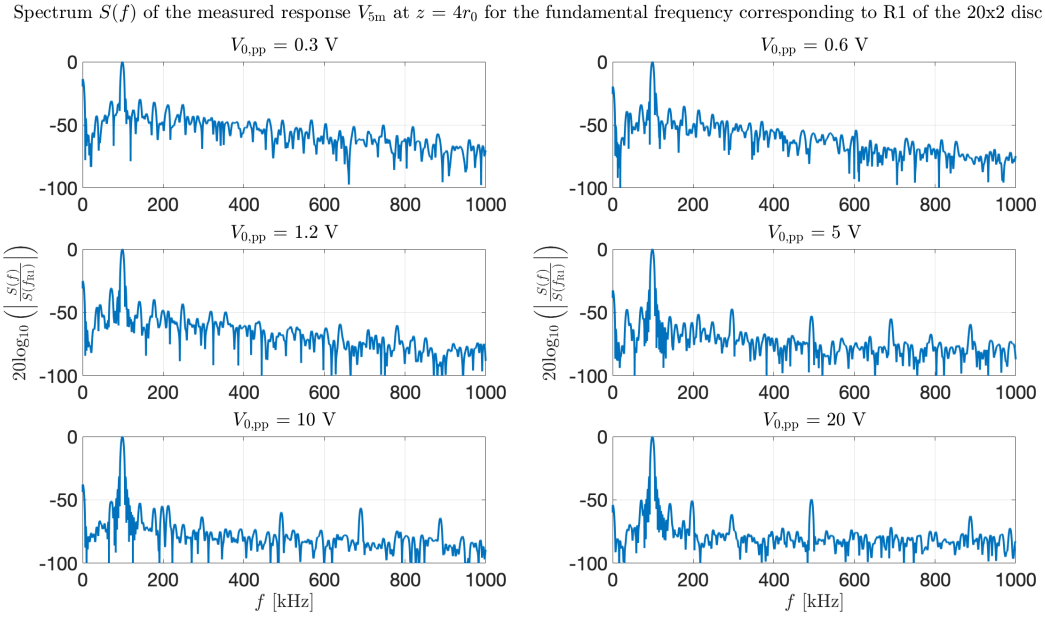

Figure B.81: Same as for Figure B.79 and B.80, but here for $z = 4r_0$.

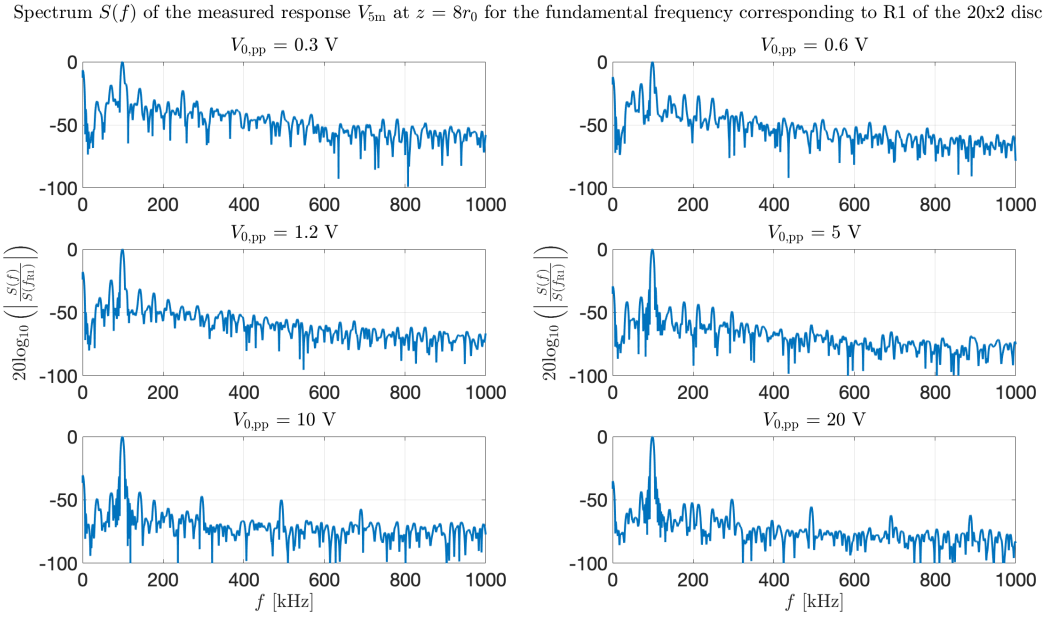

Figure B.82: Same as for Figures B.79-B.81, but here for $z = 8r_0$.

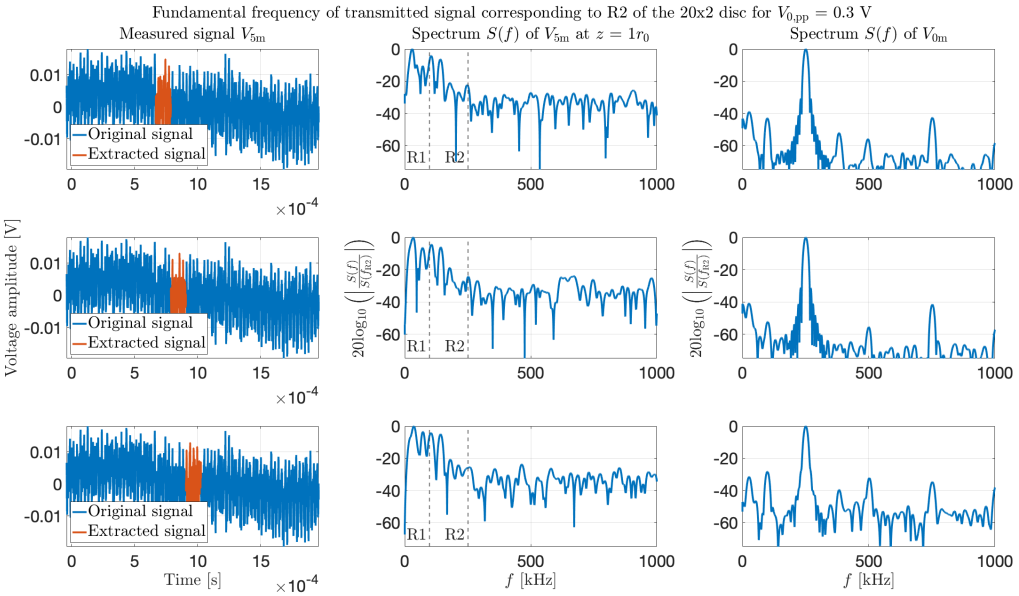

Figure B.83: Measured response of the 20x2 disc transmitting at a frequency corresponding to R2 for $V_{0,pp} = 0.3$ V, measured at $z = r_0$. In the right column, the oscilloscope reading, and marked in red the extracted signal calculated based of the speed of sound and travel distance. In column two and three, the spectrum of the extracted measured response, and the steady state of the transmitted burst, respectively. First row corresponds to the first 1/3 of the burst, and the two next rows, to the next 1/3's.

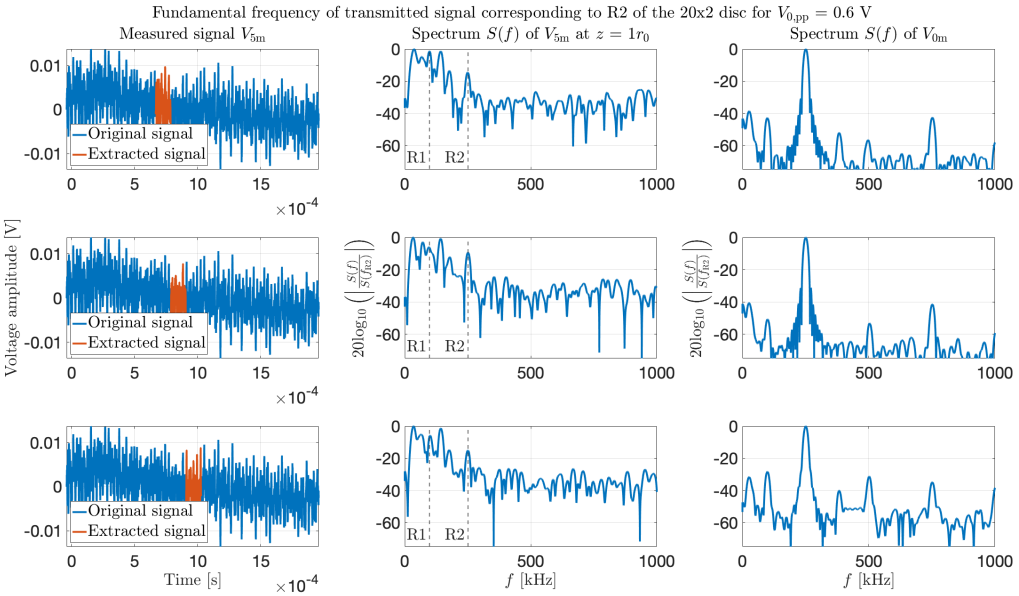

Figure B.84: Same as for Figure B.83, but here for $V_{0,pp} = 0.6$ V.

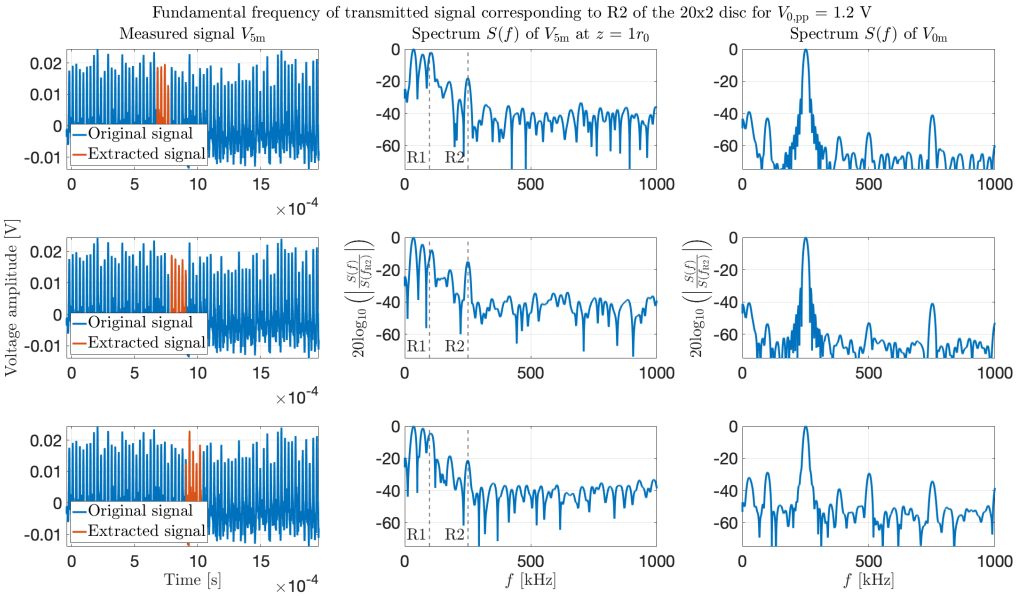

Figure B.85: Same as for Figure B.83 and B.84, but here for $V_{0,\mathrm{pp}} = 1.2$ V.

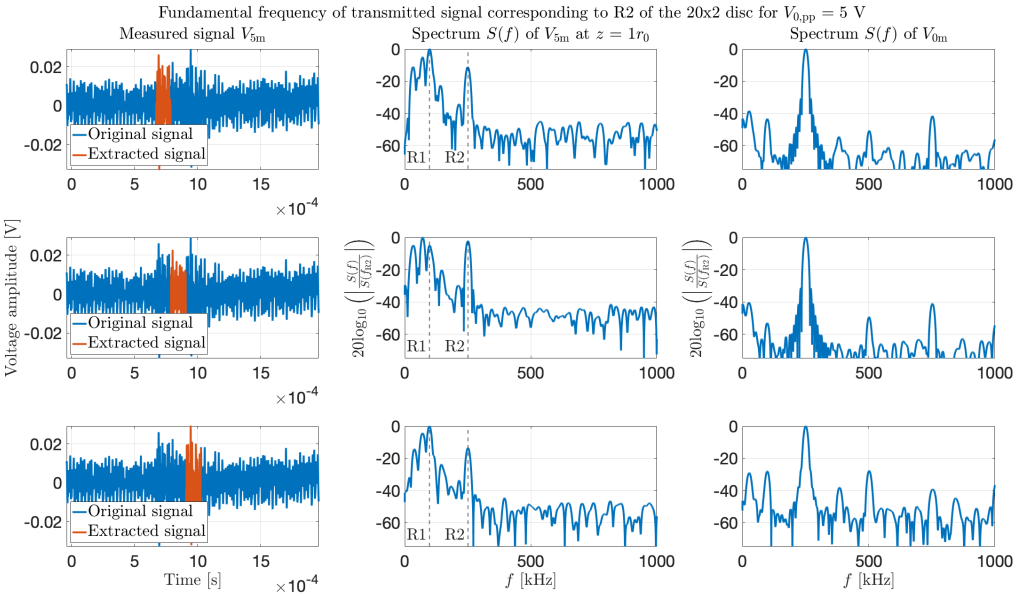

Figure B.86: Same as for Figures B.83-B.85, but here for $V_{0,\mathrm{pp}} = 5$ V.

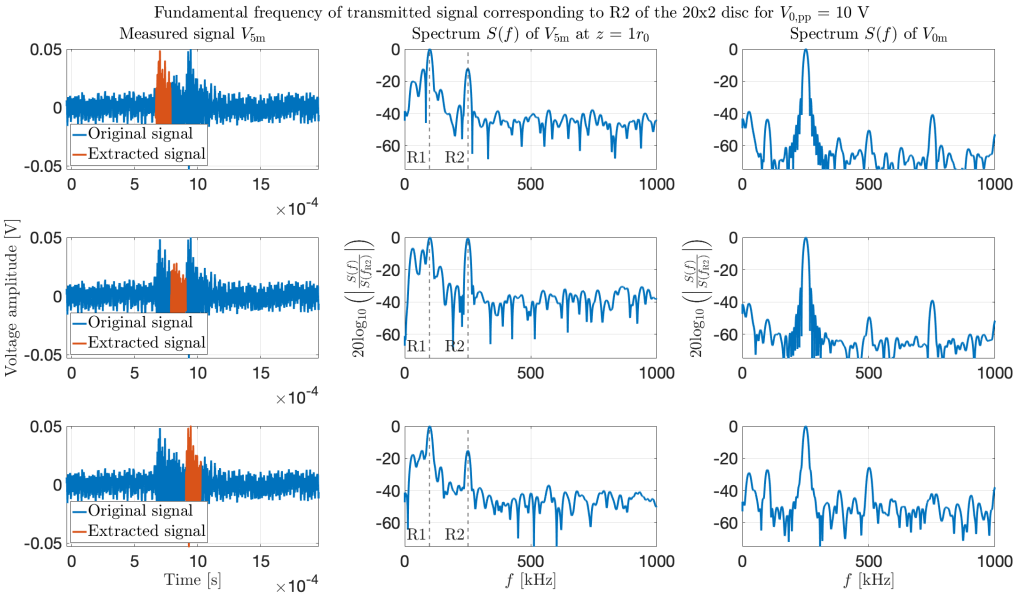

Figure B.87: Same as for Figures B.83-B.86, but here for $V_{0,pp} = 10$ V.

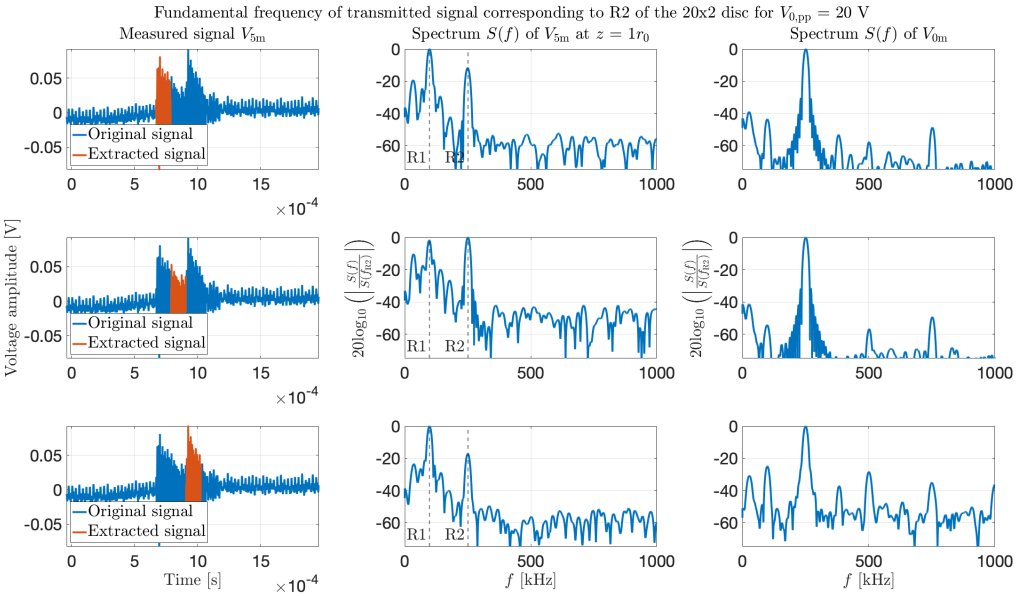

Figure B.88: Same as for Figures B.83-B.87, but here for $V_{0,pp} = 20$ V.

B.7 Curve fit to directivity measurements in MATLAB

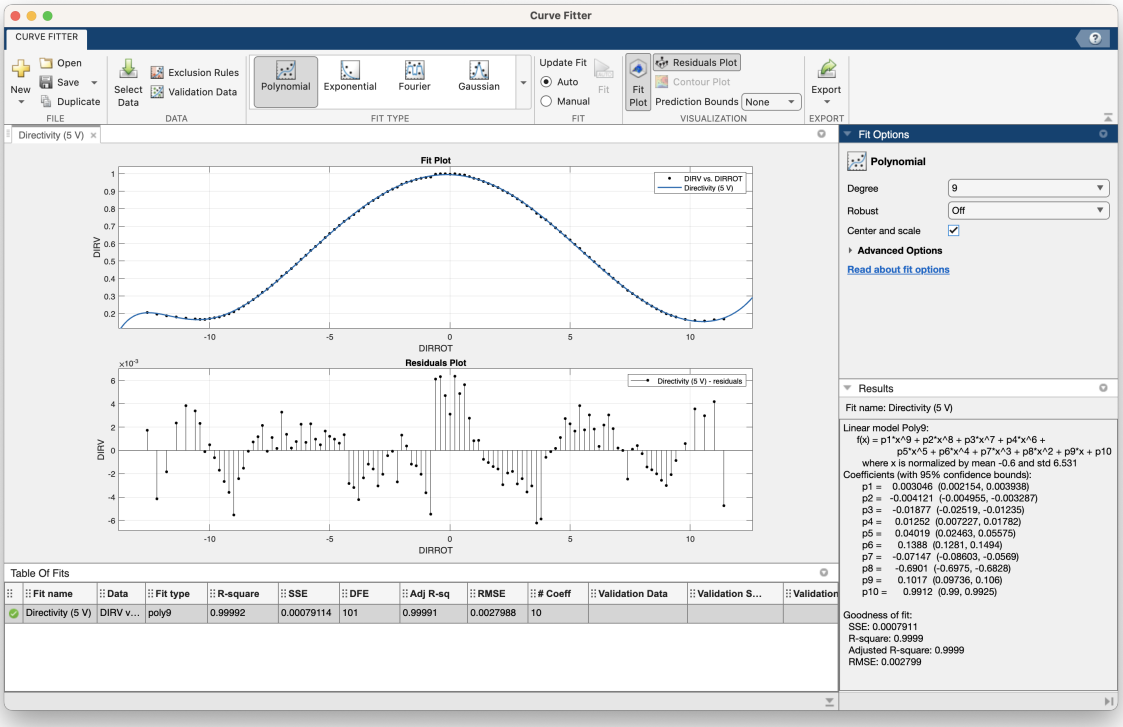

Figure B.89: Screenshot of the MATLAB curveFitter application used to test curve fits to directivity measurements. Shown in the picture is a 9^{th} order polynomial fit to the directivity function of the 20x2 piezodisc measured with a $V_{0,\text{pp}}$ of 5 V.

B.8 Curve fit to calibrated microphone sensitivity in MATLAB

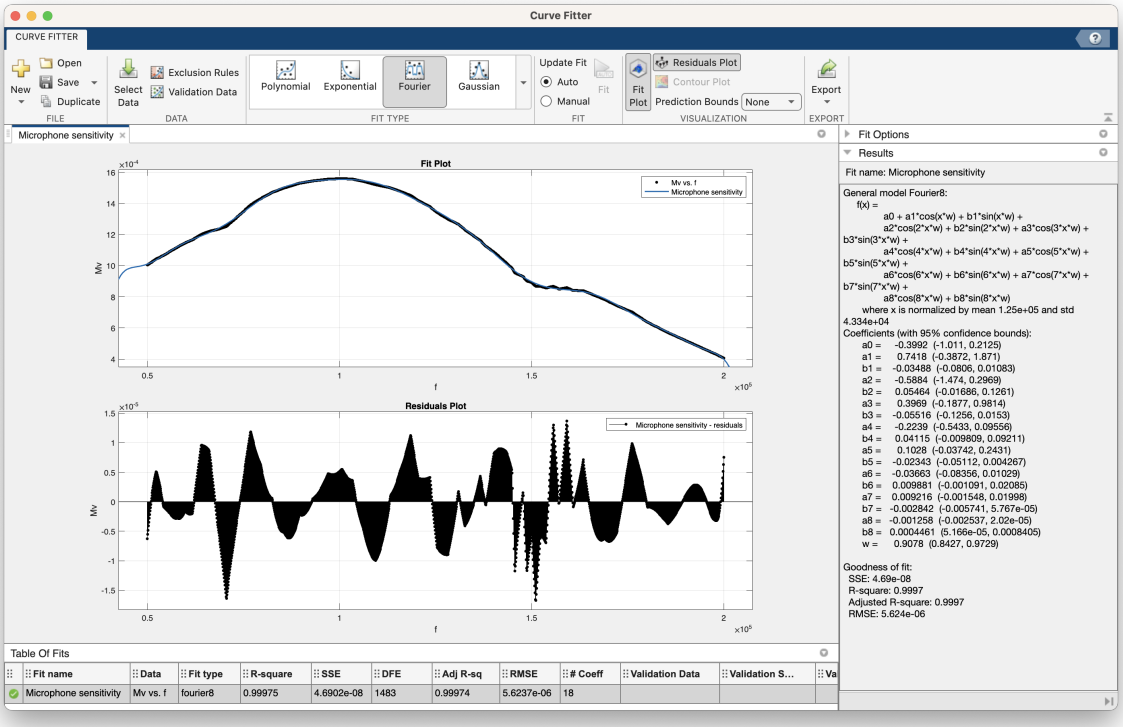

Figure B.90: A 9$^{\text{th}}$ order Fourier curve fit to the calibrated Brüel & Kjær 4138 pressure-field microphone sensitivity data using the MATLAB curveFitter application.

B.9 Simulations

B.9.1 Impact of r_1 for the simulations

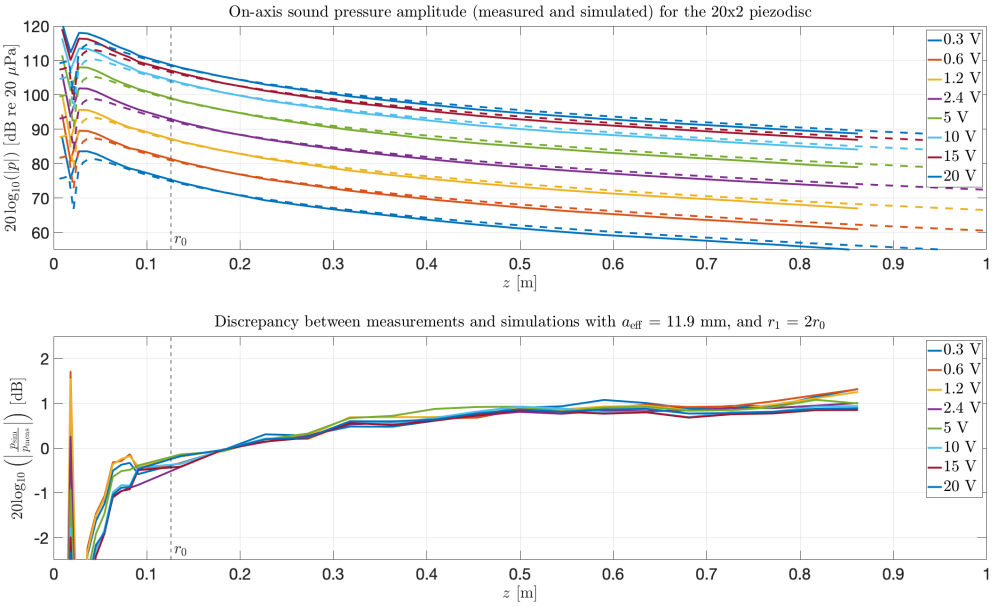

Figure B.91: Simulated and measured axial sound pressure levels for the 20x2 disc in the upper plot. Dashed graphs correspond to the simulated values for each measured pressure series. In the bottom plot, the relative difference of the simulated and measured pressure amplitudes. Pressure source condition p_0 to the Bergen Code determined from measured pressure values at $z = r_1 = 2r_0$. Effective source radius $a_{\text{eff}} = 11.90$ mm used.

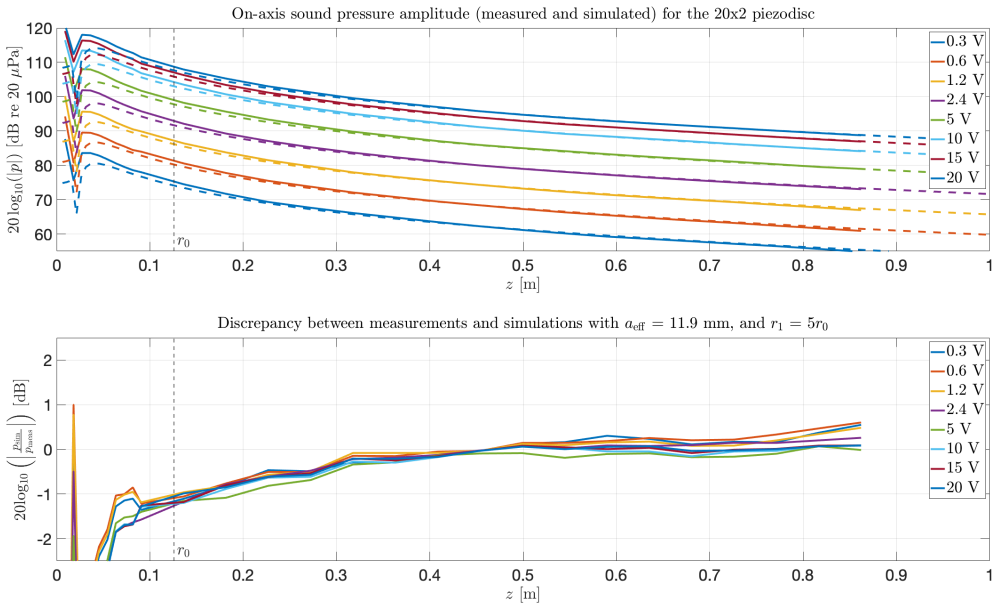

Figure B.92: Simulated and measured axial sound pressure levels for the 20x2 disc in the upper plot. Dashed graphs correspond to the simulated values for each measured pressure series. In the bottom plot, the relative difference of the simulated and measured pressure amplitudes. Pressure source condition p_0 to the Bergen Code determined from measured pressure values at $z = r_1 = 5r_0$. Effective source radius $a_{\text{eff}} = 11.90$ mm used.

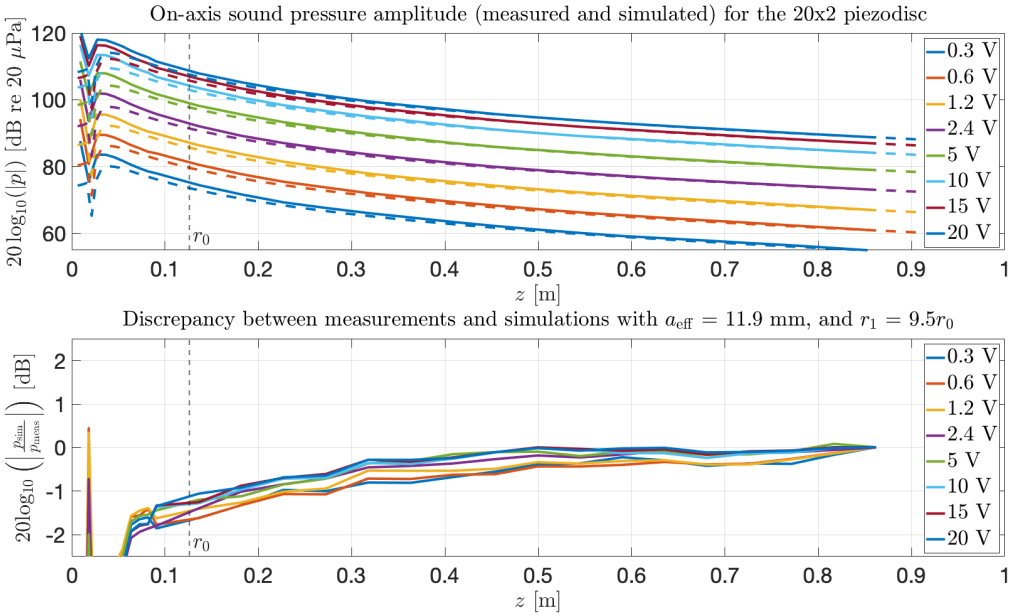

Figure B.93: Simulated and measured axial sound pressure levels for the 20x2 disc in the upper plot. Dashed graphs correspond to the simulated values for each measured pressure series. In the bottom plot, the relative difference of the simulated and measured pressure amplitudes. Pressure source condition p_0 to the Bergen Code determined from measured pressure values at $z = r_1 = 9.5r_0$. Effective source radius $a_{\text{eff}} = 11.90$ mm used.

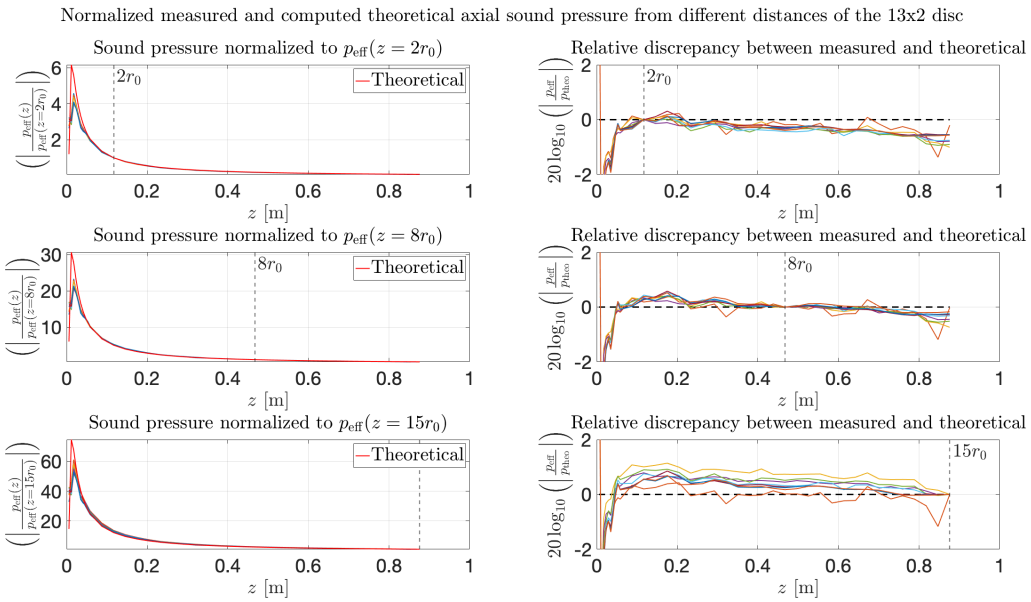

Figure B.94: To the left in the figure; measurement series of the sound pressure amplitude of the 13x2 disc normalized to the pressure amplitudes $p(r_1 = 2r_0)$, $p(r_1 = 8r_0)$, and $p(r_1 = 15r_0)$, for each corresponding series. The theoretical expression of a plane piston radiator modeled with equal parameters as the simulations for each series, calculated for the same axial distance, and normalized, before being extrapolated on the interval. To the right in the figure; relative discrepancy between the normalized measured and theoretical sound pressure amplitudes, for the three cases of r_1.

B.9.2 Reducing the effective source radius of the disc

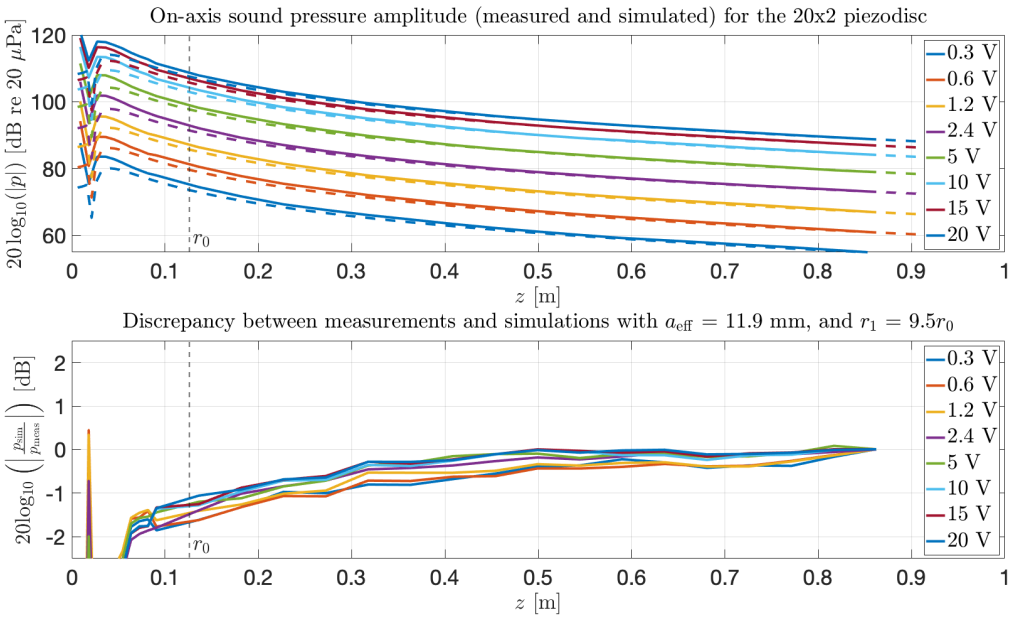

Figure B.95: Simulated and measured axial sound pressure levels for the 20x2 disc in the upper plot. Dashed graphs correspond to the simulated values for each measured pressure series. In the bottom plot, the relative difference of the simulated and measured pressure amplitudes. Pressure source condition p_0 to the Bergen Code determined from measured pressure values at $z = 9.5r_0$. Effective source radius $a_{\text{eff}} = 11.90$ mm used.

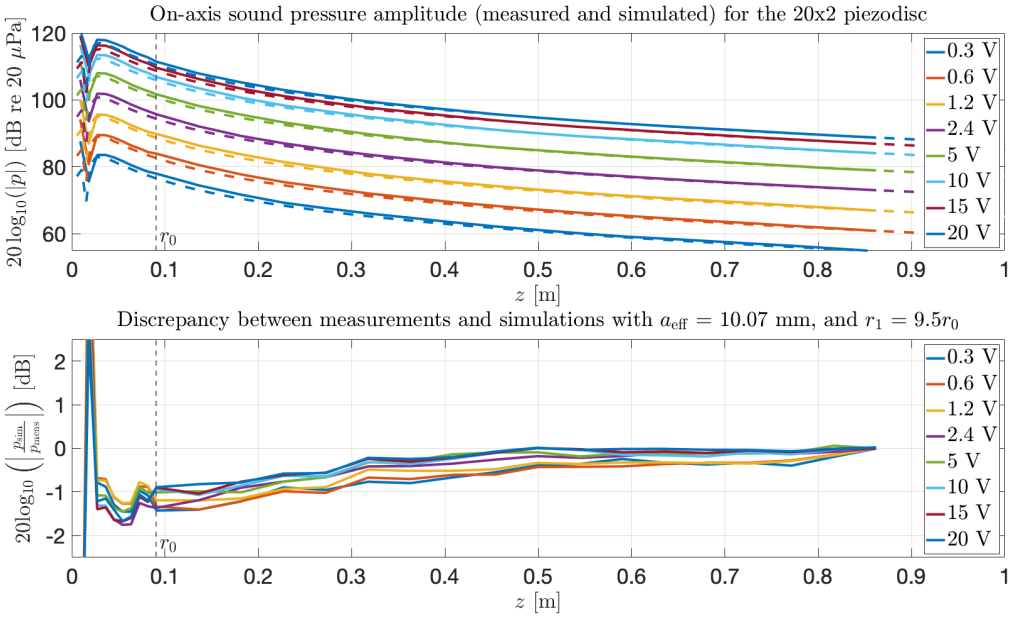

Figure B.96: Same as Figure B.95, but here for effective source radius $a_{\text{eff}} = 10.07$ mm.

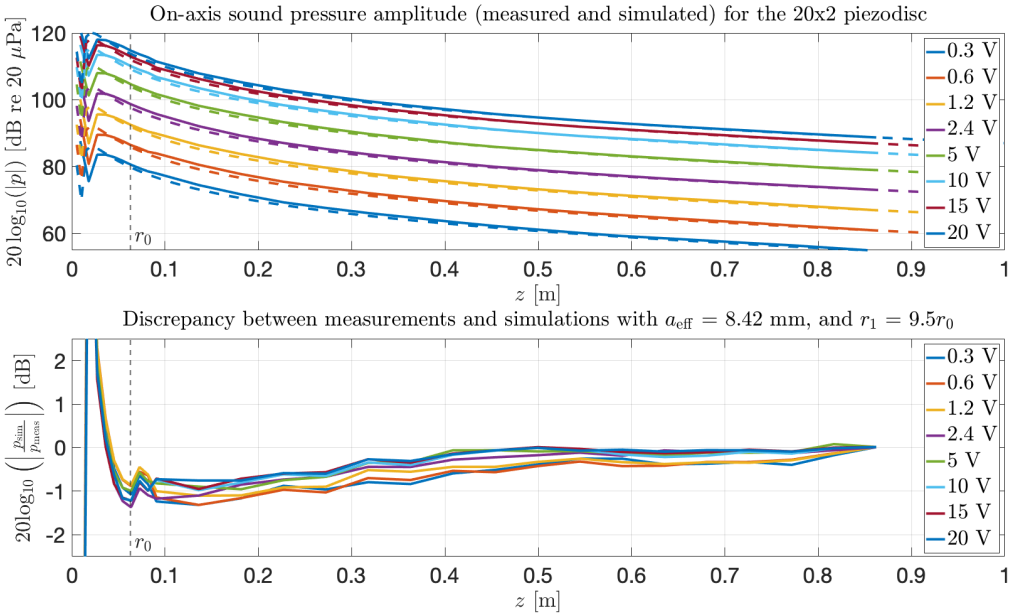

Figure B.97: Same as for Figure B.95 and B.96, but here for effective source radius $a_{\text{eff}} = 8.42$ mm.

Appendix C

MATLAB scripts

C.1 Automated measurements for the I-V circuit

C.1.1 MeasureMultiple.m

```
%% MeasureMultiple.m
% Ocean Technology (Acoustics) - Department of Physics and Technology
% Univeristy of Bergen
% By Aslak J. Thorbjoernsen, 2023
%
%%
% Clear variables, and disconnect/clear existing serial com.
clear
instrreset
pause(.5);
% Start serial communication with osc. and gen.
InitScopeAndGen

tic

% Change elem to alter folder to save
elem = ['20x2\TE1 BURST256\',datestr(datetime('today'))];'
elemDim = '20x2mm';
folderpath = fullfile('C:\Users\zez009\OneDrive - University of
    ↪ Bergen\MATLAB\Measurements\Data and scripts\',elem);'

type = 'burst';

% Enter voltage levels to measure
Vpp = [0.3 0.6 1.2 5 10 15 20];
% Enter frequencies
f = (1:1:1500) .* 1e3;
% Adjust R if replaced/changed
R = 2.175;

% Average time per frequency
if strcmp(type, 'burst')
  time_df = 52;
end
if strcmp(type, 'continuous')
  time_df = 84;
end
tot_sec = time_df * length(f);
dnow = datetime('now');
et = milliseconds(dnow - datetime(1970,1,1));
```

```
etfinish = et + tot_sec*1000;
dfinish =
    ↪ datetime(etfinish,'ConvertFrom','epochtime','TicksPerSecond',1000);

% Number of samples
numSamples = 100e3;
% Number of burst cycles
num_cycles = 120;% 1 to 1e6

disp('-----------------------------------------')
disp(['Initializing measurements over ',num2str(length(f)),'
    ↪ frequenices, '])
disp(['each over ',num2str(length(Vpp)),' nominal voltage levels.'])
disp(['Should take about ',num2str(tot_sec/3600),' hours to
    ↪ complete.'])
disp(['Estimated completion time is ',datestr(dfinish)])
disp(['Start time: ', datestr(datetime('now'))])
disp('-----------------------------------------')

for i = 1:length(f)
    try
        % Re-establish connections to instruments periodically
        if (mod(i,10) == 0)
            connected = 0;
            while ~(connected == true)
                try
                    clear id_scope id_sig
                    instrreset
                    pause(.5);
                    instrreset
                    pause(.5);
                    InitScopeAndGen
                    pause(2);
                    disp(['Re-established connections to sig and
                        ↪ scope. Current time:
                        ↪ ',datestr(datetime('now'))])

                    str = writeread(id_scope,'BUSY?');
                    if strcmp(str,"0")
                        connected = 1;
                    else
                        connected = 0;
                    end
                catch
                    connected = 0;
                    disp(['Was NOT able to re-establish connections to
                        ↪ sig and scope. Current time:
                        ↪ ',datestr(datetime('now'))])
                    disp('Trying to connect every 15 seconds til
                        ↪ success...')
                    pause(15);
                end
            end
        end

        % Display progress in command window
        if (mod(i,floor(length(f) / 40)) == 0)
            currTime = datetime('now');
            ett = milliseconds(currTime - datetime(1970,1,1));
            estfinish = ett + ((length(f)-i)*time_df)*1000;
            ddfinish =
                ↪ datetime(estfinish,'ConvertFrom','epochtime','TicksPerSecond',1000
            disp('----------')
            disp(['Progress: ',num2str(round(((i/length(f)) * 100) /
                ↪ 2.5)*2.5),' %'])
            disp(['Measuring at ',num2str(f(i) / 1e3),' kHz; looping
                ↪ over ',num2str(length(Vpp)),' voltage leves...'])
```

```
96              disp(['Frequency nr. ',num2str(i),' of
                    ↪ ',num2str(length(f))])
97              disp(['Current time: ',datestr(datetime('now')),',
                    ↪ estimated done: ',datestr(ddfinish)])
98          end
99
100         saveData = 1;
101         % Loop over voltages
102         if strcmp(type, 'burst')
103           curr = MeasureVppV2(id_scope, id_sig, Vpp, f(i), numSamples,
                  ↪ num_cycles);
104         elseif strcmp(type, 'continuous')
105           curr = MeasureVpp(id_scope, id_sig, Vpp, f(i), numSamples,
                  ↪ num_cycles);
106         else
107           error('Unsupported type of waveform.')
108         end
109         % Add readings to new struct
110         S.x1(1,1) = {curr.x1};
111         S.x2(1,1) = {curr.x2};
112         S.ch1(1,1) = {curr.ch1};
113         S.ch2(1,1) = {curr.ch2};
114         S.ts1(1,1) = {curr.ts1};
115         S.ts2(1,1) = {curr.ts2};
116         S.Fs(1,1) = {curr.Fs};
117         S.err(1,1) = {curr.err};
118     catch
119         disp('Encountered errror in try-catch statement.')
120         writeline(id_sig,'OUTP OFF');
121         pause(.5);
122         clear id_scope id_sig
123         instrreset
124         pause(.5);
125         instrreset
126         pause(.5);
127         InitScopeAndGen
128         pause(2);
129         disp(['Re-established connections to sig and scope. Current
                ↪ time: ',datestr(datetime('now'))])
130         saveData = 0;
131     end
132     S.avgs(1,1) = curr.avgs(1,1);
133     S.Vpp(:,1) = transpose(Vpp);
134     S.f = f(i);
135     S.datetime = datetime('now');
136     S.num_cycles = num_cycles;
137
138     writeline(id_sig,'OUTP OFF');
139     pause(2);
140
141     % Save data to file
142     if saveData
143         try
144             currFile = [elemDim,num2str(f(i) / 1e3),'kHz.mat'];
145             fullfilename = fullfile(folderpath,currFile);
146             if ~isfolder(folderpath)
147                 mkdir(folderpath)
148             end
149             disp(['Saving: ', currFile])
150             save(fullfilename,'S','-v7.3');
151         catch
152             disp(['Unsuccessful in saving: ',currFile])
153         end
154     end
155
156     clear S curr
157 end
158
```

```
disp(['Finished at: ', datestr(datetime('now'))])
disp('----------------------------------------')

toc
```

C.1.2 MeasureVppV2.m

```
%% measure_VppV2.m
% Ocean Technology (Acoustics) - Department of Physics and Technology
% Univeristy of Bergen
% By Aslak J. Thorbjoernsen, 2023
%
function res = measure_VppV2(id_scope,id_sig,Vpp,f,samples,num_cycles)
% Function measure() returns a struct "res" with measurements
% from both channels of the oscilloscope.
% E.g., res.x1(1,:) is the x values to the res.ch1(1,:) values
% Rows in the variables in res, corresponds to new measurements at a
% different frequency.
% Frequency and Vpp information is stored in res.f and res.Vpp,
% respectively. Each row corresponding to a row in res.x1 and res.ch1.

% Set desired number of samples from oscilloscope
writeline(id_scope,['HOR:RECO ' num2str(samples)]); % New record length
pause(.1);

% Set appropriate time scale, s/div
%Hscale = [1e-9 2e-9 4e-9 10e-9 20e-9 40e-9 100e-9 200e-9 400e-9
    ↪ 800e-9 2e-6 4e-6 10e-6 20e-6 40e-6 100e-6 200e-6 400e-6 1e-3
    ↪ 2e-3 4e-3 10e-3 20e-3 40e-3 100e-3 200e-3 400e-3 1 2 4 10 20 40
    ↪ 100 200 400]; % [s]
T = 1 / f;
nT = num_cycles / 4;
%indices = find(Hscale < T);
%t = Hscale(indices(end));
% Set horizontal scale to be about two periods per division, 10 divs
    ↪ tot
writeline(id_scope, ['HOR:SCA ', num2str(nT*T)]);
pause(.1);

% Set positive horizontal delay to center burst on oscilloscope
writeline(id_scope, ['HOR:DEL:TIM ',num2str(T*(num_cycles/2))])
pause(.1);

% Set number of averages
avgs = pow2(8); %
writeline(id_scope,['ACQ:NUMAV ' num2str(avgs)]);
pause(.1);
writeline(id_scope, 'ACQ:MOD AVE; ACQ:STOPA SEQ');
pause(.1);

% Set the appropriate output load to the signal generator
% Ask the signal generator for its current load
outpload = str2double(writeread(id_sig,'OUTP:LOAD?'));
if outpload < 10e3
    writeline(id_sig, 'OUTP:LOAD INF'); % High impedance termination
end

try
    writeline(id_scope,[strcat('CH',num2str(1)),':SCA ',
        ↪ num2str(50e-3)]);
    pause(.1);
    writeline(id_scope,[strcat('CH',num2str(2)),':SCA ',
        ↪ num2str(50e-3)]);
    pause(.1);
```

```
52      % Set scope into sample mode
53      writeline(id_scope,'ACQ:MOD SAM');
54      pause(.1);
55      % Find appropriate vertical scaling for receiver signal
56      writeline(id_scope,'ACQ:STATE RUN');
57      pause(.1);
58      % Set mode back to averaging
59      writeline(id_scope,'ACQ:MOD AVE');
60      pause(.1);
61      % Get sample rate from oscilloscope
62      Fs = str2double(writeread(id_scope,'HOR:SAMPLER?'));
63      pause(.1);
64
65      for ii = 1:numel(Vpp)
66
67          % 1. Configure the burst waveform
68          writeline(id_sig,'FUNC SIN');
69          writeline(id_sig,['FREQ ',num2str(f)]);
70          writeline(id_sig,['VOLT ',num2str(Vpp(ii))]);
71          writeline(id_sig,'VOLT:OFFS 0.0');
72          % 2. Select the triggerd or gated burst mode
73          writeline(id_sig,['BURS:MODE ','TRIG']);        % TRIG or GAT
74          % 3. Set the burst count (1 to 1e6)
75          writeline(id_sig,['BURS:NCYC ',num2str(num_cycles)]);
76          % 4. Set the burst period
77          writeline(id_sig,['BURS:INT:PER ',num2str(10*(num_cycles/f) +
                ↪ 200e-9)]);
78          % 5. Set the burst starting phase
79          writeline(id_sig,'BURS:PHAS 0.0');
80          % 6. Select the trigger source
81          writeline(id_sig,'TRIG:SOUR IMM');
82          % 7. Enable the burst mode
83          writeline(id_sig,'BURS:STAT ON');
84          % 8. Enable output
85          writeline(id_sig,'OUTP ON');
86
87          % Ask sig gen for error
88          err = writeread(id_sig,'SYST:ERR?');
89          res.err(ii,1) = err;
90          pause(.2);
91
92          % Display error in command window if gen. returns error
93          if ~strcmp(err,'+0,"No error"')
94              disp(['Signal generator encountered error : ',err])
95          end
96
97          res.Fs(ii,1) = Fs;
98          res.f(ii,1) = f;
99          res.Vpp(ii,1) = Vpp(ii);
100         res.avgs(ii,1) = avgs;
101
102         % Set channel and clear offset
103         for ch = 1:2
104             writeline(id_scope,['DAT:SOU CH' num2str(ch)]);
105             pause(.1);
106             writeline(id_scope, strcat('CH',num2str(ch),':POS 0'));
107             pause(.1);
108             writeline(id_scope, strcat('CH',num2str(ch),':OFFS 0'));
109             pause(.1);
110             writeline(id_scope,[strcat('CH',num2str(ch)),':SCA ',
                    ↪ num2str(Vpp(ii) / 2 / 3)]);
111             pause(.1);
112         end
113
114         % Set scope into sample mode
115         writeline(id_scope,'ACQ:MOD SAM');
116         pause(.1);
117         % Find appropriate vertical scaling for receiver signal
```

```
118         writeline(id_scope,'ACQ:STATE RUN');
119         pause(.1);
120         % Set mode back to averaging
121         writeline(id_scope,'ACQ:MOD AVE');
122         pause(1);
123
124         % Read both channel 1 and 2 from the scope
125         [res.x1(ii,:),res.ch1(ii,:),res.ts1(ii)] =
                ↪ DPORead(id_scope,1,samples);
126         [res.x2(ii,:),res.ch2(ii,:),res.ts2(ii)] =
                ↪ DPORead(id_scope,2,samples);
127
128         writeline(id_sig, 'OUTP OFF');
129         pause(.1);
130     end
131
132     % Turn off output from signal generator
133     writeline(id_sig, 'OUTP OFF');
134 catch
135     writeline(id_sig, 'OUTP OFF');
136 end
137 end
```

C.1.3 MeasureVpp.m

```
1  %% measure_Vpp.m
2  % Ocean Technology (Acoustics) - Department of Physics and Technology
3  % Univeristy of Bergen
4  % By Aslak J. Thorbjoernsen, 2023
5  %
6  function res = measure_Vpp(id_scope,id_sig,Vpp,f,samples)
7  % Function measure() returns a struct "res" with measurements
8  % from both channels of the oscilloscope.
9  % E.g., res.x1(1,:) is the x values to the res.ch1(1,:) values
10 % Rows in the variables in res, corresponds to new measurements at a
11 % different frequency.
12 % Frequency and Vpp information is stored in res.f and res.Vpp,
13 % respectively. Each row corresponding to a row in res.x1 and res.ch1.
14
15 % Set desired number of samples from oscilloscope
16 write(id_scope,['HOR:RECO ' num2str(samples)]); % New record length
17 pause(.2);
18
19 % Set appropriate time scale, s/div
20 %Hscale = [1e-9 2e-9 4e-9 10e-9 20e-9 40e-9 100e-9 200e-9 400e-9
       ↪ 800e-9 2e-6 4e-6 10e-6 20e-6 40e-6 100e-6 200e-6 400e-6 1e-3
       ↪ 2e-3 4e-3 10e-3 20e-3 40e-3 100e-3 200e-3 400e-3 1 2 4 10 20 40
       ↪ 100 200 400]; % [S]
21 T = 1 / f;
22 nT = 2;
23 %indices = find(Hscale < T);
24 %t = Hscale(indices(end));
25 % Set horizontal scale to be about two periods per division, 10 divs
       ↪ tot
26 write(id_scope, ['HOR:SCA ', num2str(nT*T)]);
27 pause(.2);
28
29
30 % Set number of averages
31 avgs = pow2(6); %
32 write(id_scope,['ACQ:NUMAV ' num2str(avgs)]);
33 pause(.2);
34 write(id_scope, 'ACQ:MOD AVE; ACQ:STOPA SEQ');
35 pause(.2);
```

```
36
37 % Set scope into sample mode
38 %writeline(app.instrument.scope,'ACQ:MOD SAM');
39 % Find appropriate vertical scaling for receiver signal
40 %writeline(app.instrument.scope,'ACQ:STATE RUN');
41 % Set mode back to averaging
42 %writeline(app.instrument.scope,'ACQ:MOD AVE');
43
44 % Set the appropriate output load to the signal generator
45 %writeline(id_sig, 'OUTP:LOAD 50');
46 % Ask the signal generator for its current load
47 outpload = str2double(writeread(id_sig,'OUTP:LOAD?'));
48 if outpload < 10e3
49     writeline(id_sig, 'OUTP:LOAD INF'); % High impedance termination
50 end
51
52
53 try
54     writeline(id_sig,['APPL:SIN ', num2str(f), ' HZ, ',
          ↪ num2str(Vpp(1)),' VPP, ', '0 V'])
55     pause(.2);
56     writeline(id_sig, 'OUTP ON');
57     pause(2);
58     %DPOScaleVertical(id_scope,1,samples);
59     %pause(.5);
60     %DPOScaleVertical(id_scope,2,samples);
61     %pause(.5);
62     write(id_scope,[strcat('CH',num2str(1)),':SCA ', num2str(50e-3)]);
63     pause(.2);
64     write(id_scope,[strcat('CH',num2str(2)),':SCA ', num2str(50e-3)]);
65     pause(.2);
66     % Set scope into sample mode
67     writeline(id_scope,'ACQ:MOD SAM');
68     pause(.1);
69     % Find appropriate vertical scaling for receiver signal
70     writeline(id_scope,'ACQ:STATE RUN');
71     pause(.1);
72     % Set mode back to averaging
73     writeline(id_scope,'ACQ:MOD AVE');
74     pause(.1);
75     % Get sample rate from oscilloscope
76     Fs = str2double(writeread(id_scope,'HOR:SAMPLER?'));
77
78     for ii = 1:numel(Vpp)
79         % Set new frequency, and amplitude
80         writeline(id_sig,['APPL:SIN ', num2str(f), ' HZ, ',
              ↪ num2str(Vpp(ii)),' VPP, ', '0 V'])
81         pause(.2);
82         writeline(id_sig, 'OUTP ON');
83         pause(2);
84
85         % Ask sig gen for error
86         err = writeread(id_sig,'SYST:ERR?');
87         res.err(ii,1) = err;
88         pause(.2);
89         if ~strcmp(err,'+0,"No error"')
90             disp(['Signal generator encountered error : ',err])
91         end
92
93         res.Fs(ii,1) = Fs;
94         res.f(ii,1) = f;
95         res.Vpp(ii,1) = Vpp(ii);
96         res.avgs(ii,1) = avgs;
97
98         % Set scope into sample mode
99         writeline(id_scope,'ACQ:MOD SAM');
100        pause(.2);
101        % Find appropriate vertical scaling for receiver signal
```

```
102         writeline(id_scope,'ACQ:STATE RUN');
103         pause(.2);
104         % Set mode back to averaging
105         writeline(id_scope,'ACQ:MOD AVE');
106         pause(.2);
107
108         % Scale DPO channels to optimize data sampling
109         DPOScaleVertical(id_scope,1,samples);
110         pause(.5);
111         DPOScaleVertical(id_scope,2,samples);
112         pause(.5);
113
114         % Set scope into sample mode
115         writeline(id_scope,'ACQ:MOD SAM');
116         pause(.2);
117         % Find appropriate vertical scaling for receiver signal
118         writeline(id_scope,'ACQ:STATE RUN');
119         pause(.2);
120         % Set mode back to averaging
121         writeline(id_scope,'ACQ:MOD AVE');
122         pause(2);
123
124         % Read both channel 1 and 2 from the scope
125         [res.x1(ii,:),res.ch1(ii,:),res.ts1(ii)] =
              ↪ DPORead(id_scope,1,samples);
126         [res.x2(ii,:),res.ch2(ii,:),res.ts2(ii)] =
              ↪ DPORead(id_scope,2,samples);
127
128         writeline(id_sig, 'OUTP OFF');
129         pause(1);
130     end
131
132     % Turn off output from signal generator
133     writeline(id_sig, 'OUTP OFF');
134 catch
135     writeline(id_sig, 'OUTP OFF');
136 end
137 end
```

C.1.4 DPOScaleVertical.m

```
1  %% DPOScaleVertical.m
2  % Ocean Technology (Acoustics) - Department of Physics and Technology
3  % Univeristy of Bergen
4  % By Aslak J. Thorbjoernsen, 2023
5  %
6  function DPOScaleVertical = DPOScaleVertical(id_scope,ch,samples)
7
8  % DPO Vertical scale options
9  %Vscale = [1e-3 2e-3 5e-3 10e-3 20e-3 50e-3 100e-3 200e-3 500e-3 1 2 5
       ↪ 10]; % [V]
10 Vscale = [20e-3 50e-3 100e-3 200e-3 500e-3 1 2 5 10]; % [V]
11
12 % Set channel and clear offset
13 write(id_scope,['DAT:SOU CH' num2str(ch)]);
14 write(id_scope, strcat('CH',num2str(ch),':POS 0'));
15 write(id_scope, strcat('CH',num2str(ch),':OFFS 0'));
16
17 % Scale down
18 ydata = DPOReadYdata(id_scope,ch,samples);
19 if abs(max(ydata)) < 15000
20     k = 10;
21     nit = 0;
22     while abs(max(ydata)) < 15000 && k ~= 1
```

```
23          currScale =
               ↪ str2double(writeread(id_scope,strcat('CH',num2str(ch),':SCA?')));
24          i = find(~(Vscale-currScale));
25          k = max([1,i-1]);
26          write(id_scope,[strcat('CH',num2str(ch)),':SCA ',
               ↪ num2str(Vscale(k))]);
27          pause(.5);
28          ydata = DPOReadYdata(id_scope,ch,samples);
29          nit = nit + 1;
30          if nit == 5
31              disp(['Err: Quit scaling loop after 5 scalings for channel
                   ↪ ',num2str(ch)])
32              disp(datestr(datetime('now')))
33              break
34          end
35      end
36  end
37
38  % Scale up
39  ydata = DPOReadYdata(id_scope,ch,samples);
40  if abs(max(ydata)) > 27500
41      k = 10;
42      nit = 0;
43      while abs(max(ydata)) > 27500 && k ~= length(Vscale)
44          currScale =
               ↪ str2double(writeread(id_scope,strcat('CH',num2str(ch),':SCA?')));
45          i = find(~(Vscale-currScale));
46          k = min([length(Vscale),i+1]);
47          write(id_scope,[strcat('CH',num2str(ch)),':SCA ',
               ↪ num2str(Vscale(k))]);
48          pause(.5);
49          ydata = DPOReadYdata(id_scope,ch,samples);
50          nit = nit + 1;
51          if nit == 5
52              disp(['Err: Quit scaling loop after 5 scalings for channel
                   ↪ ',num2str(ch)])
53              disp(datestr(datetime('now')))
54              break
55          end
56      end
57  end
58
59  end
```

C.1.5 DPOReadYdata.m

```
1  function ydata = DPOReadYdata(id_scope,ch,samples)
2
3  noB = 2; % Number of bytes per word (8-bit if 1, 16-bit if 2, ...)
4  write(id_scope,['DAT:SOU CH' num2str(ch)]); % Velge kanal. ch=1 betyr
       ↪ CH1
5  % Record length per visible time interval, affecting the sample rate
6  %rec_len = str2double(writeread(id_scope,'HOR:RECO?'));
7
8  % Set what samples to retrieve
9  write(id_scope,'DAT:START 1');
10 write(id_scope,['DAT:STOP ' num2str(samples)]);
11
12 % Read the data
13 writeline(id_scope,'ACQ:STATE RUN');
14 while str2double(writeread(id_scope, 'BUSY?'))
15     pause(.5);
16 end
17 write(id_scope,'CURV?');
```

```
18
19 if noB == 2
20     ydata = readbinblock(id_scope,'int16');
21 elseif noB == 1
22     ydata = readbinblock(id_scope,'int8');
23 else
24     error('Unsupported word length');
25 end
26 flush(id_scope); % Flush the termination character from the scope
27
28
29 end
```

C.1.6 DPOread.m

```
1  %% DPORead.m
2  % Adjusted 2021-11-04 by AOP:
3  % - Byte order and word length controlled by InitScope (16-bit)
4  % - Cleaned up old code (still found in GitLab)
5  % - Using visadev in InitScope instead of the deprecated visa
       ↪ statement:
6  % => Update from the deprecated binblockread function to readbinblock
7  % => Update from fprintf and freadf to write and read
8  % - Corrected an error in the calculation of wf. Now including YOF.
9
10 % Use the DPO3000 Series Programmer Guide when editing the script.
11
12 function [x,wf,tidsskala] = DPORead(id_scope,ch,samples)
13
14 noB = 2; % Number of bytes per word (8-bit if 1, 16-bit if 2, ...)
15
16 write(id_scope,['DAT:SOU CH' num2str(ch)]); % Velge kanal. ch=1 betyr
       ↪ CH1
17 pause(.1);
18 %{
19 % Record length per visible time interval, affecting the sample rate
20 rec_len = str2double(writeread(id_scope,'HOR:RECO?'));
21
22 if nargin() == 3
23     if samples > rec_len
24         warning('The record length is set too low. Adjusting and
               ↪ waiting 10 s...')
25         write(id_scope,['HOR:RECO ' num2str(samples)]); % New record
               ↪ length
26         pause(10);
27     elseif samples < rec_len
28         warning('Retrieving less than the record length (full view).')
29     end
30 else
31     samples = rec_len;
32 end
33 %}
34
35 % Set what samples to retrieve
36 write(id_scope,'DAT:START 1');
37 pause(.1);
38 write(id_scope,['DAT:STOP ' num2str(samples)]);
39 pause(.1);
40
41 % disp(['Samples: ' num2str(samples)])
42
43 % Read the data
44 writeline(id_scope,'ACQ:STATE RUN');
45 while str2double(writeread(id_scope, 'BUSY?'))
```

```
    pause(.5);
end
write(id_scope,'CURV?');
pause(.1);

if noB == 2
    ydata = readbinblock(id_scope,'int16');
elseif noB == 1
    ydata = readbinblock(id_scope,'int8');
else
    error('Unsupported word length');
end
flush(id_scope); % Flush the termination character from the scope

%% Scaling of the data
% Horizontal scaling
tidsskala = str2double(writeread(id_scope,'HOR:SCA?'));
pause(.1);
% Horizontal offset
xze = str2double(writeread(id_scope,'WFMO:XZE?'));
pause(.1);
% Horizontal increment
xin = str2double(writeread(id_scope,'WFMO:XIN?'));
pause(.1);
% Vertical multiplying factor
ymu = str2double(writeread(id_scope,'WFMO:YMU?'));
pause(.1);
% Vertical offset
yze = str2double(writeread(id_scope,'WFMO:YZE?'));
pause(.1);
% Digital vertical offset
yof = str2double(writeread(id_scope,'WFMO:YOF?'));
pause(.1);

% Time vector
x = (0:(length(ydata)-1))*xin + xze;
% Voltage/current vector
wf = (ydata-yof)*ymu + yze;
```

C.1.7 InitScopeAndGen.m

```
instrreset
pause(.2);

%num_cycles = 100;       % 1 to 1e6

% Init signal generator
id_sig = visadev('ASRL5::INSTR');
id_sig.BaudRate = 57600;
id_sig.FlowControl = 'hardware';
pause(0.2);

%{
% 1. Configure the burst waveform
writeline(id_sig,'FUNC SIN');
writeline(id_sig,['FREQ ',num2str(f)]);
writeline(id_sig,['VOLT ',num2str(V)]);
writeline(id_sig,'VOLT:OFFS 0.0');
% 2. Select the triggerd or gated burst mode
writeline(id_sig,['BURS:MODE ','TRIG']);        % TRIG or GAT
% 3. Set the burst count (1 to 1e6)
writeline(id_sig,['BURS:NCYC ',num2str(num_cycles)]);
% 4. Set the burst period
writeline(id_sig,['BURS:INT:PER ',num2str(2*(num_cycles/f) + 200e-9)]);
```

```
% 5. Set the burst starting phase
writeline(id_sig,'BURS:PHAS 0.0');
% 6. Select the trigger source
writeline(id_sig,'TRIG:SOUR IMM');
% 7. Enable the burst mode
writeline(id_sig,'BURS:STAT ON');
%}


% Init DPO
%id_scope = visadev('USB0::0x0699::0x0410::C010246::INSTR'); % original one
id_scope = visadev('USB0::0x0699::0x0410::C011044::INSTR');
write(id_scope, 'DATA:ENCDG SRIBINARY;WIDTH 2');
pause(0.2);
write(id_scope, 'CH1:COUP AC');
pause(0.2);
write(id_scope, 'CH2:COUP AC');
pause(0.2);
```

C.2 Simulation parameters

C.2.1 Density of air

```
% densityAir.m
% Ocean Technology (Acoustics) - Institute of Physics and Technology
% University of Bergen
% By Aslak Jentoft Thorbjoernsen, 2023
function rho = densityAir(t,p,hrel,xco2)
% Input parameters
%       t: temperature in degrees celsius
%       p: absolute pressure [Pa]
%       h: relative humidity [%] (e.g. 25 % as 25)
%       xco2: molecular fraction of CO2 in air
% Validity of model
%       600 hPa <= p <0 1100 hPa
%       15 C <= T <= 30 C

% Default value of the molecular fraction of CO2 (400 ppm), if not specified
if ~exist("xco2","var")
    xco2 = 0.000400;
end
if p < 50e3
    error('Pressure given as hPa or kPa? Must be [Pa].')
end
if t > 50
    error('Temperature given as Kelvin? Must be [C]')
end
if (p < 60e3) || (p > 110e3)
    warning('Model only valid for 60 kPa <= p <= 110 kPa.')
end
if (t < 15) || (t > 30)
    warning('Model only valid for 15 <= t <= 30 [C].')
end
if hrel < 1
    warning('Is relative humidity given as %, e.g., 25 % as 25?')
end

% Conversion from % to [0,1]
h = hrel / 100;
```

```
37
38 %% Constant for computing compressibility and xv
39 %   https://iopscience.iop.org/article/10.1088/0026-1394/45/2/004/met
40 %   Picard 2008
41 a0 = 1.58123e-6;          % [K/Pa]
42 a1 = -2.9331e-8;          % [1/Pa]
43 a2 = 1.11043e-10;         % [1/(K Pa)]
44 b0 = 5.707e-6;            % [K/Pa]
45 b1 = -2.051e-8;           % [1/Pa]
46 c0 = 1.9898e-4;           % [K/Pa]
47 c1 = -2.376e-6;           % [1/Pa]
48 d  = 1.83e-11;            % [K^2/Pa^2]
49 e  = -0.765e-8;           % [K^2/Pa^2]
50
51 % Constant for enhancement factor f used to compute xv
52 alp = 1.00062;
53 be  = 3.14e-8;            % [1/Pa]
54 gam = 5.6e-7;             % [1/K^2]
55
56 % Constants for vapour pressure at saturation, psv
57 A = 1.2378847e-5;         % [1/K^2]
58 B = -1.9121316e-2;         % [1/K]
59 C = 33.93711047;
60 D = -6.3431645e3;         % [K]
61
62 %% Equation for Z and constants unchanged from CIPM-81/91
63 % Picard 2008
64 %       T: temperature in Kelvin
65 %       t: temperature in degrees celcius
66 T = 273.15 + t;
67
68 % Enhancement factor f
69 f = alp + be*p + gam*(t^2);
70 % Vapour pressure at saturation
71 psv = 1 * exp(A*(T^2) + B*T + C + D/T);
72 % Molecular fraction of vater vapour
73 xv = h * f * (psv / p);
74 % Compressional constant Z
75 Z = 1 - (p/T) * (a0 + a1*t + a2*(t^2) + (b0 + b1*t)*xv + (c0 +
    ↪ c1*t)*(xv^2)) + ((p^2) / (T^2)) * (d + e*(xv^2));
76
77 %% Calculations of density
78 % Picard 2008
79 pa = ((3.483740 + 1.4446*(xco2 - 0.0004))) * (p / (Z*T))*(1 -
    ↪ 0.3780*xv) / 1e3;
80
81 rho = pa;
82 end
```

C.2.2 Absorption coefficient

```
1 % absorptionInAir.m
2 % Ocean Technology (Acoustics) - Institute of Physics and Technology
3 % University of Bergen
4 % By Aslak Jentoft Thorbjoernsen, 2023
5 function [a,alpha] = absorptionInAir(f,p,hrel,t)
6 %
7 % Calculations follows the ANSI/ASA S1.26-2014 American National
    ↪ Standard
8 % Methods for Calculation of the Absorption of Sound by the Atmosphere
9 %
10 % Input parameters
11 %       f: frequency [Hz]
12 %       p: absolute pressure [Pa]
```

```
%       hrel: relative humidity [%] (e.g. 25 % as 25)
%       t: temperatures [degrees C]
% Returns
%       a: attenuation coefficient in decibels per meter [dB/m]
%       alpha: attenuation coefficient in Neper per meter [Np/m]

if p < 20e3
    error('Pressure given as hPa or kPa? Must be [Pa].')
end
if t > 50
    error('Temperature given as Kelvin? Must be [C]')
end
if hrel < 1
    warning('Is relative humidity given as %, e.g., 25 % as 25?')
end

% Conversion to Kelvin
T = 273.15 + t;
% Conversion to kPa
P = p / 1e3;

% Reference values
T0 = 273.16;    % [K] - triple-point isothermal temperature (+0.01 C)
Pref = 101.325; % [kPa]
Tref = 293.15;  % [K] - reference room temperature 20 degrees C

V = 10.79586 * (1-(T0/T)) - 5.02808 * log10(T/T0) + 1.50474e-4 * (1 -
    ↪ 10^(-8.29692*(T/T0 - 1))) + 0.42873e-3 * (-1 + (10^(4.76955 * (1
    ↪ - (T0/T))))) - 2.2195983;
% Molar concentration h of water vapor
h = hrel * (10^V) * (P/Pref)^-1;

% Relaxation frequency for O2
fr_O = (P/Pref) * (24 + (((4.04e4 * h) * (0.02 + h)) / (0.391 + h)));
% Relaxation frequency for N
fr_N = (P/Pref) * (T/Tref)^(-1/2) * (9 + 280*h*exp(-4.170*
    ↪ ((T/Tref)^(-1/3) - 1)));

% Long version (ANSI/ASA Annex A)
%{
XO = 0.209;
XN = 0.781;
OO = 2239.1;    % [K]
ON = 3352.0;    % [K]
% Speed of sound as used in the standard
c = 343.2 * ((T/Tref)^(1/2));
% Maximum atmospheric absorption in a distance of one wavelength
% (vibrational relaxation)
alambda_maxO = 1.559 * XO * ((OO / T)^2) * exp(-OO / T);
alambda_maxN = 1.559 * XN * ((ON / T)^2) * exp(-ON / T);
% Molecular absorption caused by vibrational relaxation of
% oxygen and nitrogen, respectively
avibO = alambda_maxO * (f / c) * ((2 * fr_O * f) / (fr_O^2 + f^2));
avibN = alambda_maxN * (f / c) * ((2 * fr_N * f) / (fr_N^2 + f^2));

% acr = acl + arot
% acl: viscosity, heat conduction, and diffusion processes
% arot: molecular absorption caused by rotational relaxation
acr = (1.60e-10 * (T/Tref)^(1/2) * f^2) * (P/Pref)^(-1);

% Attenuation coefficient [dB/m]
a = (acr + avibO + avibN);
% Attenuation coefficient [Np/m]
alpha = (acr + avibO + avibN) / 8.686;
%}

% Preferred calculation of the attenuation coefficient (ANSI/ASA)
% Attenuation coefficient [dB/m]
```

```
78 a = 8.686 * f^2 * ((1.84e-11 * (P/Pref)^(-1) * (T/Tref)^(1/2)) +
       ↪ (T/Tref)^(-5/2) * (0.01275 * exp(-2239.1/T) * (fr_O/(fr_O^2 +
       ↪ f^2))) + 0.1068 * exp(-3352/T) * (fr_N / (fr_N^2 + f^2)));
79 % Attenuation coefficient [Np/m]
80 alpha = f^2 * ((1.84e-11 * (P/Pref)^(-1) * (T/Tref)^(1/2)) +
       ↪ (T/Tref)^(-5/2) * (0.01275 * exp(-2239.1/T) * (fr_O/(fr_O^2 +
       ↪ f^2))) + 0.1068 * exp(-3352/T) * (fr_N / (fr_N^2 + f^2)));
81
82 end
```

C.3 Electric calculations

C.3.1 Zero-crossing method

```
1  function times = zero_crossings(s,x,M)
2  % Finds the M first zero crossings from input s, and returns the
3  % corresponding values in x.
4  % The algorithm uses a 25-point average to smoothen the signal to
       ↪ remove
5  % noise/fluctuation at the zero crossings.
6  % Cublic spline interpolation is further used to get an appropriate
7  % value of the zero crossing.
8
9  if ~(length(s) == length(x))
10     error('Error: Input vectors s and x are of different length.')
11 end
12
13 % FIR filter
14 N = 25;
15 b = (1/N) * ones(1,N);
16 a = 1;
17 y = filter(b,a,s);
18
19 % Locate positive values
20 n = y(N:end) > 0;
21 y = y(N:end);
22 x = x(N:end);
23
24 % Counters
25 j = 1;
26 k = 0;
27 for i = 1:length(n)-1
28     % End interation if M number of zero-crossings are found
29     if k == M
30         break
31     end
32     L = 100;
33     if n(i) == 0 && n(i+1) == 1
34         % Time step
35         dt = x(i+1) - x(i);
36         % Cubic spline interpolation
37         yq = interp1(x,y,x(i):dt/L:x(i+1),'spline');
38         % Extracting the index of the value closest to zero
39         [~,ind] = min(abs(yq));
40         times(j) = x(i) + dt * ((ind-1)/(L-1));
41         j = j + 1;
42         k = k + 1;
43     elseif n(i) == 1 && n(i+1) == 0
44         dt = x(i+1) - x(i);
45         yq = interp1(x,y,x(i):dt/L:x(i+1),'spline');
46         [~,ind] = min(abs(yq));
```

```
47          times(j) = x(i) + dt * ((ind-1)/(L-1));
48          j = j + 1;
49          k = k + 1;
50      end
51  end
52  end
```

C.3.2 Sliding average filter omitting NaN values

```
1  function [Yout,Xout] = FIRavg(N,Yin,Xin)
2  % Sliding average window
3  % The function will return the filtered signal, omitting NaN values in
       ↪ the
4  % Yin vector and scaling remaining coefficients in the sliding average
5  % window, such that length(windowcoefficients) <= N.
6  %   In other words, if 4 of 20 (N) values in the current window is NaN,
7  %   then the coefficients will be (1/16) and not (1/20).
8  %
9  if ~exist('Xin','var')
10     Xin = zeros(1,length(Yin));
11 end
12
13 for n = N:length(Yin)
14     if sum(isnan(Yin(n-(N-1):n))) == N
15         y(n-(N-1)) = NaN;
16     else
17         y(n-(N-1)) = sum(Yin(n-(N-1):n) .* (~isnan(Yin(n-(N-1):n)) *
               ↪ (1 / sum(~isnan(Yin(n-(N-1):n))))) ,'omitnan');
18     end
19 end
20
21 % Return corresponding x vector to filtered y values
22 Xout = Xin(N:end);
23 Yout = y;
24 end
```